Universiteit
Leiden
The Netherlands

# Marvellous ubiquitin : avenging the MERS-coronavirus papain-like protease

Knaap, R.C.M.

**Citation**
Knaap, R. C. M. (2020, February 12). *Marvellous ubiquitin : avenging the MERS-coronavirus papain-like protease*. Retrieved from https://hdl.handle.net/1887/85167

| | |
|---|---|
| Version: | Publisher's Version |
| License: | Licence agreement concerning inclusion of doctoral thesis in the Institutional Repository of the University of Leiden |
| Downloaded from: | https://hdl.handle.net/1887/85167 |

**Note:** To cite this publication please use the final published version (if applicable).

Cover Page

Universiteit Leiden

The handle http://hdl.handle.net/1887/85167 holds various files of this Leiden University dissertation.

**Author**: Knaap, R.C.M.
**Title**: Marvellous ubiquitin : avenging the MERS-coronavirus papain-like protease
**Issue Date**: 2020-02-12

# MARVELLOUS UBIQUITIN:

## AVENGING THE MERS-CORONAVIRUS PAPAIN-LIKE PROTEASE

ROBERT C.M. KNAAP

# Marvellous ubiquitin:
## avenging the MERS-coronavirus papain-like protease

Robert Cornelis Martinus Knaap

## COLOPHON

**Marvellous ubiquitin: avenging the MERS-coronavirus papain-like protease**
Robert C.M. Knaap
PhD thesis, Leiden University Medical Center, 2020

Cover design: Renate Holtrop
Layout & printing: Optima Grafische Communicatie

ISBN: 978-94-6361-389-7

All rights reserved. No part of this thesis may be reproduced, stored in retrieval systems, or transmitted in any form or by any means without prior permission of the author.

# Marvellous ubiquitin:
## avenging the MERS-coronavirus papain-like protease

Proefschrift

ter verkrijging van
de graad van Doctor aan de Universiteit Leiden,
op gezag van Rector Magnificus prof.mr. C.J.J.M. Stolker,
volgens besluit van het College voor Promoties
te verdedigen op woensdag 12 februari 2020
klokke 16:15 uur

door

Robert Cornelis Martinus Knaap
geboren te Goes
in 1989

**Promotor**

Prof. dr. E.J. Snijder

**Co-promotor**

Dr. ir. M. Kikkert

**Leden promotiecommissie**

Prof. dr. D. van Baarle (Utrecht University)

Dr. P.P. Geurink

Prof. dr. R.C. Hoeben

Prof. dr. S. Perlman, MD (University of Iowa, USA)

A painting is finished when the artist says it is finished.

- statement attributed to Rembrandt van Rijn -

## TABLE OF CONTENTS


| | | |
|---|---|---|
| Chapter 1 - | General introduction | 9 |
| Chapter 2 - | Crystal structure of the Middle East respiratory syndrome coronavirus papain-like protease bound to ubiquitin facilitates targeted disruption of deubiquitinating activity to demonstrate its role in innate immune suppression | 27 |
| Chapter 3 - | The deubiquitinating activity of Middle East respiratory syndrome coronavirus papain-like protease delays the innate immune response and enhances virulence in a mouse model | 53 |
| Chapter 4 - | Potent and selective inhibition of pathogenic viruses by engineered ubiquitin variants | 81 |
| Chapter 5 - | Engineering improved ubiquitin variants that inhibit the papain-like protease of Middle East respiratory syndrome coronavirus | 119 |
| Chapter 6 - | Structure and function of viral deubiquitinating enzymes | 143 |
| Chapter 7 - | General discussion | 171 |
| | References | 199 |
| | List of abbreviations | 227 |
| | Dutch summary | 232 |
| | Curriculum vitae | 236 |
| | List of publications | 237 |

# 1 General introduction

## RNA VIRUSES

Our world and its health care system are continuously confronted with newly emerging viruses. In the era of changing climates and ecosystems as well as intensified international travel and trade, the emergence and spread of viruses has become more frequent and unpredictable. Despite the advances made in countermeasure development, outbreaks of (re-)emerging viruses with concomitant social and economic impact occur more often. In the last decade alone, the world witnessed outbreaks caused by human viruses such as influenza A virus, Middle East respiratory syndrome (MERS) coronavirus (CoV), Ebola virus, and Zika virus, each with major societal impact. Most emerging and re-emerging viruses have an RNA genome. RNA viruses have a high mutation frequency because their RNA polymerases exhibit low fidelity [1]. Consequently, RNA virus populations are genetically diverse and therefore referred to as quasispecies: a cloud of related viral genomic sequences that are subjected to a continuous process of genetic variation, selection and collectively contribute to the characteristics of the population [2, 3]. A part of the spontaneously introduced mutations are likely lethal or decrease viral fitness, but when the environment changes, specific variants may turn out to have a selective advantage [4]. In this manner, RNA viruses can adapt easily to changing circumstances and this has major implications. Firstly, these viruses can cross species barriers and cause so-called zoonotic infections when an animal virus jumps to the human host. Illustrative are the severe acute respiratory syndrome (SARS)- and MERS-CoVs that have caused human outbreaks as a result of zoonotic transmission. Secondly, those RNA viruses have the potential to create vaccine escape mutants and develop resistance to antiviral therapies making it difficult to target them efficiently. To date, however, there are no approved vaccines or antiviral agents at all against the zoonotic SARS- and MERS-CoVs.

## CORONAVIRUSES

The pandemic potential of CoVs was first noticed with the outbreak of SARS-CoV in Southeast Asia in 2002 and 2003 [5-8]. SARS-CoV spread to 25 countries and around 8,000 individuals were diagnosed with SARS-CoV infection, with about 10% succumbing to this novel syndrome [9]. SARS-CoV infection caused lower respiratory tract disease that can progress to an atypical pneumonia characterized by acute lung injury and acute respiratory distress syndrome (ARDS). The lungs of affected individuals showed diffuse alveolar damage, alveolar infiltrates and oedema. Human-to-human transmission of SARS-CoV was shown to rely on droplets and aerosols, and transmission primarily occurred in the healthcare setting by particular infected individuals, so-called 'super-spreaders', who were implicated in the disproportionally efficient spread of SARS-CoV to many other individuals [10-12]. The transmission chain in humans was broken within 6 months due to strict public health- and quarantine measures. Only a few close contacts of infected individuals showed seroconversion, indicating low numbers of asymptomatic SARS-CoV infections, which

eased the eradication of SARS-CoV [13]. The sequence of the SARS-CoV genome was rapidly determined and found to be genetically distinct from the other CoVs known at that time [14, 15]. Viruses closely related to SARS-CoV were however found in palm civets and a raccoon dog at a live-animal market in China [16]. Palm civets were susceptible to SARS-CoV infection but the low numbers of positive animals hinted at the existence of another natural reservoir of SARS-CoV. Two years later, Chinese horse shoe bats were identified as this reservoir [17, 18]. SARS-like CoVs from bats contained greater sequence variation than viruses isolated from palm civets suggesting that the virus had adapted to the civet host [17, 18]. Indeed, in civets, the receptor binding domain (RBD) of the spike (S) protein of SARS-like CoVs had adapted in a way that facilitated more efficient binding to the human cellular receptor, angiotensin-converting enzyme 2 (ACE2) [19-21]. Intriguingly, additional SARS-like CoVs were recently isolated from bats and showed to efficiently bind to human ACE2 and to replicate in human cells, albeit at low levels, without requiring adaptation [22]. However, for epidemic disease in humans further adaptation of these bat viruses may be required [23, 24]. Nevertheless, this highlights that SARS-like CoVs remain potential threats for the human population and underline the need to develop vaccines and therapeutics to counter future emerging CoVs.

In 2012, another pathogenic CoV was isolated from a patient in Saudi Arabia, who died of acute pneumonia and renal failure [25]. The genome sequence of this virus, initially named human CoV (HCoV)-EMC/2012, was determined and turned out to be closely related to that of the bat CoVs HKU4 and HKU5 [26]. Due to the majority of cases occurring in the Arabian Peninsula, the virus was re-named MERS-CoV [27]. Sporadic MERS-CoV cases have since been reported across the globe, but these were mainly the result of infected individuals traveling from the Middle East. The largest MERS-CoV outbreak outside the Middle East occurred in South Korea in 2017, resulting in 186 cases and 38 deaths [28, 29]. The clinical presentation of MERS-CoV infection can range from asymptomatic to severe pneumonia and ARDS [30, 31]. Like SARS-CoV, the virus has frequently been transmitted in healthcare facilities [32, 33]. Based on sequence variation in MERS-CoV genomes derived from human samples, the virus must have been introduced into the human population on multiple occasions. It was postulated that this could be the result of the movement of infected human individuals, animals or animal products, which transmitted the virus [34]. Serological evidence subsequently indicated that MERS-CoV had been circulating in dromedary camels for decades, while no evidence of the virus' presence was found in cattle, sheep, goats, horses or poultry [35-39]. In addition, neutralizing antibodies were found in individuals who had been frequently exposed to dromedary camels, like shepherds and slaughterhouse workers [40]. In dromedary camels, MERS-CoV replicates in the upper respiratory tract without causing severe disease, and from nasal swabs virus could be isolated that was able to replicate in human cells [41, 42]. Based on these observations, dromedary camels were proposed to be the intermediate source for MERS-CoV transmission to humans. Indeed, several studies demonstrated high similarity between MERS-CoV sequences from human and dromedary samples from the same farm [43, 44]. Human cases of MERS-CoV continue to be reported and most of these probably result from

virus spill-over from dromedary camels to humans. This illustrates the urgent need for vaccines and antiviral therapies against MERS-CoV to be prepared for larger outbreaks, for example due to increased transmissibility between humans. As in the case of SARS-CoV, MERS-like CoVs that are closely related to MERS-CoV were identified in bats, which can pose an additional risk when these viruses get transmitted to other hosts [45, 46].

Besides the two highly pathogenic CoVs described above, four more HCoVs have been identified, which can each cause respiratory infections associated with mild disease [47]. HCoV-OC43 and -229E were discovered in the 1960s, while HCoV-NL63 and -HKU1 were identified just after the SARS-CoV outbreak [48-53]. It has been proposed that these viruses once were zoonotic pathogens and, like SARS-CoV and MERS-CoV, originate from bats, which were found to host a large variety of CoVs [54-57]. For HCoV-NL63 and HCoV-229E, related bat CoVs were indeed identified and, interestingly, some evidence points to dromedary camels as a likely intermediate host for HCoV-229E, which would make its transmission route similar to that of MERS-CoV [58-62]. In contrast, rodents are the likely reservoir of HCoV-OC43, which can transmit the virus to livestock, after which spill-over into humans can occur [63, 64]. Similarly, for HCoV-HKU1 rodents are considered as the primary animal reservoir, while its intermediate host remains to be identified [58].

## TAXONOMY

The recent discovery of many new nidoviruses during next-generation sequencing-based metagenomics studies has resulted in an ongoing extension and revision of the nidovirus order, which now consists of seven proposed suborders, each with one or more underlying families (ICTV). The best studied nidoviruses belong to the families *Coronaviridae* (suborder *Cornidovirineae*) and *Arteriviridae* (suborder *Arnidovirineae*). The latter family (so far) does not contain viruses infecting humans; these viruses infect livestock (horses and pigs), rodents, possums and non-human primates [65]. The prototypic equine arteritis virus (EAV) was the first isolated and characterized arterivirus. EAV usually causes subclinical or influenza-like disease and may cause reproductive disease in horses [66-68]. The most economically significant arterivirus currently is porcine reproductive and respiratory syndrome virus (PRRSV), which causes severe problems in the global swine industry [69]. Estimated losses due to PRRSV infections are $664 million per year in the United States of America alone [70]. To control PRRSV, a better understanding of PRRSV evolution, replication and protective immunity is needed, in order to develop improved vaccines [71]. These may replace the currently available vaccines, which in general are only moderately effective.

The *Coronaviridae* family, subfamily *Orthocoronavirinae*, consists of four genera: α-, β-, γ-, δ-CoVs. HCoVs-229E and NL-63 belong to the α-CoVs while the four-other human-infecting CoVs, HCoV-OC43, HCoV-HKU1, SARS-CoV, and MERS-CoV, are in the *β-CoV* genus. Economically important CoVs infecting animals include porcine epidemic diarrhoea virus (PEDV), transmissible gastroenteritis coronavirus (TGEV) and feline CoV (FCoV), which all belong to the α-CoVs. Also,

infections with β-CoVs mouse hepatitis virus (MHV), bovine CoV and γ-CoV avian infectious bronchitis virus (IBV) cause substantial problems in their respective hosts, of which the latter two infections have economic impact as well. Besides respiratory disease, the CoVs that infect livestock usually also infect the gastrointestinal tract.

Interestingly, nidoviruses, such as arteriviruses and CoVs, employ a similar replication strategy and have a comparable genome organization, however, the average genome size of arteriviruses is only 12- to 16 kilobases (kb), which is less than half the size of the average CoV genome (Fig. 1A) [67, 72]. The acquisition of a proofreading exoribonuclease (ExoN) by an ancestor of CoVs and other large-genome nidoviruses may have facilitated the expansion of the CoV genome to an impressive size of 26- to 34 kb, which is extremely large for positive-stranded RNA viruses [73]. Indeed, coronaviruses had the largest known RNA virus genomes until recently, when two nidoviruses with even larger genome sizes of 35.9- and 41.1 kb were isolated from a sea hare and a planarian, respectively [74, 75]. Surprisingly, the genome organization of these two viruses contrasts with the polycistronic organization found in other commonly-known nidoviruses, as will be further discussed below [75, 76].

## THE CORONAVIRUS REPLICATION CYCLE

Coronaviruses are characterized by the crown-like appearance of their surface projections (*corona* is Latin for crown), which are formed by trimers of the S glycoprotein that are embedded in the virus envelope (Fig. 1A). The CoV replication cycle (Fig. 1B) starts with the interaction of the S protein with a cell surface receptor, making the S protein the primary determinant of cell tropism. The SARS-CoV S protein binds the ACE2 receptor that is expressed on ciliated epithelial cells of the respiratory tract [19, 77]. Surprisingly, this same receptor can be used by HCoV-NL63, in contrast to the other α-CoVs, which employ aminopeptidase N [78]. The functional receptor for MERS-CoV is dipeptidyl peptidase 4, which is present on human non-ciliated bronchial epithelial cells [79]. The S protein needs to be proteolytically cleaved into two subunits, S1 and S2, to activate fusion. The S1 subunit contains the RBD whereas the fusion peptide, located in the S2 subunit, is required for fusion of the viral envelope with primarily the endosomal membrane or alternatively the plasma membrane [80, 81].

Upon fusion, the CoV RNA genome, which is of positive polarity and contains a 5' cap structure and a 3' poly-A tail, is released into the cytosol. The cellular translation machinery translates the first two ORFs of the CoV genome, ORF1a and ORF1ab, which encode the replicative machinery of the virus. Polyprotein (pp) 1ab, translated from ORF1ab, is produced after a -1 ribosomal frameshift at the ORF1a/1b border, which is directed by a slippery sequence and a downstream RNA pseudoknot structure. ORF1a and ORF1ab together encode 16 non-structural proteins (nsps). This is not true for γ-CoVs, which express only 15 nsps as they lack a homolog of the nsp1 subunit found in other CoVs. The two polyproteins are cleaved into functional nsps by

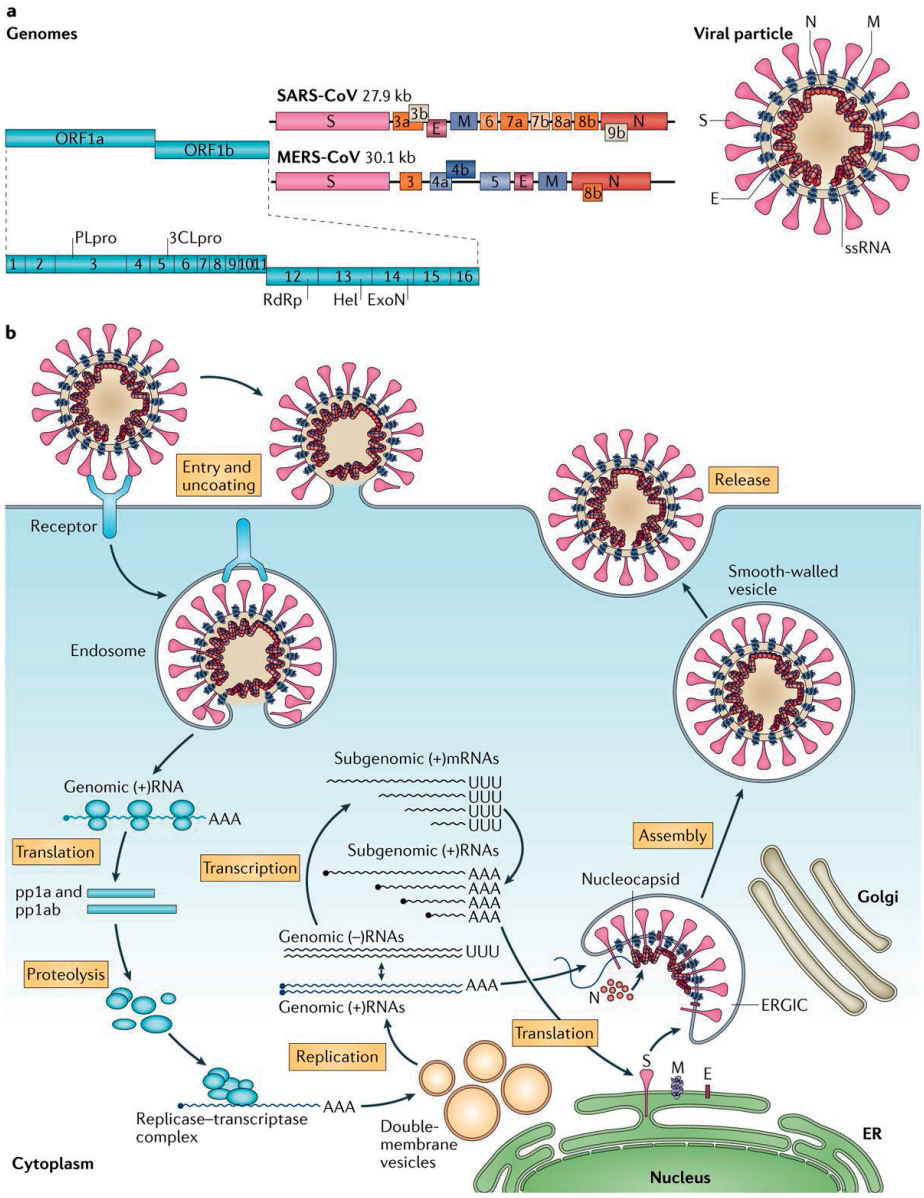


**Figure 1. Genome organisation, structure of the virus particle and replication cycle of SARS- and MERS-CoV.** (A) Organization of the SARS- and MERS-CoV genome, of which the first two thirds encode for the two replicase polyproteins pp1a and pp1ab, which are proteolytically cleaved into functional nsps. Several nsps have important enzymatic activities like $PL^{pro}$, $3CL^{pro}$, RdRp, helicase (Hel) and ExoN. From the remaining one-third of the genome, a nested set of subgenomic RNAs is produced that encode for the accessory and structural proteins. Those structural proteins include the S, envelope (E), membrane (M) and nucleocapsid (N) proteins, which form together with genomic RNA a virus particle. (B) The S protein binds to a cellular receptor to mediate entry into the host cell. Genomic RNA is released in the cytoplasm and a part is directly translated into the replicase polyproteins. The nsps derived after cleavage of those polyproteins form the replication and transcription complexes that are associated with membrane modifications. Subsequently, genomic RNA is replicated and structural proteins are produced that form the new virions, which bud from ER/ER-Golgi intermediate compartment membranes and are released from the cell. Reproduced with permission from [259].

internally encoded proteases. CoVs encode two or three such proteases depending on the virus species. Located within nsp5, all CoVs have a chymotrypsin-like cysteine protease (also referred to as 3C-like protease ($3CL^{pro}$) or main protease), which deviates from the canonical chymotrypsin-like serine proteases [82]. Lineage B (to which SARS-CoV belongs), C (including MERS-CoV) and D β-CoVs, γ-CoVs, and δ-CoVs express one functional papain-like protease (PLP, annotated as $PL^{pro}$) in nsp3 while other CoVs express two PLPs annotated as PLP1 and PLP2. The three junctions in the nsp1-nsp4 region of the replicase polyproteins are cleaved by $PL^{pro}$ or PLP1 and PLP2, whereas the remaining downstream cleavage sites are all processed by $3CL^{pro}$. Most of the resulting nsp subunits assemble into replication and transcription complexes (RTCs) that take care of viral RNA replication and subgenomic RNA synthesis (Fig. 1B). These complexes are associated with modified intracellular membranes, which derive from the endoplasmic reticulum (ER) and consist of double membrane vesicles (DMVs) and convoluted membranes [83-89]. There is still debate about the precise function(s) of these modified membranes [90-94], which are generally assumed to provide a scaffold and specialized microenvironment for viral RNA synthesis. It has also been postulated that they play a role in preventing innate immune responses by shielding the viral RNA and its replication intermediates from the innate immune sensors in the cytosol. For MERS-CoV and SARS-CoV, expression of nsp3 and nsp4 suffices to mimic DMV formation, although these DMVs are smaller compared to those formed in MERS-CoV-infected cells [95]. There seems to be an additional role for the nsp6 transmembrane protein in membrane modification, however its exact contribution remains unclear [95-97].

Important enzymes for RNA synthesis are expressed from ORF1ab, including the RNA-dependent RNA polymerase (RdRp; nsp12) and the helicase (nsp13) [98-103]. For template-dependent RNA synthesis *in vitro,* a complex of nps12 with nsp7 and nsp8 is required, which was recently crystallized [104, 105]. Additionally, multiple activities in nsp8 have been proposed, like primase activity and *de novo* RdRp activity [106, 107]. However, these were not supported in a recent study that showed 3'-terminal adenylyltransferase activity in nsp8, which was speculated to function in 3'-polyadenylation of viral RNAs [108]. The nsp7+8+12 tripartite complex associates with nsp14, which includes a 3'-to-5' ExoN domain that is thought to serve an important role in a proofreading mechanism enhancing the fidelity of RNA synthesis [105, 109-113]. A notion supported by the observation that SARS-CoV and MHV ExoN-knockout mutants have an increased mutation frequency compared to wt virus [111, 114, 115]. Interestingly, infectious virus progeny of TGEV, HCoV-229E, and MERS-CoV ExoN mutants could not be recovered and defects in RNA synthesis were observed, suggesting that ExoN has a more direct role in CoV replication [116-118]. Nsp10 was proven to stimulate the ExoN activity of nsp14 in order to efficiently excise mismatched nucleotides from double-stranded (ds) RNA [109, 119]. Modification of the 5'-terminal cap structure of CoV RNAs requires the N7-guanine methyltransferase (MTase) in nsp14, and the 2'-O-MTase in nsp16, of which the latter is also activated by nsp10 [120-125]. Besides genomic RNA, nidoviruses synthesize a nested set (*nidus* is Latin for nest) of subgenomic RNAs that are copied from the 3'-proximal region of the genome and encode the structural and accessory

proteins (Fig. 1B). Discontinuous negative strand RNA synthesis produces a separate template for each subgenomic RNA in amounts that vary per RNA [126, 127]. After production of the structural proteins from these RNAs, novel genomes are packaged by the nucleocapsid protein, and these subsequently bud from ER/ER-Golgi intermediate compartment membranes where structural proteins have accumulated. The new virions produced in this manner are released from the cell via the exocytic pathway.

## UBIQUITINATION IN THE IMMUNE RESPONSE

Interactions between hosts and viruses shape their coevolution [128]. Hosts have developed mechanisms to detect and eliminate viruses, whereas viruses have developed strategies to prevent or delay sensing by the host or to subvert the cellular countermeasures [129-131]. Important pattern-recognition receptors (PRRs) that can recognize CoV RNA in the cytosol are retinoic acid-inducible gene I (RIG-I) and melanoma differentiation-associated gene 5 (MDA5) [132, 133]. RIG-I responds to single-stranded RNA bearing 5' tri- and di-phosphates and short double-stranded RNA (dsRNA), whereas MDA5 senses long dsRNA [134, 135]. Activation of RIG-I or MDA5 will activate transcription factors interferon regulatory factor (IRF) 3, IRF7 and nuclear factor kappa-light-chain-enhancer of activated B cells (NF-κB) via distinct pathways, after which these factors then translocate to the nucleus and induce the expression of type I and type III interferons (IFNs), and other pro-inflammatory cytokines. The difference between type I and type III IFNs is that type I IFNs are expressed by almost all cell types, while type III IFNs are mainly expressed by epithelial cells. Excreted IFNs can bind cell surface receptors to induce expression of IFN-stimulated genes (ISGs) in the infected as well as neighbouring cells. This second round of signal transduction involves the Janus kinase (JAK) and signal transducers and activators of transcription (STAT) proteins and induces an antiviral state. ISGs inhibit infection by further enhancing expression of sensors and by targeting specific steps in viral replication [136]. Type III IFNs, in contrast to type I IFNs, primarily bind receptors and thus induce expression of ISGs in epithelial cells, for example of the respiratory tract, suggesting that type III IFNs are important in the innate immune response against respiratory infections [137, 138]. Type I IFNs form an important bridge between the innate and adaptive immune response, the latter encompassing humoral- and cell-mediated immunity and immunological memory [139-141]. IFNs initiate expression of cytokines by immune cells, like natural killer cells and macrophages, which attract more immune cells to the site of infection. Moreover, type I IFNs promote antigen presentation by dendritic cells and enhance the development of T and B cell responses.

Some ISGs negatively regulate the IFN response in order to prevent excessive reactions [136]. Regulation of the IFN response is crucial to ensure a balanced response against the virus while also enabling its timely termination if needed. Reversible post-translation modifications (PTMs) of the protein factors involved in the innate immune response therefore are ideal regulators

[142, 143]. PTMs are covalent molecular modifications that are enzymatically attached to specific target proteins to modulate their function, activity, subcellular localization or conformation. Innate immune signalling is regulated by phosphorylation, the attachment of a phosphate group, and ubiquitination, the conjugation of one or more ubiquitin (Ub) moieties, but also acetylation, glutamylation, and deamidation play a role [143, 144].

Ubiquitin is a stable, conserved and ubiquitously expressed protein of only 76 amino acids that can be conjugated by forming an isopeptide bond between its C-terminal glycine residue and any lysine residue in a target protein [145]. Additionally, Ub can be conjugated to the N-terminal methionine of a protein by linear peptide bond formation. Ub can also be attached to the N-terminus or each of the seven internal lysine residues of another Ub molecule to form polyUb chains. K48- and K63-linked polyUb chains are well-studied and target a protein for proteasomal degradation or are important for cell signalling, respectively. PolyUb chains with other conformations are called atypical and their functions are still less well defined [146]. Identification of heterotypic Ub linkages, in which Ub subunits in the same polyUb chain are connected by different linkage types, adds another level of complexity to the Ub code and has yet to be functionally studied in depth [147]. Intriguingly, Ub can also be modified with other PTMs such as phosphorylation and acetylation [148, 149]. To conjugate Ub to a substrate, the actions of three enzymes are required, the E1 Ub-activating enzyme, an E2 Ub-conjugating enzyme and an E3 Ub ligase. On the other hand, PTMs are reversible and in the case of Ub, deubiquitinating enzymes (DUBs) can negate signalling by proteolytically removing Ub or Ub chains from a substrate [150]. Several targets in the signalling cascade of the innate immune response become ubiquitinated, which leads to their activation, or these ubiquitinated proteins can provide a scaffold to bind other signalling proteins. Together, this plays a role in activation of RIG-I, MDA5, and TNF receptor-associated factors (TRAFs) [151, 152], which usually involves Ub chains linked through K63. Moreover, innate immune signalling factors can also be degraded following the attachment of K48-linked Ub chains. Release of transcription factor NF-κB, which allows it to translocate to the nucleus, for example, is achieved by the conjugation of K48-linked Ub and subsequent degradation of inhibitor of NF-κB-α (IκBα). Besides the prominent role of K48 and K63-linked Ub, more evidence is accumulating that points to involvement of atypical Ub chain types in innate immunity [151, 152].

## INNATE IMMUNE SUPPRESSION BY CORONAVIRUSES

Many viruses, including CoVs, employ mechanisms to avoid or delay detection by the immune system while replicating in host cells. A hallmark of CoV infection is that type I IFNs are hardly produced by most infected cell types such as airway epithelial cells and fibroblasts [153-160]. However, various forms of viral single-stranded and dsRNA are produced during virus replication, which have properties that are recognized by PRRs and would therefore be able to trigger IFN responses [88, 132, 161]. As an exception, CoV-infected human plasmacytoid dendritic cells

induce a robust type I and type III IFN response via the Toll-like-receptor 7 pathway [162, 163]. In the case of MERS-CoV, it was shown that IFN-α and type III IFN were induced just by sensing of the virus whereas active replication was required for IFN-β secretion [163]. It is thought that CoVs evade or suppress activation of the innate immune response, at least in many cell types, enabling replication to high(er) virus titers [132, 164].

CoVs modify intracellular membranes, and possibly hide their RTCs within double membrane vesicles while dsRNA replication intermediates are produced [88, 161]. Consequently, dsRNA is sequestered in these vesicles and shielded from PRRs [91, 165]. Furthermore, viral mRNA cap modification is the result of the actions of nsp14 and nsp16. This cap structure is important for the cap-dependent translation of the viral RNA to produce nsps, structural and accessory proteins. Additionally, the mRNA cap structure can prevent recognition by PRRs such as MDA5, RIG-I and IFN-induced protein with tetratricopeptide repeats (IFIT), and thus it may be an important element of the viral immune evasion strategy. MHV with substitutions in conserved residues in the N7-MTase in nsp14, which are required for its activity, was severely attenuated and viral RNA was translated with decreased efficiency, making it difficult to examine the role of the N7-MTase in innate immune evasion [166]. Ablation of the 2'-O-MTase activity in nsp16 of MHV, HCoV-22E, SARS-CoV, and MERS-CoV resulted in attenuated viruses, particularly in immune competent cells [124, 167-170]. Replication was (partially) restored in the absence of IFIT1 or MDA5, suggesting that the 2'-O-MTase prevents activation of those intracellular sensors. The endoribonuclease (EndoU) activity in nsp15 is also used to prevent sensing of CoV RNA [171, 172]. Removal of this activity attenuated the virus and resulted in increased levels of dsRNA early in infection and higher IFN-β expression in infected primary macrophages relative to wt virus infection [173]. It was clearly demonstrated that EndoU prevents activation of both MDA5 and two other IFN-induced sensors, 2',5'-oligoadenylate synthetase (OAS) and protein kinase R (PKR) [173, 174]. Binding of dsRNA activates OAS, which in turn will synthesize 2'-5' oligoadenylate that will act as a second messenger to activate RNase L. RNase L can process host and viral RNAs into small RNAs that can trigger PRRs. Besides EndoU, accessory proteins MHV NS2 and MERS-CoV NS4b prevent activation of RNase L [175, 176]. Both are 2'-5' phosphodiesterases that degrade the second messenger 2'-5' oligoadenylate. Activation of PKR after detection of viral RNA in the cytoplasm induces phosphorylation of eukaryotic translation initiation factor 2. Consequently, protein synthesis is halted and stalled translation initiation complexes form aggregates that are known as stress granules. Viruses manipulate this stress response and for MERS-CoV it has been shown that NS4a specifically inhibits this PKR-mediated response [177-179].

Besides the strategies aimed to avoid production of viral RNA that can activate the innate immune response, described in the previous paragraph, CoVs also have mechanisms to suppress the innate immune response once it is triggered. Several other CoV accessory proteins, for example, have been implicated in suppression of the type I IFN and the NF-κB-mediated pro-inflammatory response, via distinct mechanisms [180-182]. Also, SARS-CoV nsp1 was shown to suppress host gene expression by two separate mechanisms [183, 184]. Firstly, it inhibits host

mRNA translation by associating with and inactivating the 40S ribosomal subunit [185]. Secondly, nsp1 promotes degradation of host mRNAs after inducing an endonucleolytic cleavage to which viral mRNAs are resistant [186]. Disruption of both these functions in mutant SARS-CoV resulted in higher levels of IFN-β mRNA compared to those in wt SARS-CoV-infected cells, highlighting the importance of nsp1 in innate immune evasion [187]. MERS-CoV nsp1 was shown to have similar functions although degradation of host mRNAs is performed differently compared to SARS-CoV nsp1 [188]. In contrast to SARS-CoV nsp1, which is exclusively located in the cytoplasm, MERS-CoV nsp1 is distributed between nucleus and cytoplasm, does not bind to the 40S ribosomal subunit, and targets newly synthesized nuclear-transcribed mRNAs for translation inhibition and mRNA degradation. Nsp3 of CoVs contains many different domains with known and unknown functions [189]. The conserved macrodomain (domain X) in nsp3 can bind and remove mono and poly(ADP-ribose) from mono- or poly(ADP-ribosyl)ated proteins, which has been implicated in suppression of innate immunity [110, 190-193]. Recently, it was suggested that the macrodomain counters the activity of poly(ADP-ribose) polymerases, which inhibit CoV replication and enhance IFN production [194]. Another domain in SARS-CoV nsp3, the $PL^{pro}$ domain, was postulated to be a viral DUB (vDUB) [195], and later it was indeed shown that purified recombinant $PL^{pro}$ can cleave Ub and interferon-stimulated gene 15 (ISG15), the latter being an Ub-like molecule [196-198]. The DUB activity is presumed to suppress the ubiquitination-dependent innate immune response. It has indeed been clearly demonstrated that the CoV PLP domain modulates the IRF3-dependent type I IFN response and the NF-κB-mediated pro-inflammatory response ([199-205] and reviewed by [206]). Due to the publication of contradictory results in literature, it has remained unclear for some time how CoV PLPs suppress activation of the immune response and what the contribution of DUB activity is. This matter can only be directly examined upon targeted elimination of this specific PLP activity. Using luciferase reporter systems and expression of the $PL^{pro}$ domain, with specifically introduced mutations, the first direct evidence that the DUB activities of SARS-CoV $PL^{pro}$ and MHV PLP2 are responsible for IFN-β and NF-κB antagonism was obtained [207, 208]. However, to verify whether this is truly biologically relevant, such experiments should also be performed in the context of the complete viral replication cycle rather than transient expression systems, and such an approach will be described in this thesis.

## HUMAN AND VIRAL DEUBIQUITINATING ENZYMES

Almost 100 human DUBs have been identified, which can be structurally separated into seven families. Ub-specific proteases (USP), Ub C-terminal hydrolases (UCH), Ovarian tumour proteases (OTU), and Machado-Joseph disease proteases (MJD) are cysteine proteases, as are two recently discovered DUBs that were classified as members of two new families, motif interacting with Ub-containing novel DUB family (MINDY) and Zinc finger with UFM1-specific peptidase domain

protein (ZUFSP), respectively [209-211]. The JAB1/MPN/MOV34 (JAMM) enzymes, forming the seventh family of DUBs, belong to the class of zinc-dependent metalloproteases.

Initially, comparative sequence analysis predicted that CoV genomes encode PLPs [98]. It was demonstrated that the catalytic activity of PLPs was necessary to release the N-terminal cleavage product of the viral replicase polyproteins, in a similar fashion as was shown for EAV nsp1 [212-216]. In EAV a second PLP, PLP2, was later identified in nsp2, which is responsible for cleaving the nsp2↓3 junction [217]. A first suggestion that arterivirus PLP2 might be vDUBs came from sequence comparisons revealing limited similarity with OTU-like proteases, which were suggested to have a role in regulation of the Ub-system [218]. Indeed, EAV PLP2 was shown to be a zinc-dependent vDUB resembling the OTU family of DUBs, which could cleave Ub and ISG15 from substrates and suppress RIG-I dependent and NF-κB-dependent signalling [219-221]. Also in Dugbe virus, a negative-stranded RNA virus belonging to the family *Nairoviridae* (order Bunyavirales), an OTU protease was predicted [218]. For another nairovirus, Crimean-Congo haemorrhagic fever virus (CCHFV), it was first shown that overexpression of this OTU domain results in overall deconjugation of Ub and ISG15 from cellular proteins [219]. The crystal structures of CCHFV OTU in complex with Ub or ISG15 were solved and facilitated modification of the binding site to prevent binding of Ub or ISG15, so that the importance of these interactions could be studied [222-225]. Interestingly, during a CCHFV infection the nairovirus DUB seems to remove Ub from specific substrates, since compared to DUB-negative CCHFV-infected cells the overall level of ubiquitinated proteins was not affected [225]. These specific substrates remain to be identified.

For CoVs, the first indication for a DUB function of the PLPs came from a structural relationship between SARS-CoV $PL^{pro}$ and herpesvirus-associated USP (HAUSP) [195]. HAUSP contains a zinc ribbon that was also predicted for CoV PLPs [226], and furthermore, SARS-CoV $PL^{pro}$ cleaved downstream of LXGG sequences, a sequence that is similar to the C-terminal LRGG sequence of Ub that is recognized by HAUSP [195, 227, 228]. Later, it was indeed shown that SARS-CoV $PL^{pro}$ can cleave Ub and ISG15 from substrates and structurally resembles DUBs of the USP family [196-198, 229]. Subsequently, for MERS-CoV $PL^{pro}$, MHV PLP2, HCoV-NL63 PLP2, TGEV PLP1, PEDV PLP2 and IBV $PL^{pro}$, it was also proven that those PLPs possess DUB activity, which is presumed to suppress the innate immune response ([199, 201-203, 205, 230-233] and reviewed by [206]).

The $PL^{pro}$ of both MERS-CoV and SARS-CoV can cleave all di-Ub linkages except for K27-linked and linear di-Ub chains *in vitro* [234, 235]. Intriguingly, SARS-CoV $PL^{pro}$ cleaves in a di-distributive manner, meaning that it preferentially binds one di-Ub in K48-linked Ub-chains at the time, whereas MERS-CoV $PL^{pro}$ binds one Ub at a time. SARS-CoV $PL^{pro}$ prefers K48-linked polyUb chains over ISG15 and the other Ub-linkages [236]. This suggests that K48-linked polyUb chains are the primary target of SARS-CoV $PL^{pro}$. In contrast, MERS-CoV $PL^{pro}$ does not have a clear preference *in vitro*, which is in line with the properties of cellular DUBs of the USP family [237]. In contrast, most cellular OTU DUBs were found to have linkage specificity [238, 239], however whether vDUBs of the OTU family share similar preferences for certain linkage(s) will have to be investigated.

## VACCINES AND THERAPEUTICS AGAINST CORONAVIRUSES

Unfortunately, there are no approved vaccines or antiviral therapies to specifically prevent or treat CoV infections in humans or animals [240]. During the MERS-CoV outbreak, several patients received IFN-α or -β and ribavirin (a guanosine analogue and a broad-spectrum virus replication inhibitor) although this did not clearly improve the clinical outcome [241-244]. In contrast, the combination of these drugs showed an antiviral effect in cell culture and in rhesus macaques [245, 246]. These drugs are thought to have a broad-spectrum activity but do not target MERS-CoV specifically, and can therefore be ineffective and/or cause adverse side effects. Two other studies described the screening of FDA-approved compounds and identification of inhibitors that could be repurposed to treat MERS-CoV infection [247, 248]. The search for broad-spectrum inhibitors is considered the holy grail for combating both current and future emerging CoVs. Anti-CoV treatment options can be divided into virus-targeting inhibitors, such as inhibitors of viral replicative enzymes, and host-targeting approaches, like IFN treatment [240]. Virus-targeting inhibitors can for example be directed towards the well-studied S protein, to inhibit virus entry or membrane fusion, or towards nsps important for replication and transcription such as $PL^{pro}$, $3CL^{pro}$, the RdRp or the helicase. Entry can also be inhibited in a host-targeted manner, for example by using antibodies or peptides that block the cellular receptor, by preventing host-mediated cleavage of the S protein or by inhibiting the endosomal pathway. Thus far, only a few broad-spectrum inhibitors have been identified that are active against CoVs. One is the drug K22, which may interfere with DMV formation and RNA synthesis and was shown to affect the replication of HCoV-229E, SARS-CoV, MERS-CoV, MHV, FCoV and IBV in cell culture [96]. K22-resistant virus mutants contained adaptive mutations in nsp6, suggesting that K22 directly or indirectly affects the activity or function of this viral protein. Recently, nucleoside analogue GS-5734, which was initially identified as an Ebola virus inhibitor, was shown to be effective against bat CoVs, SARS-CoV and MERS-CoV in human airway epithelial cell cultures [249]. Moreover, early administration during infection reduced the SARS-CoV load in infected mice [250]. The precise mode-of-action of GS-5734 needs to be determined but partially resistant MHV was shown to have two mutations in the viral polymerase and these are associated with reduced virus fitness [250].

Monoclonal antibodies against the RBD of the MERS-CoV S protein were proven to block MERS-CoV infection in a non-lethal humanized mouse model [251]. Attempts to develop vaccines that protect against MERS-CoV infection are therefore often based on the RBD of the S protein [252-255]. The expression or presentation of (the RBD of) the S protein by a vaccine induces neutralizing antibodies, as was demonstrated in rabbits, mice, rhesus macaques and dromedary camels [256, 257]. Various vaccine prototypes have been produced, based on DNA expression plasmids, viral vectors (adenovirus or modified vaccinia virus Ankara), virus-like particles or purified recombinant protein subunits that express or present, respectively, the S protein of MERS-CoV. The first potential modified live MERS-CoV vaccine candidate that was developed lacks the gene encoding the envelope protein [258]. As a result, this recombinant virus is still able

to replicate but is propagation-defective which is advantageous in the context of biosafety. The efficacy of this modified live virus (MLV) vaccine was so far not determined in an animal model for MERS-CoV infection. Disruption of the accessory protein genes or the 2'-O-MTase function was demonstrated to attenuate MERS-CoV in mice and such virus mutants could potentially be utilized as MLV vaccines [170, 181].

## THESIS OUTLINE

This thesis focuses on MERS-CoV $PL^{pro}$ and describes potential $PL^{pro}$-based strategies for MLV vaccine development and innovative protein-based inhibitors, which both might also be applied to other DUB-expressing viruses. Coronavirus $PL^{pro}$s, including MERS-CoV $PL^{pro}$, are presumed to use their DUB function to suppress the innate immune response. In Chapter 2, the crystal structure of MERS-CoV $PL^{pro}$ in complex with Ub was determined, which facilitated the introduction of specific modifications in the Ub-binding site of MERS-CoV $PL^{pro}$. These were used to disrupt the DUB function of this protease without interfering with its role in replicase polyprotein cleavage. Additionally, ectopic expression of the DUB-negative MERS-CoV $PL^{pro}$ domain revealed for the first time that the DUB activity is suppressing IFN-β promoter activation. Chapter 3 describes the generation of recombinant DUB-negative MERS-CoV carrying substitutions in $PL^{pro}$ and the subsequent characterization of virus replication and the induction of innate immune responses, both in cell culture and in a MERS mouse model. Interestingly, mice infected with DUB-negative MERS-CoV have significantly increased survival rates over wt virus-infected mice, and infection with the former induced earlier innate immune responses. This proof-of-concept creates a basis for further characterization of DUB-negative CoV mutants and their use as MLV vaccines in general.

Viral proteases like $PL^{pro}$ are essential for virus replication and therefore constitute ideal drug targets. Screening for small-molecule inhibitors targeting viral proteases has yielded hits that - after optimization - may have potential as antiviral therapeutics, even though their development often is a tedious process with a low success rate. Instead of focusing on small-molecules, we have used the fact that vDUBs bind Ub to identify ubiquitin sequence variants (UbVs) that bind with very high affinity and specificity to the MERS-CoV- and CCHFV-encoded vDUBs, and compete with Ub for binding to the vDUB (Chapter 4). These UbVs only show specific binding to their cognate vDUB, and the MERS-CoV-specific UbVs demonstrate remarkable antiviral potency. The MERS-CoV $PL^{pro}$ activity and overall replication were severely inhibited in the presence of these UbVs. Chapter 5 describes the characterization and optimization of the stability of the UbV with the highest affinity for MERS-CoV $PL^{pro}$, by modification of amino acids in the N-terminal region of this UbV. The resulting UbVs are more stable and can be tested in a MERS-CoV infection animal model to further investigate the potency of UbVs as antiviral therapeutics.

In Chapter 6 our current knowledge regarding vDUBs from RNA viruses is summarized. An overview is provided of, in particular, the structural biology of these vDUBs and their role in innate

immune evasion and/or viral replication. Finally, in Chapter 7 the findings described in this thesis are discussed in the context of our existing knowledge about virus-host interactions, and the mysteries that remain to be resolved.

# 2

# Crystal structure of the Middle East respiratory syndrome coronavirus papain-like protease bound to ubiquitin facilitates targeted disruption of deubiquitinating activity to demonstrate its role in innate immune suppression

Robert C.M. Knaap[1,a], Ben A. Bailey-Elkin[2,a], Garrett G. Johnson[2], Tim J. Dalebout[1], Dennis K. Ninaber[1], Puck B. van Kasteren[1], Peter J. Bredenbeek[1], Eric J. Snijder[1], Brian L. Mark[2,b] and Marjolein Kikkert[1,b]

[1] Department of Medical Microbiology, Leiden University Medical Center, Leiden, the Netherlands
[2] Department of Microbiology, University of Manitoba, Winnipeg, R3T2N2, Canada
[a] These authors contributed equally to this work
[b] These authors contributed equally to this work

**Published in The Journal of Biological Chemistry Vol. 289, No. 50, pp. 34667–34682, 2014**

## ABSTRACT

Middle East respiratory syndrome coronavirus (MERS-CoV) is a newly emerging human pathogen that was first isolated in 2012. MERS-CoV replication depends in part on a virus-encoded papain-like protease ($PL^{pro}$) that cleaves the viral replicase polyproteins at three sites releasing non-structural protein (nsp) 1, nsp2 and nsp3. In addition to this replicative function, MERS-CoV $PL^{pro}$ was recently shown to be a deubiquitinating enzyme (DUB) and possesses deISGylating activity, as previously reported for other coronaviral $PL^{pro}$ domains including that of severe acute respiratory syndrome coronavirus (SARS-CoV). These activities have been suggested to suppress host antiviral responses during infection. To understand the molecular basis for ubiquitin (Ub) recognition and deconjugation by MERS-CoV $PL^{pro}$, we determined its crystal structure in complex with Ub. Guided by this structure, mutations were introduced into $PL^{pro}$ to specifically disrupt Ub binding without affecting viral polyprotein cleavage, as determined using an *in trans* nsp3↓4 cleavage assay. Having developed a strategy to selectively disable $PL^{pro}$ DUB activity, we were able to specifically examine the effects of this activity on the innate immune response. Whereas the wild-type $PL^{pro}$ domain was found to suppress IFN-β promoter activation, $PL^{pro}$ variants specifically lacking DUB activity were no longer able to do so. These findings directly implicate the DUB function of $PL^{pro}$, and not its proteolytic activity *per se*, in the inhibition of IFN-β promoter activity. The ability to decouple the DUB activity of $PL^{pro}$ from its role in viral polyprotein processing now provides an approach to further dissect the role(s) of $PL^{pro}$ as a viral DUB during MERS-CoV infection.

## INTRODUCTION

The Middle-East respiratory syndrome coronavirus (MERS-CoV) was first isolated in June 2012, from a patient in Saudi Arabia who had died from progressive respiratory and renal failure [25]. Since then, over 800 cases have been reported, with a case fatality rate surpassing 30% [260]. The progression and severity of the symptoms observed in MERS patients resemble the severe acute respiratory syndrome (SARS) observed in patients infected with SARS-CoV, which caused a global pandemic in 2003, resulting in over 8000 cases, with a case fatality rate of ~10% [261]. While the SARS-CoV outbreak was contained within months, MERS cases continue to occur two years after the emergence of MERS-CoV in the human population. Currently, dromedary camels are suspected to be one of the direct reservoirs for the zoonotic transmission of MERS-CoV, although the exact chain of transmission remains to be explored in more detail [262, 263].

MERS-CoV and SARS-CoV are enveloped, positive-sense single-stranded RNA viruses that belong to the *Betacoronavirus* genus in the family *Coronaviridae* of the Nidovirales order [26]. The CoV non-structural proteins (nsps), which drive viral genome replication and subgenomic RNA synthesis, are encoded within a large replicase gene that encompasses the 5'-proximal three quarters of the CoV genome. The replicase gene contains two open reading frames, ORF1a and ORF1b. Translation of ORF1a yields polyprotein (pp) 1a, and -1 ribosomal frameshifting facilitates translation of ORF1b to yield pp1ab [264]. The pp1a and pp1ab precursors are co- and post-translationally processed into functional nsps by multiple ORF1a-encoded protease domains. Coronaviruses employ either one or two papain-like proteases (PL$^{pro}$s), depending on the virus species, to release nsp1, nsp2 and nsp3, and a chymotrypsin-like protease (3CL$^{pro}$), that cleaves all junctions downstream of nsp4 [265]. Comparative sequence analysis of the MERS-CoV genome and proteome allowed for the prediction and annotation of 16 nsps, along with the location of the probable proteolytic cleavage sites [26]. The MERS-CoV PL$^{pro}$ domain, which resides in nsp3, has recently been confirmed to recognize and cleave after the sequence LXGG (where X is any amino acid) at the nsp1↓2 and nsp2↓3 junctions as previously defined for other CoV PL$^{pro}$s, as well as an IXGG sequence which constitutes the nsp3↓4 cleavage site [205, 266].

These recognition sequences within pp1a/pp1ab resemble the C-terminal LRGG motif of ubiquitin (Ub), an 8.5 kDa protein that can be conjugated to lysine residues or the N-terminus of target proteins as a form of post-translational modification through the action of the cellular E1/2/3 ligase system [145]. Additional Ub molecules can be linked to any of the 7 lysine residues in Ub itself, or to its amino terminus to generate polyubiquitin (polyUb) chains of various linkage types [145]. The best-studied linkages are the ones occurring at K48 of Ub, which results in the targeting of the tagged substrate to the 26S proteasome for degradation, and at K63, which generates a scaffold for the recruitment of cellular proteins to activate numerous signalling cascades, including critical antiviral and pro-inflammatory pathways [145]. The C-terminus of Ub can be recognized by deubiquitinating enzymes (DUBs), which catalyse the deconjugation of Ub thus reversing the effects of ubiquitination [267]. Interestingly, CoV PL$^{pro}$s including those of MERS-

and SARS-CoV have been suggested to act as multifunctional proteases that not only cleave the viral polyproteins at internal LXGG cleavage sites but also remove Ub and the antiviral Ub-like molecule interferon-stimulated gene 15 (ISG15) from cellular proteins, presumably to suppress host antiviral pathways [196-199, 202, 204-206].

Activation of antiviral and pro-inflammatory pathways is a critical first line of defense against virus infections, including those caused by nidoviruses. Viral RNA molecules are recognized by pattern recognition receptors such as the cytoplasmic RIG-I-like receptors (RLRs) RIG-I and MDA5, which are activated by intracellular viral RNA transcripts bearing 5' tri- and diphosphates, and double-stranded RNA (dsRNA) replication intermediates, respectively [134, 268]. Upon their stimulation, RLRs signal through the mitochondrial antiviral-signalling protein (MAVS), leading to the formation of a signalling complex at the mitochondrial membrane and ultimately to the activation of transcription factors interferon regulatory factor (IRF) 3, IRF7 and NF-κB. These transcription factors in turn regulate the expression of antiviral type I interferons (IFNs) including IFN-β, which acts through autocrine and paracrine receptor-mediated signalling pathways to induce the transcription of numerous interferon-stimulated genes (ISGs) that will interfere with virus replication, as well as pro-inflammatory cytokines such as IL-6, IL-8 and TNFα. Regulation of the antiviral and pro-inflammatory pathways is largely Ub-dependent, as multiple factors in the innate immune cascade are ubiquitinated, including RIG-I, which is critical for down-stream signalling. Cellular DUBs function to prevent excessive inflammation and immune responses during infection by removal of Ub from innate immune factors [269].

The DUB activities of MERS- and SARS-CoV $PL^{pro}$ have been implicated in the suppression of host antiviral pathways since these proteases can suppress IFN-β induction upon their ectopic expression [199, 200, 202, 204-206]. Previous work has shown that during infection, SARS-CoV indeed suppresses the host's antiviral responses by preventing the induction of IFN-β expression in cell culture [270-272]. Similarly, MERS-CoV infection has been found to elicit a poor type I IFN response in cultured monocyte-derived dendritic cells [273] and alveolar epithelial A549 cells [153], as well as *ex vivo* in bronchial and lung tissue samples [153]. Furthermore, delayed induction of pro-inflammatory cytokines in human airway epithelial cells infected with MERS-CoV has been reported [155].

Although the above observations suggest that MERS- and SARS-CoV actively suppress antiviral responses such as IFN-β production and inflammation, they do not directly implicate the DUB activity of $PL^{pro}$ as being responsible for (part of) this suppression. Due to the dependence of MERS-CoV replication on the ability of $PL^{pro}$ to cleave the nsp1-nsp3 region of the replicase polyproteins, studying the role of $PL^{pro}$ DUB activity, specifically in the suppression of the cellular innate immune response, is difficult since both activities depend on the same enzyme active site. Selective inactivation of only the DUB activity of $PL^{pro}$ would enable the study of how this activity alone affects cellular signalling; however, achieving this requires detailed information on the structural basis of Ub recognition and deconjugation by $PL^{pro}$. To this end, we determined the crystal structure of MERS-CoV $PL^{pro}$ bound to Ub to elucidate the molecular determinants of Ub

recognition. Based on the structure of this complex, mutations were introduced that selectively disrupted Ub recognition by targeting regions of the Ub-binding site on PL$^{pro}$ that were sufficiently distant from the active site of the protease. Using this approach, we were able to remove the DUB activity from PL$^{pro}$ without affecting its ability to cleave the nsp3↓4 cleavage site *in trans*. This enabled us, for the first time, to demonstrate that the DUB activity of MERS-CoV PL$^{pro}$ can suppress the MAVS-mediated induction of IFN-β expression.



## MATERIALS AND METHODS

### Cells, antibodies and plasmids

HEK293T cells were cultured in Dulbecco's modified Eagle's medium (DMEM) supplemented with 10% foetal calf serum (FCS; Bodinco BV), 100 U/ml penicillin, 100 U/ml streptomycin and 2 mM L-glutamine (cell culture medium and supplementals were obtained from Lonza).

Primary antibodies used were mouse anti-HA (ab18181; Abcam), mouse anti-V5 (37-7500; Invitrogen), mouse anti-β-actin (A5316; Sigma-Aldrich), mouse anti-FLAG (F3165; Sigma-Aldrich), and rabbit anti-GFP [221]. As secondary antibodies horseradish peroxidase (HRP)-conjugated antibodies were used (P0447 and P0217; Dako).

The following plasmids were described elsewhere: pASK3 [99], pcDNA-eGFP [221], pCMV-FLAG-Ub [274], pLuc-IFN-β [275], pEBG-RIG-I$_{(2CARD)}$ [276], pcDNA-FLAG-MAVS [277] and pEGFP-C1-IRF3$_{(5D)}$ [278].

### Construction of MERS-CoV PL$^{pro}$ expression plasmids

A cDNA fragment encoding the PL$^{pro}$ domain (amino acids 1479–1803 of the MERS-CoV pp1a/pp1ab polyprotein (NCBI ID: JX869059); pp1a/pp1ab amino acid numbering is used throughout the rest of the chapter) was cloned into bacterial expression vector pASK3 in-frame with N-terminal Ub and a C-terminal $H_6$ purification tag to produce pASK-MERS-CoV-PL$^{pro}$.

Using standard methodologies, the sequence encoding amino acids 1480-1803 of MERS-CoV pp1a/pp1ab was PCR amplified, cloned downstream of the T7 promoter of expression vector pE-SUMO (LifeSensors), and used to transform *E. coli* BL21 (DE3) GOLD cells (Stratagene) grown under kanamycin selection (35 μg/ml). Recombinant expression plasmid (pE-SUMO-PL$^{pro}$) was isolated from a single colony and DNA sequencing confirmed the expected sequence of the PL$^{pro}$ domain, and the in-frame fusion of the 5'-end to a sequence encoding a H6-SUMO purification tag, which facilitated purification of the product by immobilized metal (Ni) affinity chromatography as described below.

To obtain high expression in eukaryotic cells, the sequence of MERS-CoV nsp3-4 (amino acids 854-3246) flanked by an N-terminal HA tag and a C-terminal V5 tag was optimized based on the human codon usage frequency, and potential splice sites and polyadenylation signals were removed. This sequence was synthesized (Invitrogen), and subsequently cloned into the pCAGGS

vector (Addgene) using standard methodologies. The following expression constructs were generated: pCAGGS-HA-nsp3-4-V5 (amino acids 854-3246), pCAGGS-HA-nsp3C-4-V5 (amino acids 1820-3246, which does not include the $PL^{pro}$ domain), and pCAGGS-HA-nsp3-Myc (amino acids 854-2739). The sequence encoding MERS-CoV $PL^{pro}$ (amino acids 1479-1803) was PCR amplified using synthetic plasmid DNA as a template and cloned in frame with a C-terminal V5 tag in the pcDNA3.1(-) vector (Invitrogen). The pASK-MERS-CoV-$PL^{pro}$ and pcDNA3.1-MERS-CoV-$PL^{pro}$ expression constructs served as templates for site-directed mutagenesis using the QuickChange strategy with Pfu DNA polymerase (Agilent). All constructs were verified by sequencing. The sequences of the constructs and primers used in this study are available on request.

## Purification of MERS-CoV $PL^{pro}$ and *in vitro* DUB activity assay

*In vitro* DUB activity assays were performed with recombinant MERS-CoV $PL^{pro}$ batch-purified from lysates of *E. coli* strain C2523. Cells transformed with pASK-MERS-CoV-$PL^{pro}$ were cultured to an optical density ($OD_{600}$) of 0.6 in lysogeny broth (LB) at 37°C. Protein expression was then induced with 200 ng/ml anhydrotetracycline for 16 h at 20°C. The cells were pelleted, resuspended in lysis buffer (20 mM HEPES, pH 7.0, 200 mM NaCl, 10% (vol/vol) glycerol and 0.1 mg/ml lysozyme) and lysed for 1 h at 4°C followed by sonication. The lysate was clarified by centrifugation at 20,000 x g for 20 min at 4°C and the soluble fraction was applied to talon resin (GE Healthcare) pre-equilibrated with lysis buffer. After a 2 h rolling incubation at 4°C the beads were washed four times with wash buffer (20 mM HEPES, pH 7.0, 200 mM NaCl, 10% (vol/vol) glycerol and 20 mM imidazole) followed by the elution of the protein with elution buffer (20 mM HEPES, pH 7.0, 200 mM NaCl, 10% (vol/vol) glycerol and 250 mM imidazole). Eluted protein was dialysed against storage buffer (20 mM HEPES, pH 7.0, 100 mM NaCl, 50% (vol/vol) glycerol, 2mM dithiothreitol (DTT)) and stored at −80°C. N-terminal Ub is cleaved from the Ub- $PL^{pro}$-H6 fusion protein by the $PL^{pro}$ domain itself during expression. To achieve removal of the Ub from mutated and/or inactive $PL^{pro}$, *E. coli* strain C2523 containing pCG1, expressing the Ub-specific processing protease 1 was used [279].

*In vitro* DUB activity assays were performed as described by van Kasteren *et al*. [221]. Briefly, indicated amounts of purified MERS-CoV $PL^{pro}$ wild-type or active site mutant (C1592A) were incubated with 2.5 µg of either K48-linked polyubiquitin chains or K63-linked polyubiquitin chains (Boston Biochem) in a final volume of 10 µl. Isopeptidase T (Boston Biochem) served as a positive control. After a 2 h incubation at 37°C the reaction was stopped by addition of 4× Laemmli sample buffer (4× LSB; 500 mM Tris, 4% SDS, 40% glycerol, 0.02% bromophenol blue, 2 mM DTT, pH 6.8). SDS-polyacrylamide gels were stained with Coomassie brilliant blue (Sigma-Aldrich) and scanned using a GS-800 calibrated densitometer (Bio-Rad).

## Expression and purification of MERS-CoV $PL^{pro}$ for crystallization

*E. coli* BL21(DE3) GOLD cells harbouring pE-SUMO-$PL^{pro}$ were grown at 37°C with aeration in 500 ml of LB containing kanamycin (35 µg/ml) to an $OD_{600}$ of 0.6-0.8. Expression of the $H_6$-SUMO-$PL^{pro}$

fusion protein was then induced by the addition 1 mM isopropyl β-D-1-thiogalactopyranoside for 18 h at 16°C with aeration. Cells were pelleted by centrifugation and stored at -80°C.

Cell pellets were resuspended in ice-cold lysis buffer (150 mM tris(hydroxymethyl) aminomethane (Tris) pH 8.5, 1 M NaCl, 0.1 mM phenylmethanesulfonylfluoride (PMSF), 2 mM DTT and lysed using a French pressure cell (AMINCO). Cell lysate was clarified by centrifugation (17,211 x g at 4°C) and the supernatant containing the $H_6$-SUMO-$PL^{pro}$ fusion was applied to a column containing Ni-NTA affinity resin (Qiagen). The column was washed with 10 column volumes of lysis buffer supplemented with 25 mM imidazole, followed by elution of the fusion protein with lysis buffer containing 250 mM imidazole. The $H_6$-SUMO tag was then removed from $PL^{pro}$ by adding $H_6$-tagged Ulp1 SUMO protease to the eluted SUMO-$PL^{pro}$ fusion followed by dialysis of the protein mixture overnight against 2 L cleavage buffer (150 mM NaCl, 50 mM Tris pH 8.0, 1 mM DTT) at 4°C. Tag-free $PL^{pro}$ was separated from $H_6$-SUMO and the $H_6$-Ulp1 SUMO protease by passing the dialyzed protein mix through a Ni-NTA gravity column. The flow-through contained purified $PL^{pro}$ that was subsequently dialyzed against 20 mM Tris pH 8.5, 150 mM NaCl, 2 mM DTT and further purified by gel filtration using a Superdex 75 (GE Healthcare) gel-filtration column.

### Covalent coupling of Ub to $PL^{pro}$

$Ub_{(1–75)}$-3-bromopropylamine (Ub-3Br) is a modified form of Ub with a reactive C-terminus that forms an irreversible covalent linkage to the active site cysteine of DUB enzymes and was prepared according to Messick *et al*. [280] and Borodovsky *et al*. [281]. Purified $PL^{pro}$ was incubated with a 2-fold molar excess of Ub-3Br and incubated for 1 h at room temperature with end-over-end mixing. The resulting $PL^{pro}$-Ub complex was dialyzed into 20 mM Tris pH 8.5, 150 mM NaCl, 2 mM DTT and excess Ub-3Br was removed by gel filtration using a Superdex 75 column.

### Crystallization of $PL^{pro}$ and $PL^{pro}$-Ub complexes

The purified $PL^{pro}$-Ub complex was concentrated and crystallized at 20°C in two different conditions using the vapour diffusion method: 1) 20% PEG 4000, 0.1 M trisodium citrate pH 5.4, 20% isopropanol at 10 mg/ml, which yielded the structure of open $PL^{pro}$-Ub (see Results), and 2) 1.80 M ammonium sulphate (AmSO4) at 20 mg/ml, which yielded the structure of closed $PL^{pro}$-Ub (see Results). Crystals of unliganded $PL^{pro}$ were also grown using the vapour diffusion method in 18% PEG 4000, 0.1 M trisodium citrate pH 5.6, 16% isopropanol after concentrating the protein to 12 mg/ml. Immediately prior to crystallization 1 M DTT was added to the protein to a final concentration of 5 mM, which was found to improve crystallization.

In preparation for X-ray data collection, single crystals of open $PL^{pro}$-Ub from condition 1 above were briefly swept through a droplet of cryoprotectant composed of 22% PEG 4000, 0.1M trisodium citrate pH 5.6, 20% 1,2-propanediol before flash cooling in liquid nitrogen. Similarly, single crystals of closed $PL^{pro}$-Ub from condition 2 above and unbound $PL^{pro}$ were cryoprotected in 1.85 M $AmSO_4$, 15% glycerol and 22% PEG 4000, 0.1 M trisodium citrate pH 5.6, 10% 1,2-propanediol, respectively, before flash-cooling in liquid nitrogen.

**Table 1. Crystallographic statistics for MERS-CoV $PL^{pro}$ and $PL^{pro}$-Ub structures**

| Crystal | $PL^{pro}$ | Open $PL^{pro}$-Ub | Closed $PL^{pro}$-Ub |
|---|---|---|---|
| Crystal geometry | | | |
| Space group | $P6_3$ | $P6_3$ | $P6_522$ |
| Unit cell (Å) | *a*=*b*=137.94 *c*=57.70; α=β=90° γ=120° | *a*=*b*=136.77 *c*=57.99; α=β=90° γ=120° | *a*=*b*=176.92 *c*=84.55; α=β=90° γ=120° |
| Crystallographic data | | | |
| Wavelength (Å) | 1.28294 | 1.28280 | 1.28219 |
| Resolution range (Å) | 45.15-2.60 (2.90-2.80)* | 44.23-2.15 (2.22-2.15) | 44.24-2.60 (2.90-2.80) |
| Total observations | 137170 (13780) | 124058 (12315) | 283649 (28118) |
| Unique reflections | 15683 (1566) | 33472 (3291) | 19694 (1918) |
| Multiplicity | 8.7 (8.8) | 3.7 (3.7) | 14.4 (14.7) |
| Completeness (%) | 100.00 (100.00) | 98.73 (98.12) | 99.97 (100) |
| Anomalous completeness | 99.4 (98.5) | 92.4 (92.6) | 100 (100) |
| $R_{merge}$ | 0.085 (0.76) | 0.041 (0.79) | 0.061 (0.78) |
| CC1/2 | 0.99 (0.83) | 0.99 (0.54) | 1 (0.93) |
| CC* | 0.99 (0.95) | 1 (0.84) | 1 (0.98) |
| I/σI | 17.13 (3.42) | 20.52 (1.97) | 34.01 (3.69) |
| Wilson B-factor ($Å^2$) | 75.15 | 46.79 | 74.96 |
| Phasing statistics | | | |
| Figure of merit | 0.12 | 0.18 | 0.23 |
| FOM after RESOLVE | 0.64 | 0.63 | 0.67 |
| Refinement statistics | | | |
| Reflections in test set | 1570 | 1996 | 1609 |
| Protein atoms | 2384 | 3020 | 3020 |
| Zinc atoms | 1 | 1 | 1 |
| Solvent molecules | 26 | 205 | 65 |
| $R_{work}$ ($R_{free}$) | 0.23 (0.27) | 0.20 (0.23) | 0.24 (0.28) |
| RMSDs | | | |
| Bond lengths/angles (Å/°) | 0.002/0.60 | 0.002/0.52 | 0.002/0.54 |
| Ramachandran plot | | | |
| Favoured/allowed (%) | 95/5 | 95/5 | 93/7 |
| Average B factor ($Å^2$) | 76.70 | 66.80 | 86.50 |
| Macromolecules | 76.70 | 69.20 | 86.60 |
| Solvent | 76.65 | 65.40 | 84.20 |

*Values in parentheses refer to the highest resolution shell

### Data collection and structure determination

X-ray diffraction data were collected from all crystals at the Zn-K absorption edge at beamline 08B1-1 of the Canadian Light Source and integrated using XDS [282]. Integrated data were then scaled using Scala [283]. Initial phase estimates for reflections collected from unliganded and Ub-bound PL$^{pro}$ were determined via a single wavelength anomalous dispersion experiment. The position of the Zn anomalous scatterer was identified using HySS [284], and density modification was performed with RESOLVE [285] within the phenix.autosol pipeline [286]. Initial models were constructed using phenix.autobuild, and further model building and refinement was carried out using Coot [287] and phenix.refine [288]. Crystallographic statistics for all structures are found in Table 1.

### Protease activity assays in cell culture

HEK293T cells, grown to 80% confluence in 12-well plates, were transfected using the calcium phosphate transfection method [289]. To determine the DUB activity of MERS-CoV PL$^{pro}$, plasmids encoding FLAG-tagged Ub (0.25 µg), GFP (0.25 µg) and MERS-CoV-PL$^{pro}$-V5 (0.2 µg) were co-transfected. A combination of plasmids encoding GFP (0.25 µg), HA-nsp3C-4-V5 (0.2 µg) and MERS-CoV-PL$^{pro}$-V5 (0.15 µg) were transfected to assess the *in trans* cleavage activity of MERS-CoV-PL$^{pro}$. Total amounts of transfected DNA were equalized to 2 µg by the addition of empty pcDNA vector. At 18 h post transfection, cells were lysed in 2x LSB. Proteins were separated in a SDS-polyacrylamide gel and blotted onto Hybond-P (GE Healthcare) using the Trans-blot turbo transfer system (Bio-Rad). Aspecific binding to the membrane was blocked with dried milk powder solution and after antibody incubation, protein bands were visualized using Pierce ECL 2 Western blotting substrate (Thermo Scientific).

### Luciferase-based IFN-β reporter assay

Using the calcium phosphate method, 80% confluent HEK293T cells in 24-well plates were transfected with 5 ng *Renilla* luciferase encoding plasmid pRL-TK (Promega), IFN-β-Luc firefly reporter plasmid (25 ng), innate immune response inducer plasmids encoding RIG-I$_{(2CARD)}$, MAVS or IRF3$_{(5D)}$ (25 ng) and indicated quantities of MERS-CoV PL$^{pro}$ or MERS-CoV nsp3 encoding expression plasmids. Total amounts of transfected DNA were equalized to 1 µg by the addition of empty pcDNA vector. At 16 h post transfection, cells were lysed in 1x passive lysis buffer (Promega). Firefly and *Renilla* luciferase activity was measured using the Dual-Luciferase reporter assay system (Promega) on a Mithras LB 940 multimode reader (Berthold Technologies). Experiments were performed in triplicate and independently repeated at least four times. Firefly luciferase activity was normalized to *Renilla* luciferase and statistical significance was determined using an unpaired two-tailed Student's *t*-test. Values <0.05 were considered statistically significant. 4x LSB was added to the remaining lysates and these samples were analysed by Western blotting as described above.

## RESULTS

### DUB activity of recombinant MERS-CoV PL$^{pro}$

It was recently shown in cell culture experiments that ectopic expression of MERS-CoV PL$^{pro}$ resulted in deconjugation of polyUb and ISG15 from cellular targets [202, 290]. DUB activity of purified recombinant MERS-CoV PL$^{pro}$ was also demonstrated using Ub-7-amino-4-trifluoro-methylcoumarin (Ub-AFC) [290] or Ub-7-amino-4-methylcoumarin (Ub-AMC) [291] as a substrate. To characterize the direct activity of recombinant MERS-CoV PL$^{pro}$ towards polyUb, we purified the enzyme from *E. coli* and incubated it with either K48- or K63-linked polyUb chains. Wild-type PL$^{pro}$ degraded both K48- and K63-linked chains in a concentration-dependent manner, while mutating the active site nucleophile (C1592A) severely reduced the activity of the enzyme towards both Ub linkage types (Fig. 1). No clear preference of the enzyme for cleaving either the K63 or the K48 Ub linkage was observed under the conditions used in this *in vitro* DUB assay (compare Fig. 1A and 1B). This assay clearly demonstrated that the protease domain used throughout this study for ectopic expression and crystallisation experiments possesses DUB activity towards K48- and K63-linked Ub chains, and that this activity does not require other viral or cellular proteins. During the preparation of this manuscript, an article by Báez-Santos and co-workers was published in which similar results were presented [235].

### Crystal structures of MERS-CoV PL$^{pro}$ and PL$^{pro}$-Ub complexes

*MERS-CoV PL$^{pro}$*

The crystal structure of PL$^{pro}$ was determined both on its own and as a covalent complex with Ub (PL$^{pro}$-Ub). The PL$^{pro}$ domain crystallized in space group $P6_3$, and consistent with another recently determined crystal structure of MERS-CoV PL$^{pro}$ [291], we found the protease to adopt a fold consistent with DUBs of the ubiquitin specific protease (USP) family. The structure includes a C-terminal catalytic domain containing a right-handed fingers, palm and thumb domain organization, as well as an N-terminal Ub-like (Ubl) domain found in many USPs, including that of SARS-CoV [229, 292] (Fig. 2A). The packing of the palm and thumb domains forms a cleft leading into the active site in a manner consistent with the domain organization prototyped by the Clan CA group of cysteine proteases [293]. The Ubl domain packs against the thumb domain composed of helices α2-7, which in turn packs against the palm domain comprised of strands β6, β7 and β14-19. Extending from the palm, the fingers domain is composed of strands β10, β11, β13, β14, β19 and contains a $C_4$ Zn-ribbon motif [294] coordinating a Zn atom via residues C1672, C1675, C1707 and C1709 in tetrahedral geometry, similar to that of SARS PL$^{pro}$, transmissible gastroenteritis virus (TGEV) PL1$^{pro}$, and cellular USP2 and USP21 [229, 231, 295, 296].

*PL$^{pro}$ covalently bound to Ub*

The MERS-CoV PL$^{pro}$-Ub complex crystallized in two different space groups ($P6_3$ and $P6_522$), which revealed a considerable level of conformational flexibility in the protein. Electron density maps

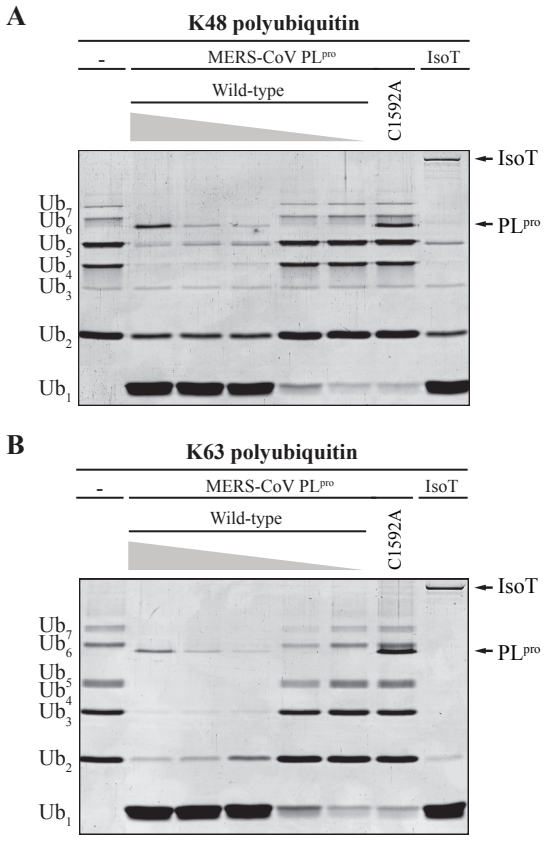


**Figure 1.** ***In vitro*** **cleavage of K48- and K63-linked polyUb chains by recombinant MERS-CoV PL$^{pro}$.** Purified recombinant MERS-CoV PL$^{pro}$ was incubated with 2.5 µg K48-linked (A) or K63-linked (B) polyUb chains of different length in each reaction for 2 h at 37°C in a final volume of 10 µl. A range of 2-fold dilutions starting at 2 µM MERS-CoV wild-type PL$^{pro}$ per reaction was used. Activity of the PL$^{pro}$ active site mutant (C1592A) was assessed at a concentration of 2 µM. Isopeptidase T (IsoT, 0.5 µg per reaction) served as a positive control [304].

calculated using diffraction data collected from PL$^{pro}$-Ub complex that crystallized in space group $P6_3$ revealed weak density for the covalently bound Ub molecule. Although the entire bound Ub molecule could be modelled within its binding site on PL$^{pro}$ in this crystal form, high temperature factors for atoms comprising the modelled Ub molecule suggested it was not rigidly bound to the protease despite being covalently linked to the active site cysteine. Further analysis of the crystal packing revealed that the Ub molecule was fully exposed to solvent and not involved in crystal contacts, which provided a degree of mobility to Ub when bound to PL$^{pro}$ (Fig. 3A). This result encouraged us to pursue additional crystallization conditions, which yielded crystals of PL$^{pro}$-Ub in space group $P6_522$ (Fig. 3B and 2B). The crystal packing in this space group allowed for multiple crystal contacts between the bound Ub monomer and surrounding symmetry mates, and resulted in clear, well-defined density for the Ub molecule (Fig. 3B). Interestingly, relative to the $P6_3$ crystal forms of PL$^{pro}$, the fingers domain in this crystal form was moved toward Ub (Fig. 2C). In light of these movements, the PL$^{pro}$-Ub structure with the fingers domain positioned away from Ub (space group $P6_3$) will hereafter be referred to as 'open' PL$^{pro}$-Ub, whereas the structure with the fingers domain shifted towards Ub (space group $P6_522$) will be referred to as 'closed'

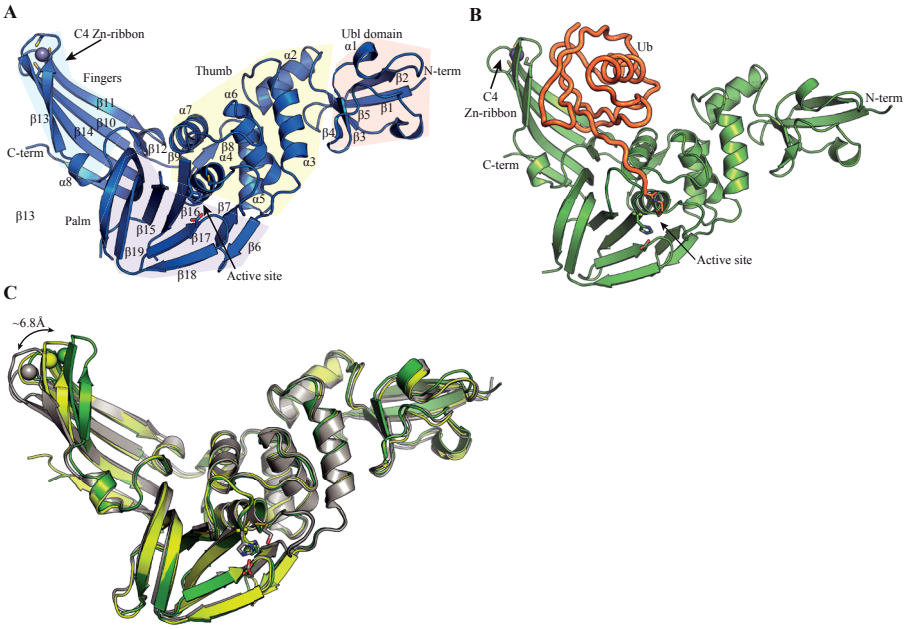


**Figure 2. MERS-CoV PL$^{pro}$ and PL$^{pro}$-Ub structures.** (A) Structure of the MERS-CoV PL$^{pro}$ domain (2.15Å resolution). The palm, thumb, fingers and N-terminal ubiquitin-like (Ubl) domains are indicated by coloured panels, and arrows indicate the active site and $C_4$ Zn-ribbon motif. The active site residues are depicted as sticks. (B) Structure of the MERS-CoV PL$^{pro}$ bound to Ub (2.8Å resolution). PL$^{pro}$ is shown in green, and the covalently bound Ub molecule is orange and shown as tubes. Active site residues are shown as sticks with G75 and the 3CN linker of Ub covalently linked to C1592 of PL$^{pro}$. (C) Superposition showing a ~6.8Å movement of the Zn-ribbon motif between the open (yellow) and closed (green) PL$^{pro}$-Ub structures and a previously reported PL$^{pro}$ structure (grey) (PDB ID: 4P16; [291]). Our PL$^{pro}$ structure is not shown since it is highly similar to the open PL$^{pro}$-Ub structure. Movement of the Zn-ribbon motif was determined by measuring the distance between the Zn atom of the respective structures. Superpositions were performed in Coot [287]. Ub was removed from the closed and open PL$^{pro}$-Ub structures for clarity. Figures were created using PyMOL [305].

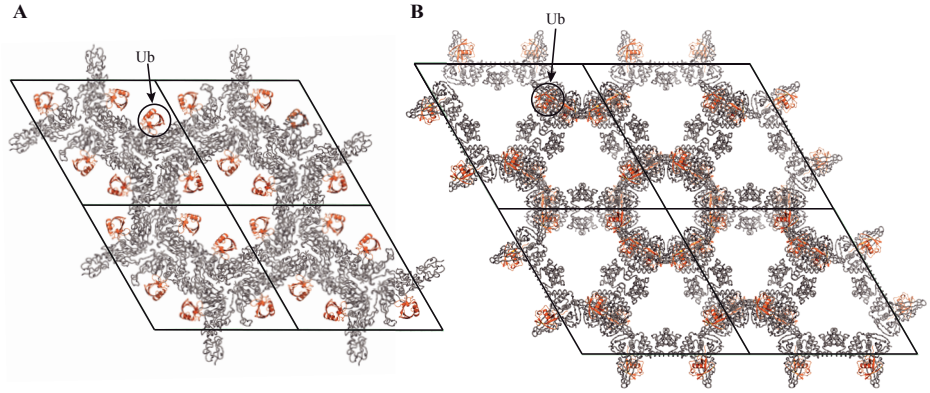


**Figure 3. Crystal packing arrangement of the open and closed MERS-CoV PL$^{pro}$-Ub structures.** The contents of 4 unit cells are shown, with PL$^{pro}$ and Ub depicted in grey and orange, respectively. (A) The open PL$^{pro}$-Ub structure crystallized in space group $P6_3$, where Ub was found to face the solvent, uninvolved in crystal contacts. (B) The closed PL$^{pro}$-Ub structure crystallized in space group $P6_522$, where Ub no longer faces the solvent, and is involved in crystal contacts. Figures were created using PyMOL [305].

PL$^{pro}$-Ub. An overlay of the different PL$^{pro}$ crystal structures that have been determined reveals that these structures vary in the position of the Zn-ribbon motif, further suggesting a high degree of mobility for this region (Fig. 2C). In line with this observation, movement of the fingers domain toward bound Ub was also reported for the SARS-CoV PL$^{pro}$ domain, which displayed a 3.8-Å movement of the Zn atom when comparing the Ub-bound and unbound structures [297]. Further comparison of the closed MERS-CoV PL$^{pro}$-Ub structure with the recently determined SARS-CoV PL$^{pro}$-Ub structure [297] revealed differences in the relative orientation of the fingers domain of the two proteases. The MERS-CoV PL$^{pro}$ fingers domain was found to be shifted approximately 26° away from the palm domain compared to that of SARS-CoV PL$^{pro}$, resulting in a slight difference in the Ub-binding orientation, with the MERS-CoV PL$^{pro}$-bound Ub being positioned closer towards helix α7 of the palm domain (Fig. 4).

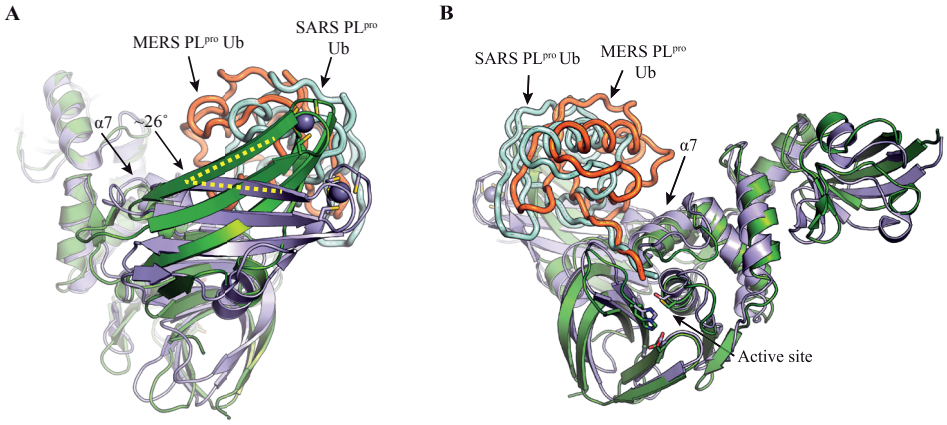


**Figure 4. Structural comparison of the SARS-CoV PL$^{pro}$-Ub and MERS-CoV PL$^{pro}$-Ub complexes.** (A) Superposition of the closed MERS-CoV PL$^{pro}$-Ub complex (green) and the SARS-CoV PL$^{pro}$-Ub complex (purple, PDB ID: 4M0W) using SSM superpose in Coot [287] (bound Ub molecules were ignored during the superposition). The Ub molecules bound to the MERS-CoV PL$^{pro}$ domain and SARS-CoV PL$^{pro}$ domain are depicted as tubes in orange and pale cyan, respectively. The ~26° shift in the fingers domain between the two respective structures is indicated. (B) Alternate orientation of the SARS-CoV PL$^{pro}$-Ub and MERS-CoV PL$^{pro}$-Ub superpositions highlighting the difference in Ub binding. In the MERS-CoV PL$^{pro}$-Ub complex, Ub is found shifted towards helix α7 compared to the SARS PL$^{pro}$-Ub complex. Helix α7 of MERS-CoV PL$^{pro}$ is indicated with an arrow. Figures were created using PyMOL [305].

## $PL^{pro}$ active site organization and interaction with the C-terminal RLRGG motif of Ub

The cleft formed between the palm and thumb domains of $PL^{pro}$ guides the C-terminal $_{72}RLRGG_{76}$ motif of Ub towards the protease active site, and the interactions between the C-terminal motif of Ub and the active site cleft are depicted in Fig. 5 (panels A and B). The $PL^{pro}$ active site is composed of a C1592-H1759-D1774 catalytic triad, which adopts a catalytically competent arrangement in both the unliganded and Ub-bound structures of $PL^{pro}$ (Fig. 5C). The oxyanion hole of the $PL^{pro}$ active site appears to be comprised of backbone amides from residues N1590, N1591 and C1592, which appear suitably arranged to stabilize the negative charge that develops on the carbonyl oxygen of the scissile bond during catalysis (Fig. 5C). Interestingly, as noted by Lei *et al.,* the MERS-CoV $PL^{pro}$ active site appears incomplete. In SARS-CoV $PL^{pro}$, W107 (amino acid numbering according to structure PDB ID: 2FE8) is positioned within the enzyme's active site with the indole nitrogen of its side chain oriented such that it likely is involved in forming part of the oxyanion hole [229]. In the case of MERS-CoV $PL^{pro}$, we and others [290, 291] have found the structurally equivalent residue in MERS-CoV $PL^{pro}$ to be L1587, which would be unable to participate in stabilizing the oxyanion during catalysis. Furthermore, it was recently shown that MERS-CoV $PL^{pro}$ L1587W mutants show greater catalytic efficiency than wild-type $PL^{pro}$ [290, 291]. Given the effect this residue has on the catalytic rate of $PL^{pro}$, it will be very interesting to understand how this residue influences MERS-CoV replication kinetics. It has been proposed that the decreased catalytic efficiency may influence maturation of the MERS-CoV polyprotein [290], and could be involved in the recognition of residues downstream of the scissile bond of the polyprotein cleavage sites or in the modulation of $PL^{pro}$ DUB activity.

Interestingly, differences were observed in the position of a loop on $PL^{pro}$ connecting strands β15 and β16, which is structurally analogous to the blocking loop (BL2) first described in the structure of USP14 [298]. This loop is disordered in our unliganded $PL^{pro}$ structure, and in a structure previously determined by others [291], however in both of our $PL^{pro}$-Ub structures we found this loop to be fully resolved, supported by the main-chain H-bonding interactions between R74 of Ub and G1758 of $PL^{pro}$, as well as a hydrophobic interaction between V1757 and P1644 - two $PL^{pro}$ residues present on opposite sides of the active site cleft (Fig. 5A). The side-chain η-amino group of the Ub residue R74 is also hydrogen bonded to the main-chain carbonyl group of $PL^{pro}$ residue T1755, however this interaction is only seen in the open $PL^{pro}$-Ub structure. The SARS-CoV $PL^{pro}$ domain has also been crystallized both in the presence [229] and absence [297] of Ub, and while the BL2 of unbound SARS-CoV $PL^{pro}$ was resolved in two of three monomers of the asymmetric unit, the third showed weak electron density for BL2 and high temperature factors indicating a high degree of mobility. In addition, in the TGEV USP domain $PL1^{pro}$ a structurally analogous BL2 was found to be in an open conformation with poorly defined electron density in the absence of substrate [231]. It is interesting to note that all three coronavirus USP DUBs crystallized to date (from MERS-CoV, SARS-CoV and TGEV) demonstrate a significant degree of flexibility within the BL2 region in the absence of substrate, and that none of the structures determined in their unbound form demonstrate obstruction of the active site via BL2.

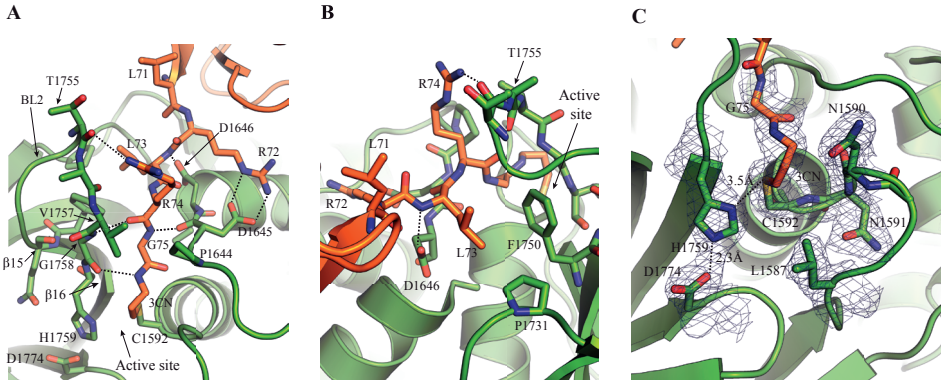


**Figure 5. Active site of MERS-CoV PL$^{pro}$ and interactions with the C-terminal RLRGG motif of Ub.** Interactions between open PL$^{pro}$ (green) and the C-terminal RLRGG motif of Ub (orange) are depicted in panels A and B. (A) The main-chain amide of the 3CN linker, which mimics G76 of Ub, forms a hydrogen bond with the main chain carbonyl of PL$^{pro}$ residue G1758. The main-chain amide of G75 of Ub forms a hydrogen bond with the carbonyl group of PL$^{pro}$ D1645, and a hydrogen bonding interaction occurs between the main-chain carbonyl of R74 of Ub and the main-chain amide of G1758 of PL$^{pro}$. The side-chain η-amino group of Ub residue R74 is hydrogen bonded to the main-chain carbonyl group of PL$^{pro}$ T1755. Hydrogen bonds also occur between the side-chain ε- and η-amino groups of Ub R72 and the carboxylate of PL$^{pro}$ D1645, as well as between the main-chain amide of Ub residue L73 and side chain PL$^{pro}$ residue D1646. The BL2 between strands β15 and β16 is indicated with an arrow. (B) Alternate orientation of the PL$^{pro}$ active site showing a hydrogen bonding interaction between the Ub L73 main-chain amide group and the side-chain carboxylate of PL$^{pro}$ residue D1646. The side chain of Ub residue L73 also undergoes hydrophobic interactions with PL$^{pro}$ residues F1750 and P1731. (C) The MERS-CoV PL$^{pro}$ C1592-H1759-D1774 catalytic triad residues are shown, as well as residues N1590 and N1591, which together with C1592 form the oxyanion hole via their backbone amide groups. The covalent 3CN molecule is shown linking the C-terminus of Ub to the active site C1592 of PL$^{pro}$. The active site L1587 residue, which is not involved in oxyanion hole formation, is also shown. The electron density is a maximum-likelihood weighted $2F_{obs}$-$F_{calc}$ map contoured at 1.0σ. Figures created using PyMOL [305].

## Structure-guided design of $PL^{pro}$ mutants defective in DUB activity

We previously demonstrated that the DUB activity of the papain-like protease 2 (PLP2) from equine arteritis virus (EAV; another member of the nidovirus order), which resembles the ovarian tumour (OTU)-domain containing family of DUBs [299], could be selectively removed without affecting its ability to process the EAV replicase polyproteins. This allowed us to establish that the DUB activity of PLP2 is directly responsible for suppressing Ub-dependent antiviral pathways during infection of primary host cells [220]. Subsequently, Ratia *et al*. [207] applied a similar strategy to the SARS-CoV $PL^{pro}$ domain in order to partially remove the DUB activity of $PL^{pro}$ while maintaining the nsp2-3 processing function. We now used the crystal structure of the USP-like MERS $PL^{pro}$-Ub complex to guide the design of mutations targeting the Ub-binding site on $PL^{pro}$ that would completely disrupt Ub binding without affecting the structural integrity of the active site. $PL^{pro}$ residues interacting directly with Ub were replaced with larger, bulkier residues that would prevent Ub binding by altering both shape and surface electrostatics of the Ub-binding site. Individual mutation of eight different $PL^{pro}$ residues – R1649, T1653, A1656, N1673, V1674, V1691, V1706 and Q1708 – and combinations thereof, were generated (Fig. 6). Importantly, these residues are located at a distance from the $PL^{pro}$ active site, and thus we hypothesized that they would only participate in DUB activity and not polyprotein processing.

Despite significant movement within the fingers domain of $PL^{pro}$, most interactions between the protease and Ub are consistent between the open and closed Ub-bound complexes. Residue I44 of Ub, which forms part of the hydrophobic patch that is commonly recognized by Ub-binding proteins [300], interacts with the hydrophobic side-chain of V1691 of $PL^{pro}$ (Fig. 6B). Residues Q49 and E51 of Ub form hydrogen-bonding interactions with T1653 that is present on helix α7, which runs through the centre of $PL^{pro}$. Two arginine residues, R1649 of $PL^{pro}$ and R72 of Ub (the latter of which forms part of the C-terminal tail of Ub that is bound in the $PL^{pro}$ active site cleft) are oriented such that the guanidinium groups of these residues are arranged in a stacked conformation (Fig. 6C). In addition, due to the inward movement towards Ub of the closed $PL^{pro}$-Ub fingers domain, a unique hydrogen-bonding interaction between Q62 of Ub and Q1708 of $PL^{pro}$, and a hydrophobic interaction between F4 of Ub and V1706 of $PL^{pro}$ were found to occur in this complex (Fig. 6D). Residue A1656 is positioned near the C-terminus of $PL^{pro}$ helix α7, and while it is not directly involved in Ub binding we believed that it was positioned such that the introduction of larger residues (e.g. arginine or phenylalanine) could disrupt Ub recognition, and thus this residue was targeted for mutation (Fig. 6C). Two residues on the solvent-facing region of the $PL^{pro}$ Zn-ribbon motif, N1673 and V1674, were also targeted for mutagenesis. Though they do not bind Ub at the S1 binding site (the substrate binding site on $PL^{pro}$ responsible for binding monoUb in our structure – see [301] for nomenclature), we hypothesized that it may inhibit association with the distal Ub on K63 polyUb chains based on a superposition of a K63-linked diUb model onto the $PL^{pro}$-bound Ub molecule of the closed $PL^{pro}$-Ub complex structure determined here (not shown). In addition, the crystal structure of USP21 bound to linear diUb was recently determined and revealed that the tip of the fingers domain of this DUB acts as an S2 recognition site, binding to the

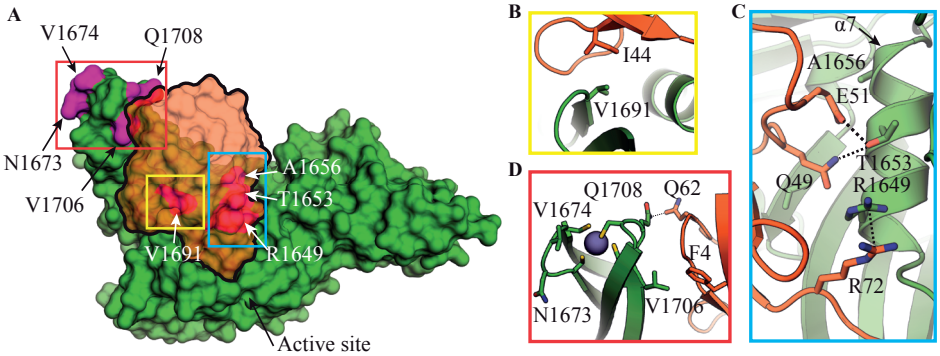


**Figure 6. Structure-guided mutagenesis of PL$^{pro}$ residues involved in Ub recognition.** (A) Surface representation of the closed MERS-CoV PL$^{pro}$-Ub complex. PL$^{pro}$ is shown in green, and Ub is shown in transparent orange. Those residues that were mutated in order to disrupt Ub binding are coloured magenta, and are indicated with arrows. Coloured boxes refer to close-up views of the PL$^{pro}$-Ub interactions, and are shown to the right. (B) Hydrophobic interaction is shown between V1691 of PL$^{pro}$ and I44 of Ub. (C) T1653 of PL$^{pro}$ is shown hydrogen bonded to Q49 and E51 of Ub, and R1649 of PL$^{pro}$ is shown interacting with R72 of Ub. (D) Hydrogen bonding interactions are shown between Q1708 of PL$^{pro}$ and Q62 of Ub, and a hydrophobic interaction is shown between V1706 of PL$^{pro}$ and F4 of Ub. N1673 and V1674 of PL$^{pro}$, which do not interact with Ub, are also displayed. Figures created using PyMOL [305].

distal Ub of a linear diUb molecule [296]. Given the structural similarity between K63 diUb and linear diUb, and the clear activity we observed for MERS-CoV PL$^{pro}$ towards K63, we hypothesized that mutating residues N1673 and V1674 near the Zn-ribbon may also disrupt Ub processing.

## Targeted mutations within the PL$^{pro}$ Ub-binding site disrupt Ub processing but not proteolytic cleavage of the nsp3↓4 site

Using a previously described ectopic expression assay [220], we monitored the effects of amino acid substitutions in PL$^{pro}$, as described above, on overall levels of Ub-conjugated proteins in HEK293T cells, as well as the ability of these PL$^{pro}$ variants to process the MERS-CoV nsp3↓4 polyprotein cleavage site *in trans*. V5-tagged PL$^{pro}$ (wild-type and mutants) was co-expressed with N-terminally HA-tagged and C-terminally V5-tagged MERS-CoV nsp3C-4 excluding the PL$^{pro}$ domain, from here on referred to as HA-nsp3C-4-V5. We assume that the successful processing of the nsp3↓4 site in HA-nsp3C-4-V5 is indicative of unaltered proteolytic cleavage capability of PL$^{pro}$, which during infection facilitates the release of nsp1, 2 and 3 from the viral polyproteins. Processing of HA-nsp3C-4-V5 *in trans* by wild-type PL$^{pro}$ and our panel of mutants was visualized *via* Western blotting (Fig. 7A). Whereas wild-type PL$^{pro}$ was able to cleave HA-nsp3C-4-V5 substrate *in trans*, the PL$^{pro}$ active site mutant C1592A was unable to cleave the nsp3↓4 site (Fig. 7A, compare lanes 5 and 6; 19 and 20). As expected, each of the substitutions in the Ub-binding site of PL$^{pro}$ only minimally affected nsp3↓4 cleavage, with the exception of the A1656R mutant that displayed a clearly reduced ability to cleave HA-nsp3C-4-V5 compared to wild-type PL$^{pro}$ (Fig. 7A, compare lanes 5 and 10). This suggests that A1656 of PL$^{pro}$ may be involved in recognizing and binding sequences in the vicinity of the nsp3↓4 cleavage site. Most double and triple substitutions tested were also slightly less efficient in cleaving HA-nsp3C-4-V5 compared to the wild-type control (Fig. 7A, compare lanes 19 and 24-26).

In order to analyse the effect of the mutations on overall DUB activity, $PL^{pro}$-V5 was co-expressed with FLAG-Ub, and the levels of FLAG-Ub-conjugated cellular proteins were visualized *via* Western blotting (Fig. 7B). Expression of wild-type $PL^{pro}$ resulted in a strong decrease of the accumulation of FLAG-Ub conjugates whereas a negligible effect was observed upon expression of active site mutant C1592A (Fig. 7B, compare lanes 3 and 4; 16 and 17). Substitutions of residue V1691, positioned on strand β12 of $PL^{pro}$, and T1653 and A1656, residues located on helix α7 (Fig. 6B and C), displayed the clearest reduction of $PL^{pro}$ DUB activity (Fig. 7B, lanes 5-8). The V1691R mutation had the most pronounced effect, and a $PL^{pro}$ T1653R/V1691R double mutant also displayed severely reduced DUB activity, comparable to that seen for the active site mutant (Fig. 7B, compare lanes 4, and 5; 17 and 22). Notably, a more conservative substitution at the same position, V1691L, had a much less pronounced effect on DUB activity (Fig. 7B, lane 6). Substitution of V1674 with either S or R impaired DUB activity, however to a much lesser extent than substitutions targeting V1691, T1653 and A1656 (Fig. 7B, compare lanes 5-8, 10 and 11). The N1673R substitution did not negatively affect DUB activity of $PL^{pro}$ at all, whereas the N1673R/V1674S double substitution resulted in slightly greater DUB activity (Fig. 7B, lanes 9 and 20). These results do not support our hypothesis based on modelling that N1673 and V1674 might form part of an S2 Ub-binding site that recognizes an additional distal Ub within a K63-linked chain. Further structural studies are needed to validate the role of these residues in binding Ub chains. It should be noted however that these mutants may still be able to process K63-linked polyUb chains by recognizing a single Ub monomer at the end of a polyUb substrate, which may explain the ineffectiveness of these mutations in disrupting DUB activity. Mutations at residues V1706 and Q1708 did not influence DUB activity of $PL^{pro}$ (Fig. 7B, lanes 18 and 19). Given that these residues were only found to interact with Ub in our closed $PL^{pro}$ structure (Fig. 6A), their failure to inhibit DUB activity in this cellular DUB assay is not surprising, and indicates that these residues are not essential for Ub recognition. Interestingly and repeatedly observed, the R1649Y mutant was found to have even greater DUB activity than wild-type $PL^{pro}$ (Fig. 7B, compare lanes 3 and 12). This residue was found to interact with residue R72 of Ub, and while this result was unexpected, it is possible that the R1649Y mutant retains the ability to interact with R72 of Ub *via* a cation-π interaction between the aromatic tyrosine inserted into $PL^{pro}$ and the positively charged arginine of Ub. Together, the findings from our mutagenesis study demonstrate that it is possible to selectively decouple the DUB and polyprotein processing activities of MERS-CoV $PL^{pro}$ through structure-guided site-directed mutagenesis.

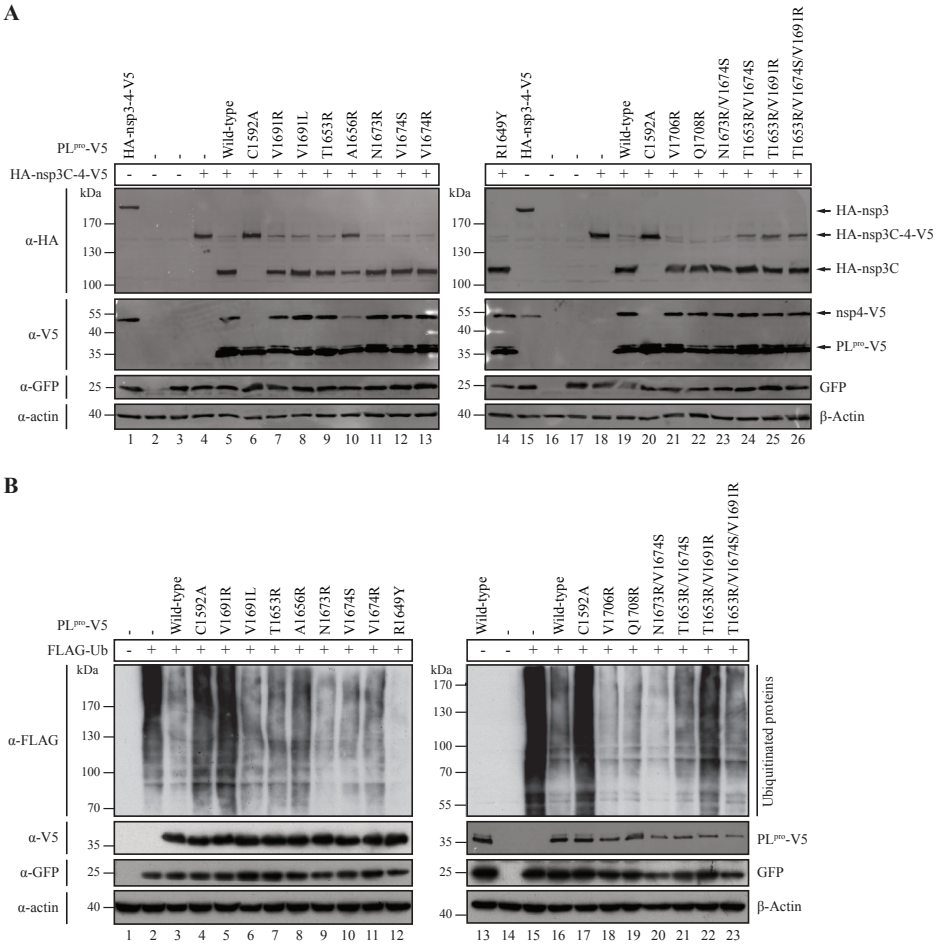


**Figure 7. Effect of PL$^{pro}$ mutations on *in trans* cleavage of nsp3↓4 and on DUB activity.** (A) HEK293T cells were co-transfected with plasmids encoding HA-nsp3C-4-V5 (which does not contain PL$^{pro}$), PL$^{pro}$-V5 (wild-type and mutants) and GFP (as a transfection control). As a control, plasmid encoding HA-nsp3-4-V5 which includes the PL$^{pro}$ domain was transfected (lanes 1 and 15), and cleavage resulted in the generation of full-length HA-tagged nsp3 and V5-tagged nsp4. Cells were lysed 18 h post transfection and expressed proteins were analysed by Western blotting. Proteolytic cleavage was measured from the generation of N-terminal HA-tagged nsp3C and C-terminal V5-tagged nsp4. (B) HEK293T cells were transfected with a combination of plasmids encoding FLAG-Ub, PL$^{pro}$-V5 (wild-type and mutants) and GFP (as a transfection control). Cells were lysed 18 h post transfection and expressed proteins were analysed by Western blotting to visualize the deconjugation of FLAG-tagged Ub from a wide range of cellular proteins by MERS-CoV PL$^{pro}$ wild-type and mutants.

## PL$^{pro}$ DUB activity suppresses the innate immune response

Conjugation and deconjugation of Ub play an important role in the regulation of the innate immune response, and not surprisingly, pathogens have evolved mechanisms to subvert these Ub-dependent pathways [269]. For arteriviruses, which are distant relatives of CoVs within the nidovirus order, it has been shown that the DUB activity of their PLP2 is involved in antagonizing IFN-β activation upon ectopic expression, and for EAV this was confirmed during infection in host cells [220, 302]. Coronavirus papain-like proteases have been suggested to act as IFN-β and NF-κB antagonists as well [199-201, 203]. MERS-CoV PL$^{pro}$ is thought to possess these properties based on its capability to inhibit RIG-I-, MDA5- and MAVS-induced IFN-β promoter stimulation, and to reduce TNFα-induced NF-κB reporter gene activity [202, 205]. We therefore designed luciferase-based reporter gene assays to establish whether the DUB activity of MERS-CoV PL$^{pro}$ alone suffices to antagonize the IFN-β pathway. To this end, we first assessed at which level of this innate immune signal transduction pathway MERS-CoV PL$^{pro}$ is most active as a suppressor.

Innate immune signalling was induced in HEK293T cells by expression of one of three signalling factors: RIG-I, MAVS or IRF3, which stimulate the pathway leading to IFN-β production at different levels. Since RIG-I and IRF3 normally need to be activated through post-translational modification (ubiquitination and phosphorylation respectively), constitutively active variants were used (RIG-I$_{(2CARD)}$ and IRF3$_{(5D)}$) which efficiently induce downstream signalling independent of these activation steps. Cells were co-transfected with plasmids encoding one of these innate immune signalling proteins and wild-type PL$^{pro}$, the PL$^{pro}$ active site mutant C1592A or full-length MERS-CoV nsp3 containing the PL$^{pro}$ domain. The inhibitory effect of the PL$^{pro}$ variants on the activation of the IFN-β promoter by the different stimuli was measured via co-expression of a firefly luciferase reporter gene under control of the IFN-β promoter. Another co-transfected plasmid encoding *Renilla* luciferase was included as an internal control in order to be able to correct for variability in transfection efficiency. At 16 h post transfection luciferase activities were measured, and activation of the IFN-β promoter induced by expression of RIG-I$_{(2CARD)}$, MAVS, or IRF3$_{(5D)}$ was set at 100% (Fig. 8). In accordance with Mielech *et al*. [202], we observed that MERS-CoV PL$^{pro}$ significantly reduced the IFN-β promoter activation that could be induced by expression of either RIG-I$_{(2CARD)}$ or MAVS. This effect was concentration-dependent, while the PL$^{pro}$ active site mutant was unable to block IFN-β promoter activation (Fig. 8A and C). MERS-CoV nsp3 expression also inhibited RIG-I- and MAVS-mediated IFN-β promoter induction (Fig. 8B and D), and together this suggested that PL$^{pro}$ inhibits innate immune signalling at least downstream of the MAVS adaptor, and possibly also in the signalling between RIG-I and MAVS. MERS-CoV PL$^{pro}$ also inhibited activation of the IFN-β promoter after stimulation with IRF3$_{(5D)}$ in a concentration-dependent manner, while the C1592A mutant did not reduce IFN-β promoter activation (Fig. 8E). However, expression of full length MERS-CoV nsp3 did not significantly inhibit IFN-β promoter activation after stimulation with IRF3$_{(5D)}$ (Fig. 8F). This suggests that the subcellular localization of the protease, which in case of full-length nsp3 is membrane anchored and in case of the PL$^{pro}$ domain is presumably cytosolic, may be important in determining its substrate specificity. Taken together, our results suggest that MERS-CoV PL$^{pro}$ primarily interferes with the IFN-β signalling pathway at the level between MAVS and IRF3.

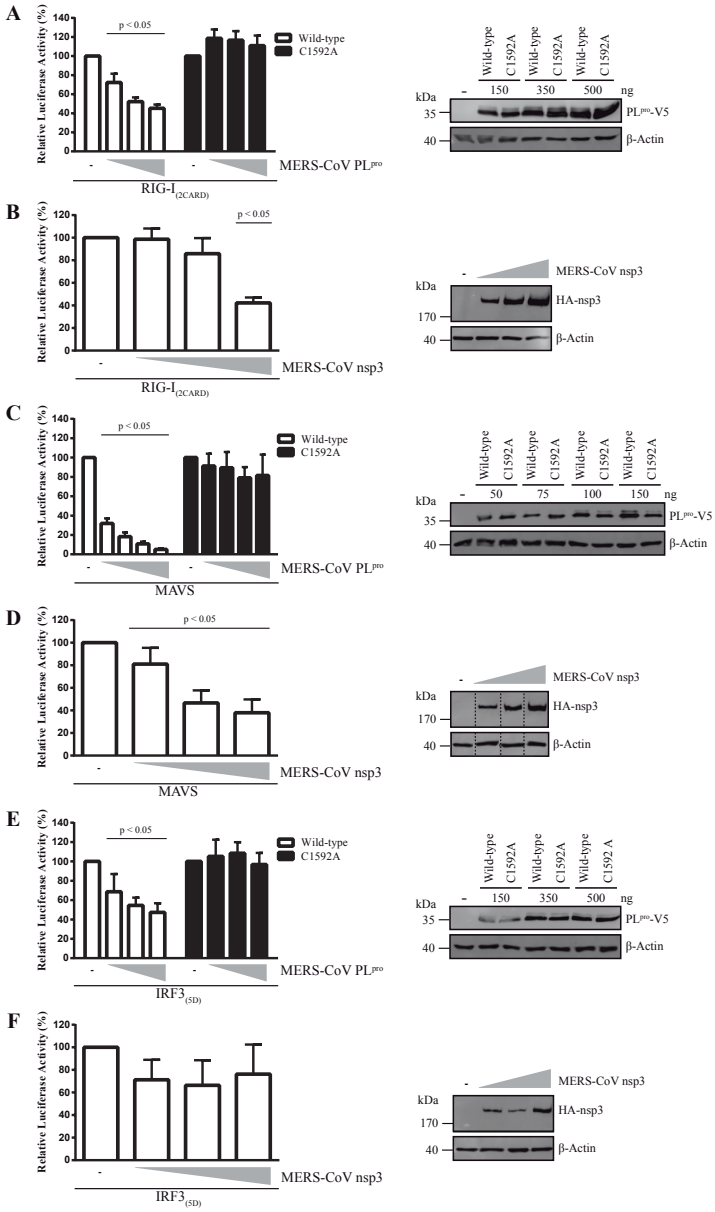


**Figure 8. MERS-CoV PL$^{pro}$ inhibits RIG-I- and MAVS-induced IFN-β promoter activity.** HEK293T cells were transfected with a combination of plasmids expressing a firefly luciferase reporter gene under control of the IFN-β promoter, *Renilla* luciferase, innate immune response inducers RIG-I$_{(2CARD)}$, MAVS or IRF3$_{(5D)}$ and increasing amounts of MERS-CoV PL$^{pro}$ wild-type, active site mutant C1592A (A, C and E) or full-length MERS-CoV nsp3 (B, D and F). Upon induction of the innate immune response with RIG-I$_{(2CARD)}$ and IRF3$_{(5D)}$, cells were transfected with the PL$^{pro}$ (0, 150, 350 or 500 ng) or nsp3 (0, 350, 500 of 1000 ng) constructs. Upon induction with MAVS, cells were transfected with 0, 50, 75, 100 or 150 ng PL$^{pro}$ construct or 0, 150, 350, 500 ng of the nsp3 expression vector. At 16 h post transfection, cells were lysed and luciferase activity was measured. All experiments were repeated independently at least four times. Significance was evaluated using an unpaired two-tailed Student's *t*-test; p values <0.05 were considered significant. Bars represent mean with error bars indicating the standard deviation. Western blotting was used to verify expression of MERS-CoV PL$^{pro}$ and nsp3.

We therefore chose to use MAVS-mediated induction of IFN-β promoter activation in subsequent experiments. This also resulted in the strongest inhibition by $PL^{pro}$, providing a maximum window to assess the effects on IFN-β promoter inhibition by the $PL^{pro}$ mutants with specifically inactivated DUB activity. Inhibition of IFN-β promoter activation by wild-type and mutant $PL^{pro}$ was determined by calculating the relative luciferase activity (Fig. 9). Expression of wild-type $PL^{pro}$ reduced MAVS-induced IFN-β promoter activity to ~20% of the control, whereas active site mutant C1592A reduced it by only a few percent compared to the untreated control (Fig. 9). Substitutions T1653R and A1656R resulted in greatly impaired DUB activity (Fig. 7B, lanes 7 and 8), and compared to wild-type $PL^{pro}$, expression of these mutants resulted in higher IFN-β promoter activity with relative luciferase values of approximately 54% and 58% respectively (Fig. 9). It should however be noted that the A1656R mutant was also impaired in cleaving the nsp3↓4 site and therefore this mutation non-specifically disrupted the two proteolytic functions of $PL^{pro}$. Strikingly, each mutant containing the V1691R substitution was completely unable to inhibit IFN-β promoter activation resulting in relative luciferase activity levels similar to those seen with the active site mutant (Fig. 9, lanes 4, 16 and 17). This strongly suggested that the DUB activity of $PL^{pro}$, which we found to be severely impaired in V1691R mutants (Fig. 7B), is responsible for supressing MAVS-induced IFN-β promoter activity in this assay. The level of reduction in DUB activity corresponded to the degree of inhibition of IFN-β promoter activation for all $PL^{pro}$ mutants tested, which strengthens this conclusion. In accordance with its increased DUB activity, mutant R1649Y suppressed MAVS-induced IFN-β promoter activity more effectively than wild-type $PL^{pro}$.

Taken together, our data show that the DUB activity of MERS-CoV $PL^{pro}$ suffices to efficiently suppress MAVS-induced IFN-β promoter activation and that this activity can be selectively disabled, without disrupting protease activity towards the nsp3↓4 cleavage site, by targeting the Ub-binding site of the enzyme. This demonstrates for the first time that the DUB activity of MERS-CoV $PL^{pro}$ is specifically responsible for suppressing the innate immune response.

## DISCUSSION

Guided by the MERS $PL^{pro}$-Ub crystal structures, we here describe how the DUB activity of $PL^{pro}$ can be selectively disabled by introducing mutations into the S1 binding pocket of the protease (Fig. 6). Particularly the substitution of V1691 with the bulky and charged arginine residue severely impaired DUB activity in our cell culture-based assays. In addition, our results demonstrate that the majority of the mutations within the S1 Ub-binding site of $PL^{pro}$ that were tested do not affect *trans* cleavage of the nsp3↓4 junction, with the exception of an A1656R mutant that did disrupt cleavage of the nsp3↓4 site. The latter result indicates that A1656 resides is in a region of $PL^{pro}$ that recognizes both Ub and a region of the nsp3C-4 construct that was used to test cleavage efficiency.

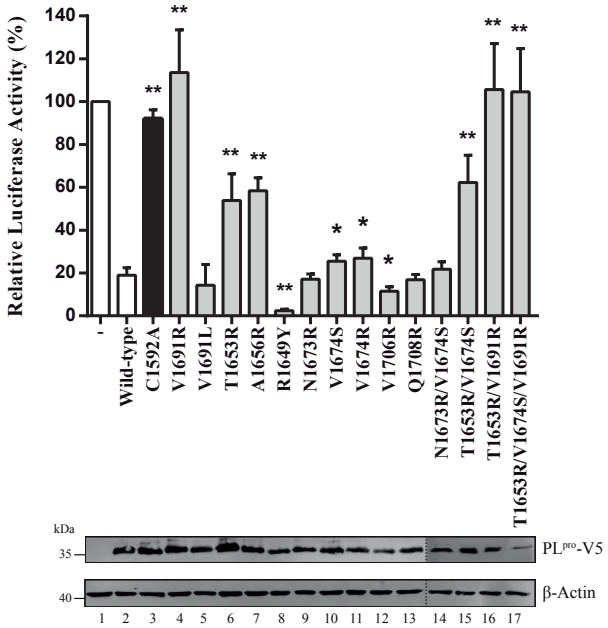


**Figure 9. DUB activity is required for IFN-β promoter antagonism by MERS-CoV PL$^{pro}$.** HEK293T cells were transfected with plasmids encoding a firefly luciferase reporter gene under control of the IFN-β promoter, *Renilla* luciferase, innate immune response inducer MAVS (25 ng) and MERS-CoV PL$^{pro}$ wild-type and mutants (75 ng). At 16 h post transfection, cells were lysed and luciferase activity was measured. All experiments were repeated independently at least four times. Significance relative to wild-type was evaluated using an unpaired two-tailed Student's *t*-test; significant values were indicated with * if p<0.05 and ** if p<0.01. Bars correspond to the mean with error bars showing the standard deviation. Western blotting was used to verify expression of MERS-CoV PL$^{pro}$.

Our results demonstrate that the DUB activity of MERS-CoV PL$^{pro}$ inhibits IFN-β promoter activation when innate immune signalling is induced by co-expression of either RIG-I or MAVS. The fact that suppression of IFN-β promoter activation was completely eliminated for several of our mutants (Fig. 9) strongly suggests that the proteolytic activity still present in those mutant enzymes has no additional role in the suppression of this particular branch of the innate immune response, for example by directly cleaving RIG-I or MAVS. A number of other CoV papain-like proteases with DUB activity have also been implicated in antagonizing the host innate immune response [199-201, 203]. In agreement with our data, recent studies have demonstrated the ability of MERS-CoV PL$^{pro}$ to inhibit RIG-I-, MDA5- and MAVS-dependent IFN-β promoter activation, as well as to down-regulate the level of IFN-β mRNA transcripts in MDA5-stimulated cells [202]. The current data supports the hypothesis that all these activities solely depend on the deubiquitinating capacities of these coronavirus enzymes. Reports regarding the dependence of MERS-CoV PL$^{pro}$-mediated IFN-β antagonism on the enzyme's protease activity have however varied thus far. Mielech *et al.* [202] recently demonstrated that a MERS-CoV nsp3 fragment containing PL$^{pro}$ but excluding the transmembrane domain can inhibit MAVS-, RIG-I- and MDA5-dependent IFN-β promoter activation, and MDA5 mediated IFN-β mRNA transcription only with a functional

$PL^{pro}$ active site. Yang *et al.* [205] on the other hand used a MERS-CoV $PL^{pro}$ expression product extending into the nsp3 transmembrane region to demonstrate that down-regulation of RIG-I-stimulated IFN-β promoter activity is seen even with an active site knock-out mutant. Here we show that inhibition of RIG-I-, MAVS- and IRF3-induced IFN-β promoter activity by the MERS-CoV $PL^{pro}$ domain is clearly dependent on a functional active site, and that it is specifically the DUB activity of the protease that mediates this inhibition. It can however not be ruled out that other parts of nsp3 contain additional innate immune suppressing activities, which may be responsible for the protease-independent effects reported with longer expression products.

Ubiquitination plays an important role in the regulation of pathways involved in detecting and counteracting viral infections, and, not surprisingly, a number of viruses of substantial diversity have been found to deploy DUB enzymes that manipulate these signalling processes by reversing the post-translational modification of cellular proteins by Ub conjugation [206, 303]. Some of these DUBs, specifically those found in positive-stranded RNA viruses, are also critical for viral replication by catalysing the proteolytic cleavage of specific sites in viral polyproteins, thus complicating our ability to study the direct effects of the additional DUB activity of these viral proteases. Ultimately, these effects need to be studied in the context of a viral infection, however a simple inactivation of the protease/DUB would not only fail to prove the specific involvement of the DUB activity, it would also prevent viral replication. The method described here selectively removed the DUB activity of the MERS-CoV $PL^{pro}$ domain while leaving polyprotein processing activity at the nsp3↓4 site unhindered, thus paving the way for the application of these mutations to recombinant MERS-CoV and the direct study of the role of DUB activity during infection.

We were able to show that K48- and K63-linked polyUb chains are processed *in vitro* by MERS-CoV $PL^{pro}$ at similar rates, which is in accordance with a recent report by Baez-Santos and co-workers [235]. In contrast, SARS-CoV $PL^{pro}$ rapidly cleaves K48-linked polyUb and displays only moderate activity for K63 linkages in similar assays [207]. It has been suggested that SARS-CoV $PL^{pro}$ may recognize K48-linked diUb via its S1 and S2 sites [207], although to date no crystal structures have been reported of SARS-CoV $PL^{pro}$ in complex with a diUb substrate. Similarly, no such structural data has been obtained for MERS-CoV $PL^{pro}$, and thus future structural studies are necessary to determine precisely how MERS-CoV $PL^{pro}$ recognizes polyUb substrates and whether the preferences observed in expression systems can be confirmed in situations representative of an infection.

In addition to deconjugating Ub, MERS- and SARS-CoV $PL^{pro}$ also recognize the antiviral Ubl molecule ISG15 [197, 202]. In the absence of a crystal structure of a DUB from the USP family in complex with ISG15, it is difficult to predict which regions of $PL^{pro}$ may be specifically responsible for ISG15 binding. However, it is interesting to note that both the palm and fingers domains of the SARS-CoV $PL^{pro}$ domain [207] and the cellular USP21 [296], respectively, have been implicated in ISG15 recognition, likely through additional interactions between $PL^{pro}$ and the N-terminal Ubl fold of ISG15. Future structural work is necessary to identify the specific determinants of ISG15 recognition by MERS-CoV $PL^{pro}$. Structure-guided mutagenesis of MERS-CoV $PL^{pro}$ to selectively

disrupt deISGylation without affecting polyprotein cleavage would further expand our insights into the role of this additional activity in coronaviral immune evasion. The specific removal of DUB and potentially deISGylating activity from viral proteases that suppress the host innate immune response may open new avenues to engineer attenuated viruses for use as modified live virus vaccines.



## ACKNOWLEDGEMENTS

We are grateful to Diede Oudshoorn for generating MERS-CoV nsp3-4 expression constructs and Kathleen C. Lehmann for excellent technical assistance. We kindly thank the following people for providing us with reagents: John Hiscott, Craig E. Cameron, Michaela U. Gack, and Adolfo García-Sastre. We thank Veronica Larmour for technical assistance and Shaun Labiuk and the staff of the Canadian Light Source (CLS) beamline 08B1-1 for assistance with data collection. The CLS is supported by Natural Sciences and Engineering Research Council of Canada (NSERC), the National Research Council, the Canadian Institutes of Health Research, and the University of Saskatchewan. This research was supported in part by NSERC Grant 311775-2010 (to B.L.M.), the Division of Chemical Sciences of the Netherlands Organization for Scientific Research (NWO-CW) through ECHO grant 700.59.008 (to M.K. and E.J.S.), and the European Union Seventh Framework Programme (FP7/2007-2013) under SILVER grant agreement no. 260644. B.L.M. holds a Manitoba Research Chair award.

*Coordinates and structure factors for the $PL^{pro}$, open $PL^{pro}$-Ub and closed $PL^{pro}$-Ub structures have been deposited to the RCSB Protein Data Bank with the accession codes 4REZ, 4RF1 and 4RF0, respectively.*

# 3 The deubiquitinating activity of Middle East respiratory syndrome coronavirus papain-like protease delays the innate immune response and enhances virulence in a mouse model

Robert C.M. Knaap[1], Raúl Fernández-Delgado[2], Tim J. Dalebout[1], Nadia Oreshkova[1], Peter J. Bredenbeek[1], Luis Enjuanes[2], Isabel Sola[2], Eric J. Snijder[1], and Marjolein Kikkert[1]

[1] Department of Medical Microbiology, Leiden University Medical Center, Leiden, The Netherlands
[2] Department of Molecular and Cell Biology, National Center of Biotechnology (CNB-CSIC), Campus Universidad Autonoma de Madrid, Madrid, Spain

## ABSTRACT

Middle East respiratory syndrome coronavirus (MERS-CoV) continues to cause zoonotic infections and serious disease, primarily in the Arabian Peninsula, due to repeated spill-over from dromedary camels and subsequent nosocomial transmission. Approved MERS vaccines for use in animals or humans are not currently available. MERS-CoV replication requires the virus-encoded papain-like protease ($PL^{pro}$) to cleave multiple sites in the viral replicase polyproteins, thereby releasing functional non-structural proteins. Additionally, $PL^{pro}$ is a deubiquitinating enzyme (DUB) that can remove ubiquitin(-like) moieties from substrates, presumably to counteract host antiviral responses. In previous work, we determined the crystal structure of MERS-CoV $PL^{pro}$ in complex with ubiquitin, facilitating the design of $PL^{pro}$ mutations that impair DUB activity without affecting viral polyprotein cleavage. Here, we introduced these DUB-inactivating mutations into the viral genome and examined their impact on MERS-CoV infection both in cell culture and in a lethal mouse model. Although overall replication of DUB-negative and wild-type (wt) recombinant MERS-CoV was comparable in multiple cell lines, infection with DUB-negative virus markedly increased mRNA levels for interferon (IFN)-β and IFN-stimulated genes. Moreover, compared to a wt virus infection, the survival rate was significantly increased when DUB-negative MERS-CoV was used to infect transgenic mice expressing a human MERS-CoV receptor. Interestingly, DUB-negative and wt MERS-CoV replicated to the same titers in lungs of infected mice, but the DUB-negative virus was cleared faster, likely due to the observed accelerated and better-regulated innate immune responses, in contrast to delayed and subsequently excessive responses in wt virus-infected mice. This study provides the first direct evidence that the DUB activity of a coronaviral protease contributes to innate immune evasion and can profoundly enhance virulence in an animal model. Thus, reduction or removal of the innate immune-suppressive DUB activity of $PL^{pro}$s is a promising strategy for coronavirus attenuation in the context of rational vaccine development.

## INTRODUCTION

The *Coronaviridae* family includes numerous viruses that can cause respiratory and enteric disease in animals or humans. To date, six coronaviruses (CoVs) have been identified that have the ability to infect humans, including two that have caused global public health concerns due to high case-fatality rates. Firstly, in 2003, an outbreak of severe acute respiratory syndrome coronavirus (SARS-CoV) led to about 8000 confirmed human infections with a case-fatality rate of around 10% [9]. Fortunately, within 6 months, the epidemic spread of SARS-CoV could be halted by conventional public health- and quarantine measures. Secondly, since 2012, about 2500 laboratory-confirmed cases of human infection with Middle East respiratory syndrome coronavirus (MERS-CoV) have been reported [306]. Given the ~35% MERS case-fatality rate, this implies that the number of MERS-related deaths now exceeds the death toll of the 2003 SARS-CoV outbreak. Although MERS cases were reported from 27 different countries, the vast majority of human infections have occurred in Saudi Arabia where the virus was also first recovered from an infected individual. It was subsequently identified as a previously unknown CoV by genome sequence analysis [25, 26]. MERS-CoV appears to be widespread among dromedary camels [307], which shed the virus from their upper respiratory tract [41] and were identified as a reservoir from which repeated spill-over to humans has occurred [43, 308]. Nevertheless, bats, which harbour many different CoV species including a variety of SARS- and MERS-like CoVs, are considered to be the most likely wildlife reservoir for both these viruses [58, 309]. The MERS problems are further augmented by secondary human infections acquired in household settings or health-care facilities [32]. To date, therapeutics nor vaccines to prevent or treat MERS-CoV infections have been approved.

Host organisms have evolved antiviral defense systems, whereas pathogens in turn have adapted to evade these systems or suppress their activation [129]. Upon infection, the vertebrate host's first line of defense is the innate immune response, which is initiated when pathogen-associated molecular patterns, such as double-stranded (ds) RNA, are sensed by pathogen recognition receptors [133]. After initial sensing, activation of subsequent signalling cascades leads to nuclear translocation of the transcription factors interferon regulatory factor (IRF) 3, IRF7 and NF-κB, which drives expression of antiviral molecules such as interferons (IFNs) and other pro-inflammatory cytokines. Type I IFNs (IFN-α/β) and type III IFNs (IFN-λ) induce expression of interferon-stimulated genes (ISGs) with the distinction that, due to receptor restrictions, IFN-λ can primarily induce ISGs in epithelial cells, whereas ISGs induced by type I IFNs can be expressed by virtually any cell type [137, 138]. ISGs are antiviral effector proteins that limit virus replication and spread. Moreover, some ISGs can enhance pathogen recognition and thereby innate immune signalling [136]. NF-κB-mediated production of cytokines like TNFα, IL-6, and IL-8, are important for the inflammatory response as well as for attracting and activating immune cells [310]. Type I IFNs also play a major role in stimulating expression and production of other immune mediators like IFN-γ and cytokines by diverse innate immune cells. Additionally, antigen presentation by dendritic cells is enhanced and also the survival and activity of B and T cells is modulated by type

I IFNs, which underlines the importance of type I IFNs in shaping adaptive immune responses [311, 312]. The fine-tuning of innate immune responses is crucial and therefore the activities of signalling molecules in these pathways are tightly regulated by post-translational modifications such as phosphorylation and ubiquitination [142]. Ubiquitination is the covalent conjugation of ubiquitin (Ub), an evolutionally conserved protein, via attachment of its C-terminal G76 residue to the N-terminal residue or any lysine residue of a protein substrate [145]. Conjugation of Ub can also occur to previously conjugated Ub moieties on the N-terminus or at any of the seven lysine residues in Ub itself, leading to the formation of polyUb chains with different topologies and functions [147, 313]. Ubiquitination is performed by a cascade of three enzymes: an E1 Ub-activating enzyme, an E2 Ub-conjugating enzyme and an E3 Ub ligase. The reverse reaction, the removal of Ub from substrates, is performed by proteases that are known as deubiquitinating enzymes (DUBs) [150]. In the context of the innate immune response, ubiquitination is essential for the activation or degradation of many factors in the signalling cascade, while specific cellular DUBs can downregulate the signalling to protect cells from adverse over-reactions of the system [151, 152]. In response, many viruses have developed means to evade activation of the immune response by modulating the Ub-system, for example by expressing viral DUBs (vDUBs) or E3 ligases, or by hijacking or blocking the activity of host DUBs or E3 ligases [314, 315].

Coronaviruses are positive-stranded RNA viruses with large genomes of 26- to 34-kb, which have a highly conserved organization [73]. The first two-thirds of their genome encode the replicase polyproteins (pp1a and pp1ab) that yield 15 or 16 non-structural proteins (nsps) following cleavage by internally-encoded proteases. Structural and accessory proteins are expressed from the remaining one-third of the genome, using a nested set of viral subgenomic RNAs that are produced in infected cells [72]. Viral RNA synthesis is thought to occur in close association with virus-induced membranous 'replication organelles', including double-membrane vesicles that label abundantly for dsRNA [88]. Melanoma differentiation-associated gene 5 (MDA5), a cytosolic innate immune sensor, was proven to be crucial for detecting murine CoV replication [132]. Despite the production of viral RNA species that can activate the host's innate immune response, IFNs and pro-inflammatory cytokines are hardly expressed or only appear late in cell culture-based infection models for various CoVs [154, 157, 160, 316, 317]. In a mouse model for SARS-CoV infection, a delayed and subsequently excessive IFN response was shown to induce severe lung immunopathology, due to the influx of inflammatory monocyte-macrophages leading to elevated levels of cytokines and chemokines [318]. Similar pathological observations were made in a mouse model for lethal MERS-CoV infection, which is based on a mouse-adapted virus obtained by serial passaging of the parental virus in mice [319]. Coronaviruses employ various strategies to prevent immune detection and actively suppress or delay activation of the immune system, which is thought to contribute to viral virulence and pathogenesis [320]. The structural membrane protein and multiple accessory proteins of MERS-CoV have been shown to antagonize type I IFN- as well as NF-κB responses [176, 179, 181, 321-323]. Several other mechanisms of interference with the innate immune response were attributed to CoV nsps, specifically nsp1, 3,

15, and 16. Nsp1 of β-CoVs has been shown to alter host antiviral gene expression by selectively targeting mRNAs for degradation [183, 188]. The CoV macrodomain in nsp3, which has de-ADP-ribosylation activity, antagonizes innate immune signalling [191, 194]. Moreover, inactivation of the nsp15 endoribonuclease led to a severely attenuated virus that strongly activated sensors MDA5, PKR, and 2',5'-oligoadenylate synthetase [173, 174], suggesting that the enzyme normally serves to prevent activation of the immune response. Inactivation of the mouse hepatitis virus (MHV) nsp16 2'-O-methyltransferase, which was shown to be pivotal for protection of CoV RNA from recognition by MDA5, enhanced IFN-β expression upon infection [169]. In contrast, inactivation of this activity in SARS-CoV did not induce a robust IFN-β response, but it did attenuate the virus in cell culture-based infections and mice [168]. Finally, the papain-like protease (PLP) in nsp3 can bind and cleave Ub and interferon-stimulated gene 15 (ISG15) from substrates, most likely to suppress the antiviral responses (reviewed by [206]). In the case of α-CoVs and lineage A β-CoVs, nsp3 contains two PLPs (PLP1 and PLP2), of which usually one has DUB activity, while the remaining β-CoVs, and also γ- and δ-CoVs, express a single PLP (PL$^{pro}$) with DUB activity. The DUB activity of CoV PLPs was first discovered for SARS-CoV and subsequently PL$^{pro}$ was shown to suppress innate immune signalling pathways upon its ectopic expression [195, 197, 200]. In similar experimental settings, these features have now been demonstrated for a variety of CoV PLPs, including MERS-CoV PL$^{pro}$ [202, 205, 206].

Disruption of antagonists of the IFN response can be an approach for modified live virus (MLV) vaccine design because such virus mutants will still be immunogenic, while being attenuated-by-design. Due to their reduced capability to evade the innate immune system, these would be anticipated to induce enhanced immune responses. This concept was successfully applied to influenza virus A and B by removing or mutating the NS1 protein, a well-characterized IFN antagonist. This yielded strongly attenuated viruses that provided protective immunity in mice and induced neutralizing antibodies in humans [324-326]. More recently, *in vivo* attenuation of MERS-CoV in a mouse model was achieved by deletion of open reading frames (ORFs) 3 to 5, or by inactivation of the nsp16 2'-O-methyltransferase [170, 181]. In our current study, we aimed to eliminate the DUB activity of MERS-CoV PL$^{pro}$ to evaluate its role during infection in cell culture as well as a mouse model, and to determine if a DUB-negative MERS-CoV is attenuated and a potential MLV vaccine candidate. Based on the crystal structure of the MERS-CoV PL$^{pro}$-Ub complex, the Ub-binding site of PL$^{pro}$ was equipped with substitutions that reduced the DUB activity but did not noticeably affect polyprotein cleavage [327]. This is important because PL$^{pro}$ plays a crucial role in virus replication during the liberation of nsp1 to nsp4 from pp1a and pp1ab. In earlier research, the impact of such DUB-inactivating substitutions was characterized in cell culture-based experiments in which mutant PL$^{pro}$ domains were overexpressed and, in accordance with the results of others, were found to have lost the ability to suppress activation of the IFN-β/NF-κB promoter [207, 208, 327]. Here we describe the generation of recombinant (r) DUB-negative MERS-CoVs with amino acid substitutions in PL$^{pro}$, to analyse for the first time, the impact of the DUB function on infection. These mutant viruses had similar growth kinetics as wild-type (wt) rMERS-CoV, how-

ever mRNA levels for IFN-β and ISGs were significantly higher in cells infected with DUB-negative rMERS-CoV. In a lethal MERS-CoV infection model in mice, the DUB-negative virus was found to be strongly attenuated as the survival rate of mice infected with this mutant was significantly higher than for wt virus-infected mice. Furthermore, DUB-negative virus was cleared faster from the lungs and mRNA levels of IFNs, ISGs, and cytokines were upregulated earlier relative to those in control mice infected with wt rMERS-CoV. Collectively, this demonstrates that CoV $PL^{pro}$'s DUB activity enhances virulence in an animal model and that selective removal of this activity could be a basis for the design of MLV vaccines.

## MATERIALS AND METHODS

### Cell culture

HuH-7 cells (a kind gift of Dr. Ralf Bartenschlager, Heidelberg University) were maintained at 37°C in 5% $CO_2$ in Dulbecco's modified Eagle's medium (DMEM; Lonza) with 8% foetal calf serum (FCS; Bodinco BV), 100 units/ml penicillin (Lonza), 100 units/ml streptomycin (Lonza), 2 mM L-glutamine and non-essential amino acids (both PAA). MRC5 cells (ATCC CCL-171) were cultured in Eagle's minimum essential medium (EMEM; Lonza) with the same supplements as used in the medium for HuH-7 cells. BHK-21 cells (ATCC CCL-10) were grown in Glasgow minimum essential medium (Gibco) supplemented with 8% FCS, 100 units/ml penicillin, 100 units/ml streptomycin, 10% tryptose phosphate broth (Gibco), and 10 mM Hepes (pH 7.4; Lonza).

### Construction and launch of mutant rMERS-CoV

A full-length MERS-CoV cDNA in a bacterial artificial chromosome (BAC) vector [258] was previously equipped with a T7 RNA polymerase promoter and a unique 3'-terminal NotI site for run-off transcription [179]. After passaging of the MERS-CoV EMC/2012 isolate in Vero cells, a premature stop codon in ORF5 was observed in the minority of sequence reads, but this substitution became fixed upon additional virus passaging [26, 319]. To limit the development of genetic variation in ORF5 upon passaging of rMERS-CoV in cells, we decided to introduce this premature stop codon at ORF5 codon 108 in the MERS-CoV full-length clone (further explanation on the use of this adaptation is provided in the Results section). This clone, pBAC-MERS-CoV-ORF5stop, was generated by two-step en-passant in vivo recombineering reactions in *E. coli* [328]. Subsequently, substitutions in the $PL^{pro}$-coding sequence were introduced in this clone using the same procedure. Primer sequences to introduce substitutions in pBAC-MERS-CoV are available upon request. Bacmids were isolated from bacteria and sequenced to verify the presence of the introduced substitution(s). pBAC-MERS-CoV-ORF5stop and derivatives thereof were linearized with *NotI* and they were purified by phenol-chloroform extraction and ethanol precipitation. Approximately 1 µg DNA was used as a template for *in vitro* transcription using the mMESSAGE mMACHINE T7 transcription kit (Thermo Fisher Scientific). BHK-21 cells ($5x10^6$) were electroporated with 5 µg

of this *in vitro* transcribed RNA using the Nucleofector 2b device (Lonza; program T-020) with Cell Line Nucleofector Kit T (Lonza). Immediately after electroporation, the cells were taken up in prewarmed cell culture medium and mixed with HuH-7 cells ($5x10^6$) before seeding in a 75-$cm^2$ flask. Virus-containing supernatants were collected when complete cytopathogenic effect (CPE) was observed, normally 3 to 4 days after the electroporation. Harvested virus was passaged once in HuH-7 cells to grow a virus stock used for further experiments.

### rMERS-CoV titration and sequencing

rMERS-CoV titers were determined by plaque assay on HuH-7 or MRC5 cells, essentially as previously described for SARS-CoV [329]. HuH-7 cells were fixed after an incubation period of 3 days whereas MRC5 cells were fixed after 4 days. To determine the 50% tissue culture infectious dose (TCID50), 5-fold serial dilutions of pre-diluted rMERS-CoV stocks were prepared and used to infect HuH-7 cells in flat-bottom microplates (96-wells). After 3 days, cells were fixed with formaldehyde, monitored for cytopathogenic effect, and the TCID50 was calculated using the Spearman & Kärber method [330].

In order to confirm the presence of the intended substitutions in the rMERS-CoV $PL^{pro}$-coding sequence, RNA was isolated from virus-containing supernatants (passage 1) with the QIAamp Viral RNA Mini Kit (Qiagen). Total RNA was reverse-transcribed to cDNA using RevertAid H minus reverse transcriptase (Thermo Fisher Scientific) and random hexamers. The $PL^{pro}$ domain (nucleotides 4435-5409 of MERS-CoV ORF1a/1ab) was amplified by PCR using Accuzyme DNA polymerase (Bioline) and after purification the PCR product was sequenced.

### Evaluation of rMERS-CoV replication and induced immune responses

HuH-7 cells were infected with wt or mutant rMERS-CoV at a multiplicity of infection (MOI) of 0.01 or 5, to analyse multi- or single-cycle infections, respectively. MOI 0.01, 1, or 3 was used to infect MRC5 cells. The rMERS-CoV inoculum was prepared in PBS containing DEAE (0.005% w/v) and 2% FCS, which was put on the cells for 1 h at 37°C. Inocula were removed and EMEM supplemented with antibiotics and 2% FCS was added to the cells. Following a high-MOI infection, cells were first washed three times with PBS before adding medium. Supernatants were harvested at various time points and rMERS-CoV titers were determined by plaque assay on HuH-7 cells. After removal of the supernatant, infected cells were washed once with PBS and then lysed with RA1 buffer supplemented with β-mercaptoethanol for total RNA isolation using the NucleoSpin RNA II kit (Machery-Nagel). RNA served as a template in a reverse transcription (RT) reaction with RevertAid H minus reverse transcriptase and a combination of oligo$(dT)_{20}$ primer (90%) and random hexamers (10%). To measure host immune responses, real-time quantitative (q) PCRs using iTaq SYBR Green Supermix (BioRad) were performed on a CFX384 Touch™ Real-Time PCR Detection System (BioRad). The following targets were amplified: IFN-β (5'-GTCACTGTGCCTGGACCATA-3' and 5'-CTTGAAGCAATTGTCCCGT-3'), IFN-induced protein with tetratricopeptide repeats 2 (IFIT2; 5'-ATGTGCAACCTACTGGCCTAT-3' and 5'-TGAGAGTCGGCCCATGTGATA-3'), viperin (5'-CGTGAG-

CATCGTGAGCAATG-3' and 5'-TCTTCTTTCCTTGGCCACGG-3'), MERS-CoV genome (5'-CCCTCGACTC-CAGGCTTCTGC-3' and 5'-ATGTGCACACCGCGAGGCAT-3'), and ribosomal protein L13a (RPL13a; 5'-AAGGTGGTGGTCGTACGCTGTG-3' and 5'-CGGGAAGGGTTGGTGTTCATCC-3'). Using NormFinder software [331], RPL13a was identified as a suitable normalization gene. Quantification was done using the standard curve method using standard dilution series that were included in the qPCR. Furthermore, data was normalized against the relative quantities of RPL13a mRNA and mRNA levels of wt-infected MRC5 were set to 1. Significance relative to wt was calculated using an unpaired Student's *t*-test and p values <0.05 were considered statistically significant.

### rMERS-CoV infection of cytokeratin 18-*hDPP4* mice

Wild-type or V1691R rMERS-CoV grown on HuH-7 cells (passage 1) was titrated by plaque assay on HuH-7 cells as described above. Mice expressing hDPP4 under control of the cytokeratin (K) 18 promoter [332] were anesthetized with isofluorane and intranasally inoculated with MERS-CoV ($1x10^5$ PFU per mouse) diluted in DMEM to a volume of 50 µl. Control mice were mock-infected with 50 µl DMEM. Mice were examined and weighed daily. The set endpoint was at 14 days post inoculation (p.i.), except for mice that died or reached a humane endpoint before that time. At other predetermined time points mice were euthanized, lungs were removed and divided for determination of the rMERS-CoV titers and for RNA isolation. In parallel, blood samples were taken and processed by centrifugation (1,000 x g for 5 min) to obtain sera, also before the rMERS-CoV infection sera was collected. Virus stocks used for the mouse experiment were prepared in the biosafety level 3 (BSL3) facilities at Leiden University Medical Center. The animal experiment itself was conducted in a BSL3 laboratory at Center for Animal Health Research (CISA-INIA) in Madrid, while sample analysis was performed at Leiden University Medical Center. Animal experimental protocols were approved by the Ethical Committee of the Center for Animal Health Research (CISA-INIA) (permit numbers: 2011–009 and 2011–09) in strict accordance with Spanish National Royal Decree (RD 1201/2005) and international EU guidelines 2010/63/UE about protection of animals used for experimentation and other scientific purposes and Spanish Animal Welfare Act 32/2007.

### rMERS-CoV isolation from K18-*hDPP4* mice

Lung parts from infected mice were weighed and placed in a gentleMACS M Tube (Miltenyi Biotec) containing 2 ml of PBS with 100 units/ml penicillin, 100 units/ml streptomycin (Lonza), 50 µg/ml gentamycin (Sigma-Aldrich), and 0.25 µg/ml Fungizone (Gibco). Lung tissues were homogenized with the gentleMACS dissociator by running program Lung_02 three times (Miltenyi Biotec). Homogenized samples were centrifuged at 9,500 x g for 5 min and supernatants were collected. Thereafter, rMERS-CoV titers were determined by plaque assay on HuH-7 cells as described before. Statistical significance ($p<0.05$) between wt and V1691R rMERS-CoV titers was determined using an unpaired Student's *t*-test.

### RNA isolation from lungs of rMERS-CoV-infected mice and RT-qPCR

To preserve the integrity of RNA, lungs were soaked in RNAlater (Thermo Fischer Scientific) directly after harvesting, and stored at -80°C. For RNA extraction, lungs were transferred to a gentleMACS M Tube containing 2 ml of RA1 buffer (Machery-Nagel) supplemented with 1% β-mercaptoethanol. Tissue was dissociated in the gentleMACS dissociator using program RNA_02 (Miltenyi Biotec). Subsequently, samples were centrifuged at 9,500 x g for 5 min and supernatants were aliquoted. RNA was then isolated following the standard protocol of the NucleoSpin RNA II kit (Machery-Nagel). RT-qPCRs and their analysis were performed as described above but with the following deviation. To measure mRNA levels of CCL5, IL-6, and IFIT2, a triplex qPCR with TaqMan probes was performed with HotStarTaq Master mix (Qiagen) whereas all other targets were amplified using gene-specific primer sets and iTaq SYBR Green Supermix (BioRad). All primers and probe sequences can be requested.

The obtained cDNA was also used to verify that the V1691R substitution in MERS-CoV PL$^{pro}$ was retained after several rounds of virus replication in mice. PCR and sequencing to determine the PL$^{pro}$-coding sequence was executed as described above.

### Virus neutralization test

Serum dilutions were prepared in round-bottom microplates (96-wells) containing EMEM supplemented with antibiotics and 2% FCS. Serum samples were heat-inactivated at 56°C for 30 min, after which two-fold serial dilutions were prepared with a 1:5 dilution as starting point. To each well, an amount of MERS-CoV equalling 100 TCID50 units was added and incubated at 37°C for 1 h, to allow virus neutralization. Subsequently, samples (volume of 150 µl) were used to infect HuH-7 cells ($1x10^4$/0.32-$cm^2$) which had been seeded in flat-bottom microplates (96-wells) one day earlier. Cells were incubated for 3 days at 37°C and subsequently fixed with the addition of 30 µl of 37% formaldehyde. Cell layers were microscopically assessed for CPE and subsequently stained with crystal violet. As a positive control for virus neutralization, rabbit antisera raised against a synthetic MERS-CoV antigen (S1-Fc, containing residues 358-588 of the viral S protein) were included [253]. Back titration of MERS-CoV, to confirm the dose of the used inoculum was within the acceptable range of 30 to 300 TCID50, was done by adding two-fold dilutions starting with the diluted MERS-CoV (100 TCID50) to HuH-7 cells. TCID50 was calculated using the Spearman & Kärber method [330]. Virus neutralization tests were performed twice, and the mean of the two measurements was used.

## RESULTS

### DUB-negative PL$^{pro}$ mutants are viable and genetically stable

In our previous work, we described amino acid substitutions in the Ub-binding site of MERS-CoV PL$^{pro}$ that specifically disrupt its DUB activity without affecting the overall proteolytic activity [327]. Using ectopic expression of mutant PL$^{pro}$ domains, we could implicate the DUB activity in antagonizing the host innate immune response [327]. However, we now aimed to obtain direct proof that the enzyme also counteracts the type I IFN response in the context of the MERS-CoV-infected cell. A BAC-based MERS-CoV reverse genetics system [179, 258], based on the sequence of the EMC/2012 isolate [26], served as the starting point for this study.

A premature stop codon in ORF5 was seen in 45% of the sequence reads of the cell culture passage 6 MERS-CoV EMC/2012 isolate and appeared to be fixed after additional virus passaging in Vero cells [26, 319]. Accessory ORFs like ORF5 are dispensable for MERS-CoV replication in cell culture and their protein products have been implicated in suppression of the innate immune response and NF-κB activation [181, 258]. Indeed, deletion of ORF5 did not alter virus replication compared to wt MERS-CoV in Vero 81, HuH-7, and Calu-3 cells [181, 333]. However, higher levels of inflammatory cytokines were produced in Calu-3 cells upon infection with virus lacking ORF5 compared to wt virus [181]. To avoid complications due to ORF5 evolution and associated changes in host immune suppression while generating PL$^{pro}$ mutant virus stocks for our studies, all PL$^{pro}$ mutants were engineered using a full-length construct containing the premature stop codon at ORF5 codon 108. Into this backbone, we subsequently introduced substitutions, based on the MERS-CoV pp1a/pp1ab amino acid numbering, V1691R, T1653R, and V1674S, as well as the combinations T1653R+V1691R and T1653R+V1674S+V1691R (named “double mutant” and “triple mutant”, respectively, from this point on). V1691 and T1653 map to the S1 Ub-binding site of MERS-CoV PL$^{pro}$ and have direct interactions with Ub, in contrast to V1674 that was hypothesized to associate with the distal Ub of polyUb chains [327]. In cell culture-based reporter assays, the V1691R substitution reduced the DUB activity of PL$^{pro}$ most effectively, T1653R impaired it to a lesser extent, whereas V1674S only marginally reduced it [327]. In all cases, proteolytic activity of the protease towards the polyprotein backbone remained intact.

To launch wt and mutant rMERS-CoV, BHK-21 cells were transfected with *in vitro* transcribed MERS-CoV RNA. Progeny virus was harvested and virus stocks were then grown in HuH-7 cells. Virus-induced CPE was observed for the wt control as well as all DUB-negative mutants listed in the previous paragraph, indicating that these viruses were viable and cytopathogenic in cell culture. Virus titers were determined by plaque assay on HuH-7 and MRC5 cells and additionally plaque phenotypes were examined. The plaque size of rMERS-CoV V1691R was slightly smaller compared to wt rMERS-CoV on both cell lines (Fig. 1). Plaques of mutants T1653R and V1674S were comparable in size to those of the wt control. However, when combined with the V1691R substitution in double or triple mutants, plaque sizes were more variable and on average slightly decreased (Fig. 1). To verify whether the substitutions were retained during virus

propagation in HuH-7 cells, RNA was isolated from virus-containing supernatant and used for RT-PCR amplification and sequencing. The PL$^{pro}$-coding region of the genome was sequenced and after one passage the presence of all engineered substitutions was confirmed, in the absence of any additional (unintended) substitutions. Together, this demonstrated that rMERS-CoV mutants carrying changes in the Ub-binding site of PL$^{pro}$ are viable and, at least initially, genetically stable in our experimental setting.

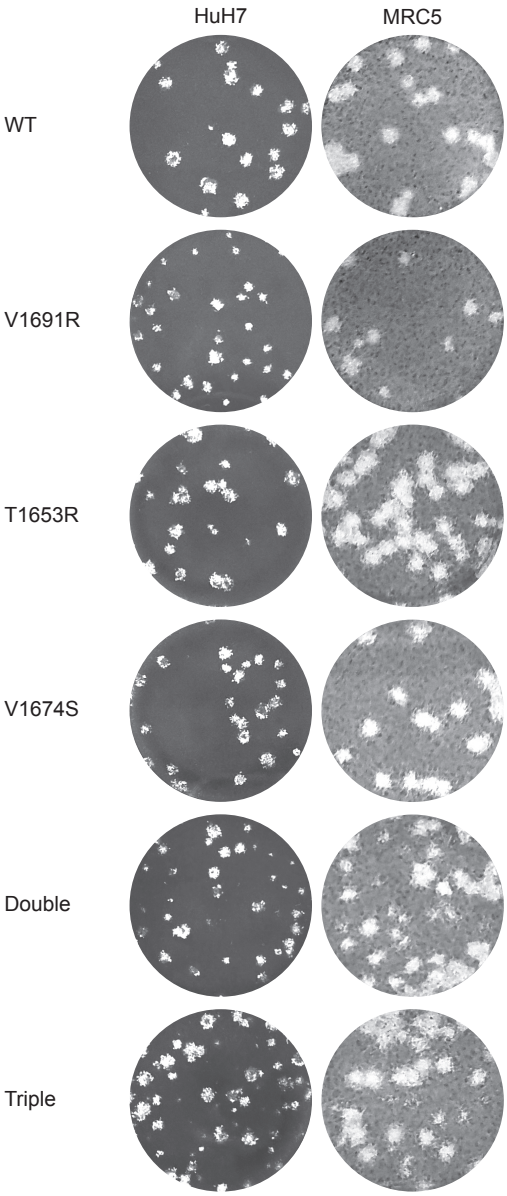


**Figure 1. Plaque phenotype of rMERS-CoV PL$^{pro}$ mutants.** Plaque assays on HuH-7 and MRC5 cells are presented for wt and DUB-negative rMERS-CoV with single, double or triple substitutions in PL$^{pro}$.

## DUB-negative MERS-CoV PL$^{pro}$ mutants have normal replication kinetics but induce an enhanced innate immune response

In order to characterize the rMERS-CoV PL$^{pro}$ DUB-negative mutants, their replication kinetics and the induced innate immune responses were analysed during single- and multi-cycle infections of HuH-7 and MRC5 cells. For single-cycle experiments, we employed an MOI of 5 or 3 for HuH-7 and MRC5 cells, respectively. V1691R, the single substitution that reduced PL$^{pro}$'s DUB activity most effectively, when engineered into rMERS-CoV showed identical replication kinetics as wt rMERS-CoV, since the two viruses grew to similar titers in both cell lines at the different time points tested (Fig. 2A and B). Also, the other mutants yielded titers comparable to wt virus 24 h p.i. when MRC5 cells were infected with MOI 1 (Fig. 2C). For multi-cycle infection experiments, cells were infected with an MOI of 0.01 and virus-containing supernatants were harvested 24 and 48 h p.i. At both these time points, there was no significant titer difference between wt virus and mutant V1691R (Fig. 2D-G). Similar results were obtained for all other DUB-negative mutants tested (Fig. 2D-G), suggesting that overall replication in human cells is not affected by substitutions in the Ub-binding site of MERS-CoV PL$^{pro}$. Notably, rMERS-CoV peak titers were approximately 1-log higher in MRC5 cells compared to HuH-7 cells.

Despite the lack of clear replication differences in cell culture, we anticipated that viruses with impaired DUB activity would be less capable of suppressing the innate immune response. Both MRC5 and HuH-7 cells can mount an IFN response upon stimulation with poly(I:C), a synthetic mimic of dsRNA (data not shown). To assess whether DUB-negative mutants indeed induce a stronger innate immune response than wt rMERS-CoV, mRNA levels of IFN-β, IFIT2, and viperin in infected cells were measured by real-time RT-qPCR. Additionally, virus replication was evaluated by monitoring the intracellular accumulation of MERS-CoV genomic RNA. Data were normalized to house-keeping gene RPL13A, and are presented as fold increase over wt-infected cells. IFN-β levels were below the detection limit (Ct values > 35) in wt or DUB-negative rMERS-CoV-infected HuH-7 cells, while these cells did have limited upregulated IFN-β upon transfection of poly(I:C) (data not shown). Also in mock-infected MRC5 cells IFN-β mRNA was hardly detectable and therefore only a comparison was made between wt and DUB-negative-infected MRC5 cells. Upon single-cycle infection of MRC5 cells, significantly higher mRNA levels of IFN-β (~4-fold), IFIT2 (~3-fold), and viperin (~4-fold) were measured upon infection with V1691R rMERS-CoV compared to wt rMERS-CoV (Fig. 3A-C). Relative to wt rMERS-CoV, also the double mutant showed a more pronounced and significant increase while the single T1653R mutation did not affect the mRNA levels of the qPCR targets at all (Fig. 3A-C). Also, cells infected with viruses carrying the V1674S substitution induced a very low response comparable to that against wt virus (Fig. 3A-C). Wild-type and mutant viral genomic RNA levels were similar in infected cells (Fig. 3D). In multicycle infections of MRC5 cells, V1691R rMERS-CoV induced higher levels of IFN-β and ISGs mRNA than wt virus (IFN-β ~3-fold, IFIT2 ~4-fold, and viperin ~8-fold; Fig. 3E-G). This was even more pronounced with the double mutant, while addition of the V1674S substitution unexpectedly reduced IFN-β and ISG responses relative to the double mutant (Fig. 3E-G). The additive effect of

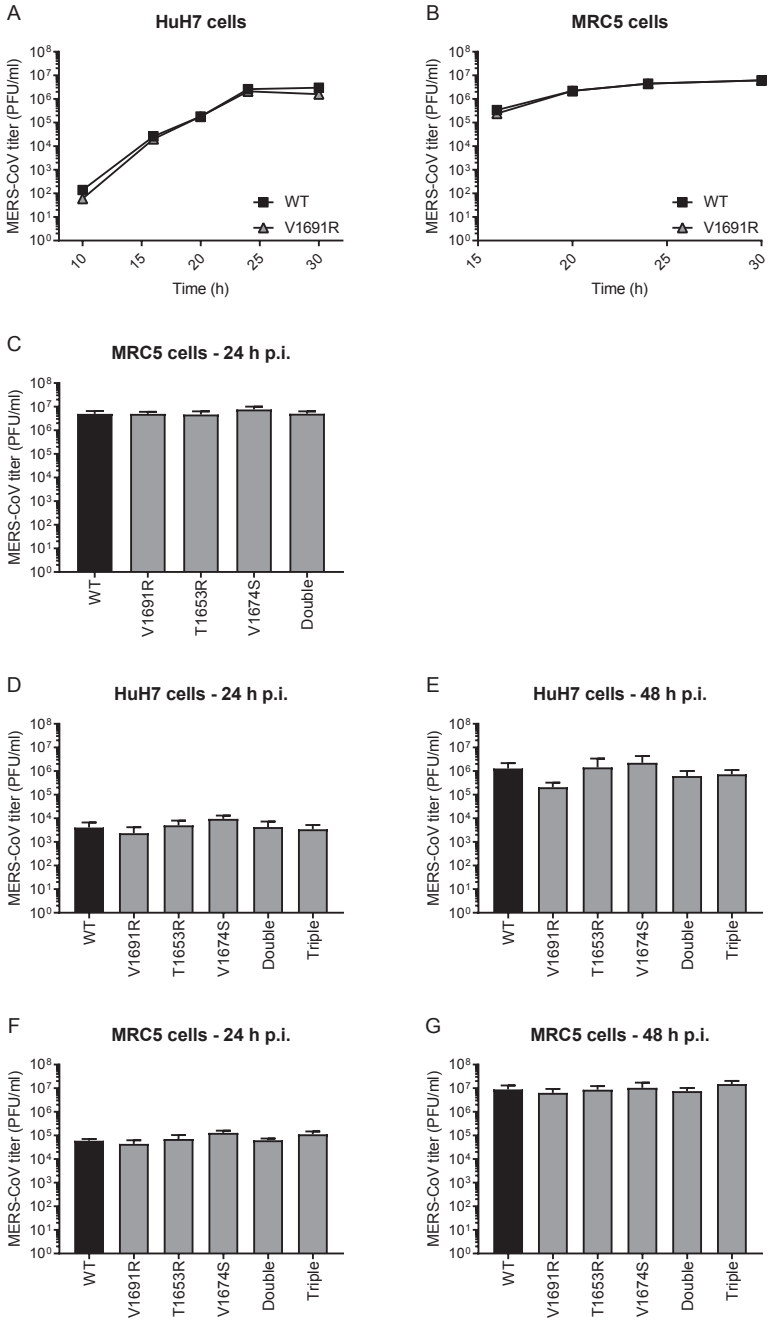


**Figure 2. Growth of rMERS-CoV PL$^{pro}$ mutants.** HuH-7 cells were infected with wt or DUB-negative rMERS-CoV with MOI 5 (A) or 0.01 (D and E), whereas an MOI of 3 (B), 1 (C) or 0.01 (F and G) was used to infect MRC5 cells. At different time points p.i., culture supernatants were harvested and rMERS-CoV progeny titers were determined by plaque assay on HuH-7 cells. Growth curves (A and B) were performed once, while all other infections were repeated independently three times. Error bars represent the standard deviation.

T1653R implies that this substitution, when combined with V1691R further reduced Ub binding. $PL^{pro}$ mutants T1653R and V1674S generated responses comparable to those against wt virus, and virus genome levels were similar (Fig. 3E-H). Interestingly, MERS-CoV genome levels were lower in cells infected with V1691R, and with the double mutant, compared to wt virus in these multicycle infections (Fig. 3H), indicating that these mutations eventually do have impact of the replication of the virus, probably due to the higher innate immune responses they elicit. Collectively, viruses containing the T1653R or V1674S substitution did not induce different host responses in MRC5 cells compared to wt virus. In contrast, V1691R rMERS-CoV elicited a clear upregulation of IFN-β and ISG mRNAs, which was even more prominent when combined with the T1653R substitution.

## Increased survival of mice infected with DUB-negative rMERS-CoV compared to wt-virus infected mice

As shown in Fig. 2, rMERS-CoV V1691R and wt virus had similar replication kinetics in mammalian cells, but infection with the former resulted in an upregulation of the mRNA levels for IFN-β and ISGs (Fig. 3). This prompted us to evaluate this DUB-negative virus in a lethal mouse model for MERS-CoV infection, which relies on transgenic mice expressing the human DPP4 (hDPP4) receptor under the control of the K18 promoter [332]. Intranasal inoculation of these mice leads to MERS-CoV replication in the lungs and production of interferons, cytokines, and chemokines. Ultimately, the animals develop pathological changes in their lungs but also in their brain, and most likely the mice die of neurological disease due to MERS-CoV infection in the brain [332].

We aimed to investigate V1691R rMERS-CoV infection of these transgenic mice with respect to its lethality and the innate immune responses in the lung. To this end, mice were infected intranasally with $1x10^5$ PFU of either wt or DUB-negative rMERS-CoV, whereas a third group of mice was mock-infected. Each group contained a total of 16 mice of which 12 animals per group were euthanized at early time points. The remaining four animals from each of these three groups were monitored for a period of 14 days to assess their survival and measure their body weight on a daily basis. All four mice infected with wt rMERS-CoV died or had to be euthanized after reaching a humane endpoint by day 7 or 8 p.i. (Fig. 4A). In contrast, only one of the four mice infected with DUB-negative rMERS-CoV died at day 8 p.i., while the other three mice survived for the full 14-day period (Fig. 4A). Even with the small number of animals used for this experiment, this difference in survival between mice infected with wt or DUB-negative rMERS-CoV is statistically significant (log-rank test p value = 0.028). Both wt and DUB-negative rMERS-CoV-infected mice lost weight over the course of infection (Fig. 4B), but in all three surviving mice infected with DUB-negative rMERS-CoV this weight loss was reversed from day 10 p.i. forward (Fig. 4C). The results clearly suggested that the virulence of the DUB-negative virus was reduced compared to wt virus.

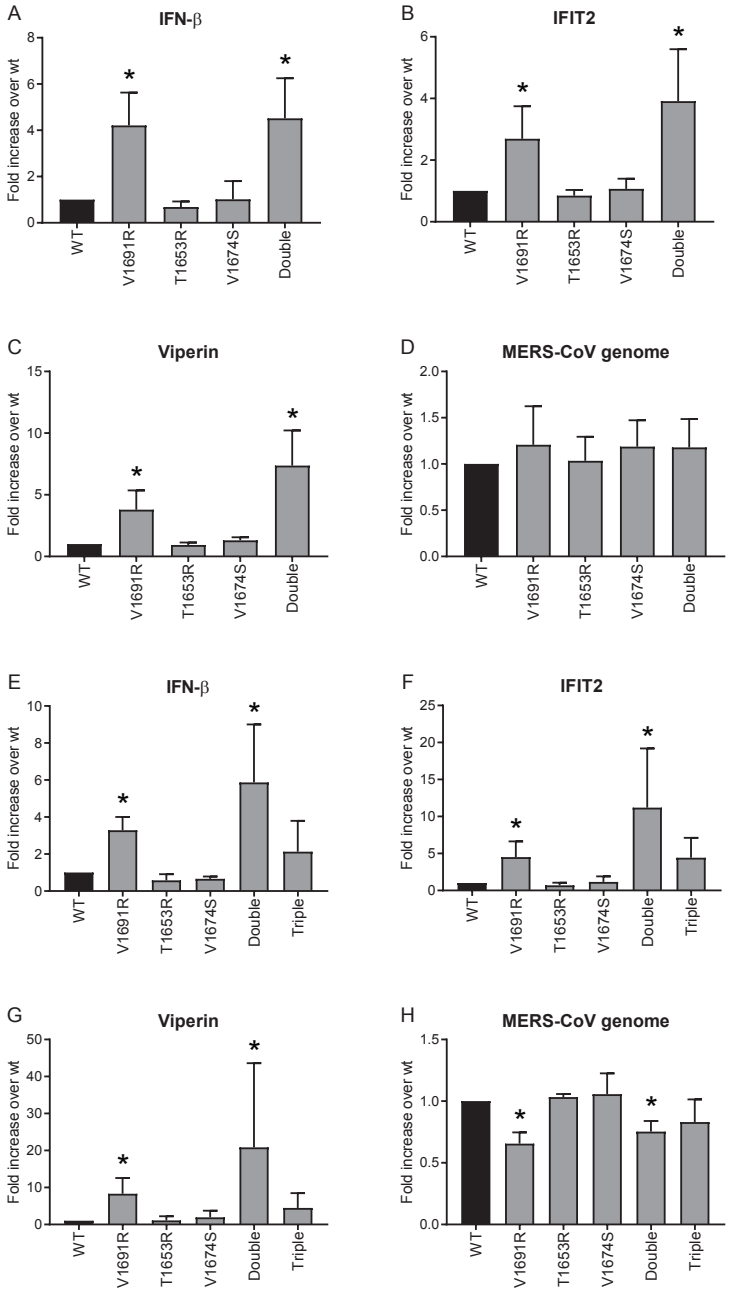


**Figure 3. Immune responses in MRC5 cells infected with wt or DUB-negative rMERS-CoV.** MRC5 cells were infected with wt or DUB-negative rMERS-CoV with MOI 1 (A-D) or 0.01 (E-H) and intracellular RNA was isolated at 24 h or 48 h p.i., respectively. Levels of IFN-β mRNA (A and E), IFIT2 mRNA (B and F), viperin mRNA (C and G), and MERS-CoV genomic RNA (D and H) were determined by real-time RT-qPCRs and normalized to transcript levels of RPL13a. Results were obtained in three independent experiments, error bars represent the standard deviation, and asterisks show a significant difference in elicited responses between wt and DUB-negative rMERS-CoV ($p<0.05$).

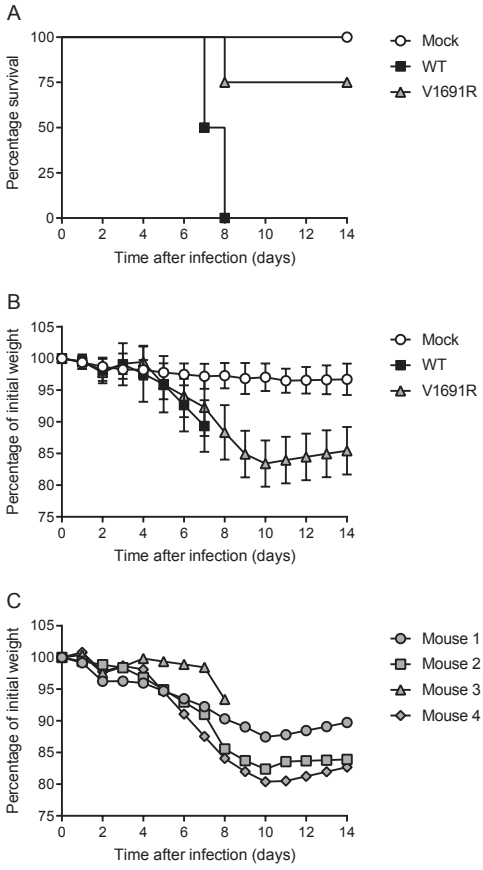


**Figure 4. Survival and weight loss of mice infected with wt or DUB-negative rMERS-CoV.** Mice that express hDPP4 under the control of the K18 promoter were infected with $1x10^5$ PFU wt or DUB-negative V1691R rMERS-CoV, or were mock-infected. Survival data (A) are from four infected animals per group. The weight of the mice (B) was monitored daily and the mean of the group of four mice is presented with error bars showing the standard deviation. The weight of each individual mouse infected with DUB-negative rMERS-CoV is presented in (C).

## DUB-negative rMERS-CoV is cleared faster from mouse lungs than wt virus

To measure rMERS-CoV replication and the innate immune responses the viruses elicited in lungs of infected mice, we euthanized four animals from each group at days 1, 2, and 4 p.i. Lungs were removed and part of the material was homogenized and used for virus titration. For wt rMERS-CoV, progeny titers were approximately $1x10^6$ PFU per g of lung tissue during the first four days after infection (Fig. 5). The DUB-negative virus reached similar virus titers as the wt control during the first two days p.i., indicating that this virus also replicates well in mice. Unexpectedly, however, it proved impossible to recover virus from the lungs of three of the mice infected with DUB-negative rMERS-CoV (twice in the day 1 p.i. group, and once in the day 2 p.i. group; Fig. 5). Consequently, it remains unclear whether these three animals had been successfully inoculated. All DUB-negative rMERS-CoV-infected mice that were euthanized at day 4 p.i. were virus-positive, and their lung titers were significantly lower than in wt virus-infected mice at that time point (Fig. 5), suggesting that the DUB-negative virus is cleared faster from the lungs than wt rMERS-CoV. Virus titers were also determined in mice that died from the infection at day 7-8 p.i. and in

survivors of the infection at day 14. By day 7-8 p.i., the rMERS-CoV wt titers were around $1x10^4$ PFU per g of lung tissue, signifying that virus titers decreased over time (Fig. 5). The virus titer of the single mouse that died of the DUB-negative virus infection was $2x10^3$ PFU per g of lung tissue (Fig. 5). Virus could not be recovered from the lungs of any of the mice that had survived the infection with DUB-negative rMERS-CoV after 14 days (Fig. 5).

In order to verify whether the DUB-inactivating substitution in the MERS-CoV mutant was stably maintained during the animal experiment, sequencing of the PL$^{pro}$-coding region of the genome was performed. To this end, lung tissue was homogenized, RNA was isolated, and the PL$^{pro}$-coding sequence was amplified by RT-PCR and sequenced. In wt virus-infected mice, the consensus sequence of the PCR product was found to be identical to the sequence of the BAC-based cDNA clone from which the rMERS-CoV had been launched (data not shown). RT-PCR and sequencing were successful using RNA isolated from all mice infected with DUB-negative rMERS-CoV from which also DUB-negative rMERS-CoV was recovered (Fig. 5), and revealed the presence of the V1691R substitution in PL$^{pro}$ without additional substitutions in PL$^{pro}$ (data not shown). No virus-specific RT-PCR product could be obtained from the lungs of mice that were found negative for infectious virus at day 1 or 14 p.i. (data not shown; Fig. 5). For one mouse inoculated with DUB-negative rMERS-CoV, although virus could not be isolated at 2 days p.i. (Fig. 5), a virus-specific RT-PCR product could be obtained using another piece of its lung, after which the presence of the PL$^{pro}$ mutation could be confirmed by sequencing. Possibly, in this particular mouse, the virus was distributed unequally in the lungs during intranasal inoculation, explaining why only some parts were virus-positive at 2 days p.i. Similar issues may explain the lack of virus isolation for the two mice that were negative for the mutant virus at 1 day p.i., as for the described experiments not the entire lungs were used, and as there was no obvious technical reason to suggest inoculation failure. Overall, our data established that the DUB-negative virus, which stably maintained the V1691R substitution, is cleared faster from the lungs of infected mice than wt virus.

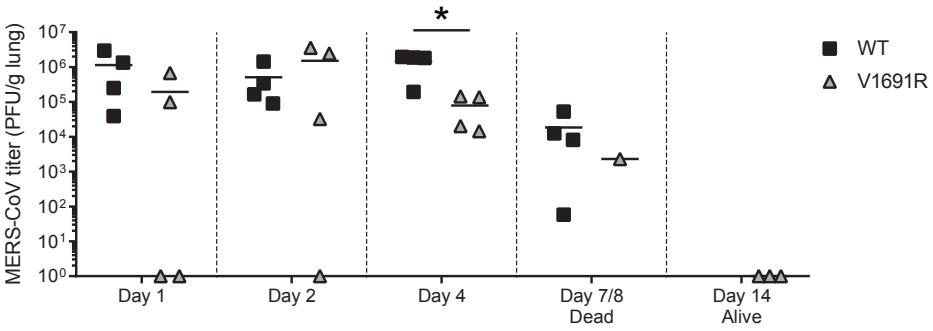


**Figure 5. Replication of wt and DUB-negative rMERS-CoV in mice.** Groups of four K18-*hDPP4* mice infected with wt or V1691R rMERS-CoV were euthanized at days 1, 2, or 4 after infection. Lungs were removed and homogenized, and rMERS-CoV lung titers were measured by plaque assay on HuH-7 cells. Recombinant MERS-CoV titers in lungs were also determined in mice that died at day 7 or 8 after the infection, and in the three DUB-negative rMERS-CoV-infected mice that were euthanized at 14 days p.i. The mean per group and the rMERS-CoV titer in PFU per gram of lung tissue are presented for each mouse. The asterisk indicates a significant difference between wt and V1691R rMERS-CoV, determined with a Student's *t*-test ($p<0.05$).

## Accelerated innate immune responses following infection with DUB-negative rMERS-CoV

We hypothesized that the significantly higher survival rate of mice infected with the V1691R mutant and the faster clearance of DUB-negative rMERS-CoV from the lungs were the result of enhanced innate immune responses due to the loss of $PL^{pro}$'s DUB activity. To investigate this, we analysed the mRNA levels of innate immune factors and cytokines from the lungs of infected mice. Real-time RT-qPCRs were performed and results were normalized to the mRNA of RPL13A, a housekeeping gene selected for its stability in the infected mice. The selected mRNA targets were representative for innate immune responses that are relevant for MERS-CoV infection and included IFNs (IFN-β and IFN-λ), ISGs (ISG15 and IFIT2), the cytokine TNFα that is controlled by NF-κB activation, the pro-inflammatory cytokine IL-6, and the chemokine CCL5 (Fig. 6) [164].

After the first day of infection, the mRNA levels for all targets were similarly low in wt and DUB-negative rMERS-CoV-infected mice (Fig. 6). At 2 days p.i., transcript levels in wt rMERS-CoV-infected mice were comparable to those in mock-infected mice while a clear increase was measured in DUB-negative rMERS-CoV-infected mice (Fig. 6). For ease of visualization, the mean fold increase for each target is presented in Fig. 6, while the fold increase for each individual mouse is displayed in Fig. S1 to be able to show the variation in the responses between mice in the same group. Notably, the IFN-β and IFN-λ values for the wt MERS-CoV-infected mice showed less variation than those of the mock-infected animals, suggesting that the wt virus efficiently suppressed the expression of these cytokines at day 2 p.i. (Fig. S1A and B, compare fold increase of mock and wt-infected mice at day 2 p.i.). The mean level of IFN transcripts in DUB-negative rMERS-CoV-infected mice was clearly, although not statistically significant, higher than in the mock and wt virus-infected mice (Fig. 6A and B). ISG15 and IFIT2 mRNA levels were found to be slightly elevated in wt rMERS-CoV-infected mice relative to mock-infected mice, while an even more pronounced increase was seen in DUB-negative rMERS-CoV-infected mice (Fig. 6C and D). The upregulation of IFN-β mRNA in individual DUB-negative MERS-CoV-infected mice corresponded to the increased levels of ISG mRNAs in the same mice at 2 days p.i. (Fig. S2) This illustrates that the ISG responses measured were likely induced by upregulation of type I IFNs in these animals. Due to the limited group size and considerable variation in the responses between the four mice that received DUB-negative rMERS-CoV (Fig. S1, see fold increase of DUB-negative virus-infected mice at day 2 p.i.), the difference in mRNA levels between wt and DUB-negative rMERS-CoV-infected mice at 2 days p.i. was not statistically significant. However, the trend of an accelerated increase of mRNA levels was clearly seen for all innate immune targets upon infection with DUB-negative rMERS-CoV. This strongly suggests that, compared to the wt control virus, the DUB-negative virus is less able to suppress innate immune responses resulting in an earlier response.

By day 4 p.i., a very different innate immune response in the mice was seen compared to the response at 2 days p.i. (Fig. 6). In the DUB-negative virus group, the increase of innate immune transcripts was slightly lower relative to 2 days p.i. (Fig. 6), and the variation in mRNA levels between the four mice was smaller in this group at 4 days than at 2 days p.i. (Fig. S1, compare

e.g. the IFN-β fold increase of each individual V1691R-infected mouse at day 2 p.i. with day 4 p.i.), suggesting down-regulation of the response by day 4 p.i. in this group of mice. Wild-type virus-infected mice showed, however, a very strong increase in transcript levels for all tested targets between 2 and 4 days p.i. Especially the mRNA levels of IFN-β, IFN-λ, and IL-6 were remarkably upregulated (Fig. 6A, B, and F). Together, this demonstrates that between 2 and 4 days p.i. the mRNA levels of innate immune factors, cytokines, and chemokines were already down-regulated in the DUB-negative virus-infected mice, in contrast to the strong upregulation observed for rMERS-CoV wt-infected mice.

We expected that the early immune responses would be further down-regulated over time in the mice infected with the DUB-negative mutant. To confirm this, mRNA levels were determined in lungs of the three surviving mice infected with V1691R rMERS-CoV and mock-infected mice at 14 days p.i. The number of transcripts of innate immune factors and cytokines was similar between these two groups, indicating that all mRNAs in surviving animals were back to an almost basal level (Fig. S3). In summary, DUB-negative MERS-CoV induced an earlier, and subsequently again downregulated, innate immune response, whereas wt virus-infected mice show a relatively late and excessive response.



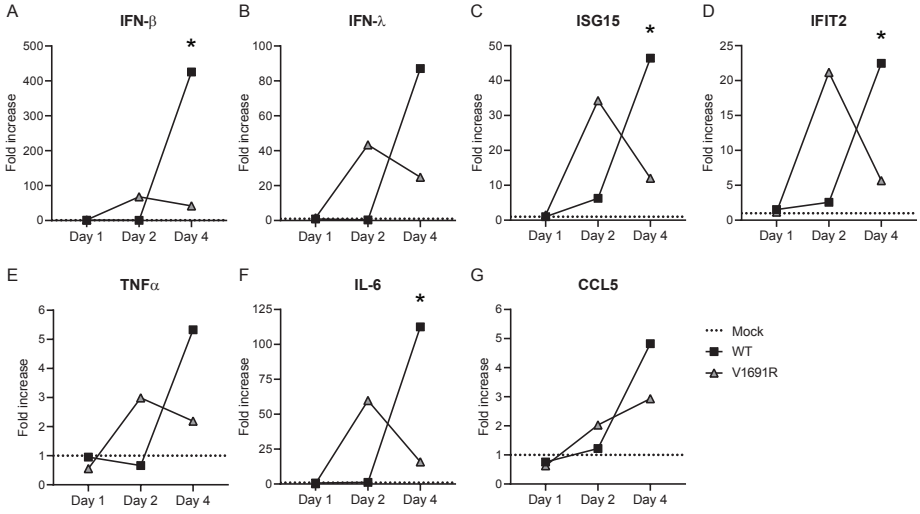


**Figure 6. Innate immune responses of mice infected with wt or DUB-negative rMERS-CoV.** RNA was isolated from lungs of mice infected with wt or DUB-negative rMERS-CoV, or mice that had been mock-infected. RNA was used in real-time RT-qPCRs to measure the fold induction of the mRNA levels of IFN-β (A), IFN-λ (B), ISG15 (C), IFIT2 (D), TNFα (E), IL-6 (F) and CCL5 (G). Results were analysed using the standard curve method and normalised to the mRNA level of the RPL13a gene. The mean per group is presented and the dashed line represents the average that was set to 1 for the mock-infected mice. Statistical significance between wt and DUB-negative MERS-CoV-infected mice is shown (* $p<0.05$).

### Neutralizing antibodies in DUB-negative rMERS-CoV-infected mice

The three mice that survived the infection with DUB-negative mutant rMERS-CoV V169R were euthanized 14 days p.i. and their sera were collected. Prior to infection, their pre-immune sera had also been obtained. To determine whether a neutralizing antibody response against MERS-CoV had developed, despite the relatively recent infection, we performed virus neutralization tests (VNTs). Pre-immune sera did not contain antibodies that could neutralize MERS-CoV (VNT titer <5) (data not shown). This was also true for the day 14 p.i. serum of one mouse. However, in the two other mice low levels of virus-neutralizing antibodies were measured (VNT titers of 15 and 20), suggesting that their adaptive immune system had been activated by the infection with DUB-negative rMERS-CoV, resulting in the production of antibodies that have neutralizing capacity.

## DISCUSSION

Many viral proteases with a primary role in virus replication have evolved to target host cell proteins, and often these accessory cleavage events indirectly affect viral replication and pathogenesis [334]. Coronaviral $PL^{pro}$s constitute a striking example of this kind of dual functionality, as they not only cleave multiple sites in the replicase polyproteins of which they are part, but can also deconjugate Ub, and Ub-like modifiers such as ISG15, presumably to suppress innate immune responses [206]. Studying this DUB activity in the context of the CoV-infected cell is difficult because both $PL^{pro}$ functionalities rely on the same enzymatic active site, which cannot be inactivated without killing virus replication. Therefore, in our earlier research, we explored an alternative approach to selectively inactivate the DUB activity of MERS-CoV $PL^{pro}$. Based on the available crystal structure of the $PL^{pro}$-Ub complex, we disrupted the enzyme's Ub-binding site to minimize its affinity for Ub [327]. Based on assays carried out in expression systems, it was concluded that the DUB activity of $PL^{pro}$ could indeed be inactivated almost completely without affecting the proteolytic activity needed for viral polyprotein cleavage [327]. Subsequently, our study suggested that the DUB activity of MERS-CoV $PL^{pro}$ may indeed be involved in suppressing innate immune responses, as DUB-negative $PL^{pro}$ was no longer able to downregulate IFN-β promoter activity. We have now engineered mutant DUB-negative viruses, thereby convincingly extending these observations to MERS-CoV infected-cells, in culture and *in vivo*. We characterized the replication and the innate immune responses these viruses induce in comparison to wt virus.

Interestingly, some of the DUB-negative viruses, specifically those containing the V1691R substitution, induced higher levels of IFN-β and ISG mRNAs than wt virus in MRC5 cells, confirming a role of $PL^{pro}$ in innate immune suppression, now demonstrated during infection (Fig. 3). However, this upregulation of the type I IFN response did not reduce the progeny titers of DUB-negative rMERS-CoV in MRC5 cells (Fig. 2). We did observe that the plaque size of rMERS-CoV containing the V1691R substitution was slightly smaller when compared to wt virus (Fig. 1),

suggesting that the mutant virus was somehow affected after all. Also, in multi-cycle infections, MERS-CoV genome levels were reduced upon infection with DUB-negative MERS-CoVs carrying the V1691R substitution (Fig. 3H), confirming a modest effect on virus RNA replication in cell culture. This suggests that, in this experimental set-up, the increased IFN expression and subsequent ISG response somewhat influences viral RNA replication but not, at least not noticeably, the production of infectious progeny. The decrease in MERS-CoV genome RNA levels was not observed in single-cycle infections in cell culture, highlighting that primary replication of the mutant viruses is not affected by the substitution in PL$^{pro}$. In summary, by specifically disrupting the PL$^{pro}$ interaction surface that binds Ub, we have demonstrated that the DUB activity of PL$^{pro}$ indeed contributes to innate immune evasion in the context of the MERS-CoV-infected cell.



The importance of vDUB activity in the context of infection has thus far been tested for only a few viruses. Previously, the vDUB activity of equine arteritis virus (EAV), belonging to the order Nidovirales like CoVs, and Crimean-Congo haemorrhagic fever virus (CCHFV), a nairovirus in the order Bunyavirales, were specifically eliminated by mutagenesis [220, 225]. These vDUBs are members of the ovarian tumour domain-containing family of DUBs and are structurally different from CoV PL$^{pro}$s, which belong to the ubiquitin-specific protease DUB family. The replication of CCHFV was attenuated in IFN-competent cells upon DUB inactivation, due to the induction of a more robust immune response [225]. DUB-negative EAV replicated like wt virus in equine lung fibroblasts, but did elicit enhanced innate immune responses [220]. Nevertheless, *in vivo* the mutant virus provided an equal level of protection as the parental (attenuated) virus [335]. Recently, the structural equivalent of the MERS-CoV V1691R substitution was introduced into SARS-CoV PL$^{pro}$, yielding mutant SARS-CoV with a M1748R substitution (using SARS-CoV pp1a/pp1ab amino acid numbering) [336]. Compared to the wt control, replication of this mutant virus was slightly delayed in cell lines that can mount an innate immune response, and it induced higher IFN-β mRNA levels [336]. We here took the characterization of DUB-negative CoV mutants to the next level, by testing a DUB-negative MERS-CoV mutant in an animal model for the first time.

Recombinant MERS-CoV V1691R was tested in a transgenic mouse model for lethal MERS-CoV infection, which is based on hDPP4 expression under control of the K18 promoter [332]. Consequently, hDPP4 was expressed in the lungs, brain, and various other organs. After intranasal inoculation, MERS-CoV replication was observed in lungs and wt rMERS-CoV titers were stable over the first four days of infection, showing $1x10^6$ PFU per g of lung tissue (Fig. 5). Although this is lower than the previously reported peak titer at 2 days p.i. of $6x10^7$ PFU per g of lung tissue [332], it shows that we obtained robust virus replication of rMERS-CoV in these mice. In the previous study by Li *et al*., mice died at 6-7 days p.i. most likely due to neurological disease as a result of the infection in the brain in which MERS-CoV titers increased over time, although a contribution of lung damage to the eventual cause of death may also be likely [332]. In wt MERS-CoV-infected K18-*hDDP4* mice lung pathology was indeed observed, characterized by vascular thrombi, alveolar oedema, degenerating cells, and cellular debris in lymphatic vessels [332]. In accordance with those data, wt rMERS-CoV infection was lethal also in our hands, and all mice died at 7-8

days after infection (Fig. 4A). Likely, the mice that succumbed to the infection also had MERS-CoV infection of the brain, however, the experimental circumstances did not allow us to take samples to support this assumption. Strikingly, infection with the DUB-negative virus resulted in a significantly increased survival compared to the animals infected with the wt virus (Fig. 4A). The DUB-negative virus reached the same titers in the lungs as the wt virus by 2 days p.i., but these had dropped significantly by 4 days p.i. while they stayed high in the wt virus-infected mice (Fig. 5). In future research, it will be interesting to determine whether histopathology is reduced in mice infected with DUB-negative rMERS-CoV to confirm that earlier virus clearance and reduced tissue damage correlates with increased survival, relative to in wt virus-infected mice.

Messenger RNA levels for IFNs (IFN-β and IFN-λ), ISGs (ISG15 and IFIT2), and pro-inflammatory cytokines (IL-6 and TNFα) started to rise in lungs of DUB-negative rMERS-CoV-infected mice at 2 days p.i. (Fig. 6). Although there was no statistically significant difference compared to wt virus-infected mice, the trend of faster upregulation of these mRNAs was quite clear. Moreover, the fact that the levels for all these transcripts increased simultaneously strengthens the conclusion that the DUB-negative rMERS-CoV induced an accelerated innate immune response compared to the wt virus, again confirming the role of the $PL^{pro}$ DUB activity in suppression of innate immune responses, now also in the context of a mouse model. The transcript levels of IFNs and cytokines slightly decreased in DUB-negative rMERS-CoV-infected mice at 4 days p.i., but in wt rMERS-CoV-infected mice the mRNA levels were extremely upregulated (Fig. 6). We therefore hypothesize that the difference in survival rate is likely due to an accelerated, and after induction properly down-regulated, innate immune response in DUB-negative virus-infected mice, which is likely more effectively clearing the virus and preventing tissue damage, protecting these mice from lethality (Figs. 4-6). In contrast, the response in wt virus-infected mice is first suppressed and then at later time points it is extremely upregulated (Fig. 6). These results resemble the late and excessive IFN and pro-inflammatory cytokine response that likely contributes to lung immunopathology as observed for SARS-CoV infection in mice [164, 318]. Recently, it was also demonstrated that the timing of the type I IFN response was crucial in the outcome of a MERS-CoV infection in mice [337]. In line with our results, early administration of type I IFN was protective (comparable to responses induced by DUB-negative rMERS-CoV) whereas late administration promoted lethality (like in wt rMERS-CoV-infected mice) [337]. Together, these observations support a concept in which delayed and aberrantly regulated innate immune response as a result of viral innate immune evasion importantly contributes to pathogenesis during infection. Notably, it is possible that other cellular processes besides innate immunity are influenced by $PL^{pro}$s DUB activity, which might also affect mice survival. Therefore, it remains important to make a full inventory of cellular protein targets that are deubiquitinated by $PL^{pro}$, and to assess how such targets affect host responses and survival by influencing the innate immune system and other cellular processes. Thus, the DUB-negative rMERS-CoV can be an important tool to further explore CoV-host interactions.

In two of the mice that survived the DUB-negative rMERS-CoV infection, we could measure neutralizing antibodies against MERS-CoV. The third surviving mouse did, at this relatively early

time point of 14 days p.i., not have a detectable neutralizing antibody titer. The observed variation might be related to the course of infection, as the weight loss of this third mouse was the smallest of the three mice that survived the infection (Fig. 4C, mouse 1), suggesting that MERS-CoV infection was milder than in the other two animals. It will be interesting to measure the acquired protection in the DUB-negative MERS-CoV infected mice by challenging them with (lethal) MERS-CoV. Although more in-depth characterization is necessary, the DUB-negative MERS-CoV may be a MLV vaccine candidate that can induce antibody responses as well as T-cell responses, which both are important for providing long-term effective protection against CoV infections [254, 255, 338]. Interestingly, for MERS-CoV, vaccines are currently being designed for use in humans as well as dromedary camels, the latter aiming to reduce virus circulation and transmission to humans [254, 255, 257].



In summary, our results demonstrate, for the first time, that the presence of PL$^{pro}$'s DUB activity causes a delay in the innate immune response, which has a major impact on pathogenesis in the mouse model used. Pathogenesis and lethality can thus be reduced by removal of the DUB activity, resulting in earlier, better-regulated and therefore likely more effective innate immune response that helps to clear the virus and decreases pathogenicity, despite the initial viral replication being similar to that seen in wt virus infections. Our study has thus also provided the proof-of-concept for the *in vivo* attenuation of MERS-CoV, which provides a basis to advance the analysis of the innate response as well as antibody and T-cell-mediated responses triggered by infection with DUB-negative MERS-CoV. It creates the opportunity to apply this strategy to develop MLV vaccines against MERS-CoV as well as other CoVs of societal or economic importance, such as porcine epidemic diarrhoea virus, feline CoV, avian infectious bronchitis virus, and bovine CoV. Also in the CoV field, the "attenuation-by-design" approach to eliminate one or more innate immune evasive functions may offer a general and effective strategy for MLV development.

## ACKNOWLEDGEMENTS

We are grateful to Jelle Goeman (Leiden University Medical Center) for assisting with the statistical analysis of the mouse experiment. We kindly thank Clara C. Posthuma and Jessika C. Zevenhoven-Dobbe (both Leiden University Medical Center) for initial modifications to pBACMERS-CoV. We are grateful to Irina C. Albulescu (Leiden University Medical Center) for developing the VNT for MERS-CoV and to Els van der Meijden (Leiden University Medical Center) for setting up the triplex RT-qPCR for monitoring mouse innate immune response. We thank Ralf Bartenschlager (Heidelberg University) and Berend Jan Bosch (Utrecht University) for providing reagents. We are grateful for regular inspiring discussions with Ben A. Bailey-Elkin and Brian L. Mark (both University of Manitoba).

## SUPPLEMENTAL FIGURES

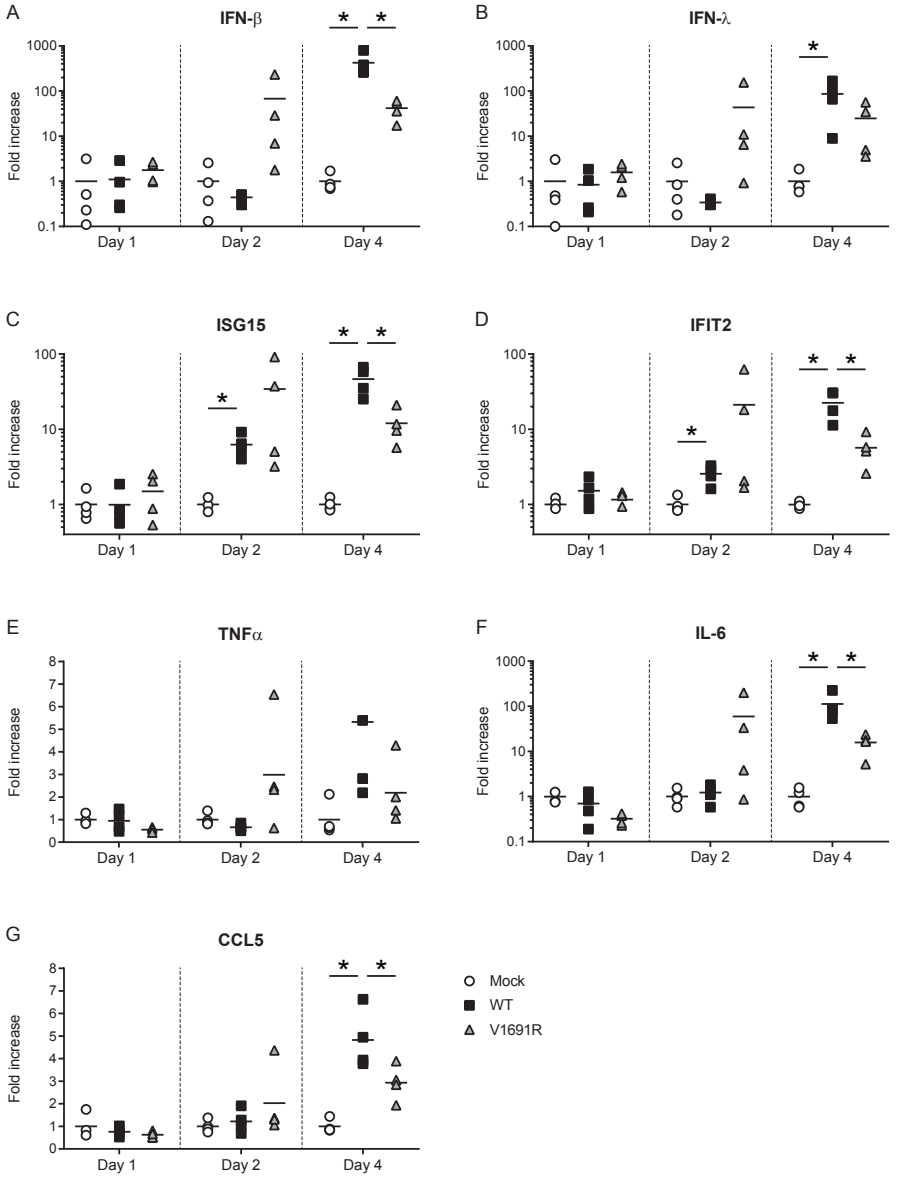


**Fig S1. Innate immune responses of each infected mouse.** In the lungs of wt virus, DUB-negative virus, or mock-infected mice, the fold induction in mRNA levels of IFN-β (A), IFN-λ (B), ISG15 (C), IFIT2 (D), TNFα (E), IL-6 (F) and CCL5 (G) was measured by real-time RT-qPCR. The mean per group as well as the results per individual mouse are presented, and statistical significance is shown (* $p<0.05$).

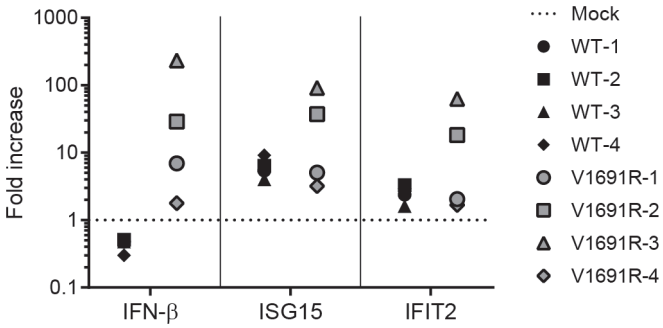


**Fig S2. Innate immune responses of individual rMERS-CoV-infected mice.** Real-time RT-qPCR were performed on RNA isolated from wt or V1691R rMERS-CoV-infected mice at 2 days p.i. mRNA levels of IFN-β, ISG15 and IFIT2 for each individual mouse are shown, the dashed line at a fold increase of 1 indicates the set average of mock-infected mice.

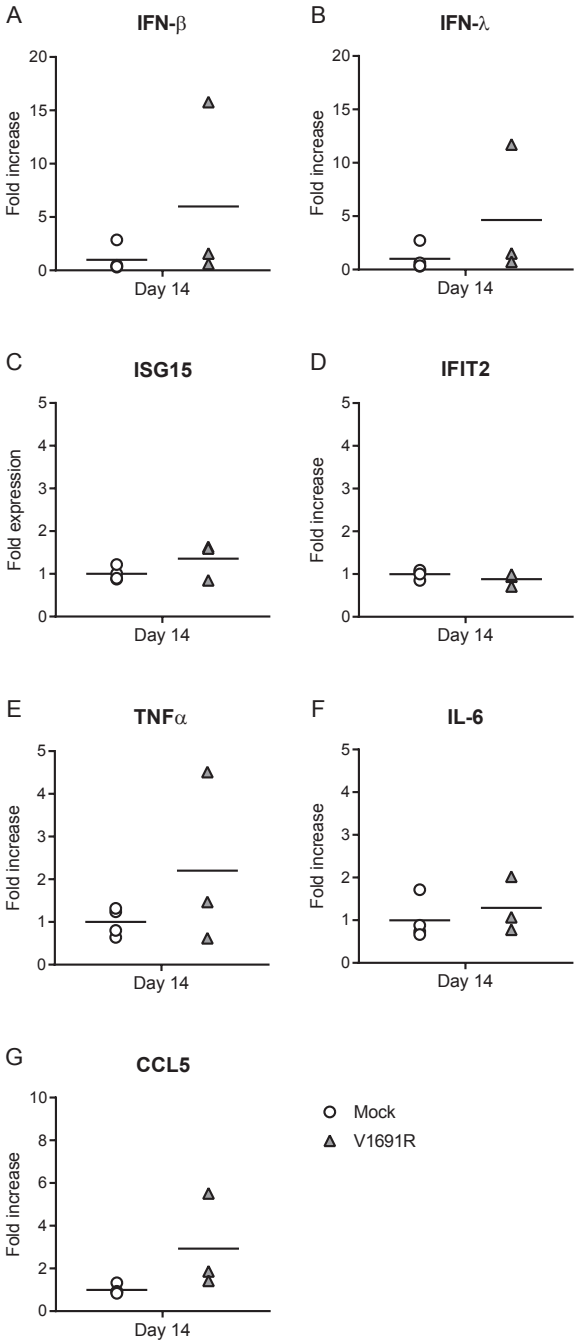


**Fig S3. Immune responses in mice that survived the infection with DUB-negative rMERS-CoV.** Isolated RNA from lungs of mice infected with DUB-negative rMERS-CoV or mice that were mock-infected was used in real-time RT-qPCRs. mRNA levels of IFN-β (A), IFN-λ (B), ISG15 (C), IFIT2 (D), TNFα (E), IL-6 (F) and CCL5 (G) were analysed using the standard curve method and were normalized to relative levels of RPL13a. The mean and the value of each individual mouse is presented.

# 4 Potent and selective inhibition of pathogenic viruses by engineered ubiquitin variants

Robert C.M. Knaap[1,a], Wei Zhang[2,a], Ben A. Bailey-Elkin[3,a], Baldeep Khare[3], Tim J. Dalebout[1], Garrett G. Johnson[3], Puck B. van Kasteren[1], Nigel J. McLeish[3], Jun Gu[2], Wenguang He[3], Brian L. Mark[3,b], Sachdev S. Sidhu[2,b], and Marjolein Kikkert[1,b]

[1] Department of Medical Microbiology, Leiden University Medical Center, Leiden, The Netherlands
[2] Donnelly Centre for Cellular and Biomolecular Research, Banting and Best Department of Medical Research, and Department of Molecular Genetics, University of Toronto, Toronto, M5S3E1, Canada
[3] Department of Microbiology, University of Manitoba, Winnipeg, R3T2N2, Canada
[a] These authors contributed equally to this work
[b] These authors contributed equally to this work

**Published in PLOS Pathogens Vol. 13, No. 5, e1006372, 2017**

## ABSTRACT

The recent Middle East respiratory syndrome coronavirus (MERS-CoV), Ebola and Zika virus outbreaks exemplify the continued threat of (re-)emerging viruses to human health, and our inability to rapidly develop effective therapeutic countermeasures. Many viruses, including MERS-CoV and Crimean-Congo haemorrhagic fever virus (CCHFV) encode deubiquitinating enzymes (DUBs) that are critical for viral replication and pathogenicity. They bind and remove ubiquitin and interferon-stimulated gene 15 from cellular proteins to suppress host antiviral innate immune responses. A variety of viral DUBs (vDUBs), including the MERS-CoV papain-like protease, are responsible for cleaving the viral replicase polyproteins during replication, and are thereby critical components of the viral replication cycle. Together, this makes vDUBs highly attractive antiviral drug targets. However, structural similarity between the catalytic cores of vDUBs and human DUBs complicates the development of selective small-molecule vDUB inhibitors. We have thus developed an alternative strategy to target the vDUB activity through a rational protein design approach. Here, we report the use of phage-displayed ubiquitin variant (UbV) libraries to rapidly identify potent and highly selective protein-based inhibitors targeting the DUB domains of MERS-CoV and CCHFV. UbVs bound the vDUBs with high affinity and specificity to inhibit deubiquitination, deISGylation and in the case of MERS-CoV also viral replicative polyprotein processing. Co-crystallization studies further revealed critical molecular interactions between UbVs and MERS-CoV or CCHFV vDUBs, accounting for the observed binding specificity and high affinity. Finally, expression of UbVs during MERS-CoV infection reduced infectious progeny titers by more than four orders of magnitude, demonstrating the remarkable potency of UbVs as antiviral agents. Our results thereby establish a strategy to produce protein-based inhibitors that could protect against a diverse range of viruses by providing UbVs via mRNA or protein delivery technologies or through transgenic techniques.

## INTRODUCTION

Ubiquitination is a post-translational modification mediated by an enzyme cascade that results in the conjugation of ubiquitin (Ub) to cellular proteins [145, 147]. This process is regulated in part through activity of cellular deubiquitinating enzymes (DUBs), which remove Ub from cellular proteins [145, 147]. Given the essential role of the Ub-system in regulating a large number of critical cellular processes, it is not surprising that viruses have acquired the means to modulate this system in order to promote infection and replication in host cells [269]. In particular, viral DUBs (vDUBs) reverse the ubiquitination process to alter host signalling pathways critical to the induction of cellular antiviral and pro-inflammatory innate immune responses [269]. In addition to removing Ub molecules from host proteins, many vDUBs also remove the Ub-like protein interferon-stimulated gene 15 (ISG15) to further suppress antiviral responses [206, 339]. Importantly, a number of vDUBs also play an essential role in viral replication [206, 339, 340]. Together, the replicative and/or deubiquitinating activities of viral proteases contribute directly to pathogenesis during viral infection *in vivo* [341], making them ideal antiviral drug targets.



The Middle East respiratory syndrome coronavirus (MERS-CoV) and the severe acute respiratory syndrome coronavirus (SARS-CoV) viruses have caused significant concern globally due to their rapid emergence, high lethality rates in humans [259], and high potential for genetic recombination. Coronaviruses initially express their non-structural proteins (nsps) as large viral polyproteins, which are processed into functional domains by proteases encoded within the polyproteins to establish a viral replication-transcriptase complex. SARS- and MERS-CoV release nsp1-3 through the activity of a papain-like protease ($PL^{pro}$) domain situated within nsp3, in a process that is indispensable for replication [206]. The chymotrypsin-like protease ($3CL^{pro}$), corresponding to nsp5, is responsible for cleaving the remaining part of the polyproteins, releasing mature nsps [259]. Strikingly, coronaviral $PL^{pro}$s also act as vDUBs to suppress host antiviral innate immune responses by targeting cellular Ub-conjugated substrates [199-203, 327]. The CoV proteases are well-recognized drug targets, and since the emergence of these zoonotic CoVs, research has focused on the identification and development of small-molecule inhibitors targeting these enzymes [342, 343]. Another highly pathogenic virus that encodes a vDUB is the nairovirus Crimean-Congo haemorrhagic fever virus (CCHFV). The CCHFV vDUB domain is located within the large segment of the genome, and has also been explicitly implicated in the evasion of host Ub- and ISG15-dependent innate immune responses [219].

Crystal structures of $PL^{pro}$ from MERS- and SARS-CoV revealed that these proteases share structural similarity with cellular DUBs belonging to the ubiquitin-specific protease (USP) family [229, 291, 327]. Conversely, structural studies of nairovirus vDUBs revealed resemblance to the ovarian tumour (OTU)-domain family of DUBs [223, 224]. In addition to these well characterized vDUBs, which are conserved in the coronavirus and nairovirus families respectively, numerous other vDUBs have been identified across diverse and distantly related virus lineages of significant concern to human health and agriculture. They include arteriviruses, herpesviruses, adenovi-

ruses, picornaviruses, hepadnaviruses and tymoviruses, further emphasizing the broad potential utility of vDUB-specific antivirals [344].

The importance of vDUBs in viral replication and innate immune evasion make them attractive pharmacological targets, although their structural similarity with human DUBs has posed a significant challenge that complicates the successful development of highly selective small-molecule vDUB inhibitors [345]. Despite intensive efforts, only a handful of inhibitors targeting vDUB proteases have been reported, and none have been approved for clinical use [346]. To meet this challenge, we have developed a strategy to target the vDUB activity as an antiviral approach by the rapid identification of virus-specific, protein-based vDUB inhibitors from a phage-displayed library of billions of Ub variants (UbVs). The exquisite specificity of identified UbVs has also enabled us to isolate UbVs that potently inhibit human Ub-binding proteins with equally high specificity [347, 348]. Here we describe UbVs that selectively block the deubiquitinating and deISGylating activities of MERS-CoV and CCHFV vDUB domains, respectively. Importantly, UbVs specific for MERS-CoV abolished replicative polyprotein processing activities. Expression of MERS-CoV-specific UbVs during MERS-CoV infection reduced infectious progeny titers by more than four orders of magnitude, demonstrating the remarkable potency of UbVs as antiviral agents.

## MATERIALS AND METHODS

### Selection of UbVs

The phage-displayed UbV library used in this study was re-amplified from Library 2 as previously described [347]. Protein immobilization and the following UbV selections were done according to established protocols [348, 349]. Briefly, purified viral proteases were coated on 96-well MaxiSorp plates (Thermo Scientific) by adding 100 µl of 1 µM proteins and incubating overnight at 4°C. Afterwards, five rounds of selections using the phage-displayed UbV library were performed against immobilized proteins including the following steps: (a) Each phage particle in the library pool displays a unique UbV and encapsulates the encoding DNA; (b) Binding phages are captured with an immobilized protein; (c) Non-binding phages are washed away; and (d) Bound phages are amplified by infection of bacteria. The enriched phage pool is cycled through additional rounds of selection to further enrich for protein-binding UbVs. After the fifth round of binding selections, individual phages with improved binding properties were identified by phage ELISA using established techniques and subjected to DNA sequencing of the phagemids to obtain UbV sequences [348, 349].



### Protein crystallization

*1. MERS-CoV $PL^{pro}$-ME.2 and -ME.4 complexes*

To form the non-covalent MERS-CoV $PL^{pro}$-UbV complexes, a 4-fold molar excess of ME.4 or ME.2 was incubated with MERS-CoV $PL^{pro}$ overnight at 4°C. The excess, unbound UbVs were removed from the sample using a Superdex 75 size exclusion column and fractions containing the MERS-CoV $PL^{pro}$-UbV complex were pooled and concentrated to 10 mg/ml. The MERS-CoV $PL^{pro}$-ME.4 complex was found to crystallize under similar conditions to those previously reported for the MERS-CoV $PL^{pro}$-Ub complex [327], with optimal crystals appearing in 0.1 M trisodium citrate pH 5.6, 20% (w/v) polyethylene glycol (PEG) 4000 and 20% (v/v) isopropanol. Crystals of the MERS-CoV $PL^{pro}$-ME.2 complex were grown in 0.1 M trisodium citrate pH 5.6, 19% (w/v) PEG 4000 and 19% (v/v) 1,2-isopropanediol. Crystals were grown by mixing $PL^{pro}$-UbV (10 mg/ml and 9 mg/ml for $PL^{pro}$-ME.4 and $PL^{pro}$-ME.2, respectively) with crystallization solution at a 1:1 volumetric ratio (2 µl MERS-CoV $PL^{pro}$-UbV + 2 µl well solution). Immediately prior to mixing, 1 M DTT was added to the MERS-CoV $PL^{pro}$-UbV complexes to a final concentration of 10 mM to prevent oxidation of the sample.

*2. CCHFV $OTU_{169}$-CC.2 and CCHFV $OTU_{185}$-CC.4 complexes*

Purified CCHFV OTU was pooled with 2-3-fold molar excess of purified UbV and dialyzed overnight against 50 mM Tris pH 8.0, 150 mM NaCl and 2 mM DTT. Protein complexes were concentrated and loaded onto a Superdex 75 size exclusion column and eluted in 50 mM Tris, 150 mM NaCl and 2 mM DTT. For all samples, a single peak corresponding to the respective complex was observed in the gel filtration profile and two bands corresponding to the CCHFV OTU and respective UbV

were observed by SDS-PAGE, indicating the high purity of the complexes. The CCHFV $OTU_{169}$-CC.2 complex was concentrated to 12 mg/ml for crystallization trials, and initial crystals and crystalline material obtained from preliminary screens were used to prepare seed stocks for microseed matrix screening [350, 351], which was set up for the hanging drop vapor diffusion method in 48-well VDX plates (Hampton Research) and carried out using conventional screens (Qiagen) at 4°C, with and without heterogeneous nucleation using 0.3-0.4 cm strands of human hair [352]. Total drop volume was 2 µl containing equal volumes of the protein complex and the well solution. Crystals of the CCHFV $OTU_{169}$-CC.2 complex were grown in 30% (w/v) PEG 4000, 0.2 M $CaCl_2$ and 0.1 M HEPES pH 7.5 and appeared after 5-8 days.

The CCHFV $OTU_{185}$-CC.4 complex was concentrated to 23 mg/ml and initial leads were observed with a combinatorial approach using microseed matrix screening with crystallization screens (Qiagen) along with the Silver Bullets screen (Hampton Research) and micro-seeding using crystals of a CCHFV $OTU_{185}$-CC.5 (a weaker binding variant selected by phage display) complex. Using the hanging drop vapor diffusion method and 48-well VDX trays (Hampton Research), screens were set up at 20°C with a reservoir volume of 150 µl, and a drop size of 3.5 µl, which comprised of 1.5 µl of the protein complex, 1 µl of the reservoir solution and 1 µl of Silver Bullet additive, added in this order. Crystals were obtained with 25% (w/v) PEG 3350, 0.1 M Tris pH 7.0 and 0.2 M sodium chloride. The Silver Bullet formulation in the drop was as follows: 0.16% (w/v) each of 5-Sulfosalicylic acid dehydrate, dodecanedioic acid, hippuric acid, mellitic acid, oxalacetic acid, suberic acid and 0.02 M HEPES sodium pH 6.8. Data collection procedures are described in Supplemental materials and methods.

### Lentivirus transduction and MERS-CoV infections

To produce lentiviruses, HEK293T cells (Virgin lab, Washington University School of Medicine) grown in a T175 flask were transfected with packaging vectors pMDLg/pRRE and pRSV-REV, envelope protein-expressing vector pCMV-VSVG [353] and the transfer vector (pLenti6.3/TO/V5-DEST containing GFP or FLAG-UbVs) using polyethylenimine (Polysciences Inc.). Medium was replaced 24 h post transfection and 48 h and 72 h post transfection supernatant was collected, centrifuged (1000 x g for 10 min) and filtered through a 0.45 µm filter before storage at -80°C. Titers of the lentivirus particles were determined by p24 antigen ELISA (ZeptoMetrix). HuH-7 (Bartenschlager lab, Heidelberg University) and MRC5 cells (CCL-171; American Type Culture Collection) grown in a 12-well plate were transduced with lentiviruses encoding GFP or FLAG-ME.1 diluted in DMEM containing 2% FCS and 8 µg/ml Polybrene (Sigma Aldrich). Medium was replaced 24 h post transduction (pt), and 32 h or 48 h pt protein lysates were obtained by adding 250 µl 2xLSB containing 25 mM NEM to each well while cells grown on coverslips were fixed with 3% paraformaldehyde in PBS.

GFP and FLAG-ME.1 expression was analysed by Western blotting as described in the Supplemental materials and methods. Fixed cells that were grown on coverslips were permeabilized with 0.1% Triton X-100 in PBS and subsequently indirect immunofluorescence assays were carried

out. Primary and secondary antibodies were diluted in PBS containing 5% FCS and Hoechst 33258 was added to the secondary antibody dilution to stain nuclear DNA. Coverslips were analysed with a Zeiss Axioskop 2 fluorescence microscope with an Axiocam HRc camera.

To obtain a cell population in which >90% of the cells expressed GFP, the amount of lentivirus yielding 120 ng of p24 was required to transduce $1x10^5$ HuH-7 cells and 40 ng of p24 for $1x10^5$ MRC5 cells was required. HuH-7 or MRC5 cells ($1x10^5$/12-well) were transduced with lentiviruses encoding GFP, FLAG-Ub.AA, FLAG-ME.1 or FLAG-ME.4. Cells were infected with MERS-CoV with a multiplicity of infection (MOI) of 0.01 at 32 h or 48 h pt. MERS-CoV inocula were prepared in PBS containing 50 µg/ml DEAE-dextran and 2% FCS. Cells were inoculated for 1 h at 37°C and the inoculum was replaced with EMEM containing 2% FCS. Supernatants were harvested 32 h post MERS-CoV infection and simultaneously cells were lysed in 4x LSB for Western blotting analysis. MERS-CoV titers were determined by plaque assays on Vero cells (Department of Viroscience, Erasmus Medical Center) as described by van den Worm et al. [329]. MERS-CoV infection experiments were performed at least twice and plaque assays were performed in duplicate in order to determine MERS-CoV titers. Work with MERS-CoV was performed inside biosafety cabinets in biosafety level 3 facilities at Leiden University Medical Center.

Full details of materials and methods are described in Supplemental materials and methods.

## RESULTS

### Potent and selective UbV inhibitors of MERS-CoV and CCHFV vDUBs

The UbV library [347] was screened against the MERS-CoV $PL^{pro}$ domain (MERS-CoV $PL^{pro}$) and the CCHFV OTU domain (CCHFV OTU). Within three weeks, UbVs were identified that bound with high affinity to either MERS-CoV $PL^{pro}$ (ME.1 to ME.4) or CCHFV OTU (CC.1 to CC.5) (Fig. 1A). To confirm the specificity of the UbVs towards their cognate vDUBs, the phage-displayed UbVs were challenged against a diverse panel of 11 DUBs from several species representing distinct DUB families (USP, OTU, and ubiquitin C-terminal hydrolases (UCH)). All UbVs bound to their cognate viral proteins but not to any of the 11 additional DUBs (Fig. 1B). To determine the binding affinity of each UbV, phage enzyme-linked immunosorbent assays (Fig. S1) and bio-layer interferometry (BLI) measurements were performed (Table S1). Each UbV was found to bind its cognate vDUB with affinities in the low to sub-nanomolar range, whereas wild-type Ub (Ub.wt) showed binding to MERS-CoV or CCHFV vDUBs only in the high micromolar range (Fig. S1B and Table S2). Consistent with the high affinities observed for the UbVs toward their respective vDUBs, each UbV also potently inhibited the deubiquitinating and deISGylating activities of MERS-CoV $PL^{pro}$ or CCHFV OTU as measured using the fluorogenic substrates Ub-AMC or ISG15-AMC, respectively (Fig. 1C and Fig. S2). The most potent inhibitors of MERS-CoV $PL^{pro}$ and CCHFV OTU were ME.4 (deubiquitination $IC_{50}$ = 0.8 nM and deISGlyation $IC_{50}$ = 1.2 nM) and CC.4 (deubiquitination $IC_{50}$ = 3.3 nM and deISGlyation $IC_{50}$ = 11 nM), respectively (Table S2). Furthermore, the UbVs were confirmed to inhibit processing of K48- and K63-linked tetra-Ub substrates by their respective vDUBs (Fig. 1D).

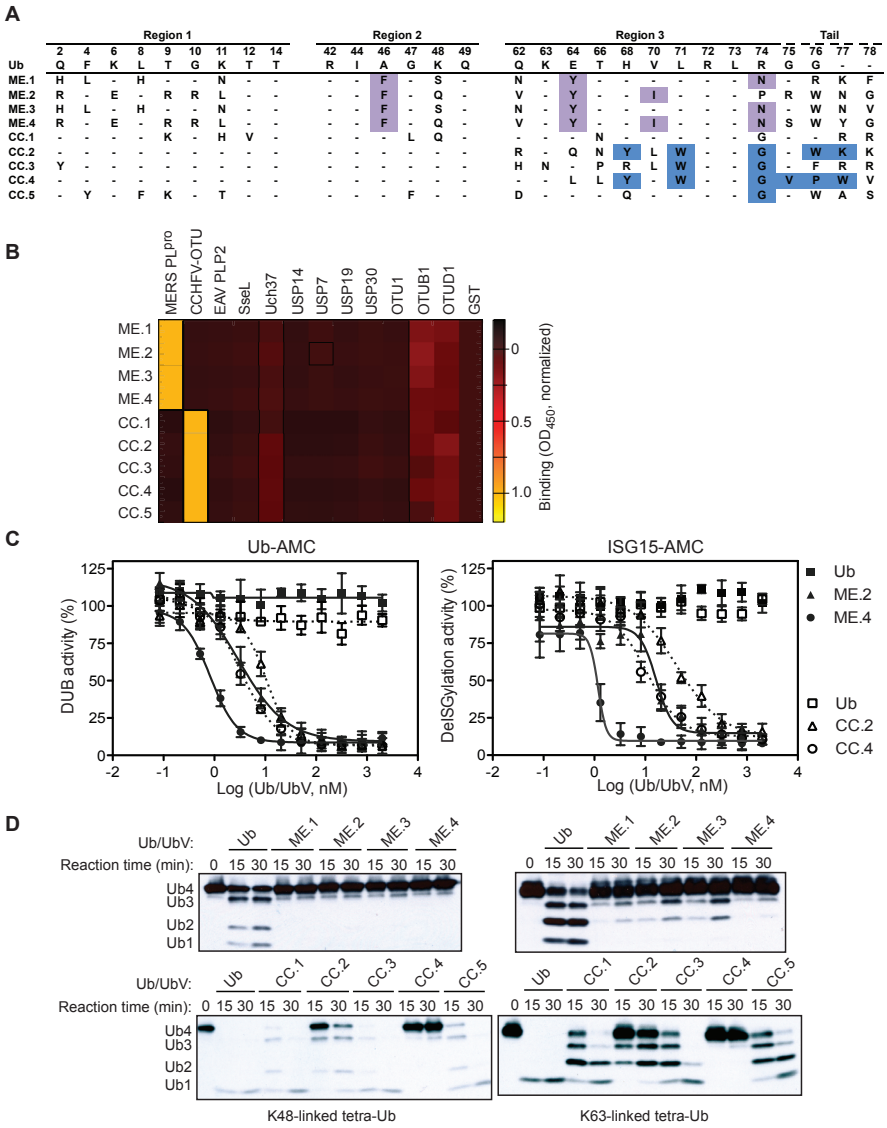


**Figure 1. UbVs inhibit activity of MERS-CoV PL$^{pro}$ and CCHFV OTU *in vitro*.** (A) Sequences of UbVs that bind MERS-CoV or CCHFV vDUBs. Only regions subjected to diversification relative to Ub.wt in the phage-displayed library are shown. Amino acids discussed in the text are highlighted. (B) The binding specificities of phage-displayed UbVs (y-axis) on a group of 12 DUBs (x-axis), as assessed by phage ELISA. Sub-saturating concentrations of phage were added to immobilized proteins as indicated. Bound phages were detected by the addition of anti-M13-HRP and colorimetric development of TMB peroxidase substrate. The mean value of absorbance at 450 nm is shaded in a black-red-yellow gradient. (C) Inhibition of MERS-CoV PL$^{pro}$ (solid lines) or CCHFV OTU (dashed lines) by the cognate UbVs shown as dose-response curves using Ub-AMC (left) or ISG15-AMC (right) as a substrate. The $IC_{50}$ value was determined as the concentration of UbV that reduced proteolytic activity by 50% (Table S1). The Ub.wt data obtained in the deISGylation assay cannot be fitted by GraphPad Prism so no lines are shown. (D) Effects of UbV inhibitors on vDUB activity against K48/K63-linked tetra-Ub substrates. Purified MERS-CoV PL$^{pro}$ (top panels) or CCHFV OTU (bottom panels) was incubated with the indicated UbV or Ub.wt (negative control) and biotinylated tetra-Ub at 37°C for a time course of 30 minutes. Western blots were probed with ExtrAvidin-HRP (EA-HRP) to detect biotin-Ub. Inhibition of proteolysis was shown by a delay of appearance of the digestion products triUb (Ub3), diUb (Ub2) and monoUb (Ub1).

## Structural basis for vDUB inhibition by UbVs

To reveal the molecular basis for the inhibition of MERS-CoV $PL^{pro}$ by UbVs, crystal structures of the enzyme were determined bound to ME.2 or ME.4 (Fig. 2A and 2B and Table 1). Both UbVs bound in nearly identical orientations as Ub.wt (Fig. 2C and Fig. S3A) with interface surface areas of ~1000 $Å^2$ [327, 354]. Substitutions common to both ME.4 and ME.2 at positions 46, 64 and 70 (Fig. 1A) were found to promote more favourable hydrophobic interactions with the enzyme relative to Ub.wt. In comparison to Ub.wt residue V70, UbV residue I70 extends further into a hydrophobic pocket of $PL^{pro}$ formed by residues $T1730^*$ and $V1691^*$ (*asterisks* denote amino acid numbering of MERS-CoV polyprotein) (Fig. 2D). UbV residue F46 inserts into a hydrophobic pocket formed by $PL^{pro}$ residues $W1668^*$, $E1670^*$, $V1680^*$, $L1682^*$, $Y1690^*$ and $Y1705^*$, and forms a cation-π interaction with $R1715^*$ (Fig. 2E). These extensive interactions are not formed at the $PL^{pro}$-Ub.wt interface with the Ub.wt residue A46. In addition, UbV residue Y64 makes more extensive hydrophobic interactions with $V1706^*$ and $G1710^*$, compared to Ub.wt residue E64 (Fig. 2F). The UbVs also differ in their C-terminal residues at positions 74, 75 and 77 (Fig. 1A). In ME.4, N74 extends into the active site and forms a hydrogen bonding network with $D1645^*$ and $G1758^*$ (Fig. 2G), which mimics hydrogen bonds formed by the same region of MERS-CoV $PL^{pro}$ with Ub.wt residues R74, G75 and G76 (Fig. 2H). In ME.2, P74 cannot form an analogous hydrogen bonding network, which likely contributes to the decreased inhibitory potency of ME.2 compared to ME.4 (Fig. 1D and Fig. S2A and S2B). Instead, P74 and the C-terminal tail are excluded from the active site and the main-chains interact through a hydrogen bond formed between the main-chain amide nitrogen of R75 and the backbone carbonyl of $E1754^*$ (Fig. 2I). A structural comparison of the C-terminal regions of ME.2 and ME.4 near the $PL^{pro}$ active site is shown in Fig. S4. Additional substitutions in the N-terminal region of ME.4 and ME.2 (Fig. 1A, region 1) do not make favourable contacts with MERS-CoV $PL^{pro}$, and in fact, residues 8-10 and 7-10 of ME.4 and ME.2, respectively, failed to resolve in electron density maps (Fig. S5). Taken together, our structural analyses revealed that a small subset of substitutions is sufficient to enhance hydrophobic packing and hydrogen bond networks to endow ME.4 and ME.2 with highly potent and specific inhibitory activity against MERS-CoV $PL^{pro}$.

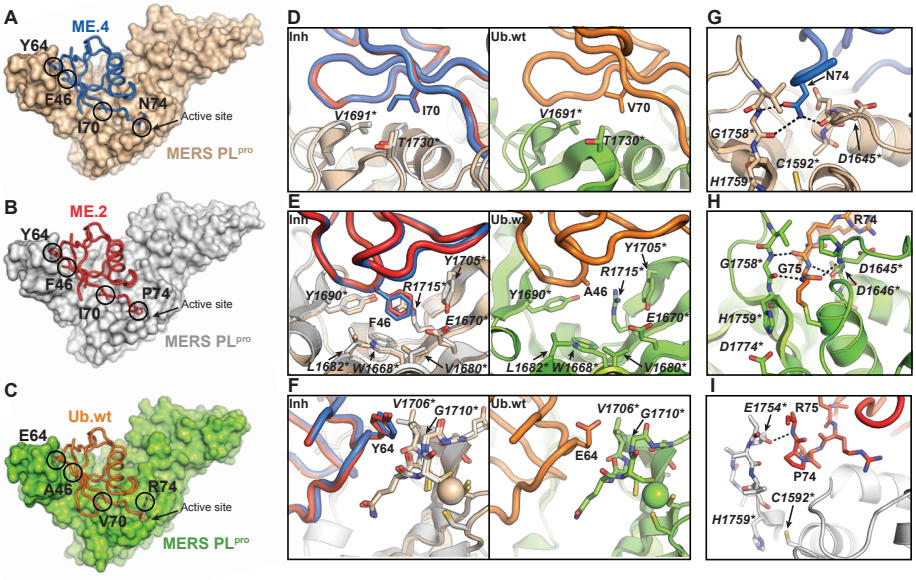


**Figure 2. Structural basis for UbV inhibition of MERS-CoV PL$^{pro}$.** (A-C) Crystal structure of (A) the MERS-CoV PL$^{pro}$-ME.4 complex, (B) the MERS-CoV PL$^{pro}$-ME.2 complex, and (C) the MERS-CoV PL$^{pro}$-Ub.wt complex (PDB ID: 4RF0). PL$^{pro}$ domains are shown as surface representations, and coloured in wheat, grey and chartreuse for the PL$^{pro}$-ME.4, -ME.2 and -Ub.wt complexes, respectively. ME.4, ME.2 and Ub.wt are shown as tubes and coloured in marine, red and orange, respectively. (D) Close up of a superposition of the MERS-CoV PL$^{pro}$-ME.4 and -ME.2 complexes (left panel) showing detailed interactions between PL$^{pro}$ and residue I70 of ME.4 or ME.2, and a comparison (right panel) of the same region in the PL$^{pro}$-Ub.wt complex. PL$^{pro}$ residues are shown as sticks and labelled with in italics with asterisks. (E) Close up of the MERS-CoV PL$^{pro}$-ME.4 and -ME.2 complexes (left panel) showing detailed interactions between PL$^{pro}$ and residue F46 of ME.4 or ME.2, and a comparison (right panel) of the same region in the PL$^{pro}$-Ub.wt complex. (F) Close up of the MERS-CoV PL$^{pro}$-ME.4 and -ME.2 complexes (left panel) showing detailed interactions between PL$^{pro}$ and residue Y64 of ME.4 or ME.2, and a comparison (right panel) of the same region in the PL$^{pro}$-Ub.wt complex. (G) Close up of ME.4 residue N74 bound near the active site of PL$^{pro}$. Hydrogen bonds are represented by dashed black lines. (H) Close up of the C-terminus of Ub.wt covalently bound in the active site of PL$^{pro}$. (I) Close up of ME.2 residue P74 bound near the active site of PL$^{pro}$. Figures were generated using PyMOL [373].

Similarly, crystal structures of CCHFV OTU were determined bound to CC.2 or CC.4 to gain insight into how they selectively block the DUB and deISGylating activities of the viral protease (Fig. 3A and 3B and Table 1). CC.2 and CC.4 were bound in the same orientation as Ub.wt with similar buried surface areas of ~1000 Å$^2$ (Fig. 3C and Fig. S3B) [223, 224]. Interestingly, substitutions in these UbVs were concentrated in the C-terminal region (Fig. 1A) and only substitutions at position 68 and downstream were found to interact with the enzyme. In both UbVs, Y68 improves hydrophobic packing with T10*, V12* and V18* (*asterisks* denote amino acid numbering of the large segment-encoded protein of CCHFV), relative to H68 in Ub.wt (Fig. 3D). In CC.2, residue L70 projects further into a hydrophobic cavity in CCHFV OTU formed by residues V12*, I14*, V18* and I131*, than does the equivalent Ub.wt residue V70 (Fig. 3E). The conformational freedom of a glycine substitution at position 74 enables the C-terminal tail of each UbV to form numerous favourable interactions with the enzyme. Residues G75 and V75 of CC.2 and CC.4, respectively, occupy space on the CCHFV OTU surface, which in the case of Ub.wt is occupied by the side-chain of R74 (Fig. 3E-3G). This alternative conformation permitted by G74 in CC.2 and CC.4 allows the side-chain of W76 or W77 of CC.2 or CC.4, respectively, to pack within different adjacent grooves near the CCHFV OTU active site, with W76 of CC.2 forming a cation-π interaction with R92* (Fig. 3E), and the amide nitrogen group of CC.4 residue W77 forming a hydrogen bond with the side chain of Q149* (Fig. 3F). Conversely, W71 in both CC.2 and CC.4 does not interact with CCHFV

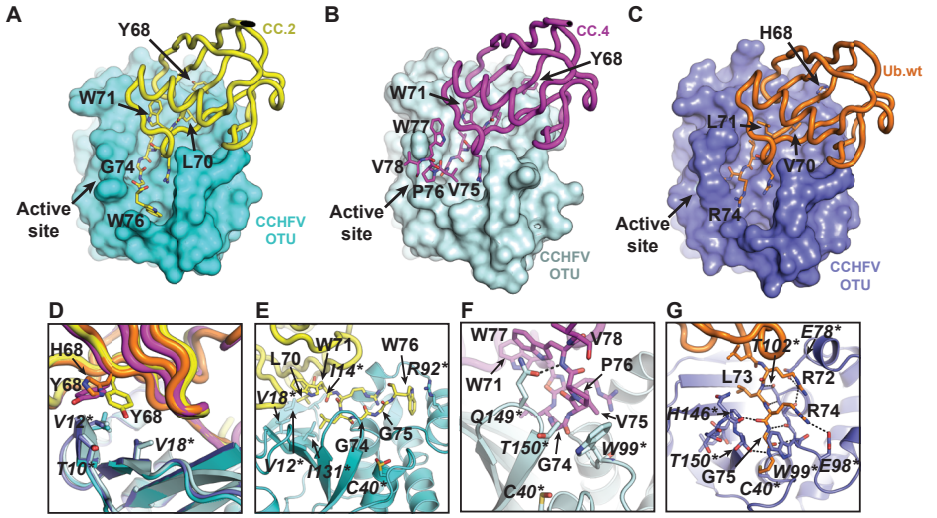


**Figure 3. Structural basis for UbV inhibition of CCHFV OTU**. (A-C) Crystal structure of (A) the CCHFV OTU-CC.2 complex, (B) the CCHFV OTU-CC.4 complex, and (C) the CCHFV OTU-Ub.wt complex (PDB ID: 3PT2). OTU domains are shown as surface representations, and coloured in cyan, light cyan and slate for the OTU-CC.2, -CC.4 and -Ub.wt complexes, respectively. CC.2, CC.4 and Ub.wt are shown as tubes and coloured in yellow, magenta and orange, respectively. (D) Overlay of the CCHFV OTU-CC.2, -CC.4 and -Ub.wt structures showing interactions between CCHFV OTU and CC.2 or CC.4 residue Y68 or Ub.wt residue H68. UbV and Ub.wt residues are shown as sticks and labelled in regular font. CCHFV OTU residues are shown as sticks and labelled in italics with asterisks. (E) Close up of interactions between the C-terminus of CC.2 and CCHFV OTU. (F) Close up of interactions between the C-terminus of CC.4 and CCHFV OTU. (G) Close up of interactions between the C-terminus of Ub.wt and the active site of CCHFV OTU. Figures were generated using PyMOL [373].

OTU, but instead packs into a hydrophobic cavity within each UbV (Fig. 3E and 3F). Differences between the orientations of the C-terminal tails of CC.2 and CC.4 arise from the variation at positions 75 and 76. In CC.4, residue V75 packs against CCHFV OTU residue W99*, and P76 appears to restrict conformational freedom and enable hydrophobic interactions with W99* and T150* (Fig. 3F). Together with the packing orientation of W77, these additional contacts likely account for the high binding affinity of CC.4 for CCHFV OTU (Table S1).

**Table 1. Crystallographic and refinement statistics for MERS-CoV $PL^{pro}$ and CCHFV OTU bound to UbVs.**

| Crystal | MERS-CoV $PL^{pro}$-ME.4 | MERS-CoV $PL^{pro}$-ME.2 | CCHFV OTU-CC.4 | CCHFV OTU-CC.2 |
|---|---|---|---|---|
| **X-ray source** | Rigaku R-AXIS IV++ | CLS 08B1-1 | CLS 08ID-1 | CLS 08ID-1 |
| Crystal geometry | | | | |
| Space group | $C222_1$ | $C222_1$ | $P4_32_12$ | C2 |
| Unit cell (Å) | *a*=48.21 *b*=110.96 *c*=185.90; α=β=γ=90° | *a*=47.07 *b*=109.78 *c*=183.96; α=β=γ=90° | *a*=*b*=64.31 c=277.58 α=β=γ=90° | *a*=101.4, *b*=33.60 *c*=71.25 *a*=*c*=90°, *β*=96.51° |
| **Crystallographic data** | | | | |
| Wavelength (Å) | 1.5419 | 1.2811 | 0.979 | 0.979 |
| Resolution range (Å) | 47.64-2.55 (2.64-2.55) * | 45.97-2.70 (2.80-2.70) | 47.17-2.10 (2.10-2.16) | 43.43-1.50 (1.53-1.50) |
| Total observations | 53264 (5257) | 57650 (5719) | 209641 (17075) | 141907 (6821) |
| Unique reflections | 16565 (1629) | 13337 (1291) | 34979 (2828) | 38017 (1876) |
| Multiplicity | 3.2 (3.2) | 4.3 (4.4) | 6.0 (6.0) | 3.7 (3.6) |
| Completeness (%) | 99.0 (100) | 98.7 (97.6) | 99.5 (99.8) | 98.7 (96.6) |
| $R_{merge}$ | 0.11 (0.63) | 0.073 (0.68) | 0.084 (0.89) | 0.03 (0.62) |
| CC1/2 | 0.99 (0.68) | 0.99 (0.88) | 0.998 (0.926) | 0.99 (0.79) |
| I/σI | 10.9 (1.80) | 16.69 (2.34) | 12.2 (2.2) | 18.7 (2.1) |
| Wilson B-factor ($Å^2$) | 37.21 | 54.23 | 33.96 | 18.63 |
| **Refinement statistics** | | | | |
| Reflections in test set | 1656 (163) | 1267 (99) | 1998 (197) | 1999 (195) |
| Protein atoms | 3042 | 2976 | 3878 | 1926 |
| Zinc atoms | 1 | 1 | | |
| Solvent molecules | 97 | 20 | 212 | 223 |
| $R_{work}/R_{free}$ | 0.1972 / 0.2455 | 0.2169 / 0.2732 | 0.1743 / 0.2291 | 0.1563 / 0.1775 |
| RMSDs | | | | |
| Bond lengths/angles (Å/°) | 0.002/0.49 | 0.001/0.41 | 0.010/1.04 | 0.008/0.97 |
| Ramachandran plot | | | | |
| Favored/allowed (%) | 96/4 | 95/4.1 | 98/2 | 100/0 |
| Average B factor ($Å^2$) | 38.16 | 57.52 | 40.59 | 28.27 |
| Macromolecules | 38.22 | 57.36 | 40.44 | 26.98 |
| Solvent | 36.74 | 52.53 | 43.57 | 38.29 |

*Values in parentheses refer to the highest resolution shell

### UbVs inhibit MERS-CoV PL$^{pro}$ activity in cell culture assays

To explore the effects of UbVs on MERS-CoV PL$^{pro}$ activity in cells, deubiquitination assays were performed by transfecting cells with combinations of plasmids encoding the following proteins: HA-tagged Ub (which becomes conjugated to cellular proteins), MERS-CoV PL$^{pro}$, and UbVs (which are unconjugatable due to substitutions in the C-terminal diglycine motif). A clear decrease of cellular HA-Ub conjugates was observed during co-expression of MERS-CoV PL$^{pro}$, while there was no effect upon expression of a catalytically inactive mutant (Fig. 4A, compare lanes 3 and 4). The co-expression of increasing doses of different UbVs attenuated MERS-CoV PL$^{pro}$ DUB activity to varying degrees (Fig. 4A and Fig. S6A). In a dose-dependent manner, ME.4 co-expression resulted in severe inhibition of HA-Ub deconjugation mediated by MERS-CoV PL$^{pro}$, whereas co-expression of an unconjugatable form of Ub.wt as a negative control (Ub.AA, which contains G75A and G76A substitutions) had no effect on the DUB activity of MERS-CoV PL$^{pro}$ at any dose (Fig. 4A, compare lanes 5-7 to 8-10). Like ME.4, ME.2 had a strong effect resulting in near complete inhibition of MERS-CoV PL$^{pro}$ DUB activity at the lowest UbV dose, whereas the inhibitory effect of ME.1 and ME.3 was apparent only at higher UbV doses (Fig. S6A). Notably, none of the UbVs inhibited the DUB activity of the closely related SARS-CoV PL$^{pro}$, highlighting their specificity for MERS-CoV PL$^{pro}$ (Fig. S7A). A superposition of ME.4 onto the Ub domain of a previously determined SARS-CoV-Ub complex suggests that F46 and I70 of ME.4 clash with V188$^{*}$ and M209$^{*}$ of SARS-CoV PL$^{pro}$, respectively, and offers a plausible explanation for the specificity of ME.2 and ME.4 toward MERS-CoV PL$^{pro}$ (Fig. S8).

We previously found that the DUB activity of MERS-CoV PL$^{pro}$ suppresses IFN-β promoter activity upon activation of cellular innate immune signalling [327]. In a luciferase-based IFN-β reporter assay we show that ectopically expressed UbVs competed with endogenous Ub for binding to MERS-CoV PL$^{pro}$ resulting in an alleviated suppression of the IFN-β promoter activity (Fig. 4B and Fig. S6B). ME.2 and ME.4 were more potent than ME.1 and ME.3 at blocking the ability of MERS-CoV PL$^{pro}$ to suppress IFN-β promoter activation, whereas none of the UbVs were able to block suppression of the IFN-β promoter activity by SARS-CoV PL$^{pro}$ (Fig. S7B). The UbVs thus prevented MERS-CoV PL$^{pro}$-mediated suppression of cellular anti-viral innate immune responses, and in a remarkably selective, virus-specific manner.

A critical step in the replication cycle of MERS-CoV is the processing of viral polyproteins into functional non-structural proteins (nsps) that is accomplished in part by the protease activity of PL$^{pro}$, which cleaves the nsp1↓2, nsp2↓3, and nsp3↓4 junctions [205]. In order to assess the ability of UbVs to inhibit MERS-CoV PL$^{pro}$-mediated polyprotein processing activity, an *in trans* cleavage assay was performed [327]. FLAG-tagged UbVs and V5-tagged MERS-CoV PL$^{pro}$ were co-expressed with N-terminally HA-tagged and C-terminally V5-tagged nsp3C-4 (HA-nsp3C-4-V5), a fragment of the viral polyprotein encompassing the C-terminal part of nsp3 (excluding the PL$^{pro}$ domain) and nsp4. *In trans* cleavage of the nsp3↓4 junction is indicative of proteolytic activity of PL$^{pro}$ during infection [327]. MERS-CoV PL$^{pro}$ efficiently cleaved HA-nsp3C-4-V5 into HA-nsp3C and nsp4-V5 products, whereas the active site mutant did not (Fig. 4C, compare lanes 3 and 4).

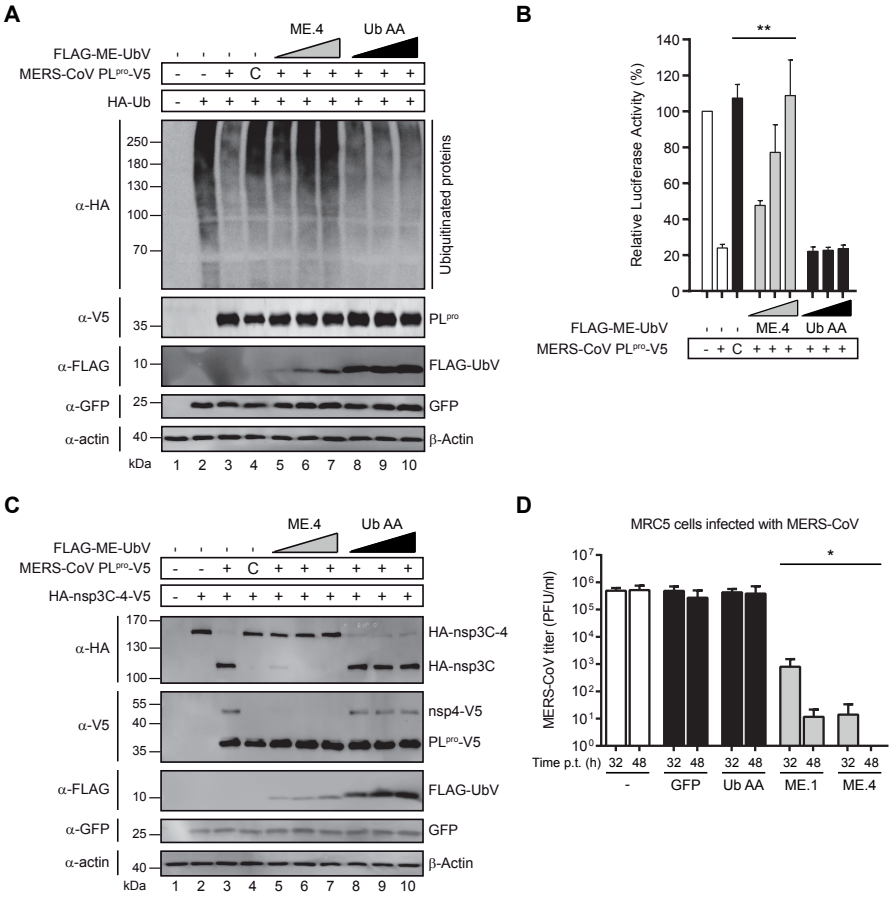


**Figure 4. UbVs inhibit proteolytic activity of MERS-CoV PL$^{pro}$ in cell culture and affect MERS-CoV replication.** (A) The effects of UbVs on the DUB activity of MERS-CoV PL$^{pro}$ was determined by co-transfecting HEK293T cells with plasmids encoding HA-Ub, MERS-CoV PL$^{pro}$-V5 (wild-type or the active site mutant C1592A annotated as "C" throughout the rest of the figure), FLAG-ME-UbV as indicated (in increasing dose) and GFP (as a transfection control). Cells were lysed 18 h post transfection and expressed proteins were analysed by Western blotting. DUB activity of MERS-CoV PL$^{pro}$ was visualized by the deconjugation of HA-Ub from cellular proteins. (B) Assessment of the inhibitory effects of UbVs on the suppression of the IFN-β promoter by MERS-CoV PL$^{pro}$. HEK293T cells were transfected with plasmids encoding firefly luciferase reporter gene under control of the IFN-β promoter, *Renilla* luciferase, innate immune response inducer mitochondrial antiviral signalling protein (MAVS), MERS-CoV PL$^{pro}$-V5 (wild-type or the active site mutant C) and FLAG-tagged UbVs (in increasing dose). Cells were lysed 16 h post transfection and both firefly and *Renilla* luciferase activities were measured. Results represent at least three independent experiments. Significance relative to wild-type PL$^{pro}$ without expression of a UbV was calculated using an unpaired two-tailed Student's *t*-test and significant values were indicated: ** p<0.01. Bars represent mean and error bars represent standard deviation. (C) Proteolytic cleavage capability of MERS-CoV PL$^{pro}$ was assessed in the presence of the UbVs. N-terminally HA-tagged and C-terminally V5-tagged nsp3C-4 (excluding the PL$^{pro}$ domain) was co-expressed with V5-tagged MERS-CoV PL$^{pro}$-V5 (wild-type or the active site mutant C), FLAG-ME-UbV (with increasing doses) and GFP (as a transfection control). Cells were lysed 18 h post transfection and proteolytic cleavage activity was assessed by Western blotting to detect generation of N-terminal HA-tagged nsp3C and C-terminal V5-tagged nsp4 cleavage products. (D) MERS-CoV titers of collected supernatants from lentivirus transduced and, subsequently, MERS-CoV infected MRC5 cells. MRC-5 cells were transduced with lentiviruses encoding FLAG-UbVs, FLAG-Ub.AA or GFP (latter two as controls) and, either 32 h or 48 h pt, the cells were infected with MERS-CoV at an MOI of 0.01. After another 32 h, culture supernatants were harvested and MERS-CoV titers were determined by plaque assays on Vero cells. Significant difference relative to MERS-CoV titers from lentivirus transduced MRC5 cells expressing Ub.AA is indicated: * p<0.05. Bars represent mean and error bars represent standard deviation.

The cleavage of the nsp3↓4 site was not affected upon expression of the negative control Ub.AA, whereas only a fraction of HA-nsp3C-4-V5 was cleaved upon expression of ME.4 or ME.2 at the lowest dose, and cleavage was completely blocked at higher UbV doses (Fig. 4C compare lanes 5-7 to 8-10, Fig. S6C). Increasing doses of ME.1 and ME.3 also resulted in reduced cleavage as gradually more HA-nsp3C-4-V5 precursor was observed (Fig. S6C).

### UbVs block MERS-CoV replication in cells

To directly assess the ability of UbVs to inhibit MERS-CoV replication, MERS-CoV $PL^{pro}$-specific UbVs were ectopically expressed in cell culture, and cells were subsequently infected with MERS-CoV. MRC5 and HuH-7 cell lines were transduced with lentiviruses encoding FLAG-tagged UbVs, Ub.AA, or GFP. Efficient expression of FLAG-ME.1 and GFP in these cells was confirmed by fluorescence microscopy and by Western blotting (Fig. S9). Either 32 or 48 h pt, cells were infected with MERS-CoV at an MOI of 0.01, and MERS-CoV titers were determined from supernatants harvested 32 h post infection (Fig. 4D). In MRC5 cells, ME.1 and ME.4 expression resulted in significantly lower virus titers as these dropped from 5 x $10^5$ plaque-forming units (PFU)/ml recovered from control cells to 1,000 or 10 PFU/ml, respectively, when the MERS-CoV infection was started 32 h pt (Fig. 4D). The effect of the UbVs was even more pronounced in MRC5 cells that were infected with MERS-CoV 48 h pt, as virus titers dropped below 10 PFU/ml upon expression of ME.4, which represented a reduction in infectious progeny titers of more than four orders of magnitude (Fig. 4D) and correlated with higher expression of the UbVs at this time point (Fig. S9 and Fig. S10). In HuH-7 cells the expression of GFP or Ub.AA did not affect MERS-CoV titers compared to the non-transduced cells, whereas ME.1 expression led to a two orders of magnitude reduction in virus titer, and an even greater reduction of more than three orders of magnitude was observed upon ME.4 expression (Fig. S11). The effect of UbVs on MERS-CoV progeny titers was more severe in MRC5 cells compared to HuH-7 cells, which might be due to generally higher expression of UbVs in MRC5 cells than in HuH-7 cells (Fig. 4D, Fig. S9B and Fig. S11). Taken together, these studies show that UbVs readily inhibit the proteolytic activities of MERS-CoV $PL^{pro}$ in cells and provide extremely effective protection from MERS-CoV infection.

## DISCUSSION

The continued introduction of viruses from zoonotic sources into human populations poses a serious and constant threat to human health [259]. In the case of CoV infection, therapeutic options are limited, and vaccine development remains in progress [257, 259]. Here, we describe a unique protein engineering platform that can be used to rapidly generate UbVs to selectively block the activity of vDUBs from a range of evolutionarily distinct viral lineages. Indeed, UbVs generated against MERS-CoV almost completely abolished the replication of this virus in host cells. Meanwhile, none of the UbVs generated in this study likely cross-reacted with human DUBs and no toxicity was observed upon expression of UbVs, demonstrating their potential therapeutic safety.

Targeting intracellular targets with protein-based inhibitors is currently not a therapeutic option due to the practical limitations of immunogenicity and the lack of efficient means for delivering proteins into cells *in vivo*. However, progress continues to be made on methods for intracellular delivery of mRNA or proteins [355-357], and strategies to reduce immunogenicity, including the use of mirror-image proteins [358], have been developed. Thus, in the future, we are hopeful that UbVs may become bona fide drug candidates, but at present, they are best viewed as tool compounds that can enable drug discovery. For example, while the interface between the UbVs and vDUBs is large, we have recently used combinatorial mutagenesis to reveal a smaller site on human USPs within the UbV interaction interface, which may be amenable as a target for small-molecule inhibitor design [359]. Indeed, while the design of small-molecules that target protein-protein interfaces remains challenging, there are successful examples where polypeptide-based tools have facilitated design and screening of small-molecule inhibitors [360].

A plethora of viruses causing human disease encode for vDUBs implicated in replication and/or pathogenesis, emphasizing the potential clinical importance of vDUBs as therapeutic targets [196, 197, 230, 327, 361-363]. The UbV development platform can also be readily extended to target viruses that infect plants and animals of economic importance, including porcine reproductive and respiratory syndrome virus, equine arteritis virus, bovine coronavirus, transmissible gastroenteritis virus, porcine epidemic diarrhoea virus and turnip yellow mosaic virus, all of which encode vDUBs that are essential for virus replication [344]. In contrast, some vDUBs, like the CCHFV OTU protease, do not appear to process viral polyproteins and are instead dedicated to increasing viral pathogenicity by suppressing cellular innate immunity [219, 364]. Interestingly, the CCHFV OTU protease comprises a domain on the viral polymerase, and targeting it with a UbV may not only suppress viral pathogenicity but RNA replication as well, since it has been found that viral OTU DUB activity can suppress proteasome-dependent viral polymerase degradation [365]. Additionally, the strong binding of UbV to the viral polymerase could cause steric hindrance and in this way affect polymerase function.

With current transgenic technologies [366], livestock and plant crops expressing virus-specific UbVs could be readily engineered to generate virus-resistant organisms. Significant progress has

also been made towards the development of animal models of MERS-CoV infection ([251, 319, 332, 367, 368] and reviewed in [369]), which includes mouse models used in concert with mouse-adapted MERS-CoV strains, together mimicking MERS-CoV pathology observed in humans [370]. These technologies will provide attractive platforms to assess the efficacy of UbV delivery systems to treat MERS-CoV infection *in vivo*.

The utilization of the Ub scaffold as a template for vDUB inhibitor development exploits the large Ub-binding interface to provide a high degree of specificity in comparison to small-molecule-based approaches, since the latter usually rely on targeting the active site of the viral protease, thereby invoking the risk of cross-reactivity with cellular proteases. The amino acid substitutions in UbVs that confer potent inhibition of vDUBs are distributed across relatively large binding interfaces, and we speculate that resistance to UbVs is less likely to develop in comparison to small-molecule inhibitors. The larger binding surface and the much tighter binding affinities of UbVs (low to sub-nanomolar, Fig. 1C) compared to reported micromolar affinities for small-molecule inhibitors of MERS-CoV $PL^{pro}$ [371] imply that rather extensive mutations in the viral protease will be necessary to efficiently repel the UbV. Since development of resistance mutations requires virus replication, the extreme reduction in MERS-CoV progeny titers upon expression of UbVs during infection is therefore expected to severely delay occurrence of resistance. Additionally, if a resistant virus happens to be already present in the quasi species it is likely that mutations to repel the UbV from the vDUB will concomitantly lead to less optimal binding of the viral protease to Ub/ISG15 itself and maybe even the virus replicase polyproteins. Therefore, the resistant virus is expected to be attenuated and to have at least reduced deubiquitinating/deISGylating activity that is important for the virus' capacity to suppress host innate immune responses [220, 327]. This idea is supported by described escape mutants for MHV to a broad-spectrum CoV $3CL^{pro}$ inhibitor where the inhibitor-resistant virus was attenuated in mice, highlighting that the mutant was generated at the cost of replicative fitness [372]. In future experiments we will experimentally assess the development of UbV resistance during infection in cell culture and mouse models, which will show whether our speculations are correct.

Ultimately, in the event that resistant strains do emerge in a clinical setting, new UbVs targeting these strains can also be generated rapidly. Most importantly, unlike small-molecule approaches that can take years to implement and often fail, phage display yields potent and selective viral inhibitors in weeks, a rate that could allow therapeutic development to keep pace with the continued emergence of pathogenic viruses and limit their pandemic potential. Together, these findings make further exploration of UbVs as potent and rapidly developed antiviral agents an exciting and promising venture.

## ACKNOWLEDGEMENTS

We thank Natalia Frias-Staheli, Michaela U. Gack and Paul N. Moynagh for providing reagents. Erasmus Medical Center and Bart L. Haagmans are thanked for providing Vero cells and a MERS-CoV stock. We are grateful to Eric J. Snijder for helpful discussions, and Veronica Larmour, Nick Jarvik, Peter J. Bredenbeek, Adriaan H. de Wilde, Clara C. Posthuma, and the beamline staff at the Canadian Light Source (CLS) for technical support.

*Coordinate files and structure factors have been deposited to the Protein Data Bank under accession codes 5V6A and 5V69 for the MERS-CoV $PL^{pro}$-ME.2 and –ME.4 structures, respectively, and 5V5H and 5V5G for the CCHFV OTU-CC.2 and –CC.4 structures, respectively.*

## SUPPLEMENTAL MATERIALS AND METHODS

### ELISAs to evaluate binding and specificity

Proteins under study were immobilized on 384-well MaxiSorp plates (Thermo Scientific) by adding 30 µl of 1 µM proteins for overnight incubation at 4°C. Phage and protein ELISA against immobilized proteins was performed as previously described [347, 348]. Binding of phage was detected using anti-M13-HRP antibody (GE Healthcare) and binding of FLAG-tagged UbVs was detected using anti-FLAG-HRP antibody (Sigma-Aldrich). To measure the half maximal binding concentration (EC50) of UbVs binding to viral proteases, the concentration of UbVs or Ub.wt was varied from 0 to 4 µM (24 points, 1:2 dilution), while the concentration of target proteins immobilized on the plate remained at 1 µM. $EC_{50}$ values were calculated using the GraphPad Prism software with the built-in equation formula (non-linear regression curve).

### Octet bio-layer interferometry

Experiments were performed as previously described [348]. Concentrated analyte and ligand proteins were diluted into BLI reaction buffer (25 mM HEPES pH 7.0, 150 mM NaCl, 0.1 mg/ml bovine serum albumin and 0.01% tween 20). Experiments of BLI were carried out on Octet RED96 system (ForteBio) using anti-GST antibody biosensors for GST-tagged ligands and His-tagged analytes at 25˚C. 7-9 concentration points of analytes covering a wide titration range were applied for BLI experiments. Sensorgram raw data was processed and extracted by Octet Analysis 9.0. Dissociation constants $K_D$ were obtained by fitting the response wavelength shifts in the steady-state regions using single-site binding system (Eq. 1) shown below.

$$R_{eq} = R_{max} \frac{[C]}{K_D + [C]}$$

where $R_{eq}$ is the value of the response shift in the steady-state region in each sensorgram curve, *[C]* is the titrant concentration, $R_{max}$ is the maximal response in the steady-state region, $K_D$ is the dissociation constant for the single-site binding system. In both equations, $R_{max}$ and $K_D$ values are unknown and the Levenberg–Marquardt algorithm was used to perform iterative non-linear least squares curve fitting in Profit 6.2 (QuantumSoft) to obtain the fitted $R_{max}$ and $K_D$.

### Deconjugation assays

*Ub/ISG15-AMC*

Inhibition assays using Ub-AMC or ISG15-AMC (both Boston Biochem) as deconjugation substrates were performed as described before [347, 359]. Experiments were performed in assay buffer (50 mM HEPES, pH 7.5, 0.01% Tween 20, 1 mM dithiothreitol (DTT)) containing 1 µM Ub-AMC substrate, 10 nM vDUBs and 12 serial dilutions of UbVs. vDUBs and UbV were mixed in assay buffer as indicated and incubated at room temperature for 2 min prior to the addition of Ub-AMC. All serial dilutions were performed in 96-well plates and subsequently transferred

to 384-well black plates (Thermo Scientific) for making measurements. Deconjugation activity was measured by monitoring the increase of AMC fluorescence emission at 460 nm (excitation at 360 nm) for 30 min using a BioTek Synergy2 plate reader (BioTek Instruments, Winooski, VT). $IC_{50}$ values were calculated using the GraphPad Prism software with the built-in equation formula (non-linear regression curve).

*K48/K63-linked tetra-Ub*

Inhibition assays using Biotin Tetra-Ub/Ub4 WT Chains (K48- or K63-linked, Boston Biochem) as deubiquitination substrates were performed in assay buffer (50 mM HEPES, pH 7.5, 100 mM NaCl, 1 mM DTT) containing 1 µM substrate, 1 µM vDUB and 10 µM UbV as indicated. After incubation at 37°C for the indicated times, reactions were stopped by the addition of 10 mM EDTA and SDS-PAGE sample buffer and resolved using 4-20% gradient gels (Bio-Rad). The cleavage of K48/K63 tetra Ub chains was evaluated by Western blotting, probed with ExtrAvidin®-Peroxidase (Sigma).



## Protein expression and purification

*UbVs ME.2 and ME.4*

Plasmids named pET53-ME.2, and -ME.4 were transformed into $CaCl_2$-competent *E. Coli* BL21 (DE3) Gold cells (Agilent) to allow for T7 polymerase-driven expression of N-terminally H6-tagged UbVs ME.2 and ME.4 respectively. Cells were grown at 37°C in the presence of 150 µg/ml ampicillin to an optical density ($OD_{600}$) of 0.6 and then induced at 16°C by addition of isopropyl β-D-1-thiogalactopyranoside (IPTG; final concentration 1 mM). After overnight incubation, cells were resuspended in lysis buffer (500 mM NaCl, 50 mM Tris pH 8.0) and lysed via French press. The cell lysate was clarified by centrifugation at 17,211 x g at 4°C for 30 min, then incubated with 2 ml Ni-NTA Superflow resin (Qiagen) at 4°C for 30 min, and poured into a gravity column. The column was washed with 50 ml of lysis buffer, followed by 50 ml of lysis buffer containing 50 mM imidazole. Protein was eluted in lysis buffer containing 250 mM imidazole. Following affinity purification, UbVs were further purified using a Superdex 75 size exclusion column (GE Healthcare), eluting in 20 mM Tris pH 8.5, 150 mM NaCl and 2 mM DTT.

*UbVs CC.2 and CC.4*

Plasmids encoding UbVs CC.2 and CC.4, named pET53-CC.2 and -CC.4 respectively, were transformed into $CaCl_2$-competent *E. coli* BL21 (DE3) Gold cells, and grown in Luria-Bertani media supplemented with 150 µg/ml ampicillin at 37˚C with shaking to an $OD_{600}$ of 0.8-1.5. Protein expression was induced by the addition of a final concentration of 1 mM IPTG for 19-21 h at 28˚C. Cells were resuspended in lysis buffer (for CC.2: 50 mM Tris pH 7.2, 150 mM NaCl; for CC.4: 50 mM Tris pH 8.0, 150 mM NaCl) and lysed using either French Press or a freeze-thaw cycle that was performed three times. For the latter, cells were frozen at -80˚C after addition of 150 µl of 20 mg/ml lysozyme followed by incubation on ice for 20 min, and thawed at room temperature. Lysis was followed by addition of 100-300 µl of DNase I (10 mg/ml) while mixing on a magnetic stirrer.

Lysates from French Press or the freeze-thaw procedure were clarified by centrifugation at 48,298 x g for 30-40 min. Supernatants were loaded onto a gravity column containing Ni-NTA Superflow resin (Qiagen) that had been pre-equilibrated with Buffer A (50 mM Tris pH 8.0, 150 mM NaCl). The column was washed with 2-3 column volumes (CV) of Buffer A supplemented with 20 mM imidazole and eluted in a step-wise manner with Buffer A containing 500 mM imidazole. Fractions of interest, as determined from SDS-PAGE, were pooled and dialyzed twice against Buffer A. The proteins were concentrated and loaded onto the Superdex 75 size exclusion column. CC.2 was eluted in 20 mM Tris pH 7.4, 150 mM NaCl and 1 mM DTT, and CC.4 was eluted in 50 mM Tris pH 8.0, 150 mM NaCl and 2 mM DTT.

*MERS-CoV $PL^{pro}$*

The MERS-CoV $PL^{pro}$ domain was expressed and purified as described previously [327]. Briefly, *E. coli* BL21 (DE3) Gold cells transformed with plasmid pE-SUMO $PL^{pro}$ were grown to an $OD_{600}$ of 0.6-0.8 at 37˚C in the presence of 35 μg/ml kanamycin. Protein expression was induced by the addition of a final concentration of 1 mM IPTG and overnight incubation at 16˚C. Cells were resuspended in lysis buffer (150 mM Tris, pH 8.5, 1 M NaCl, 2 mM DTT), lysed via French press and clarified via centrifugation at 17,211 x g. Clarified lysate was loaded onto a Ni-NTA gravity column and washed with lysis buffer, followed by lysis buffer supplemented with 25 mM imidazole and subsequent elution in lysis buffer supplemented with 250 mM imidazole. The SUMO-$PL^{pro}$ fusion was cleaved overnight in 150 mM NaCl, 50 mM Tris, pH 8.0, 1 mM DTT in the presence of Ulp1 SUMO protease. Cleaved, tagless MERS-CoV $PL^{pro}$ was subsequently passed through a second Ni-NTA column, and further purified on a Superdex 75 size exclusion column equilibrated in 20 mM Tris, pH 8.5, 150 mM NaCl, 2 mM DTT.

*CCHFV $OTU_{169}$ and CCHFV $OTU_{185}$*

Plasmids encoding the CCHFV OTU domain residues 1-169 (pGEX-*CCHFV $OTU_{169}$)* and residues 1-185 (pET49b-*CCHFV $OTU_{185}$*) fused with a GST tag and an HRV3c protease cleavage site were used for the expression and purification of the CCHFV OTU domain as described previously [219, 223]. Briefly, *E. coli* BL21-Gold (DE3) cells transformed with either of the plasmids were grown to an $OD_{600}$ of 0.9-1.0 at 37˚C with shaking, and protein expression was induced with a final concentration of 1 mM IPTG at 30˚C for 19-21 hrs. Cells were resuspended in 25 ml of lysis buffer (50mM Tris-Cl pH 7.2, 200 mM NaCl, 5 mM EDTA, 5 mM DTT) and lysed via French Press. The lysate was clarified by centrifugation at 48,298 x g for 30-40 min. The supernatant was loaded onto GST-Bind resin (VWR) in a gravity column pre-equilibrated with the lysis buffer, and proteins were eluted in 50 mM Tris-Cl pH 7.2, 500 mM NaCl, 5 mM EDTA, 5 mM DTT and 15 mM reduced glutathione. The GST tag was cleaved by addition of GST-tagged HRV 3c protease during overnight dialysis against 50 mM Tris pH 7.4, 150 mM NaCl, 1 mM EDTA, 1 mM DTT. Cleaved CCHFV OTU proteins were collected as flow-through by passing the digest through a recharged GST-Bind column, concentrated

and loaded onto the Superdex-75 column (GE Healthcare). Purified proteins, eluted in 20 mM Tris pH 7.2, 150 mM NaCl and 1mM DTT, were then used for further analyses.

## Protein crystallization data collection

*MERS-CoV $PL^{pro}$-ME.2 and -ME.4 complexes*

Crystals were harvested by sweeping through a cryoprotectant solution containing 0.1M trisodium citrate pH 5.6, 22% (w/v) PEG 4000, 21% (v/v) 1,2-propanediol ($PL^{pro}$-ME.4), or harvested directly from the crystallization solution ($PL^{pro}$-ME.2) and flash-cooled in liquid nitrogen. X-ray diffraction data for $PL^{pro}$-ME.4 crystals were collected using a Rigaku 007HF MicroFocus X-ray generator and R-AXIS IV++ detector. $PL^{pro}$-ME.2 data collection was carried out at the Canadian Light Source on beamline 08B1-1. Diffraction data for the $PL^{pro}$-ME.4 and –ME.2 crystals were integrated and scaled using XDS [282], followed by merging using Aimless within the CCP4 software suite. Initial phase estimates were determined via molecular replacement within phenix.phaser using the previously determined MERS-CoV $PL^{pro}$ domain (PDB ID: 4RF0) and a polyAla Ub model (PDB ID: 4RF0) as independent search models [374]. Model building and refinement were performed using Coot and phenix.refine, respectively [287, 288].

*CCHFV $OTU_{169}$-CC.2 and CCHFV $OTU_{185}$-CC.4 complexes*

Single crystals of the CCHFV $OTU_{169}$-CC.2 and CCHFV $OTU_{185}$-CC.4 complexes were swept through cryoprotectant containing well solution supplemented with 20-30% ethylene glycol, and X-ray diffraction data were collected at the CLS on beamline 08ID-1 at 100K. X-ray diffraction data were indexed and scaled using XDS [282] and merged with Aimless [375]. Initial phases for the CCHFV $OTU_{169}$-CC.2 and CCHFV $OTU_{185}$-CC.4 complexes were determined by molecular replacement within phenix.phaser [374] using the previously reported CCHFV OTU domain bound to Ub (PDB 3PT2) [223] as a search model. The structures of CC.2 and CC.4 bound to CCHFV OTU were subsequently modelled and refined into the MR maps using Coot [287] and phenix.refine, respectively [288].

## Plasmids used for cell culture work

The following plasmids were described elsewhere or provided by others: pcDNA3.1-MERS-CoV-$PL^{pro}$ wild-type and active site mutant C1592A [327], pCAGGS-HA-nsp3C-4-V5 [327], pcDNA-eGFP [221], pCAGGS-MAVS (provided by N. Frias-Staheli), pLuc-IFN-β [275] and pRL-TK (Promega). pcDNA3-HA-Ub was generated by cloning PCR-amplified Ub (using pCMV-FLAG-Ub [274] as a template) in pcDNA3.1(-) (Invitrogen) in frame with an N-terminal HA tag. Codon optimized SARS-CoV-$PL^{pro}$ (amino acids 1541-1855 of the SARS-CoV pp1a/pp1ab (NCBI ID: AY291315.1)) with removed potential splice sites and polyadenylation signals (IDT) was cloned into pcDNA3.1(-) in frame with a C-terminal V5-tag generating pcDNA3.1(-)-SARS-CoV-$PL^{pro}$-V5. pcDNA3.1(-)-SARS-CoV-$PL^{pro}$-V5 was used as template for site-directed mutagenesis using the QuikChange™ strategy

(Stratagene using Accuzyme DNA polymerase from Bioline) to mutate the active site cysteine to alanine (C1651A).

In the UbV-containing pDONR-221 vectors (Thermo Fisher Scientific) a methionine was introduced before the already present N-terminal FLAG tag using the QuikChange™ strategy. In pDONR-221-FLAG-Ub substitutions G75A+G76A were introduced in Ub to generate pDONR-221-FLAG-Ub.AA. FLAG-UbVs were cloned in destination vectors pcDNA3.1-DEST or pLenti6.3/TO/V5-DEST (Thermo Fisher Scientific) using the Gateway technology (Thermo Fisher Scientific). Primer sequences are available upon request.

## Cell culture and antibodies

HEK293T were grown in Dulbecco's modified Eagle's medium (DMEM) supplemented with 10% foetal calf serum (FCS; Bodinco BV), 100 units/ml penicillin, 100 units/ml streptomycin and 2 mM L-glutamine. Vero cells (Erasmus Medical Center) and MRC5 cells (ATCC CCL-171) were cultured in Eagle's minimum essential medium (EMEM) with 8% FCS, 100 units/ml penicillin and streptomycin, 2 mM L-glutamine and non-essential amino acids (PAA). HuH-7 cells were maintained in DMEM containing 8% FCS, antibiotics and non-essential amino acids. DMEM, EMEM and supplements were obtained from Lonza.

Proteins on Western blot were visualized using the following primary antibodies: mouse anti-FLAG (F3165; Sigma-Aldrich), mouse anti-V5 (37-7500; Invitrogen), mouse anti-HA (ab18181; Abcam), rabbit anti-GFP [221], rabbit anti-SARS-CoV nsp4 [376], rabbit anti-MERS-CoV p4b [377] and mouse anti-actin (A5316; Sigma-Aldrich). Primary antibodies were detected with horseradish peroxidase-conjugated secondary antibodies (P0447 and P0217; Dako). In an indirect immunofluorescence assay primary antibody mouse anti-FLAG (F3165; Sigma-Aldrich) and secondary antibody Alexa488-conjugated goat anti-mouse immunoglobulin G (IgG) antibody (A-11001; Thermo Fisher Scientific) were used.

## Protease activity assays in cell culture

Protease activity assays as described in Bailey-Elkin et al. [327] were performed with slight modifications. Briefly, to assess the DUB activity of MERS-CoV $PL^{pro}$ in the presence of UbVs, HEK293T cells were co-transfected using the calcium phosphate transfection method with plasmids encoding HA-tagged Ub (0.25 µg), MERS-CoV-$PL^{pro}$-V5 (0.2 µg), FLAG-tagged UbVs (0.5; 0.75 or 1 µg, as indicated) and GFP (0.25 µg). In order to establish whether the MERS-CoV-directed UbVs target SARS-CoV $PL^{pro}$, DUB assays were also performed with SARS-CoV-$PL^{pro}$-V5 (0.2 µg) instead of MERS-CoV-$PL^{pro}$-V5. The *in trans* cleavage activity of MERS-CoV $PL^{pro}$ in the presence of UbVs was determined by co-expressing HA-nsp3C-4-V5 (0.2 µg), MERS-CoV-$PL^{pro}$-V5 (0.15 µg), FLAG-tagged UbVs (0.5; 0.75 or 1 µg) and GFP (0.25 µg) in HEK293T cells. Empty pcDNA vector was added to supplement to a total of 2 µg of plasmid DNA transfected per well of a 12-wells cluster. At 18 h post transfection, cells were lysed in 2x Laemmli sample buffer (LSB) containing 25 mM N-ethylmaleimide (NEM; Sigma). Proteins were separated in an SDS-PAGE gel, blotted

onto Hybond-P (0,45 µm pore size, GE-Heathcare) and visualized after antibody incubation steps using Pierce ECL 2 Western blotting substrate (Thermo Fisher Scientific). To visualize FLAG-tagged UbVs, the proteins separated in an SDS-page gel were blotted onto 0,2 µm PVDF membranes (GE-Heathcare). The membranes were blocked with dried milk powder in PBS containing 0,05% Tween-20 followed by antibody incubation steps.

### Luciferase-based IFN-β reporter assay

In a luciferase-based IFN-β reporter assay the effect of the UbVs on the suppression of IFN-β promoter activity by viral $PL^{pro}$s was investigated. HEK293T cells grown to 80% confluency in a 24-wells plate were co-transfected with a combination of plasmids encoding the firefly luciferase reporter gene under control of the IFN-β promoter (25 ng), *Renilla* luciferase (5 ng), innate immune inducer MAVS (25 ng), MERS-CoV $PL^{pro}$-V5 (250 ng) and FLAG-tagged UbVs (250, 500, 750 ng). Alternatively, SARS-CoV $PL^{pro}$-V5 (100 ng) and FLAG-tagged UbVs (750 ng) were co-expressed with firefly luciferase under control of the IFN-β promoter, *Renilla* luciferase and MAVS. Total amounts of transfected DNA were equalized by the addition of empty pcDNA vector. Both firefly and *Renilla* luciferase activities were measured (Mithras LB 940 multimode reader; Berthold Technologies) using the Dual-Luciferase reporter assay system (Promega) 16 h post transfection. After normalizing the firefly luciferase activity to *Renilla* luciferase activity, an unpaired two-tailed Student's *t*-test was performed and p values $<0.05$ were considered statistically significant. Firefly and *Renilla* luciferase activities were measured in triplicate and assays were repeated independently at least three times.

## SUPPLEMENTAL TABLES

**Table S1. Binding affinities of viral proteases and UbVs evaluated by BLI.**

| Ligands | Analytes | $K_D$ |
|---|---|---|
| CCHFV-OTU | CC.1 | 463 ± 44.3 nM |
| | CC.2 | 158 ± 11.2 nM |
| | CC.3 | 453 ± 17.2 nM |
| | CC.4 | 9.0 ± 0.4 nM |
| | CC.5 | 10.4 ± 0.7 nM |
| | CC.4.4 | no binding |
| | CC.4.5 | no binding |
| MERS-CoV $PL^{pro}$ | ME.1 | 19.4 ± 0.7 nM |
| | ME.2 | 53.2 ± 2.2 nM |
| | ME.3 | 15.6 ± 0.4 nM |
| | ME.4 | 35.9 ± 1.6 nM |
| | ME.4.1 | 1030 ± 297 nM |

**Table S2. $EC_{50}$ (Ub/UbV) and $IC_{50}$ (UbV) values to cognate viral DUBs.**

| Ub/UbV | $EC_{50}$ (mean) | 95% confidence intervals | Ub-AMC $IC_{50}$ (nM, mean) | 95% confidence intervals (nM) | ISG15-AMC $IC_{50}$ (nM, mean) | 95% confidence intervals (nM) |
|---|---|---|---|---|---|---|
| **Ub** | 325 **µM** | 290 to 363 | | | | |
| **ME.1** | 0.7 nM | 0.65 to 0.79 | 3.9 | 3.52 to 4.27 | 10.8 | 6.80 to 17.08 |
| **ME.2** | 0.9 nM | 0.77 to 0.93 | 3.0 | 2.14 to 4.24 | 16.4 | 11.94 to 22.57 |
| **ME.3** | 4.5 nM | 3.31 to 6.00 | 13.7 | 10.22 to 18.23 | 88.9 | 47.62 to 165.8 |
| **ME.4** | 0.2 nM | 0.17 to 0.21 | 0.8 | 0.75 to 0.91 | 1.2 | 1.00 to 1.38 |
| **Ub** | 512 **µM** | 475 to 552 | | | | |
| **CC.1** | 50 nM | 42.7 to 58.6 | 770 | 11.97 to 49610 | Out of range | |
| **CC.2** | 8.9 nM | 8.05 to 9.74 | 10.3 | 8.76 to 12.12 | 42.1 | 32.28 to 52.86 |
| **CC.3** | 9.6 nM | 9.28 to 9.98 | 8.8 | 7.32 to 10.52 | 102.4 | 66.26 to 158.1 |
| **CC.4** | 0.9 nM | 0.85 to 0.93 | 3.3 | 2.64 to 4.00 | 10.9 | 7.56 to 15.68 |
| **CC.5** | 35.6 nM | 32.2 to 39.3 | 390 | 230.4 to 659.4 | Out of range | |

Note: In the figures, data are represented as mean ± standard deviation of three independent experiments.

## SUPPLEMENTAL FIGURES

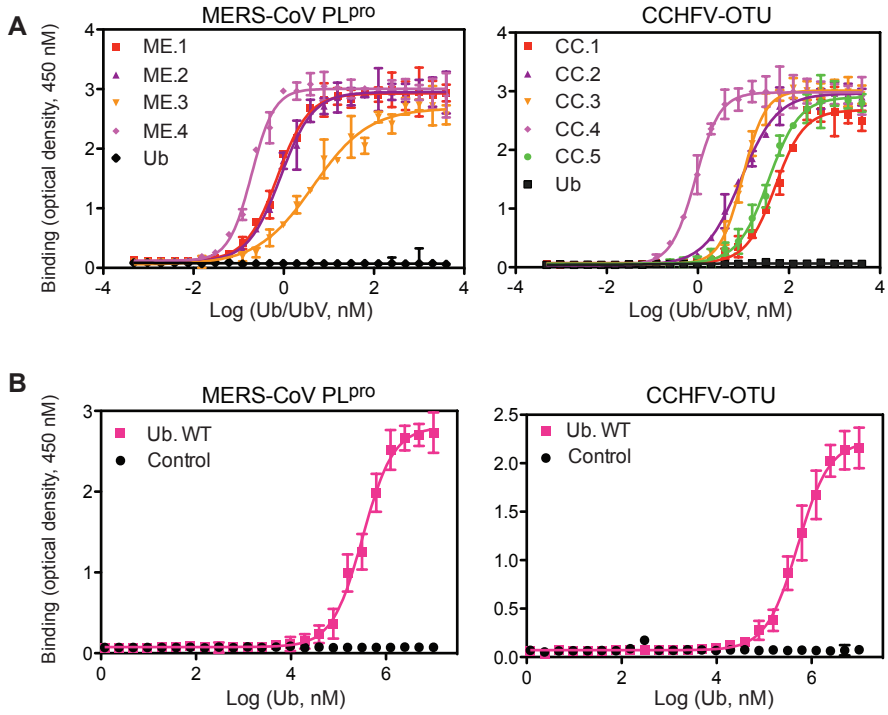


**Figure S1. UbVs bound with high affinity to MERS-CoV PL$^{pro}$ and CCHFV OTU**. (A) Binding curves of UbVs to the cognate viral proteases (left panel: MERS-CoV PL$^{pro}$; right panel: CCHFV OTU), measured by ELISA. The half maximal binding concentrations ($EC_{50}$) of UbVs to indicated vDUBs were determined by established methods [348] and are listed in Table S1. Viral proteases (1 µM) were immobilized in microtiter plates. Serial dilutions of FLAG-tagged UbV or Ub (up to 4 µM, 24 points) were added and incubated for 20 min at room temperature. Wells were washed and bound UbV/Ub was detected by anti-FLAG-HRP conjugate antibody and colorimetric development of TMB peroxidase substrate. The absorbance at 450 nm (y-axis) was plotted against Log (UbV/Ub concentration, nM) (x-axis). Data were presented as the mean ± standard deviation (N = 3). (B) Binding curves of Ub.wt to MERS-CoV PL$^{pro}$ (left ) and CCHFV OTU (right). Experiments were performed as described in (A) except the concentration of Ub was increased (up to 10 mM, 24 serial dilutions). Data were presented as the mean ± standard deviation (N = 3).

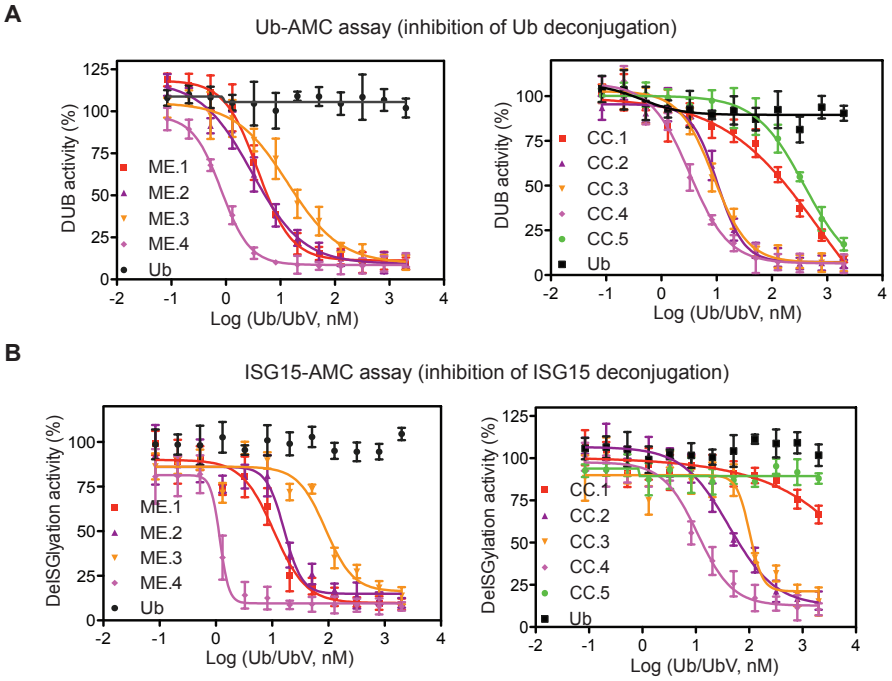


**Figure S2. MERS-CoV PL$^{pro}$ and CCHFV OTU are inhibited by UbVs *in vitro***. (A and B) Inhibition of MERS-CoV PL$^{pro}$ (left) or CCHFV OTU (right) by the cognate UbVs shown as dose-response curves using Ub-AMC (A) or ISG15-AMC (B) as a substrate. The $IC_{50}$ values were determined as the concentrations of UbVs that reduced deubiquitination or deISGylation activity by 50% (Table S1). The wt Ub data obtained in the deISGylation assay cannot be fitted by GraphPad Prism so no lines were shown.

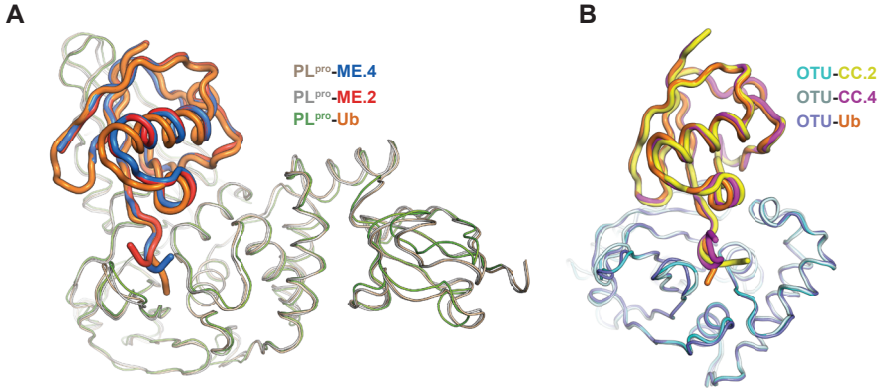


**Figure S3. MERS-CoV- and CCHFV-specific UbVs bind their cognate DUBs in comparable orientations to Ub.wt.** (A) Superposition of the MERS-CoV PL$^{pro}$-Ub.wt, -ME.2 and -ME.4 complexes. PL$^{pro}$ is displayed as ribbons, and coloured in chartreuse, grey and wheat in the PL$^{pro}$-Ub.wt, -ME.2 and -ME.4 structures, respectively. The Ub and UbV structures are displayed as tubes, and coloured in orange, red and marine in the PL$^{pro}$-Ub.wt, -ME.2 and -ME.4 structures, respectively. (B) Superposition of the CCHFV OTU-Ub.wt, -CC.2 and -CC.4 complexes. CCHFV OTU is displayed as ribbons, and coloured in slate, cyan and pale cyan in the CCHFV OTU-Ub.wt, -CC.2 and -CC.4 structures, respectively. The Ub and UbV structures are displayed as tubes, and coloured in orange, yellow and magenta in the CCHFV OTU-Ub.wt, -CC.2 and -CC.4 structures, respectively. Structures were aligned within PyMOL [373].

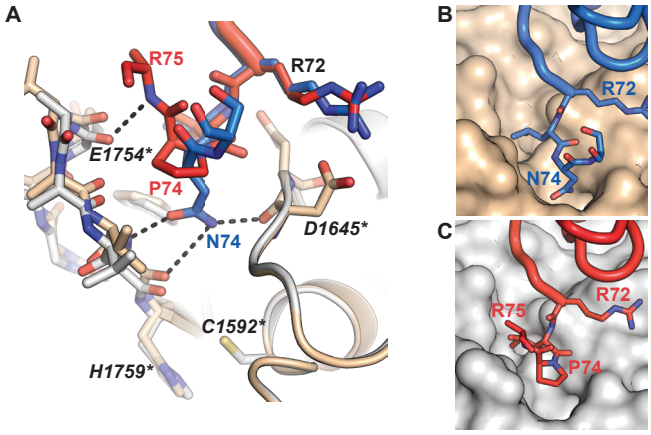


**Figure S4. Comparison of the C-terminal regions of ME.2 and ME.4 in the active site of MERS-CoV PL$^{pro}$.** (A) Superposition of the C-terminal regions of the MERS-CoV PL$^{pro}$-ME.2 and -ME.4 structures. PL$^{pro}$ is coloured in grey and wheat in the MERS-CoV PL$^{pro}$-ME.2 and -ME.4 structures, and ME.2 and ME.4 are coloured in red and marine, respectively. PL$^{pro}$ active site residues H1759 and C1592 are shown as sticks, along with additional PL$^{pro}$, ME.2 and ME.4 residues involved in binding. (B) Close up of the C-terminus of ME.4 in the MERS-CoV PL$^{pro}$-ME.4 complex, with PL$^{pro}$ depicted in a surface representation. (C) Close up of the C-terminus of ME.2 in the MERS-CoV PL$^{pro}$-ME.2 complex, with PL$^{pro}$ depicted in a surface representation.

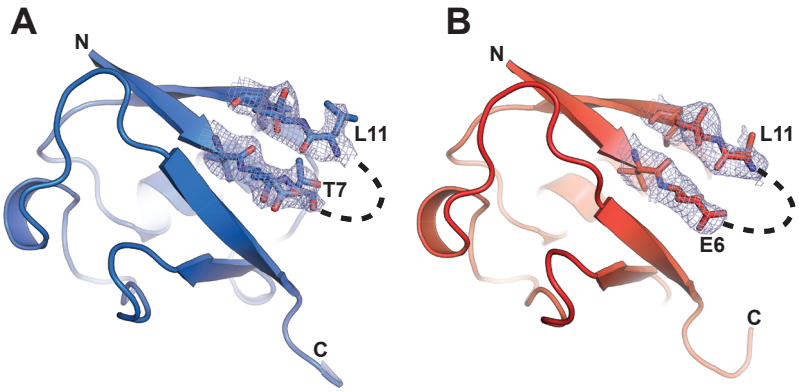


**Figure S5. Residues in the N-terminal β-hairpin of ME.4 and ME.2 are disordered.** (A) Cartoon representation of ME.4 (marine). Dashed line indicates missing residues 8-10 which were not resolved in the electron density maps. A $2F_o$-$F_c$ electron density map is displayed as blue mesh and contoured at 1.0 RMSD. (B) Cartoon representation of ME.2 (red). Dashed line indicates missing residues 7-10. Figure generated with PyMOL [373].

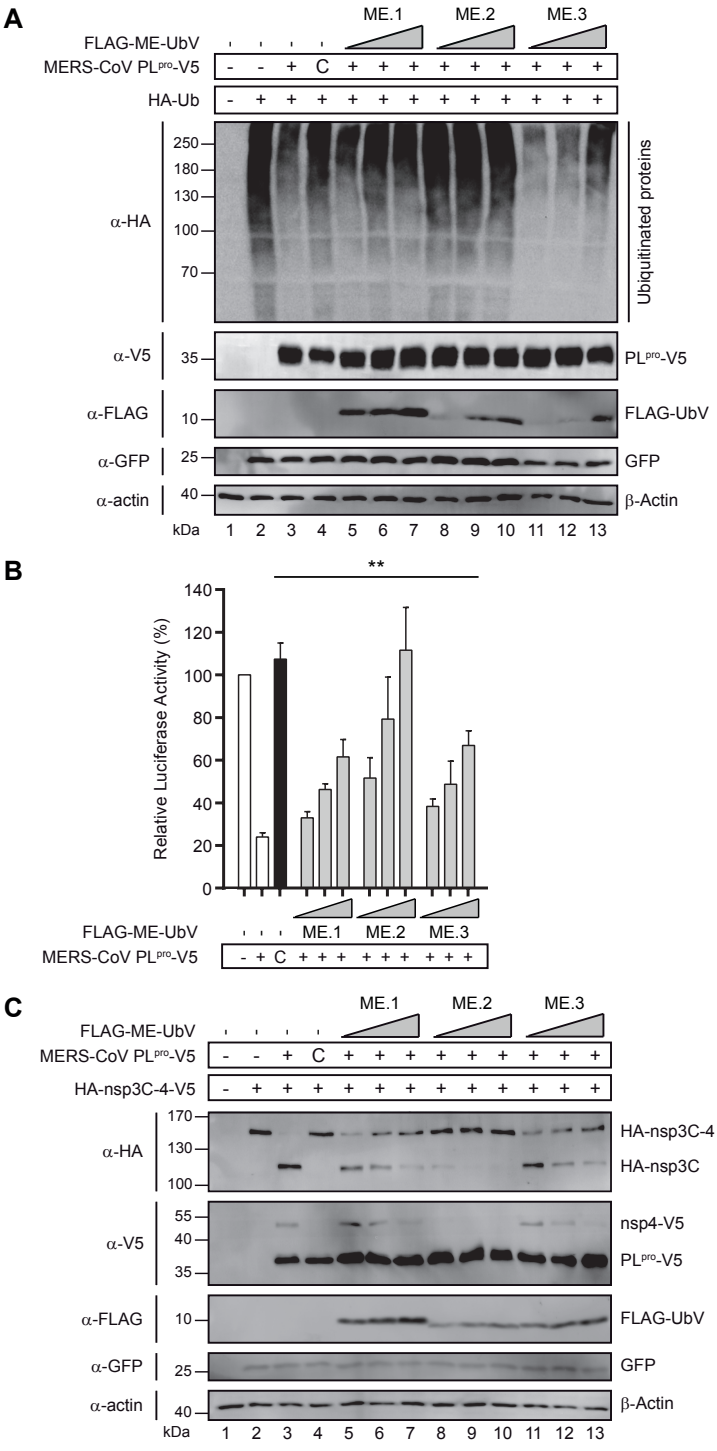
A
ME.1
ME.2
ME.3
FLAG-ME-UbV
MERS-CoV PLpro-V5
HA-Ub
α-HA
Ubiquitinated proteins
α-V5
PLpro-V5
α-FLAG
FLAG-UbV
α-GFP
GFP
α-actin
β-Actin
kDa
B
**
Relative Luciferase Activity (%)
C
HA-nsp3C-4-V5
HA-nsp3C-4
HA-nsp3C
nsp4-V5

**Figure S6. Proteolytic activity of MERS-CoV PL$^{pro}$ is inhibited by UbVs.** (A) Inhibition of MERS-CoV PL$^{pro}$ DUB activity by ME.1, ME.2 and ME.3 was determined by expressing HA-Ub, MERS-CoV PL$^{pro}$-V5 (wild-type or the active site mutant C1592A designated as C), FLAG-ME-UbV (500, 750 or 1000 ng of the appropriate plasmid) and GFP (as a transfection control) in HEK293T cells. After obtaining protein lysates the expressed proteins were separated on a SDS-PAGE gel, blotted and visualized after antibody incubations. (B) Suppression of the IFN-β promoter activity by MERS-CoV PL$^{pro}$ in the presence of UbVs was assessed by transfecting plasmids encoding firefly luciferase reporter gene under control of the IFN-β promoter, *Renilla* luciferase, MAVS, MERS-CoV PL$^{pro}$-V5 (wild-type or the active site mutant C) and FLAG-tagged UbVs (250, 500 or 750 ng). Firefly and *Renilla* luciferase activities were measured 16 h post transfection and significance relative to wild-type without expression of a UbV was calculated using an unpaired two-tailed Student's *t*-test. Significant values were indicated: ** $p<0.01$. Bars represent mean and error bars represent standard deviation (N=3). (C) Proteolytic cleavage capability of MERS-CoV PL$^{pro}$ was assessed in the presence of the UbVs. N-terminally HA-tagged and C-terminally V5-tagged nsp3C-4 (a polyprotein fragment excluding PL$^{pro}$) was co-expressed with MERS-CoV PL$^{pro}$-V5 (wild-type or the active site mutant C), FLAG-ME-UbV (at increasing concentrations) and GFP (as a transfection control). Cells were lysed 18 h post transfection and expressed proteins were analysed by Western blotting.

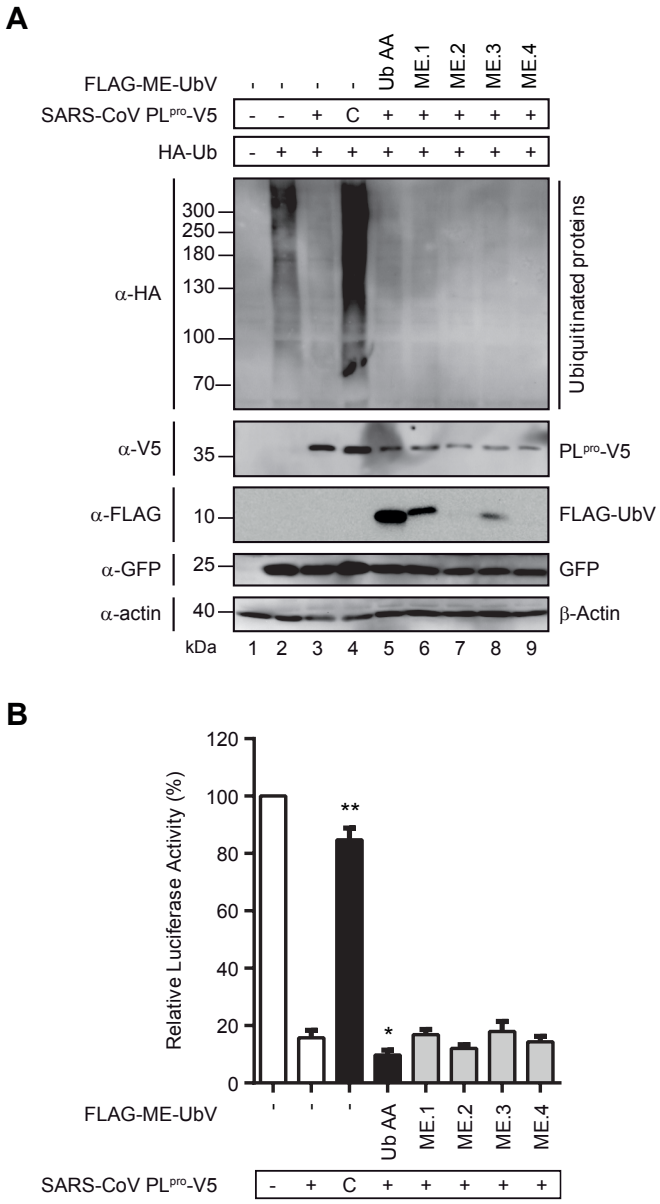


**Figure S7. MERS-CoV-directed UbVs do not inhibit the DUB activity of SARS-CoV PL$^{pro}$.** (A) SARS-CoV PL$^{pro}$'s DUB activity in the presence of UbVs was determined by co-transfecting HEK293T cells with plasmids encoding HA-Ub, SARS-CoV PL$^{pro}$-V5 (wild-type or the active site mutant C1651A designated as C), FLAG-ME-UbV (1000 ng) and GFP (as a transfection control). 18 h post transfection cells were lysed and deconjugation of HA-tagged Ub by SARS-CoV PL$^{pro}$ was visualized via Western blotting. (B) HEK293T cells were transfected with plasmids encoding firefly luciferase reporter gene under control of the IFN-β promoter, *Renilla* luciferase, MAVS, SARS-CoV PL$^{pro}$-V5 (wild-type or the active site mutant C; 100 ng) and FLAG-tagged UbVs (750 ng). Cells were lysed 16 h post transfection and both firefly and *Renilla* luciferase activities were measured. Significance relative to wild-type PL$^{pro}$ without expression of a UbV was measured using an unpaired two-tailed Student's *t*-test; significant values were indicated: ** p<0.01. Bars represent mean and error bars represent standard deviation (N=3).

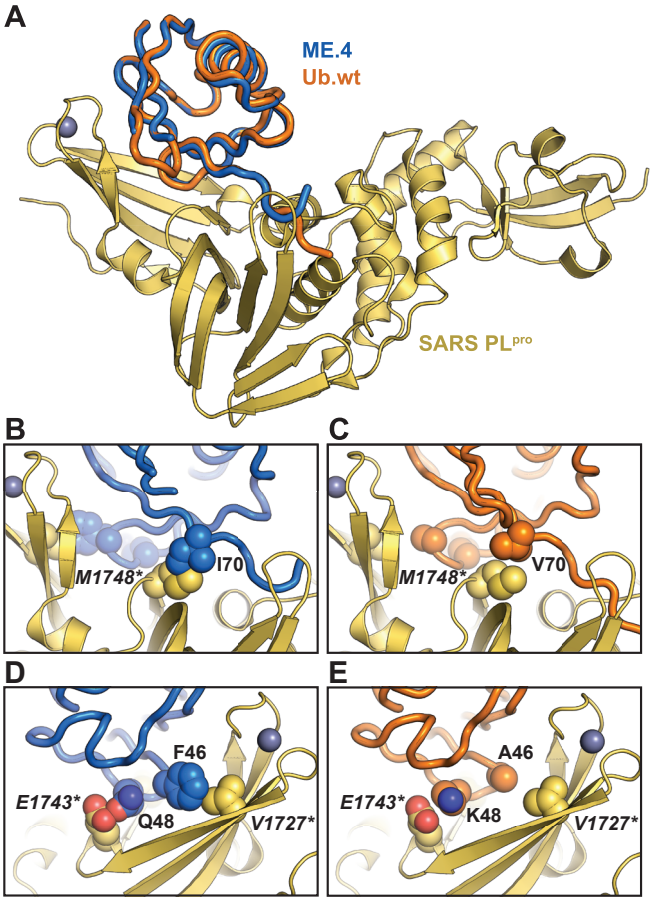


**Figure S8. Structural model of the SARS-CoV PL$^{pro}$ domain bound to the MERS-CoV PL$^{pro}$-specific ME.4.** (A) The SARS-CoV PL$^{pro}$ domain is shown as a cartoon representation (yellow-orange). ME.4 and Ub.wt are shown in tubes (marine and orange, respectively). The ME.4 structure determined herein was superposed over Ub bound to the SARS-CoV PL$^{pro}$ domain (4M0W [297]) (B) Close-up of residue clashes occurring between SARS-CoV PL$^{pro}$ and ME.4. Residues are shown as spheres, with SARS-CoV PL$^{pro}$ residues, numbered according to the SARS-CoV pp1a/ab, indicated with asterisks and in italics. SARS-CoV PL$^{pro}$ residue M1748 clashed with ME.4 residue I70, compared with Ub residue V70 (C). (D) SARS-CoV PL$^{pro}$ residues E1743 and V1727 clash with ME.4 residues Q48 and V188, respectively, compared to Ub.wt residues K48 and A46 (E). Figure generated in PyMOL [373].

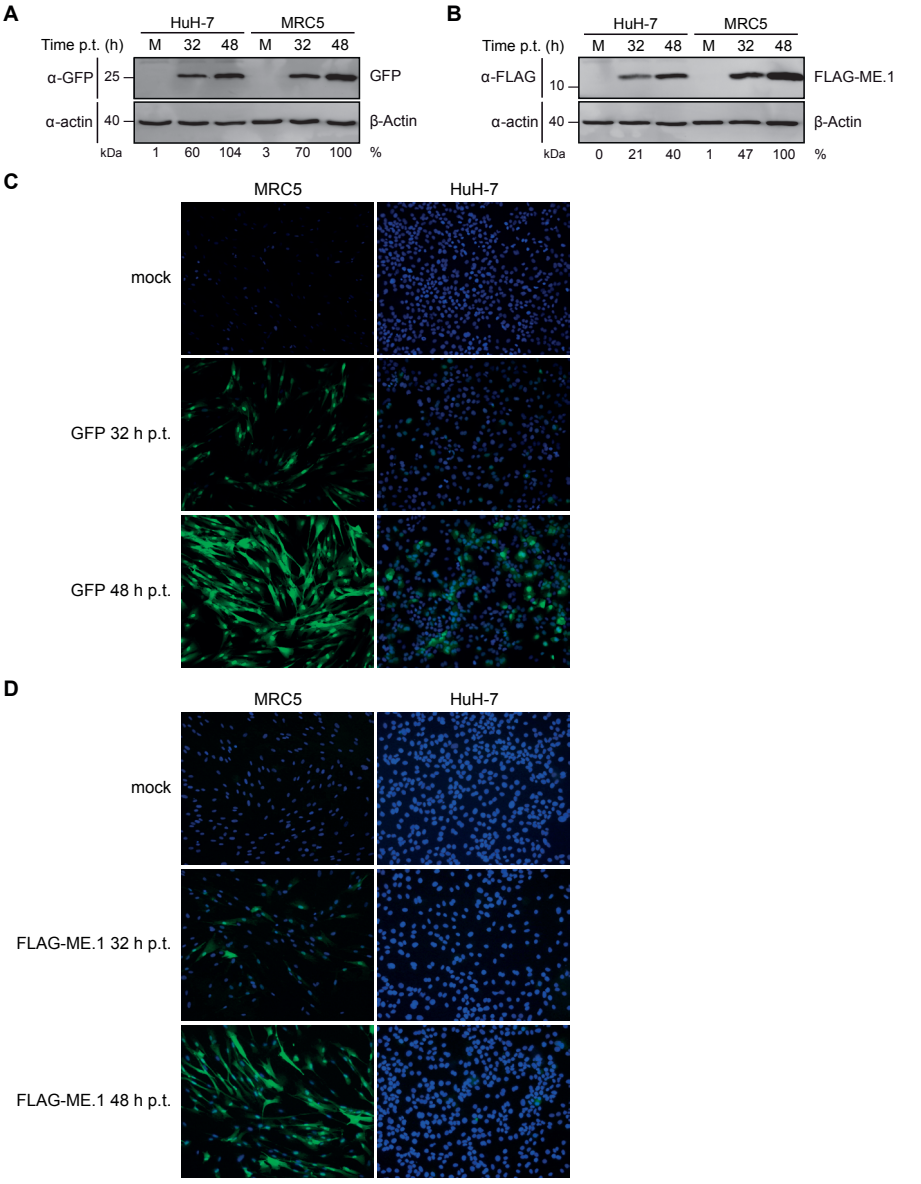


**Figure S9. Analysis of lentivirus transduction of MRC5 and HuH-7 cells.** (A and B) Western blot analysis of transduced MRC5 and HuH-7 cells with lentiviruses encoding GFP (A) or FLAG-ME.1 (B) both 32 h and 48 h pt. As a control cells, were mock transduced (designated as M). Relative expression of GFP and FLAG-ME.1 was quantified and normalized to actin and expression levels in MRC5 cells 48 h pt were set at 100%. (C) GFP transduced MRC5 and HuH-7 cells were fixed 32 h or 48 h pt and nuclear DNA was stained using Hoechst. Images were taken using fixed exposure times for both the GFP and Hoechst signal. (D) Immunofluorescence assay of FLAG-ME.1-transduced MRC5 and HuH-7 cells that were fixed 32 h or 48 h pt. Cells were labelled with a mouse monoclonal antibody recognizing FLAG followed by labelling with a secondary Alexa488-conjugated goat anti-mouse antibody. Exposure times were kept the same for each image.

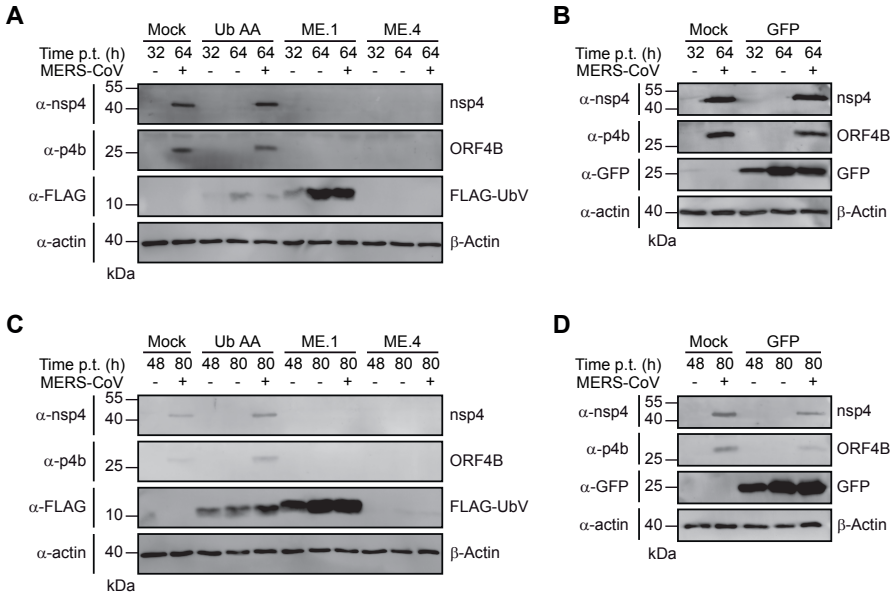


**Figure S10. Western blot analysis of MERS-CoV infection on transduced MRC5 cells shows decreased viral protein production as a result of UbV expression.** Upon collection of supernatants after MERS-CoV infection of transduced MRC5 cells protein lysates were obtained. Expression of two viral proteins was analysed by Western blotting, MERS-CoV nsp4 (using cross-reacting SARS-CoV nsp4 antiserum), and MERS-CoV ORF4B. Lentivirus-induced expression of FLAG-UbVs or GFP was confirmed and actin was used as a loading control. Representative Western blots are shown for transduced MRC5 cells that were infected with MERS-CoV at an MOI of 0.01 either 32 h pt (A and B) or 48 h pt (C and D).

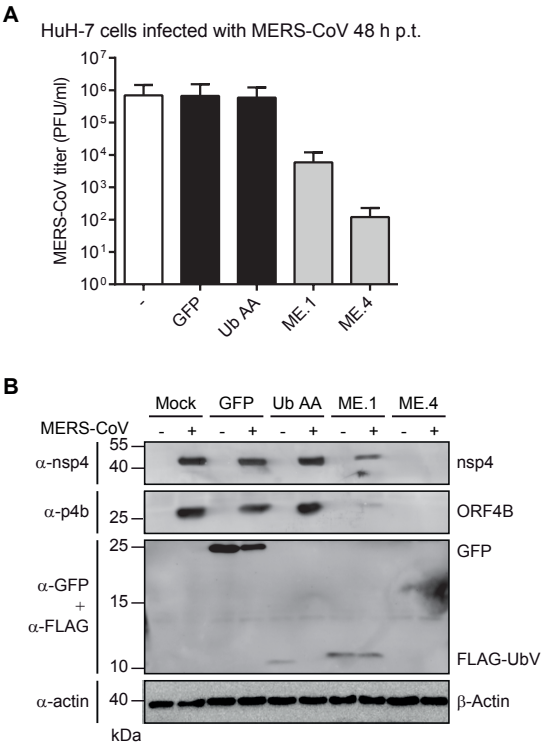


**Figure S11. Titers of MERS-CoV progeny decreased upon infection of HuH-7 cells expressing UbVs.** (A) HuH-7 cells were transduced with lentiviruses encoding FLAG-UbVs or GFP (as control) respectively and 48 h pt these cells were infected with MERS-CoV at an MOI of 0.01. Culture supernatants were collected 32 h post MERS-CoV infection and infectious progeny titers were determined by plaque assays. (B) Lentivirus transduced and MERS-CoV infected HuH-7 cells were 32 h post MERS-CoV infection lysed and expression of MERS-CoV nsp4, MERS-CoV ORF4B as well as expression of FLAG-UbVs or GFP was visualized via Western blotting.

# 5 Engineering improved ubiquitin variants that inhibit the papain-like protease of Middle East respiratory syndrome coronavirus

Robert C.M. Knaap[1], Xavier Martiáñez Vendrell[1], Ben A. Bailey-Elkin[2], Wei Zhang[3], Sachdev S. Sidhu[3], Brian L. Mark[2], Marjolein Kikkert[1]

[1] Department of Medical Microbiology, Leiden University Medical Center, Leiden, The Netherlands
[2] Department of Microbiology, University of Manitoba, Winnipeg, R3T2N2, Canada
[3] Donnelly Centre for Cellular and Biomolecular Research, Banting and Best Department of Medical Research, and Department of Molecular Genetics, University of Toronto, Toronto, M5S3E1, Canada

## ABSTRACT

Human infections with Middle East respiratory syndrome coronavirus (MERS-CoV) can be asymptomatic or lead to mild or even severe disease. About 35% of the diagnosed, hospitalized patients succumb to the infection, which has led to 838 MERS-related deaths by the end of April 2019. Currently there are no approved vaccines or antiviral treatments for this disease. Viral proteases are well-established drug targets and MERS-CoV replication relies on two such proteases for the processing of its two large replicase polyproteins. One of those proteases is a papain-like protease ($PL^{pro}$) that presumably has a secondary role: the binding and subsequent removal of ubiquitin (Ub) and Ub-like proteins from protein targets, in order to limit activation of the host's innate immune response. In previous work, we described an innovative approach for the development of antivirals targeting such deubiquitinating viral proteases, which is based on the selection of Ub sequence variants (UbVs) that bind those enzymes with extremely high affinity and can thus compete with regular substrates for $PL^{pro}$ binding. We identified four such UbVs that inhibit both the activity of individually expressed MERS-CoV $PL^{pro}$ as well as replication of MERS-CoV in cell-based assays. In this study, these original UbVs were characterized in more detail by examining their mutations relative to wild-type Ub. Moreover, we set out to further improve their antiviral activity by modification of specific residues. Although these efforts did not result in higher affinities for $PL^{pro}$ or stronger $PL^{pro}$ inhibition, these studies did reveal that the most active UbV was instable. This problem could be addressed successfully by optimizing the sequence of the N-terminal region, amino acids 1-14, by introducing substitutions in this domain that did not affect binding or inhibition, but increased UbV levels found in cells. The engineering of high-affinity UbVs with enhanced stability will facilitate challenge studies to establish the level of protection that UbVs can provide in an animal model for MERS-CoV infection.

## INTRODUCTION

Coronaviruses (CoVs) can infect humans and a wide variety of animal hosts and have the ability to cause disease, the severity of which in part depends on interactions between the virus and the host species. The potential lethality of CoV infections in humans was first illustrated by the outbreak of severe acute respiratory syndrome (SARS) CoV that started in China in 2002 [9]. More recently, in 2012, another pathogenic CoV emerged in Saudi Arabia [25]. This Middle East respiratory syndrome (MERS) CoV generally causes subclinical to mild disease, but in patients with underlying conditions infection can lead to severe respiratory failure, acute renal impairment and (multi)organ failure. Infections with MERS-CoV are mainly reported in the Arabian Peninsula or are the result of an infected person traveling from that region. The latter scenario applied to a significant MERS-CoV outbreak in South Korea in 2015, involving multiple hospitals and resulting in 186 clinical MERS cases and the death of 38 individuals [28].

Taxonomically, MERS-CoV belongs to clade c of the genus *Betacoronavirus*, together with several bat CoVs [26]. Bats may be the original reservoir of MERS-CoV, as bat CoVs with genome sequences very closely related to that of MERS-CoV have been identified [45, 46]. However, dromedary camels were found to serve as intermediate host, based on high seroprevalence of MERS-CoV-specific antibodies in dromedaries and, interestingly, also in dromedary-exposed individuals [40, 307, 378]. In addition, MERS-CoV could also be isolated from nasal swabs from dromedaries and this virus was able to replicate in human cells [42]. A human MERS-CoV isolate with a high sequence similarity to viruses found in dromedary camels was identified after a patient had been in contact with infected dromedaries, which suggests MERS-CoV transmission occurred between dromedary camels and humans [43, 44, 308]. Most secondary MERS-CoV cases derive from contact with asymptomatic or symptomatic-infected individuals in households and particularly in nosocomial settings [32]. Human-to-human transmission requires a long exposure time, which is why healthcare workers have an increased risk of becoming infected. As spread of the virus among humans is relatively inefficient, MERS-CoV evolution occurs predominantly in dromedaries, which do not develop severe symptoms and efficiently transmit the virus among themselves [379, 380]. The emergence in dromedaries of a MERS-CoV variant with enhanced transmission potential in humans and its subsequent spill-over into the human population would pose a serious pandemic threat. Currently there are no approved vaccines or antiviral therapies to prevent or treat MERS-CoV infection in camels or humans.

MERS-CoV enters the host cell by binding of the viral spike glycoprotein to the cellular receptor dipeptidyl peptidase 4 (DPP4) [79]. After the release of the positive-sense RNA genome, the most 5'-proximal open reading frames (1a and 1ab) are translated by host ribosomes to yield the replicase polyproteins 1a and 1ab, with the latter being a C-terminally extended version of the former, which derives from ribosomal frameshifting. These polyproteins are cleaved into 16 nonstructural proteins (nsps) that together form the viral replication and transcription machinery [381]. Cleavage is performed by two ORF1a-encoded proteases, the papain-like protease ($PL^{pro}$)

located in nsp3 that releases nsp1 to nsp3, and the 3C-like (or 'main') protease in nsp5 that takes care of all remaining cleavages. Besides cleaving the viral replicase polyproteins, MERS-CoV $PL^{pro}$ can bind and cleave the cellular protein ubiquitin (Ub) from protein substrates, making it a deubiquitinating enzyme (DUB) [202, 205, 266]. Additionally, it is also capable of cleaving the Ub-like proteins interferon-stimulated gene 15 (ISG15) and NEDD8, but not small Ub-like modifier (SUMO) from protein targets [202, 382]. SARS-CoV $PL^{pro}$ was the first discovered and characterized CoV DUB that can remove both Ub and ISG15 [196-198, 229]. These properties seem to be conserved among all CoV $PL^{pro}$s [206]. Interestingly, MERS-CoV and SARS-CoV $PL^{pro}$s have different specificities: whereas MERS-CoV $PL^{pro}$ has a broad linkage specificity, SARS-CoV $PL^{pro}$ preferably cleaves K48-linked polyUb chains [207, 234-236]. In CoV-infected cells, $PL^{pro}$ is thought to remove Ub and ISG15 modifications to suppress activation of the innate immune response since Ub plays an important role in activation of the innate immune response and ISG15 has antiviral properties [151, 327, 383]. Crystal structures of MERS-CoV $PL^{pro}$, on its own or in complex with Ub or ISG15, have shed light on the fold of this protease and its specific interactions, and thereby facilitated structure-based drug design [291, 327, 343, 371, 384].

Coronavirus therapeutic targets include the structural spike protein and viral enzymes that play an important role in replication such as the proteases, the RNA-dependent RNA polymerase and the helicase [240]. Attempts to target MERS-CoV $PL^{pro}$ were initially focused on re-employment of small-molecules that previously had been found to inhibit SARS-CoV $PL^{pro}$, but unfortunately these did not cross-react with MERS-CoV $PL^{pro}$ [235, 371]. One reason for this is the structural difference between SARS- and MERS-CoV $PL^{pro}$, particularly at the flexible blocking loop 2, to which the tested inhibitors bind and thereby block the entrance of the active site, in the case of SARS-CoV $PL^{pro}$ [235, 371]. From a high-throughput screen a noncovalent inhibitor was identified that inhibits both viral proteases but in a different manner, acting as a competitive inhibitor of MERS-CoV $PL^{pro}$ but as an allosteric inhibitor of SARS-CoV $PL^{pro}$ [371]. Later it was shown that this compound, F2124-0890 (LifeChemicals), also inhibits other viral and human cysteine proteases but only under non-reducing conditions [385]. In the presence of the reducing agent DTT or in cells, inhibition of SARS- and MERS-CoV $PL^{pro}$ was severely reduced [385]. Together, this indicates that F2124-0890 lacks specificity and potency.

Previously, we employed the knowledge that MERS-CoV $PL^{pro}$ binds Ub and has DUB activity to identify inhibitors that are based on the Ub protein scaffold. Sequence variants of Ub were displayed using phage libraries and Ub variants (UbVs) that bound a particular target most strongly were selected [347, 386]. This approach was used successfully to identify UbVs that can either inhibit or enhance the activity of human DUBs, Ub-conjugating enzymes, Ub ligases and viral DUBs (vDUBs) [348, 387-389]. We demonstrated that selected individual UbVs targeting either MERS-CoV $PL^{pro}$ or the vDUB of the nairovirus Crimean-Congo haemorrhagic fever virus could specifically inhibit the activity of these respective viral proteases [389]. Moreover, intracellular expression of selected UbVs during MERS-CoV infection reduced virus replication quite strongly, highlighting the antiviral power of these UbVs [389]. Here we describe the further characteriza-

tion of these MERS-CoV PL$^{pro}$-specific UbVs and the development of UbVs with improved stability. The generation of a stable UbV that has high affinity for MERS PL$^{pro}$ will facilitate the *in vivo* evaluation of the potential of UbVs as antiviral therapeutics.

## MATERIALS AND METHODS

### Cell culture, antibodies and expression plasmids

HEK293T cells (provided by Dr. Herbert Virgin, Washington University School of Medicine), MRC5 cells (ATCC CCL-171) and Vero cells (ATCC CCL-81) were cultured as described previously [389]. Primary and secondary antibodies used in this study were also described by Zhang et al. [389]. The following expression plasmids were described elsewhere or provided by others: pDONR-221-FLAG-Ub.wt/UbV vectors [389], pcDNA3.1-MERS-CoV-PL$^{pro}$ wild-type (wt) and active site mutant C1592A [327], pCAGGS-MAVS (provided by Dr. N. Frias-Staheli), pLuc-IFN-β [275] and pRL-TK (Promega).

pET53-ME.4-R10G was generated via around-the-horn PCR [390]. UbV-containing pDONR-221 vectors (Thermo Fisher Scientific) were used to modify region 1 of ME.4 to create more stable variants of ME.4. By classical cloning, this region was replaced with region 1 of Ub.wt or ME.1 resulting in the generation of pDONR-221-FLAG-ME.4.Nwt and .N1, respectively. Other amino acid substitutions were introduced using the QuikChange™ strategy with a pDONR-221-FLAG-UbV as a template to develop pDONR-221-FLAG-ME.1.1, -ME.3.1, -ME.4.1, -ME4.2, -ME.4.Nwt.1-3, ME.4.N1.1. The newly generated FLAG-UbVs were cloned into destination vectors pcDNA3.1-DEST or pLenti6.3/TO/V5-DEST (Thermo Fisher Scientific) using the Gateway technology (Thermo Fisher Scientific).

### Protein purification

Protein purification for differential scanning calorimetry (DSC) was performed as previously described [389], and UbVs were flash-frozen in liquid nitrogen. UbVs were dialyzed against PBS (pH 7.4) prior to analysis. Bovine Ub, used as a control, was purchased from Sigma.

For protein thermal shift assays, cultures of *E. coli* BL21 (DE3) Gold cells harbouring UbV encoding plasmids were grown in lysogeny broth supplemented with 150 µg/ml ampicillin at 37°C with aeration to an optical density of 0.8. UbV expression was subsequently induced overnight at 16°C with the addition of IPTG to a final concentration of 1 mM. After centrifugation, the cell pellets were stored at -80°C until use. Cell pellets were resuspended in lysis buffer (50 mM Tris pH 8.5, 500 mM NaCl, 100 µM PMSF, 5 µg/ml DNase) and lysed by sonication. Cell lysates were clarified by centrifugation at 16,100 x g, subsequently His Mag Sepharose Ni resin (GE Healthcare) was added to the clarified lysate and incubated at room temperature for 30 min with end-over-end mixing. His Mag resin was washed with buffer (50 mM Tris pH 8.5, 500 mM NaCl), followed by two

additional wash steps with buffer containing 25 mM imidazole and 50 mM imidazole respectively, before elution of the UbVs in buffer with 250-500 mM imidazole.

### Differential scanning calorimetry analysis of UbVs

DSC curves were collected on a Nano DSC (TA Instruments) with a scan rate of 1°C/min at 304 kPa, using protein concentrations of 2-3.25 mg/ml. Data analysis was performed using NanoAnalyze software, and DSC curves were fit to a two-state scaled model for melting temperature ($T_m$) determination.

### Protein thermal shift analysis of UbVs

Thermal shift assays were performed using 4 µg UbV and a final concentration of 5x SYPRO orange (Sigma). Assays were performed in 96-well format using a StepOnePlus Real-Time PCR System (Applied Biosystems), with a scan rate of 1°C/min. Fluorescence melt curves were fit to a Boltzmann equation with $T_m$ values corresponding to the midpoint of the transition curve using Protein Thermal Shift Software Version 1.1 (Thermo Fisher Scientific). All $T_m$ values are reported as an average of 3 replicates.

### Enzyme-linked immunosorbent assays to evaluate binding

Enzyme-linked immunosorbent assays with immobilized MERS-CoV $PL^{pro}$ as substrate were performed as previously described [389].

### Determination of UbV mRNA and protein levels

HEK293T cells grown to 80% confluency in a 12-well plate were transfected with 1 µg pcDNA3.1-DEST-FLAG-UbV using the calcium phosphate transfection method [289]. At 18 h post transfection, cells were lysed either in 2x Laemmli sample buffer (LSB) containing 25 mM N-ethylmaleimide (NEM; Sigma) to obtain protein samples or in RA1 buffer supplemented with β-mercaptoethanol for total RNA isolation using the NucleoSpin RNA II kit (Machery-Nagel). Protein samples were loaded on SDS-polyacrylamide gels which were blotted onto PVDF membranes (GE-Heathcare) using the semi-dry blotting system (Trans-Blot turbo Transfer System, BioRad). Membranes were blocked with 5% dried milk powder in PBS containing 0.05% Tween-20, followed by antibody incubation steps. Subsequently, the protein bands were visualized using Amersham ECL Plus detection reagent (GE Healthcare). Protein quantification was performed using ImageJ software on Western blots of at least three independent experiments [391]. FLAG-UbV protein levels were normalized to actin that was used as a loading control, Ub.AA was set to 100% and significance relative to ME.1 was calculated using an unpaired two-tailed Student's *t*-test.

Isolated total RNA was treated with DNase (TURBO DNA-free™ Kit, Thermo Fisher Scientific) to ensure removal of DNA contaminants before it was used as a template for cDNA synthesis using RevertAid H minus reverse transcriptase (Thermo Fisher Scientific) and oligo$(dT)_{20}$ primer. Samples were analysed in triplicate by real-time reverse-transcriptase (RT) quantitative (q)

PCR using iTaq SYBR Green Supermix (BioRad) on a CFX384 Touch™ Real-Time PCR Detection System (BioRad). Primers targeting mRNAs encoding human β-actin (Forward (Fwd): 5'-AGGCAC-CAGGGCGTGAT-3'; Reverse (Rev): 5'-GCCCACATAGGAATCCTTCTGAC-3'), neomycin resistance gene (Fwd: 5'-CTCCTGCCGAGAAAGTATCC-3', Rev: 5'-GCTCTTCGTCCAGATCATCC-3') and Ub.wt/UbV (Fwd: 5'-CAGCTGGAAGATGGACGTAC-3', Rev: 5'-CCAGTGTGGTGGAATTCTGC-3') were used. In all PCR runs, a standard dilution series was included and melting-curve analysis was done. PCR efficiencies were determined which allowed quantification using the standard curve method. For relative quantification of UbVs mRNA levels, the results were normalized to the transfection efficiency (derived from expression of the neomycin resistance gene on the plasmid) and to the normalization gene (actin). The normalization gene in the sample set was determined using NormFinder software [331]. Significance relative to ME.1 was determined with an unpaired two-tailed Student's *t*-test.

### Luciferase-based reporter assay for IFN-β promoter activity

Activation of the IFN-β promoter is suppressed by MERS-CoV PL$^{pro}$ [327]. In this assay, the inhibitory effect of UbVs on MERS-CoV PL$^{pro}$ is determined by measuring the luciferase activity that correlates to the level of activation of the IFN-β promoter. HEK293T cells were co-transfected with a combination of plasmids encoding the firefly luciferase reporter gene under control of the IFN-β promoter (50 ng), *Renilla* luciferase (5 ng), innate immunity inducer MAVS (25 ng), MERS-CoV PL$^{pro}$-V5 (250 ng) and FLAG-tagged UbVs (500 ng). At 16 h post transfection, firefly and *Renilla* luciferase activities were measured (EnVision; PerkinElmer) using the Dual-Luciferase reporter assay system (Promega). Firefly and *Renilla* luciferase activities were measured in triplicate and the firefly luciferase activity was normalized to the *Renilla* luciferase activity. Assays were repeated independently at least three times and an unpaired two-tailed Student's *t*-test was performed to determine statistical significance (p values <0.01).

### Lentivirus transduction and MERS-CoV infection

Lentiviruses expressing FLAG-tagged UbVs were produced as previously described [389]. Lentivirus particle titers were measured using the p24 antigen ELISA (ZeptoMetrix). As determined previously using lentiviruses encoding GFP, the amount of lentivirus containing 40 ng of p24 was required to transduce 1x10$^5$ MRC5 cells and get a population in which >90% of the cells expressed GFP [389]. MRC5 cells (1x10$^5$ cells/3.8 cm$^2$) were transduced with lentiviruses encoding GFP or FLAG-UbVs (40 ng of p24), which were diluted in DMEM containing 2% FCS and 8 µg/ml Polybrene (Sigma Aldrich). Protein lysates of transduced MRC5 cells were analysed via Western blotting as described above. Cells were lysed 24 h post transduction (pt) or medium was replaced 24 h pt and cells were lysed by the addition of 2xLSB containing 25 mM NEM at 48 h pt. For MERS-CoV infection experiments, transduced cells were washed once with PBS at 24 h pt and subsequently infected with MERS-CoV at a multiplicity of infection (MOI) of 3. Inocula were prepared in PBS containing 50 µg/ml DEAE-dextran and 2% FCS. After 1 h at 37°C, the inoculum was removed and

cells were washed three times with PBS before Eagle's Minimum Essential Medium (Lonza) containing 2% FCS was added to the cells. Supernatants were harvested after an incubation period of 24 h at 37°C and MERS-CoV titers were determined by plaque assay on Vero cells [389]. MERS-CoV infection experiments were performed independently at least three times and an unpaired two-tailed Student's *t*-test was used to determine significance relative to lentivirus-transduced MRC5 cells expressing Ub.AA. All work with live MERS-CoV was done inside biosafety cabinets in biosafety level 3 facilities at Leiden University Medical Center.

## RESULTS

### Introduction of the V70I substitution does not improve the activity of ME.1 or ME.3

Earlier described UbVs targeting MERS-CoV $PL^{pro}$, ME.1 to .4, contained 12-14 amino acid changes relative to wild-type Ub (Ub.wt), and bound $PL^{pro}$ in the same orientation as Ub.wt but with extremely high affinity [389] (Fig. 1A and 1B). The efficacy of these UbVs as inhibitors of MERS-CoV $PL^{pro}$ in cell culture was convincingly demonstrated, with variant ME.4 being the strongest inhibitor of MERS-CoV $PL^{pro}$ activity, followed by ME.1, ME.2 and ME.3, in this order [389]. Based on structural analysis, mainly four amino acid residues in ME.4, namely F46, Y64, I70 and N74, were predicted to contribute to the enhanced affinity for MERS-CoV $PL^{pro}$ compared to Ub.wt [389]. ME.1 and ME.3 had lower affinity for MERS-CoV $PL^{pro}$ than ME.4, however in these variants the V70I substitution is not present in contrast to the other three substitutions. To determine whether the V70I substitution in the background of ME.1 or ME.3 increases the affinity for MERS-CoV $PL^{pro}$, we generated variants ME.1.1 and ME.3.1, both containing this replacement (Fig. 1A). The binding affinity of these second-generation UbVs was measured as the half maximal effective binding concentration ($EC_{50}$), defined as the UbV concentration required to bind half of the immobilized $PL^{pro}$. For ME1.1, hardly any difference with the original ME.1 was measured, while the V70I substitution in ME.3.1 slightly increased the affinity compared to ME.3 (Fig. 1B).

Upon activation of the innate immune pathway, expression of MERS-CoV $PL^{pro}$ can suppress activation of the IFN-β promoter by virtue of its DUB activity [327]. Using a luciferase reporter assay for IFN-β promoter activity, we showed that ectopically expressed UbVs can inhibit the DUB activity of MERS-CoV $PL^{pro}$ and thus increase the activation of the IFN-β promoter [389]. The second-generation UbVs were tested in this same experimental set-up. An increasing dose of UbVs was previously tested [389], which can be achieved by transfecting different amounts of UbV-encoding plasmids, however here we decided to test a single UbV dose. At this dose, the original UbV did inhibit suppression of the IFN-β promoter but not completely, so that for the new UbVs both an increase or a decrease in IFN-β promoter activation could be measured. Ub.AA was used as a control and, like our UbVs, lacks the C-terminal double glycine residue that is key to isopeptide bond formation during conjugation of Ub.wt. As before, $PL^{pro}$ inhibited activation of the IFN-β promoter upon a MAVS-induced innate immune pathway and expression of the Ub.AA

control did not affect this inhibition (Fig. 1C). ME.4 and ME.2 alleviated suppression of the IFN-β promoter more than ME.1 and ME.3 (Fig. 1C). Despite the different affinities of ME.2 and ME.4 for $PL^{pro}$ (Fig. 1B), these UbVs reduced IFN-β promoter activation to the same level (Fig. 1C). Also, between ME.1 and ME.3 no difference was observed despite their different affinities for $PL^{pro}$ (Fig. 1B and C). Consistent with their minimally changed affinity, ME.1.1 and ME.3.1 blocked the ability of MERS-CoV $PL^{pro}$ to suppress IFN-β promoter activation to the same extent as ME.1 and ME.3, respectively (Fig. 1B and C).

The inhibitory capability of the second-generation UbVs was also tested in the more relevant setting of MERS-CoV-infected cells. To this end, we first transduced MRC5 cells with UbV-expressing lentiviruses. At 24 h pt, the cells were infected with MERS-CoV at an MOI of 3, sufficient to infect 95% of the cells in the first round of a control infection. After an incubation period of another 24 h, cell culture supernatants were harvested and MERS-CoV progeny titers were determined. As controls, virus titers in the medium from MERS-CoV-infected non-transduced cells or MERS-CoV-infected Ub.AA-expressing cells were determined and found to be approximately $10^6$ plaque forming units (PFU) per ml (Fig. 1D). All UbVs reduced the virus progeny titers, in a manner that was consistent with their affinity for MERS-CoV $PL^{pro}$ (Fig. 1B and 1D). The weakest binder, ME.3, reduced the titer by 1-log while expression of ME.4, the strongest binder, reduced the MERS-CoV titer by 3-logs relative to the control infections (Fig. 1B and 1D). Expression of ME.1.1 and ME.3.1 did not significantly alter MERS-CoV progeny titers when compared to ME.1 and ME.3, respectively (Fig. 1D). Nevertheless, in all performed experiments the expression of second-generation UbV variants containing the V70I substitution resulted in slightly lower MERS-CoV titers compared to expression of the parental UbVs. Collectively, our data demonstrated that introduction of the V70I substitution in either ME.1 or ME.3 barely increases the $PL^{pro}$ affinity or inhibitory capability of these UbVs.

As the MERS-CoV infection was started at 24 h pt, we tried to determine UbV expression levels at this timepoint as well, but hardly any protein was detected (data not shown). Transduced but not MERS-CoV-infected MRC5 cells were also lysed at 48 h pt to verify UbV protein expression levels. Strikingly, protein levels for ME.2 and ME.4 were markedly lower compared to the other UbVs and the Ub.AA control at 48 h after transduction, suggesting their relative instability (Fig. 1E, compare lanes 5 and 8 with 2-4, 6 and 7). Besides illustrating the potential of UbVs as antiviral agents, these results suggest that in transduced cells inhibitory UbV levels, capable of effectively reducing the production of progeny virions, are increasing while infection with MERS-CoV is progressing, as was previously observed as well [389].

A

| | Region 1 | | | | | | | | | | Region 2 | | | | | | Region 3 | | | | | | | | | | | | Tail | | |
|---|---|---|---|---|---|---|---|---|---|---|---|---|---|---|---|---|---|---|---|---|---|---|---|---|---|---|---|---|---|---|
| | 2 | 4 | 6 | 8 | 9 | 10 | 11 | 12 | 14 | | 42 | 44 | 46 | 47 | 48 | 49 | 62 | 63 | 64 | 66 | 68 | 70 | 71 | 72 | 73 | 74 | 75 | 76 | 77 | 78 |
| Ub.wt | Q | F | K | L | T | G | K | T | T | | R | I | A | G | K | Q | Q | K | E | T | H | V | L | R | L | R | G | G | | |
| ME.1 | H | L | - | H | - | - | N | - | - | | - | - | F | - | S | - | N | - | Y | - | - | - | - | - | - | N | - | R | K | F |
| ME.1.1 | H | L | - | H | - | - | N | - | - | | - | - | F | - | S | - | N | - | Y | - | - | I | - | - | - | N | - | R | K | F |
| ME.2 | R | - | E | - | R | R | L | - | - | | - | - | F | - | Q | - | V | - | Y | - | - | I | - | - | - | P | R | W | N | - |
| ME.3 | H | L | - | H | - | - | N | - | - | | - | - | F | - | S | - | N | - | Y | - | - | - | - | - | - | N | - | W | N | V |
| ME.3.1 | H | L | - | H | - | - | N | - | - | | - | - | F | - | S | - | N | - | Y | - | - | I | - | - | - | N | - | W | N | V |
| ME.4 | R | - | E | - | R | R | L | - | - | | - | - | F | - | Q | - | V | - | Y | - | - | I | - | - | - | N | S | W | Y | - |

B

| UbV | $EC_{50}$ (nM, mean) | 95% confidence intervals (nM) |
|---|---|---|
| Ub.wt* | $3.25x10^5$ | $2.9x10^5$ to $3.63x10^5$ |
| ME.1* | 0.7 | 0.65 to 0.79 |
| ME.1.1 | 0.8 | 0.56 to 1.03 |
| ME.2* | 0.9 | 0.77 to 0.93 |
| ME.3* | 4.5 | 3.31 to 6.00 |
| ME.3.1 | 3.2 | 2.40 to 4.38 |
| ME.4 | 0.2 | 0.15 to 0.22 |

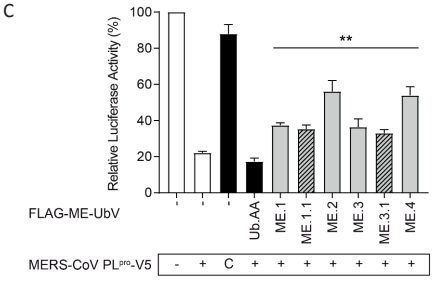


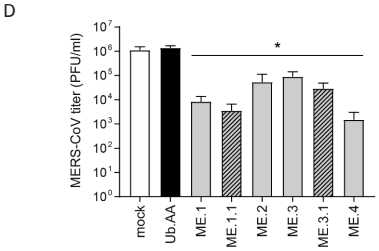


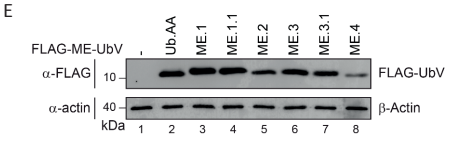


**Figure 1. Introduction of the V70I substitution does not affect the antiviral capability of ME.1 or ME.3.** (A) Sequences of originally selected UbVs (ME.1-ME.4) showing only the regions subjected to diversification relative to Ub.wt in the phage-displayed library. Black boxes indicate the UbV residues that were initially recognized as the main contributors to the increased affinity for MERS-CoV $PL^{pro}$ compared to Ub.wt. Sequence variation introduced into the second-generation UbVs ME.1.1 and ME.3.1 is highlighted in grey. (B) MERS-CoV $PL^{pro}$ was immobilized in microtiter plates to which serial dilutions of FLAG-tagged UbVs were added. Binding affinities of UbVs to $PL^{pro}$ were measured by ELISA and are presented as mean half-maximal effective binding concentrations ($EC_{50}$) with 95% confidence interval of three independently performed measurements. Asterisks indicate previously published results by Zhang *et al*. [389]. (C) In the luciferase-based reporter assay for IFN-β promoter activity, HEK293T cells were transfected with plasmids encoding MAVS, *Renilla* luciferase, firefly luciferase under control of the IFN-β promoter, MERS-CoV $PL^{pro}$ (wt or C1592A indicated as C) and FLAG-Ub.wt/UbVs. Firefly and *Renilla* luciferase activities were measured 16 h post transfection. Data from three independent experiments are presented as the mean (bars) ± standard deviation (error bars). Asterisks indicate a significance difference relative to wild-type $PL^{pro}$ without expression of Ub.AA/UbV (** p<0.01). (D) MRC5 cells were transduced with lentiviruses expressing UbVs or Ub.AA as control. At 24 h pt, transduced cells were infected with MERS-CoV at an MOI of 3. Culture supernatants were harvested 24 h post infection and MERS-CoV titers were determined by plaque assay. Mean (bars), standard deviation (error bars) and statistical significance relative to lentivirus transduced MRC5 cells expressing Ub.AA (* p<0.05) are shown based on at least three independently performed MERS-CoV infection experiments. (E) Lentivirus-transduced MRC5 cells were lysed at 48 h pt and Ub.wt/UbV expression was analysed by Western blotting.

## Instability of UbVs ME.2 and ME.4 is linked to the sequence of their N-terminal domain

Upon expression of UbVs in mammalian cells, either by transfecting equal amounts of UbV-encoding plasmids into HEK293T cells or by transduction at an equal MOI with FLAG-UbV-expressing lentiviruses in MRC5 cells, lower protein levels were observed for ME.2 and ME.4 compared to ME.1, ME.3 and control Ub.AA (Fig. 1E). Moreover, stability differences were also suspected after the observation that ME.1 and ME.3 were markedly more soluble than ME.2 and ME.4 when expressed in *E. coli* (data not shown). Subsequent differential scanning calorimetry (DSC) assays with purified UbVs revealed that ME.1 and ME.3 exhibited a higher $T_m$ (83.7°C and 83.9°C, respectively) than ME.2 and ME.4 (47.5°C and 46.6°C, respectively) (Fig. 2A). This means that a higher temperature was required to unfold ME.1 and ME.3 than ME.2 and ME.4 and also indicates that the former UbVs are more stable.

Comparison of the primary sequences of ME.2 and ME.4 with ME.1 and ME.3 showed that their N-terminal domains contain several differential substitutions, specifically in UbV region 1 (amino acids 1-14; Fig. 1A), one of the three regions of Ub.wt that was mutated in the phage library [347]. We therefore hypothesized that these substitutions could impart UbV instability. Specifically, Ub.wt residue G10 has been replaced with R in ME.2 and ME.4, and this residue is known to be critical for the formation of a G1-type β-bulge at the juncture of strands β1 and β2 of Ub [392]. The crystal structures of ME.2 and ME.4 are lacking electron density in the region representing the Ub β-bulge (residues 8–10 and 7–10 of ME.4 and ME.2, respectively), signifying that this region is unstructured in these UbVs [389]. As a final indication that this β-bulge region may contribute to the instability of ME.2 and ME.4, previous studies on the folding dynamics of Ub have suggested that the hairpin structure formed by strands β1 and β2 constitutes a folding nucleus, representing an ensemble of high-energy folding intermediates during formation of the mature tertiary Ub structure [393].

In order to assess the role of amino acid residue 10 in UbV stability, an R10G mutation was introduced into ME.4, converting this position to the Ub.wt residue. To determine the $T_m$ of ME.4-R10G, thermal shift assays were performed in the presence of the dye Sypro® orange, which fluoresces upon interaction with the hydrophobic core that is exposed upon protein unfolding after heating of the protein [394]. The measured $T_m$ values for ME.2 and ME.4 using this method were 53.3 ± 0.2°C and 51.4 ± 0.2°C, respectively (Fig. 2B and C), which was consistent with the DSC data (Fig. 2A). Thermal shift analysis of ME.4-R10G revealed a $T_m$ of 71.6 ± 0.1°C, demonstrating that the introduction of the R10G mutation stabilized this UbV, increasing the $T_m$ by almost 20°C (Fig. 2D). This value is however still lower than that of Ub.wt, ME.1 or ME.3, indicating that the stability of ME.4 must also be affected by other substitutions, most likely those residing in the β-bulge region. Nevertheless, it does indicate that particularly R10 of ME.4 plays a role in the observed instability of this variant and most likely the same is true for ME.2.

A

| UbV | $T_m$ (°C) |
|---|---|
| Ub.wt | 91,6 |
| ME.1 | 83,7 |
| ME.2 | 47,5 |
| ME.3 | 83,9 |
| ME.4 | 46,6 |

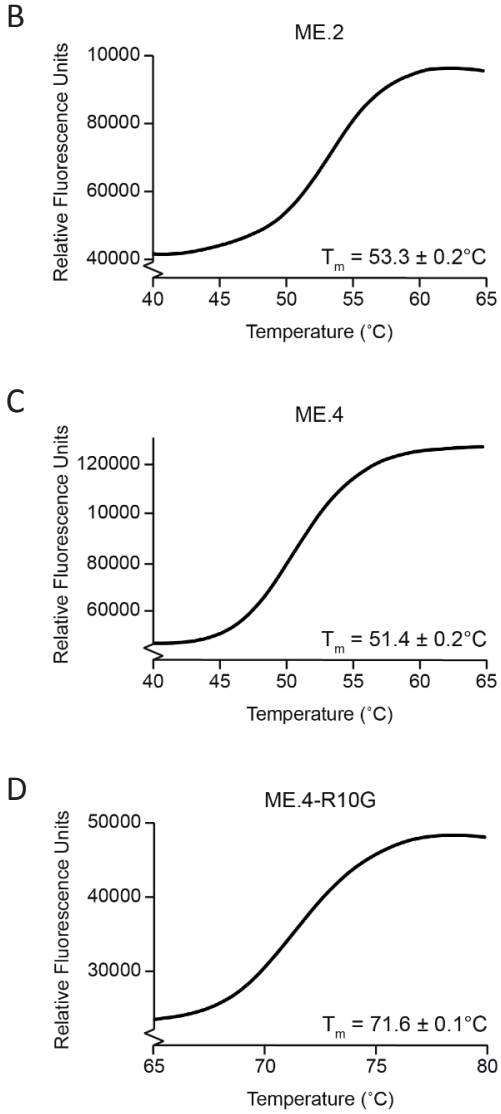


**Figure 2. Partial stabilization of ME.4 by the R10G substitution.** (A) $T_m$ values of UbVs were derived from DSC curves. Data was obtained from a single experiment. (B-D) Melting curves are shown for (B) ME.2, (C) ME.4 and (D) ME.4-R10G. Thermal shift assays were performed in triplicate, and representative curves for each UbV are reported, with the $T_m$ and standard deviations indicated.

### Replacement of region 1 of ME.4 increases its stability in mammalian cells

Region 1 of ME.2 and ME.4 appeared to be uninvolved in PL$^{pro}$ binding [389], suggesting that it should be possible to reverse these mutations in order to stabilize the molecules, while retaining their inhibitory capability. To generate additional second-generation UbVs in this manner, we replaced this N-terminal region 1 of ME.4 by region 1 of Ub.wt or ME.1, generating ME.4.Nwt and ME.4.N1 respectively (Fig. 3A). Expression levels of the newly generated UbVs were determined by transfecting HEK293T with equal amounts of plasmids encoding the different FLAG-tagged UbVs. Cells were lysed 18 h post transfection and protein levels were analysed by Western blotting. Expression of ME.2, ME.4 and ME.4.1 (a variant of ME.4 with substitutions that decrease the affinity for MERS-CoV PL$^{pro}$ as will be discussed below) was markedly lower compared to Ub.AA and the other first-generation variants (Fig. 3B, compare lanes 4, 6 and 7 with 2, 3 and 5). Interestingly, ME.4.Nwt and ME.4.N1 were expressed to higher levels than ME.4, suggesting that the amino acid changes in region 1 of ME.4 influence protein abundance (Fig. 3B, compare lane 6 with 8 and 9). Quantification of the Western blots from at least three independent experiments confirmed that the relative FLAG-UbV protein levels of ME.4.Nwt and ME.4.N1 were higher than that of ME.4 (Fig. 3C). Although stability differences may be the most obvious explanation for these differences, we wanted to rule out effects at the level of transcription of the different UbV constructs. Therefore, the mRNA level was measured for each UbV variant used. Notably, many studies have reported a poor correlation between mRNA and protein abundances, due to the fact that multiple processes and regulatory mechanisms influence the conversion of the mRNA code into protein, for instance the rate of translation [395, 396]. This experiment, however, was solely performed to determine if the observed differences at the protein level were or were not due to major changes at the mRNA level. To this end, RNA was isolated from HEK293T cells that had been transfected with plasmids encoding the different FLAG-tagged UbVs. Next, mRNA levels for each UbV were measured by RT-qPCR and normalized to the mRNA of the household gene actin. To correct for differences in transfection efficiency, we determined the mRNA level of the neomycin resistance gene, which is also present in the expression vector used. Overall, the relative mRNA level derived from each of the UbV constructs was lower compared to that of Ub.AA (Fig. 3D). Interestingly, the least abundant variants (ME.2, ME.4 and ME.4.1) were the ones with the highest relative UbV mRNA levels (Fig. 3D). This again suggests that these variants are less stable and likely have a shorter half-life. ME.4.Nwt and ME.4.N1 had similar relative levels of mRNAs as ME.1 and ME.3 but lower levels than ME.4, while Western blotting revealed higher protein levels, suggesting better stability of these products in mammalian cells. Collectively, these data show that removing the substitutions in region 1 of ME.4 does increase the protein levels in cells.

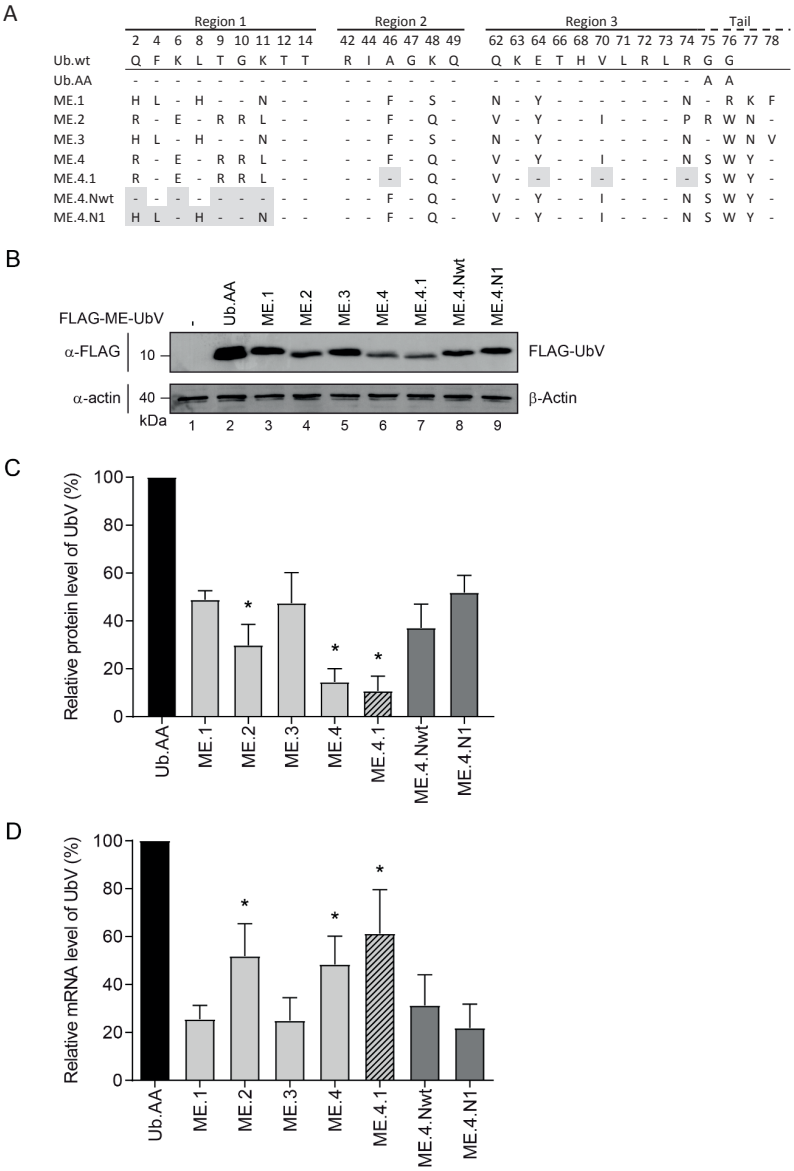


**Figure 3. Replacement of region 1 of ME.4 results in increased protein abundance.** (A) Sequences of the first-generation UbVs and three second-generation UbVs are shown. Only the residues that are different compared to Ub.wt are depicted. Changes in the second-generation UbVs relative to ME.4 are highlighted in grey. (B) HEK293T cells were transfected with plasmids encoding the various FLAG-tagged UbVs. Cells were lysed at 18 h post transfection and UbV expression was visualized by Western blotting. The result of a representative experiment is shown. (C) Relative FLAG-UbV protein levels quantified from Western blots of at least three independent experiments. Error bars indicate the standard deviation and significant relative to ME.1 was determined using an unpaired two-tailed Student's *t*-test (* $p<0.05$). (D) Relative mRNA levels of FLAG-UbVs were determined by RT-qPCR. Measurements were done using total RNA isolated from transfected HEK293T cells that expressed FLAG-tagged UbVs. UbV mRNA levels were normalized to the mRNA of household gene actin and were corrected for the transfection efficiency, using mRNA levels of the neomycin resistance gene that was expressed from the same plasmid as the UbV. Error bars show the standard deviation and asterisks indicate significance relative to ME.1 (* $p<0.05$).

## Affinity and inhibitory effect of stabilized variants of ME.4 are unchanged

Enzyme-linked immunosorbent assays were performed to examine whether modifications in region 1 of the second-generation UbVs affect their intrinsic affinity for MERS-CoV PL$^{pro}$ (Fig. 4A). The observed (in)stability of UbVs in mammalian cells does not play a role in this assay because a concentration range of purified FLAG-tagged UbVs, expressed in *E. coli*, was used to test UbV binding to immobilized PL$^{pro}$. ME.4.Nwt and ME.4.N1 bound strongly to PL$^{pro}$ with an affinity comparable to that of the original ME.4 ($EC_{50}$ of 0.1-0.2 nM; Fig. 4B and 4C). This indicated that changing region 1 of ME.4 did not alter the affinity for PL$^{pro}$ and confirmed that this region is not involved in PL$^{pro}$ binding [389]. Compared to Ub.wt, the F46, Y64, I70 and N74 substitutions in ME.4 were previously predicted to be the main contributors to the enhanced affinity for PL$^{pro}$ [389]. To verify this hypothesis, these residues were now all at once restored to the Ub.wt sequence in ME.4.1, ME.4.Nwt.1 and ME.4.N1.1 (derivatives of ME.4, ME.4.Nwt and ME.4.N1, respectively; Fig. 4A). These UbVs had severely reduced affinity for PL$^{pro}$ ($EC_{50}$ > 715 nM) confirming the importance of these residues (Fig. 4B and 4C).

A

| | Region 1 | | | | | | | | | Region 2 | | | | | | Region 3 | | | | | | | | | | Tail | | |
|---|---|---|---|---|---|---|---|---|---|---|---|---|---|---|---|---|---|---|---|---|---|---|---|---|---|---|---|
| | 2 | 4 | 6 | 8 | 9 | 10 | 11 | 12 | 14 | 42 | 44 | 46 | 47 | 48 | 49 | 62 | 63 | 64 | 66 | 68 | 70 | 71 | 72 | 73 | 74 | 75 | 76 | 77 |
| Ub.wt | Q | F | K | L | T | G | K | T | T | R | I | A | G | K | Q | Q | K | E | T | H | V | L | R | L | R | G | G | |
| ME.4 | R | - | E | - | R | R | L | - | - | - | - | F | - | Q | - | V | - | Y | - | - | I | - | - | - | N | S | W | Y |
| ME.4.1 | R | - | E | - | R | R | L | - | - | - | - | - | - | Q | - | V | - | - | - | - | - | - | - | - | - | S | W | Y |
| ME.4.Nwt | - | - | - | - | - | - | - | - | - | - | - | F | - | Q | - | V | - | Y | - | - | I | - | - | - | N | S | W | Y |
| ME.4.Nwt.1 | - | - | - | - | - | - | - | - | - | - | - | - | - | Q | - | V | - | - | - | - | - | - | - | - | - | S | W | Y |
| ME.4.N1 | H | L | - | H | - | - | N | - | - | - | - | F | - | Q | - | V | - | Y | - | - | I | - | - | - | N | S | W | Y |
| ME.4.N1.1 | H | L | - | H | - | - | N | - | - | - | - | - | - | Q | - | V | - | - | - | - | - | - | - | - | - | S | W | Y |

B

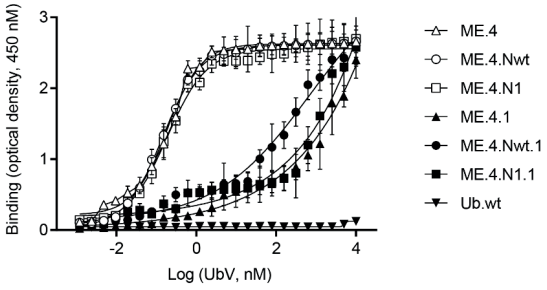


C

| UbV | $EC_{50}$ (nM, mean) | 95% confidence intervals (nM) |
|---|---|---|
| ME.4 | 0.2 | 0.15 to 0.22 |
| ME.4.1 | Out of range | |
| ME.4.Nwt | 0.1 | 0.13.to 0.16 |
| ME.4.Nwt.1 | 715 | 118 to 4322 |
| ME.4.N1 | 0.2 | 0.15 to 0.23 |
| ME.4.N1.1 | Out of range | |

**Figure 4. Analysis of the affinity of second-generation UbVs derived from ME.4 for PL$^{pro}$.** (A) Overview of second-generation UbVs with changes relative to ME.4 highlighted in grey. Critical residues that largely contribute to the enhanced affinity for MERS-CoV PL$^{pro}$ relative to Ub.wt are indicated in black boxes. (B) Binding curves of UbVs to immobilized MERS-CoV PL$^{pro}$ were measured by ELISA. Data is presented as the mean ± standard deviation from three independent experiments. (C) Mean $EC_{50}$ values of the UbVs derived from ME.4 with 95% confidence interval, from three independently performed experiments.

The luciferase-based reporter assay for IFN-β promoter activity, described above, was also used to analyse the inhibitory capability of the stabilized ME.4 variants. Expression of ME.4 did alleviate the $PL^{pro}$-driven suppression of IFN-β promoter activity, whereas expression of the second-generation UbVs ME.4.Nwt and ME.4.N1 had less of an effect (Fig. 5A). Variants with reduced binding affinity (ME.4.1, ME.4.Nwt.1 and ME.4.N1.1) did marginally affect $PL^{pro}$-mediated suppression of the IFN-β promoter (Fig. 5A). These experiments established that ME.4.Nwt.1 and ME.4.N1.1 were less effective in counteracting the DUB activity of $PL^{pro}$ in mammalian cells, an observation at odds with the binding affinities measured *in vitro* (Fig. 4C).

To verify the inhibitory effect of the stabilized ME.4 variants once more, experiments were performed in a more relevant setting than an overexpression system. To this end, MRC5 cells were transduced with lentiviruses to induce the expression of stabilized ME.4 variants and these cells were subsequently challenged with MERS-CoV, after which progeny virus titers were determined. Expression of ME.4, ME.4.Nwt and ME.4.N1 lowered the MERS-CoV titers with 3 to 3.5 orders of magnitude compared to titers from MERS-CoV-infected controls that were non-transduced or Ub.AA-expressing MRC5 cells (Fig. 5B). However, no significant difference was measured between ME.4 and the two stabilized ME.4 derivatives (Fig. 5B). When using the UbVs in which critical residues for binding to $PL^{pro}$ had been replaced, the inhibitory effect was abolished completely, as the MERS-CoV titers released from cells expressing ME.4.1, ME.4.Nwt.1 and ME.4.N1.1 were comparable to those of the controls (Fig. 5B). Transduced but not MERS-CoV-infected MRC5 cells were lysed at 48 h pt to analyse UbV protein expression levels. Similar to what had been observed before in HEK293T cells, ME.4.Nwt and ME.4.N1 were more abundantly present than ME.4 (Fig. 5B, compare lanes 3, 5 and 7). In conclusion, the stabilized variants of ME.4 reach higher protein expression levels in mammalian cells and have the same affinity for $PL^{pro}$ as the original ME.4, but under the conditions tested we did not observe stronger inhibition of MERS-CoV infection when comparing ME.4 and its stabilized derivatives.

## Substitutions at positions 48 and 62 of ME.4 are important for its affinity for MERS-CoV $PL^{pro}$

F46, Y64, I70 and N74 in ME.4 are important for the enhanced binding to MERS-CoV $PL^{pro}$ compared to Ub.wt as demonstrated above. This is further corroborated by results obtained with ME.4.Nwt.2. In this variant, N74 was mutated back to the residue present in Ub.wt, resulting in a decrease of its affinity by approximately 4.5-fold relative to ME.4.Nwt (Fig. 6A and 6B). Vice versa, when N74 was the only mutation present, as in UbV ME.4.2, the binding affinity was increased compared to ME.4.1 in which all four positions are identical to the Ub.wt sequence (Fig. 6A and 6B).

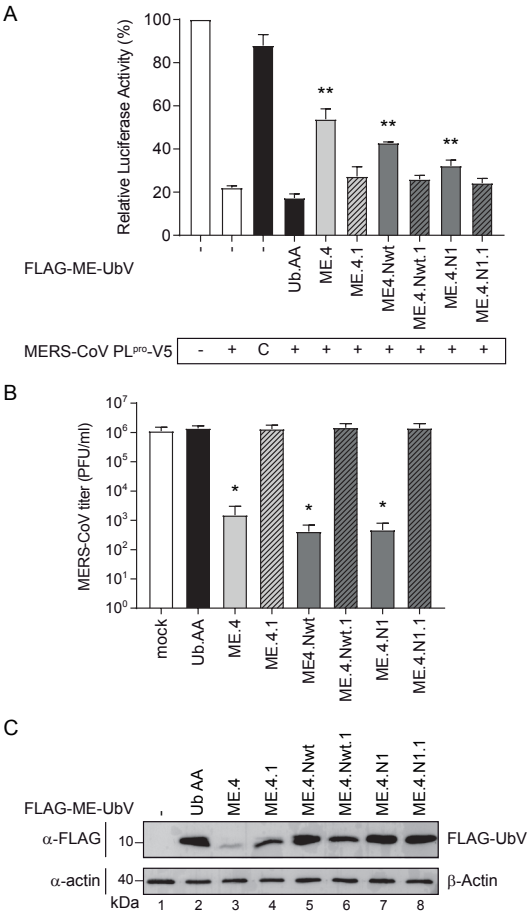


**Figure 5. Analysis of the inhibitory effect of second-generation UbVs derived from ME.4.** (A) UbVs were tested in the luciferase-based reporter assay for IFN-β promoter activity. Relative luciferase expression was measured in three independent experiments. Bars represent mean, error bars represent standard deviation, and using an unpaired two-tailed Student's *t*-test significance relative to wild-type PL$^{pro}$ without expression of Ub.AA/UbV was determined (** p<0.01). (B) First-generation ME.4 and stabilized second-generation derivatives of ME.4 were expressed in MRC5 cells using lentivirus expression vectors. At 24 h pt, these cells were challenged with MERS-CoV and MERS-CoV titers were measured 24 h later. Mean MERS-CoV progeny titers (bars) with standard deviation (error bars) are shown. Asterisks indicate a significance difference relative MRC5 cells expressing Ub.AA (* p<0.05). (C) Western blot analysis to examine lentivirus-induced expression of UbVs in MRC5 cells 48 h pt.

Interestingly, in all four first-generation UbVs amino acid residues 48 and 62 differed from the Ub.wt sequence, with K48S and Q62N in ME.1 and ME.3 and K48Q and Q62V in ME.2 and ME.4 (Fig. 1A). To investigate if these substitutions play a role in $PL^{pro}$ binding, these two amino acids were changed into the Ub.wt residues in variant ME.4.Nwt.3 (Fig. 6A). Due to this double substitution, the $EC_{50}$ value of this UbV increased by approximately 10-fold compared to ME.4.Nwt, indicating a lower affinity for $PL^{pro}$ and establishing the importance of these substitutions for UbV binding (Fig. 6B). To investigate the molecular basis of this finding, the crystal structures of MERS-CoV $PL^{pro}$ in complex with Ub and ME.4 were examined closely at these positions [389]. The K48Q substitution in ME.4 likely influences binding by two mechanisms (Fig. 6C). First, the size and flexibility of the sidechain are lowered, which reduces the entropic penalty of binding. Larger flexible side chains can exist in more conformations than smaller side chains, and if binding requires the side chain to be confined to a specific conformation, this restriction is associated with a decrease in entropy, which is unfavourable. Therefore, the presence of the original lysine at position 48 is less favourable than the smaller and less flexible glutamic acid. Second, the K48Q replacement relieves charge repulsion by removing a positive charge (K48 in Ub) that is positioned close to a positively charged residue in $PL^{pro}$ (K1686). The benefits of the Q62V substitution in this respect are less obvious, although it seems that the hydrophobic V62 has a tighter association with the non-polar region of Q1708 in MERS-CoV $PL^{pro}$ (Fig. 6D). The inclusion of a hydrophobic residue on the surface of ME.4 may make it energetically more favourable for the residue (as part of an interface) to associate, as opposed to remaining surface exposed. Collectively, these results demonstrate the importance of the substitutions at residues 48 and 62 in ME.4 for the binding of this UbV to MERS-CoV $PL^{pro}$.

## DISCUSSION

Previously, screening of a phage-displayed library yielded four UbVs that bound MERS-CoV $PL^{pro}$ with high affinity and strongly inhibited the activity of this protease [389]. The highly conserved Ub sequence is considered to constitute a highly stable protein, however, mutations like those present in our selected UbVs could reduce protein stability. Combinations of substitutions in Ub may for example disrupt its fold and therefore cause stability problems. Our current results demonstrate that purified ME.2 and ME.4, exhibited reduced thermostability when compared to Ub.wt (Fig. 2). Moreover, upon expression in mammalian cells, lower levels of ME.2 and ME.4 were detected compared to Ub.wt, ME.1 and ME.3 (Fig. 3). Despite its low levels, ME.4 was the strongest MERS-CoV $PL^{pro}$ inhibitor that we have found [389], illustrating its high potential as an antiviral agent. Our efforts aimed to increase the relative (thermo)stability of ME.4 to facilitate the further characterization of this variant as a MERS-CoV-specific antiviral option. The sequence differences between ME.1 and ME.3, both stable UbVs, and ME.2 and ME.4, mainly map to UbV region 1, which comprises amino acids 1-14. Replacement of the entire first region with either

A

| | Region 1 | | | | | | | | | Region 2 | | | | | | Region 3 | | | | | | | | | | | Tail | |
|---|---|---|---|---|---|---|---|---|---|---|---|---|---|---|---|---|---|---|---|---|---|---|---|---|---|---|---|
| | 2 | 4 | 6 | 8 | 9 | 10 | 11 | 12 | 14 | 42 | 44 | 46 | 47 | 48 | 49 | 62 | 63 | 64 | 66 | 68 | 70 | 71 | 72 | 73 | 74 | 75 | 76 | 77 |
| Ub.wt | Q | F | K | L | T | G | K | T | T | R | I | A | G | K | Q | Q | K | E | T | H | V | L | R | L | R | G | G | |
| ME.4 | R | - | E | - | R | R | L | - | - | - | - | F | - | Q | - | V | - | Y | - | - | I | - | - | - | N | S | W | Y |
| ME.4.1 | R | - | E | - | R | R | L | - | - | - | - | - | - | Q | - | V | - | - | - | - | - | - | - | - | - | S | W | Y |
| ME.4.2 | R | - | E | - | R | R | L | - | - | - | - | - | - | Q | - | V | - | - | - | - | - | - | - | - | N | S | W | Y |
| ME.4.Nwt | - | - | - | - | - | - | - | - | - | - | - | F | - | Q | - | V | - | Y | - | - | I | - | - | - | N | S | W | Y |
| ME.4.Nwt.2 | - | - | - | - | - | - | - | - | - | - | - | F | - | Q | - | V | - | Y | - | - | I | - | - | - | - | - | - | - |
| ME.4.Nwt.3 | - | - | - | - | - | - | - | - | - | - | - | F | - | - | - | - | - | Y | - | - | I | - | - | - | N | S | W | Y |

B

| UbV | EC$_{50}$ (nM, mean) | 95% confidence intervals (nM) |
|---|---|---|
| ME.4 | 0.2 | 0.15 to 0.22 |
| ME.4.1 | Out of range | |
| ME.4.2 | 313.8 | 186.0 to 529.4 |
| ME.4.Nwt | 0.1 | 0.13.to 0.16 |
| ME.4.Nwt.2 | 0.7 | 0.51 to 0.90 |
| ME.4.Nwt.3 | 1.5 | 0.86 to 2.65 |

C

D

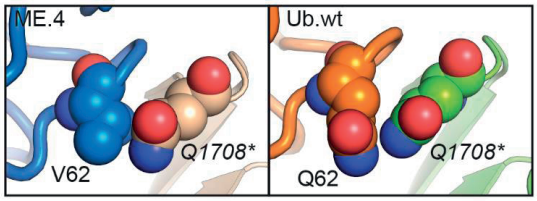


**Figure 6. Identification of ME.4 residues that are important for its high binding affinity.** (A) The sequence of ME.4 and additional variants are shown. Substitutions are indicated in grey boxes whereas the predicted critical residues that promote favourable interaction contacts with MERS-CoV PL$^{pro}$ are highlighted in black boxes [389]. (B) From three independent ELISAs, mean EC$_{50}$ values and 95% confidence intervals were obtained. (C and D) Crystal structures of MERS-CoV PL$^{pro}$-ME.4 (PDB ID: 5V69) and the MERS-CoV PL$^{pro}$-Ub.wt complex (PDB ID: 4RF0) were used to show detailed interactions between PL$^{pro}$ and ME.4/Ub. MERS-CoV PL$^{pro}$ is coloured in wheat and chartreuse for the PL$^{pro}$-ME.4 and -Ub.wt complexes, respectively, PL$^{pro}$ residues are labelled in italics with asterisks and numbered according to the MERS-CoV polyprotein. ME.4 and Ub.wt were shown as tubes and coloured in marine and orange, respectively. (C) Close-up of the MERS-CoV PL$^{pro}$-ME.4 complex (left panel) showing detailed interactions between PL$^{pro}$ and residue Q48 of ME.4 (shown as sticks), and a comparison (right panel) of the same region in the PL$^{pro}$-Ub.wt complex. (D) Close-up of the MERS-CoV PL$^{pro}$-ME.4 complex (left panel) showing detailed interactions between PL$^{pro}$ and residue V62 of ME.4, and a comparison (right panel) of the same region in the PL$^{pro}$-Ub.wt complex. For a clearer representation, the involved residues of PL$^{pro}$ and ME.4/Ub.wt were shown as spheres. Figures were generated using PyMOL [373].

the Ub.wt sequence or the sequence of region 1 as present in ME.1 resulted in higher protein abundance, despite lower mRNA levels, upon expression of these UbVs in mammalian cells (Fig. 3). To obtain direct proof that these second-generation UbVs are indeed more stable in mammalian cells, a pulse-chase metabolic labelling approach could be used to assess UbV turn-over. It would be interesting to perform this assay in the presence or absence of MG132, a proteasome inhibitor. To confirm its instability and determine whether proteasomal degradation of ME.4 is faster than for ME.4.Nwt and ME.4.N1, possibly due to folding problems caused by the substitutions in region 1 of ME.4.

The second aim of the research described here was to characterize the original UbVs by studying their substitutions relative to Ub.wt. Based on the crystal structures of $PL^{pro}$ in complex with ME.4, it was predicted that substitutions A46F, E64Y, V70I and R74N in ME.4 could be responsible for the high affinity for $PL^{pro}$ [389]. This was confirmed by reversing these substitutions, yielding UbVs with severely reduced affinities that were no longer able to block MERS-CoV infection (Fig. 4 and 5). Interestingly, ME.1 and ME.3 contained three of these important substitutions but lacked the V70I change. The benefits of adding the V70I substitution in those two originally selected UbVs were minor (Fig. 1), demonstrating that it is hard to improve their affinity. This raises the question whether the affinity of the original UbVs can be further increased beyond what had been obtained during screening of the original UbV phage display library. In five rounds of selection, the four strongest binders to $PL^{pro}$ had been isolated from a library of over 7 billion UbVs, in which only residues that could interact with DUBs were varied [347]. An important characteristic of the selected UbVs is that changes leading to their high binding affinity are located across the binding surface for $PL^{pro}$ [389]. Together, this might suggest that optimal UbVs were selected but more efforts should be made to confirm this statement.

Important differences compared to conventional methods to screen and develop small-molecule inhibitors that target $PL^{pro}$ are also outlined in the previous paragraph. In comparison, the most successful inhibitors targeting SARS-CoV $PL^{pro}$ were identified from a high-throughput screen, with only 50,000 compounds [397]. The initial hits were subsequently optimized to improve their affinity with medicinal chemistry using co-crystal structures [342, 397]. Interestingly, inhibitors were shown to inhibit activity of SARS-CoV $PL^{pro}$ but not of MERS-CoV $PL^{pro}$ because the compounds bind to a non-conserved region of $PL^{pro}$ [235].

The four first-generation UbVs all have different affinities for $PL^{pro}$ despite sharing three of the four above-mentioned substitutions that, in the case of ME.4, were demonstrated to be responsible for the high affinity for $PL^{pro}$. This indicates that also other sequence changes in the UbVs must contribute to their affinity. A role for the substitutions in UbV region 1 can be ruled out because the binding affinities of ME.4, ME.4.Nwt and ME.4.N1 were comparable (Fig. 4). Consequently, the responsible changes must involve amino acid positions 48 and/or 62, and/or the tail region of the UbV. This is supported by results obtained with ME.4.Nwt.3, in which the substitutions at positions 48 and 62 were reverted to the Ub.wt sequence in the background of ME.4.Nwt, which strongly reduced the affinity for $PL^{pro}$, as evident from a 10-fold increase of the $EC_{50}$ value (Fig. 6).

In-depth analysis of previously determined crystal structures revealed that these substitutions in the ME.4 increase $PL^{pro}$-binding, by increasing hydrophobic interactions, reducing charge repulsion and reducing the entropic penalty of ME.4 binding. The amino acid changes at positions 48 and 62 in ME.1 and ME.3 are different compared to ME.2 and ME.4, which could make a difference in the affinity for $PL^{pro}$. Furthermore, the affinity differences observed between ME.2 and ME.4 as well as between ME.1 and ME.3 must result from substitutions in the UbV tail region, as this is the only part that differs between those sets of UbVs. To gain more insight into the differences in UbV affinity, the substitutions should be reversed one-by-one to determine what the exact contribution of each of these substitutions is. In summary, it is clear that the substitutions in regions 2, 3 and the tail region all contribute to the enhanced $PL^{pro}$-binding of the selected UbVs relative to Ub.wt, although likely to a different extent.

The UbV affinity for $PL^{pro}$ can be correlated to the degree of inhibition when UbVs are expressed during a MERS-CoV infection (Fig. 1B, 1D, 4 and 5B). However, this may not be entirely true for all UbVs as lower protein abundance of ME.2 and ME.4 might play a role in the MERS-CoV infection experiment, as will be elaborated below. In contrast, the same correlation was definitely not observed in the luciferase-based reporter assay for IFN-β promoter activity. There was no difference between ME.1 and ME.3 as well as between ME.2 and ME.4, although the individual UbVs within these two sets have clearly different binding affinities (Fig. 1B and C). Likewise, ME.4, ME.4.Nwt and ME.4.N1 had similar binding affinities but alleviated IFN-β promoter suppression to a different extent (Fig. 4C and 5A). Furthermore, ME.1 had a higher affinity than ME.2 but alleviated IFN-β promoter suppression by $PL^{pro}$ to a lesser extent than ME.2 (Fig. 1B and C). When using this reporter assay, we assumed that UbVs only inhibit the DUB activity of MERS-CoV $PL^{pro}$, which is key to preventing the activation of the IFN-β promoter, however this was not consistently observed. In this assay, the affinity of the UbVs for $PL^{pro}$ was variable but based on the other experiments we observed that also the UbV mRNA and protein levels differed (Fig. 3). The latter variations and the inconsistent results are the reason that the results of this IFN-β promoter assay should be interpreted with caution. As an alternative, induction of IFN-β expression could be measured through RT-qPCR in other cell-based overexpression systems. This would rule out artefacts associated with the specific set-up of the reporter assays used above to measure $PL^{pro}$ DUB activity and its inhibition by UbVs.

As anticipated, changing region 1 in ME.4 did not affect the binding for $PL^{pro}$ of the second-generation UbVs (ME.4.Nwt and ME.4.C1; Fig. 4). Despite their higher protein abundance upon lentivirus-induced expression in MRC5 cells, no significant difference in inhibition of MERS-CoV infection was measured compared to ME.4 (Fig. 5B). Initially, when designing the infection experiment, we made changes compared to the previously published experiment [389]. The time pt was shortened from 48 h to 24 h, to have less UbV present at the time of the MERS-CoV infection and reduce inhibition. Furthermore, the transduced cells were infected with MERS-CoV at an MOI of 3 instead of 0.01, so that a single-cycle infection could be analysed. This resulted in higher MERS-CoV progeny titers upon expression of ME.4, with $10^3$ PFU/ml being retrieved now while

earlier almost no MERS-CoV was recovered (Fig. 1) [389]. Lentivirus transduction leads to CMV promoter-driven UbV expression that results in a strong expression of UbVs in the cell, which inhibits MERS-CoV replication, the extent of which depends on the affinity of the UbV for $PL^{pro}$ and the UbV protein abundance. A possible explanation for the fact that no difference was observed between ME.4 and the stable derivatives of ME.4, is that UbV protein abundance did not play a role in this experiment. Meaning that enough of the variants was expressed in cells to maximally inhibit MERS-CoV replication, regardless of whether this UbV is instable. The remaining progeny virus ($10^3$ PFU/ml when ME.4 is expressed in cells) is most likely produced in cells that were not transduced and fully support MERS-CoV replication. To investigate the importance of UbV stability, and show that improving the stability of ME.4 could be beneficial, some more modifications to the experimental set-up could be made. One approach would be to further lower UbV expression levels, as this would render protein turnover more critical and thus increase the importance of UbV stability. The period between lentivirus transduction and MERS-CoV infection could again be shortened. Alternatively, the CMV promoter that drives UbV expression could be replaced with a weaker promoter such as the phosphoglycerate kinase 1 (PGK) or the Ub C promoter [398, 399]. Another option would be the use of HuH-7 cells instead of MRC5 cells. HuH-7 cells are also susceptible to MERS-CoV infection, but CMV promoter-driven UbV expression levels were substantially lower than in MRC5 cells [389]. Of note, ME.2, another instable UbV that has a lower affinity for $PL^{pro}$ than ME.4, reduced the MERS-CoV progeny titers by 1.5-log (Fig. 1D). Modification of region 1 of ME.2 will likely increase its stability and with the experimental set-up described in this chapter a difference in inhibition of MERS-CoV replication might be observed between ME.2 and a stable variant of ME.2, as a maximum 3-log reduction can probably be measured.

Applying these strategies may additionally provide an opportunity to examine whether viral resistance to UbVs will develop. As the expression levels of UbVs will be lower in cells, there will be less inhibition of MERS-CoV replication, possibly allowing the virus to adapt to UbV interference. When this would occur, it will be interesting to map resistance-associated mutations which are expected to reside either in $PL^{pro}$ itself or in viral proteins interacting with $PL^{pro}$. As previously addressed, the substitutions in the UbV relative to Ub.wt that infer stronger $PL^{pro}$-binding are located across the entire binding surface. To reduce UbV-binding, the virus would presumably need to acquire multiple adaptive mutations in $PL^{pro}$, which probably would affect overall virus fitness, e.g. by impairing replicase polyprotein processing cleavage or the innate immune evasive DUB function of the viral protease [389].

We have now increased the stability of the strongest UbV inhibitor targeting MERS-CoV $PL^{pro}$, thus enabling the further validation and development of UbVs as antiviral treatment options. The observed high specificity to MERS-CoV $PL^{pro}$ combined with low cross reactivity to other DUBs and lack of toxicity in mammalian cells allow proof-of-concept experiments in an animal model. Naturally, MERS-CoV can infect dromedary camels, rhesus macaques, rabbits and common marmosets [369]. Alternatively, mice can be sensitized by adenovirus-mediated expression of the human DPP4 receptor (hDPP4) [368] or by developing transgenic hDPP4 mice [319, 369, 370]. Previously,

the hDPP4 gene was introduced into replication-deficient adenovirus 5 (Ad5) to induce expression of hDPP4 in the lungs of mice. Subsequently, local MERS-CoV infection was supported in these animals, resulting in virus replication, some occasional weight loss as a measurable symptom, but eventually the virus was cleared [368]. In the constructs used for these experiments, UbV-encoding genes can be co-inserted under the control of e.g. a CMV or PGK promoter in the E1 position of hDPP4-Ad5, in a similar fashion as described for shRNAs [400]. With this approach, a double infection can be performed, first the mice will be transduced with such a hDPP4- and UbV-expressing Ad5 and subsequently they can be challenged with MERS-CoV. After the Ad5 transduction, lung cells will express hDPP4 and become susceptible to the MERS-CoV infection, but will also express an UbV so that inhibition of MERS-CoV replication can be directly correlated to UbV expression. Adenovirus-mediated expression could also be a way to express UbVs in other animal models or even in humans, but other delivery methods for intracellular delivery of mRNA or protein should be explored as well.

The UbV phage display approach can be used to identify more UbVs targeting the vDUBs of different viruses in the CoV family and beyond. Many of the currently known vDUBs are important for virus replication or pathogenesis [315]. UbVs were originally developed to target human DUBs, Ub-conjugating enzymes and Ub ligases that play a role in for example cancer [347]. Viruses can manipulate the Ub-system in various ways and, besides encoding their own DUBs, may express viral Ub ligases or other Ub-binding proteins. If these enzymes are essential for productive infection, they can potentially be targeted with UbVs as well [303, 341]. Proof-of-concept experiments in infection models and the development of efficient delivery methods will be prerequisites for the further exploration of UbVs as potential antiviral therapeutics.



## ACKNOWLEDGEMENTS

We kindly thank Herbert W. Virgin (Washington University School of Medicine), Michaela U. Gack (University of Chicago), Natalia Frias-Staheli (Mount Sinai School of Medicine), Paul N. Moynagh (NUI Maynooth), Ron A.M. Fouchier and Bart L. Haagmans (both Erasmus Medical Center Rotterdam) for providing materials. We are grateful to Eric J. Snijder for helpful discussions and for critical reading of this manuscript. This work was supported in part by an EIT Health DPhil/PhD Transition Fellowship to Robert C.M. Knaap.

# 6 Structure and function of viral deubiquitinating enzymes

Ben A. Bailey-Elkin[1], Robert C.M. Knaap[2], Marjolein Kikkert[2] and Brian L. Mark[1]

[1] Department of Microbiology, University of Manitoba, Winnipeg, R3T2N2, Canada
[2] Department of Medical Microbiology, Leiden University Medical Center, Leiden, the Netherlands

**The content of this chapter was published, in modified form, in The Journal of Molecular Biology, Vol. 429, No. 22, pp. 3441-3470, 2017**

## ABSTRACT

Post-translational modification of cellular proteins by ubiquitin (Ub) regulates numerous cellular processes, including innate and adaptive immune responses. Ub-mediated control over these processes can be reversed by cellular deubiquitinating enzymes, which remove Ub from cellular targets and depolymerize polyUb chains. The importance of protein ubiquitination to host immunity has been underscored by the discovery of viruses that encode proteases with deubiquitinating activity, many of which have been demonstrated to actively corrupt cellular Ub-dependent processes to suppress innate antiviral responses and promote viral replication. Deubiquitinating enzymes have now been identified in diverse viral lineages and their characterization is providing valuable insights into virus biology and the role of the ubiquitin system in host antiviral mechanisms. Here we provide an overview of the structural biology of these fascinating viral enzymes and their role innate immune evasion and viral replication.

## VIRUSES AND THE UBIQUITIN SYSTEM

Viruses have had a significant impact on society throughout history, and it is only since we have started to understand how they establish infection and how they interact with their hosts that we have been able to develop the means to control the diseases they cause. Although viruses depend on the molecular machineries of their host cells for replication, they also express their own specialized replication enzymes to support the production of new virus particles and the spread of infection. Not only do they have to find ways to exploit the cellular machinery they need to establish infection (while often competing with the interests of the cell), they also have to deal with elaborate antiviral mechanisms that are triggered immediately upon entry of viral material into the cell. Many of these challenges are met by specialized viral enzymes that hijack or manipulate critical cellular systems, and it is therefore not surprising that the study of viruses has repeatedly led to insights into the biology of the cell itself, since viruses have had to "learn" how the cell works in order to survive.

One of the important cellular machineries that is manipulated by viruses is the ubiquitin (Ub) system. Ubiquitination involves the covalent attachment of the C-terminal G76 residue of Ub via an isopeptide bond to the ε-amino group of a lysine residue or the α-amino group of the N-terminal residue of a protein substrate [145]. Ub is a small, 76 amino acid protein that is highly conserved, stable, structured and ubiquitously expressed in virtually all cell types. It adopts a β-grasp fold, consisting of a mixed β-sheet structured around a central α-helix, and harbours a C-terminal diglycine motif (Fig. 1A). An exposed hydrophobic patch is centralized around residue I44 (frequently referred to as the I44 patch) and often facilitates recognition by Ub-binding domains (Fig. 1A) [300, 401]. The process of Ub conjugation to substrates is regulated by the E1, E2 and E3 enzymatic cascade leading to (multi)monoubiquitination, or formation of polyUb chains upon the modification of a substrate-attached Ub at M1, K6, K11, K27, K29, K33, K48, K63 residues on Ub [145, 146, 313]. PolyUb chains can be homogeneous when Ub is attached to the same lysine residue on each Ub in the chain, however mixed-linkage polyUb chains and branched Ub chains can also be formed [147]. Classically, K48-linked chains adopt compact conformations (Fig. 1B) and play an important role in proteasomal degradation whereas K63-linked chains adopt an extended conformation (Fig. 1C), and have been implicated in positively mediating signal transduction [145]. Both types of ubiquitination are involved in regulating the signalling that directs the antiviral innate immune response [151, 152]. Additional Ub-like (Ubl) proteins such as SUMO or NEDD8 are structured around a β-grasp fold and possess a C-terminal diglycine motif similar to Ub, which allows for covalent conjugation to substrates by their respective E1, E2 and E3 enzymes [402-404]. In contrast, the Ubl protein interferon-stimulated gene 15 (ISG15) is comprised of two tandem Ubl folds that are connected by a short linker, however it retains the distinctive diglycine motif at its C-terminus for attachment to target proteins (Fig. 1D). While ISG15 conjugation has been shown to mediate protection from a number of viruses in mice [339, 405], its role in antiviral immunity remains poorly understood. Interestingly, human ISG15 (hISG15) deficiencies do not

appear to alter susceptibility to viral infections [406], and curiously, soluble ISG15 in fact appears to downregulate IFN signalling [407].

The ubiquitination process is highly dynamic and reversible, allowing cells to regulate signal transduction pathways as a response to different stimuli such as virus infections. Deubiquitinating enzymes (DUBs) catalyse the removal of Ub or Ubl proteins from cellular substrates, resulting in either complete deubiquitination or editing/trimming of Ub chains [267]. Around 100 human DUBs can be classified into five major families based on their catalytic mechanism and structural features [267, 408]. The majority of DUBs are cysteine proteases, which contain an active site catalytic dyad comprised of a cysteine nucleophile and a histidine base arranged in close proximity. The histidine appears to activate the cysteine nucleophile by lowering the pKa of the sidechain and stabilizing the negatively charged thiolate [267]. Often a third polar residue is present, which likely helps orient the histidine residue appropriately to facilitate activation of the nucleophile [267]. The cysteine protease DUB families include Ub-specific proteases (USPs), ovarian tumour proteases (OTUs), Ub C-terminal hydrolases (UCHs) and Machado-Joseph disease proteases (MJDs); whereas, the fifth family of DUBs consisting of JAB1/MPN/MOV34 (JAMM) are metalloproteases. More than half of the human DUBs belong to the USP family, and generally cleave all Ub linkage types without a clear preference [237]. This is in contrast to the sixteen human OTU DUBs that hydrolyse defined subsets of Ub linkage types [238].

Almost all important cellular processes are regulated (in part) by ubiquitination. Whether it is, for example, gene expression, protein trafficking, protein degradation, autophagy, cell cycle progression, programmed cell death, cell survival, or innate immune response, all are regulated by Ub and/or Ubl proteins, either positively or negatively, or both. As viruses are extensively using or dealing with some, if not all, of these processes during infection, it is not surprising that several interactions between viruses and the Ub(-like) system in the context of these kinds of cellular processes have been identified. These interactions have been reviewed from several different perspectives by others [344, 409-417]. In particular, however, from all these data it has become apparent that Ub-mediated regulation of the antiviral innate immune response may be one of the most important targets of viral manipulation.

## ANTIVIRAL INNATE IMMUNE RESPONSE AND ITS REGULATION BY UBIQUITIN

The innate immune system of host cells is triggered upon infections with pathogens such as parasites, bacteria and viruses. In the case of viruses, sensing of viral proteins or specific forms of viral nucleic acid will initiate activation of the innate immune response leading to expression of antiviral molecules, including interferons (IFNs), pro-inflammatory cytokines and chemokines [418]. Type I interferons (IFN-α/β) will induce an antiviral state by upregulating the expression of hundreds of interferon stimulated genes (ISGSs) in infected and neighbouring cells to limit virus replication and spread [136]. Furthermore, the adaptive immune system becomes activated,

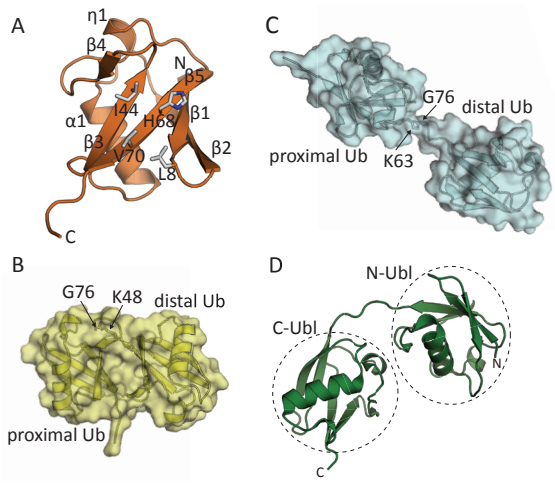


**Figure 1. Structure of Ub and ISG15.** (A) Ubiquitin (PDB ID: 1UBQ) is shown in cartoon representation, with the residues forming the I44 patch shown as sticks. (B) Crystal structure of the compact, K48-linked diUb (PDB ID: 1AAR) is shown as a cartoon with transparent surface, with the isopeptide bond between K48 and G76 indicated. (C) Crystal structure of the extended, K63-linked diUb (PDB ID: 2JF5) is shown as a cartoon with transparent surface, with the isopeptide bond between K63 and G76 indicated. (D) crystal structure of ISG15 (PDB ID: 1Z2M) is shown as cartoon, with the N- and C-terminal Ub-like domains indicated. All structural images were generated using PyMOL [373].

promoting antigen presentation and developing effective T and B cell responses that may ultimately result in clearance of the virus. Excessive activation of the innate immune system can, however, cause chronic inflammation and autoimmune disorders [419], and antiviral signalling pathways are therefore strictly regulated. Key mechanisms that trigger and fine-tune these immune responses in eukaryotes are the post-translational phosphorylation and ubiquitination of cellular immune factors, which can alter their interaction, localization, stability or activity (Fig. 2) [143, 151, 152, 420, 421].

The first step of the innate immune response is the detection of pathogen-associated molecular patterns by a large repertoire of pattern-recognition receptors (PRRs) present on immune and non-immune cells. On the surface, and in endosomal compartments of immune cells, toll-like receptors (TLRs) play an important role as viral PRRs. Subsequent signalling is directed via MyD88, TIR-domain-containing adaptor-inducing IFN-β (TRIF), interleukin-1 receptor-associated kinase 1 (IRAK1) and -4, and receptor-interacting protein 1 (RIP1), ultimately leading to production of type I IFNs. Intra-cytosolic sensors for the detection of viral nucleic acids in virtually all cells are RIG-I-like receptors (RLRs), NOD-like receptors and viral DNA sensors (cyclic-GMP-AMP synthase (cGAS) and IFI16 are the key sensors) [422, 423]. RLRs include retinoic acid-inducible gene I (RIG-I) and melanoma differentiation factor 5 (MDA5), which bind different forms of viral RNA leading to their activation and oligomerization that will induce the interaction with mitochondrial antiviral signalling protein (MAVS). MAVS recruits signalling molecules such as E3 ligases of the TNF receptor-associated factor (TRAF) protein family to activate kinase complexes. TRAF6 will recruit the TAK complex that will phosphorylate inhibitor of NF-κB kinase (IKK) γ (also known as

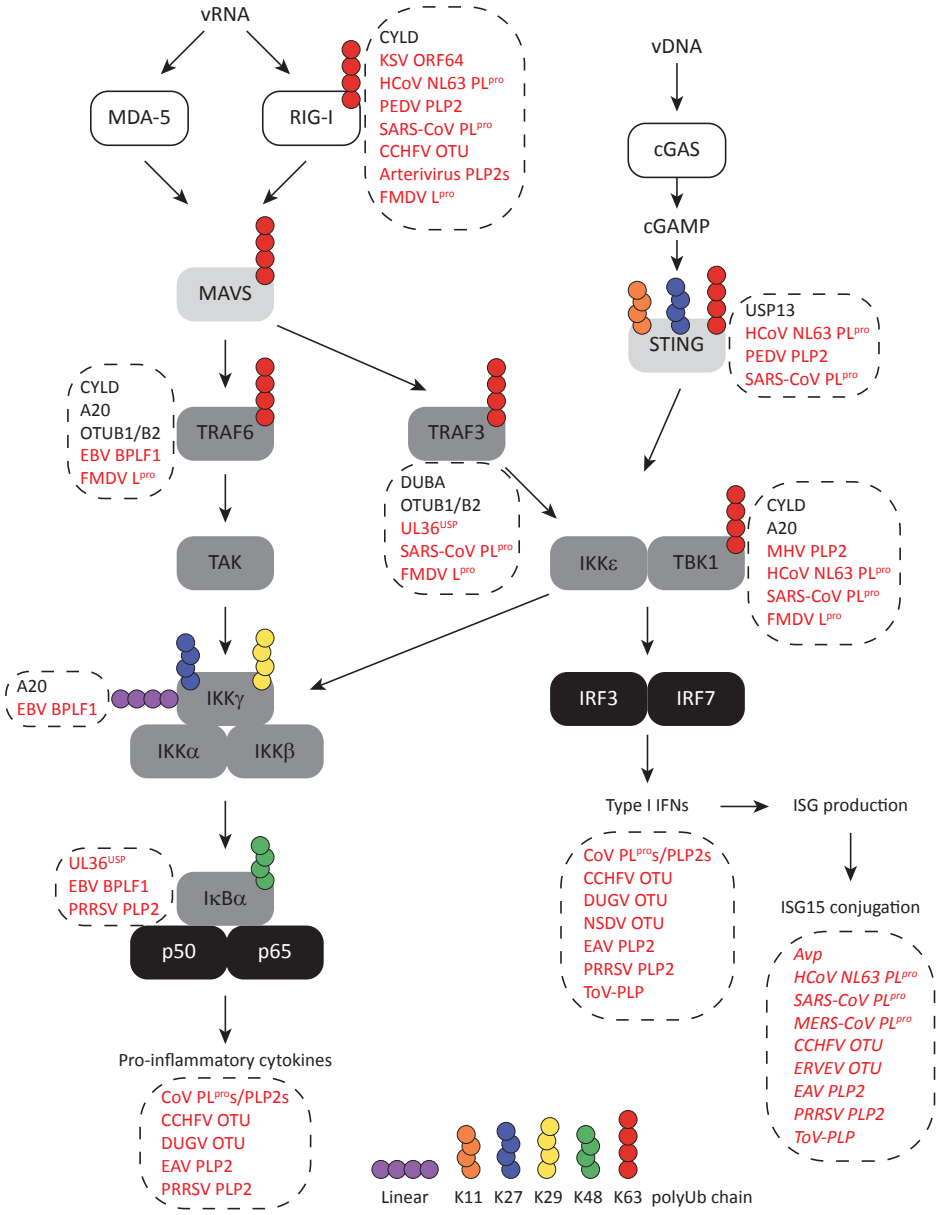


**Figure 2. Illustration of the activation of the innate immune response and its manipulation by human or viral DUBs.** White boxes highlight the cytoplasmic receptors RIG-I, MDA5 and cGAS that can sense viral RNA or DNA via adaptor proteins MAVS or STING, in light grey, which in turn activate kinase complexes (partly depicted in dark grey). Ultimately, transcription factors IRF3, IRF7, p50 and p65 (black boxes) are activated and translocate to the nuclease to induce the transcription of type I IFNs and pro-inflammatory cytokines. Differently linked polyUb chains involved in the activation of the innate immune response are shown by the different coloured polyUb chains. Dashed boxes placed next to innate immune signalling factors contain human or viral DUBs that remove Ub chains from these specific targets. DUBs placed below the type I IFN or NF-κB pathway (inducing the expressing of pro-inflammatory cytokines) interfere with these pathways without knowing their exact substrate(s). Human DUBs are shown in black, vDUBs in red and vDUBs having deISGylating activity are shown in red italic.

NF-κB essential modulator (NEMO)) which in turn will form a complex with IKKα/β. This complex will initiate degradation of the NF-κB inhibitor IκBα, which frees NF-κB to promote transcription of pro-inflammatory cytokines. Another protein recruited to MAVS, TRAF3, activates a complex comprised of TANK-binding kinase 1(TBK1)/IKKε to phosphorylate interferon regulatory factor 3 (IRF3) and IRF7. Phosphorylation enables the IRF transcription factors to dimerize and induce the expression of type I IFNs in concert with NF-κB [143, 418]. Secreted IFN-α/β will bind to IFN receptors and activate the Janus kinase–signal transducer and activator of transcription pathway resulting in the transcription of ISGs. ISG-encoded proteins, including ISG15, have antiviral activity by interfering with processes like viral replication or translation [136]. With respect to the detection of DNA viruses, virus-derived cytosolic DNA binds to sensor cGAS, which stimulates the synthesis of cyclic-GMP-AMP (cGAMP) [424]. cGAMP then activates stimulator of interferon genes (STING), a membrane bound protein on the endoplasmic reticulum (ER), which recruits TBK1 and initiates IRF3-mediated transcription of type I IFNs and pro-inflammatory cytokines.

Activation of innate immune signalling is regulated, besides by phosphorylation, through ubiquitination performed by specialized E3 ligases such as the members of the family of TRIM E3 ligases [425]. These and several other E3s conjugate K63-linked and K48-linked Ub chains to RIG-I, MAVS, TBK1 and STING, as well as MyD88, TRIF, IRAK1 and RIP1, while TRAF3 and 6 induce their K63-linked auto-ubiquitination, which triggers activation [143, 151, 152]. IκBα is degraded by the proteasome after K48-linked Ub chains are conjugated, which enables downstream signalling [426]. Atypical Ub chains also play a role in activation of the innate immune response since NEMO is a substrate for conjugation by K27, K29 and linear polyUb chains, and STING can be modified with K11 and K27 polyUb chains [427, 428]. Besides conjugated Ub, unanchored ubiquitin chains (K63- or K48-linked) also seem to play a role in the regulation of innate immune signalling by providing a multimeric scaffold for activation of RIG-I and MDA-5 complexes [429-431]. In addition, ubiquitination of IRF3 has been observed, and implicated in the induction of cellular proapoptotic pathways [432], and in the negative regulation of IFN-β signalling [433].

Negative regulation of the innate immune response is achieved by conjugation of K48-linked polyUb to degrade signalling factors and thereby dampen expression of type I IFNs and pro-inflammatory cytokines. Additionally, actions of E3 ligases that attach different Ub linkage chains can be counteracted by several specific cellular DUBs [151, 434]. CYLD (USP) is able to cleave linear and K63-linked Ub chains and it deubiquitinates RIG-I, TRAFs and TBK1 [435]. OTUB2 (an OTU domain containing DUB) removes K63-linked Ub chains from TRAF3 and TRAF6, as well as does OTUB1, however *in vitro* this latter enzyme preferentially cleaves K48-linked Ub chains [238]. Interference with the K63-linked autoubiquitination of TRAF3 is performed by DUBA (OTUD5), which interacts with TRAF3 [436]. A20 is a complex regulator since it contains an OTU domain at its N-terminus that cleaves K63-linked polyUb chains, as well as a C-terminal E3 ligase domain for conjugating K48-linked Ub [437, 438]. Deubiquitination of TRAF6 and NEMO by A20 leads to suppression of NF-κB activation. A20 also disrupts the activation of TBK1 complexes containing TRAF3 however the interference mechanism is unknown [439]. Additionally, A20 can also bind

to specific E2 enzymes and induce their degradation as a mechanism to prevent ubiquitination of other proteins [440]. Several more DUBs that play a role in the regulation of the immune response have been identified such as OTU DUBs Cezanne, OTULIN and UPS DUBs USP3, 13 and 21 [151, 441-444]. Mutations in genes encoding DUBs involved in negative regulation of innate immune signalling, like CYLD and A20, can lead to the development of diseases including cancer, autoimmune and inflammatory disorders, highlighting the importance of DUB-controlled immune signalling [445, 446].

## VIRUS-ENCODED DEUBIQUITINATING ENZYMES

Constant co-evolution of hosts and pathogens both shape the cellular antiviral system in order to efficiently eliminate invading pathogens as well as the pathogens that will evolve and adapt to facilitate efficient replication of their genomes [128]. Particularly viruses with an RNA genome have a high mutation frequency, which is triggered by the lack of proof-reading activity in the viral RNA polymerases that drive their replication [447]. As a result, virus populations are genetically diverse, enabling them to rapidly adapt to changing circumstances. This also enables viruses to acquire diverse genes from various sources or evolve viral enzymes to expand their activities [448]. Mechanisms to avoid or delay activation of the innate immune system are exploited by viruses to manipulate the host cell environment [130, 449]. Modifying Ub signalling to evade activation of the innate immune response is used by both DNA and RNA viruses, and methods include for example blocking activity or hijacking host E3 ligases or DUBs [341]. Another elaborate viral approach is the expression of virus-encoded E3 ligases or DUBs that can suppress the innate immune response, but also potentially affect many other Ub-dependent signalling pathways in the host [303, 341, 450]. In this chapter, we focus on viral DUBs (vDUBs) (listed in Table 1) that have been identified in RNA viruses (corona-, arteri-, nairo-, picorna- and tymo-viruses), with an emphasis on the structural biology of these vDUBs and their (potential) innate immune suppressive mechanisms.

### Coronaviridae

Coronaviruses (CoVs) are enveloped viruses within the order Nidovirales with the largest known positive-sense single-stranded RNA (ssRNA) genomes (26-34 kilobases). They are grouped further into *alpha-*, *beta-* and *gammacoronavirus* lineages based on sequence similarity [451]. A number of CoVs cause respiratory disease in humans. Notably, in November 2002 a case of atypical pneumonia in Guangdong, China [452] led to the identification of the severe acute respiratory syndrome coronavirus (SARS-CoV) [5, 6, 8], which rapidly caused a global pandemic. Ultimately, successful infection control measures brought the SARS-CoV pandemic to an end in July 2003. More recently, in June 2012 a novel CoV was isolated from a 60-year-old male from Saudi Arabia following a fatal case of severe pneumonia and renal failure [25]. This virus, now referred to as

Middle East respiratory syndrome coronavirus (MERS-CoV) has since led to 1917 confirmed cases and 684 deaths as of March 2017 [453]. Currently no MERS- or SARS-CoV-specific therapies exist. Both MERS- and SARS-CoV are expected to have emerged into human populations through animal vectors, with camels and palm civets expected as the primary zoonotic sources, respectively [16, 42].

The SARS-CoV outbreak prompted deeper investigation into CoVs as respiratory pathogens, and post-SARS, the human coronavirus (hCoV)-NL63 was identified, with retrospective analysis suggesting the virus had been circulating in human populations for some time prior to its discovery [49]. HCoV-NL63 is most closely related to HCoV-229E, which is one of two CoVs identified pre-SARS in the 1960s and recognized as a causative agent of the common cold [51]. HCoV-NL63 has also been associated with croup in young children [454].

Coronaviruses also cause disease in several animals. The neurotropic mouse hepatitis virus (MHV) strains JHM and A59, which group along with SARS-CoV in the *betacoronavirus* genus, cause demyelinating encephalomyelitis in mice and have served as disease models for multiple sclerosis [455]. The porcine transmissible gastroenteritis virus (TGEV) and porcine epidemic diarrhoea virus (PEDV) are *alphacoronaviruses* that cause significant financial burdens in the pork industry [456].

The non-structural proteins (nsps) of CoVs are encoded within two open reading frames, ORF1a and ORF1b, with translation yielding polyprotein (pp) 1a or pp1ab, the latter arising from a -1 ribosomal frameshift that provides access to ORF1b [265]. The CoV polyproteins are post-translationally processed into functional nsps by protease domains encoded within, including a 3C-like cysteine protease ($3CL^{pro}$) which functions as the main protease, and either 1 or 2 additional papain-like proteases (PLPs), which are numbered sequentially according to their position within the polyprotein. In cases where only a single PLP is present, it is referred to simply as $PL^{pro}$.



*Severe acute respiratory syndrome coronavirus $PL^{pro}$*

Full-length genomic sequences from a number of clinical isolates of SARS-CoV became available shortly after the pandemic [14, 15, 457] and their analysis predicted the presence of a single papain-like protease ($PL^{pro}$) encoded within nsp3 [110]. The absence of a second paralogous PLP domain, combined with an analysis of putative cleavage sites, suggested that $PL^{pro}$ was responsible for cleaving three sites within the SARS-CoV polyprotein, and releasing nsp1, nsp2 and nsp3 from the viral polyprotein [110]. This activity was soon confirmed experimentally, with $PL^{pro}$ recognizing the consensus site LXGG [227, 228]. Structural modelling of SARS-CoV $PL^{pro}$ based on the crystal structure of the cellular deubiquitinating enzyme herpesvirus-associated ubiquitin-specific protease (HAUSP) suggested that the viral enzyme adopts a papain-like fold with a circularly permutated C4 zinc finger domain [195]. The structural similarity between $PL^{pro}$ and a cellular DUB, along with the compatibility of the $PL^{pro}$ consensus cleavage sequence with the C-terminal RLRGG motif of Ub, led to the hypothesis that $PL^{pro}$ may possess DUB and possibly ISG15 deconjugating (deISGylating) activity [195].

**Table 1. Viral deubiquitinating enzymes and their characterized structures and substrates.**

| Virus family/ genus | Virus | DUB domain | Location | *In vitro* DUB activity | Cellular targets | PDB ID |
|---|---|---|---|---|---|---|
| *Coronaviridae / α-CoVs* | Human coronavirus NL63 | HCoV-NL63 PLP2 | Membrane- associated nsp3 that is part of the replication-transcription complex | K48/63 polyUb [199, 230], ISG15 [473] | RIG-I, TBK1, IRF3, STING [474] | |
| | Porcine epidemic diarrhoea virus | PEDV PLP2 | | N/A | RIG-I, STING [201] | |
| | Porcine transmissible gastroenteritis coronavirus | TGEV PL1$^{pro}$ | | K48/63 polyUb [231] | Unknown | 3MP2 |
| *Coronaviridae / β-CoVs* | Severe acute respiratory syndrome coronavirus | SARS-CoV PL$^{pro}$ | Membrane- associated nsp3 that is part of the replication-transcription complex | K48 polyUb [197, 234, 235], K63 polyUb [235], ISG15 [197, 235], K6/11/27/29/33/48/63 diUb [234] | RIG-I, TRAF3, STING, TBK1, IRF3 [535] | 4M0W, 5E6J, 3E9S, 3MJ5, 4MM3, 4OVZ, 4OW0, 2FE8, 5TL6, 5TL7 |
| | Middle East respiratory syndrome coronavirus | MERS-CoV PL$^{pro}$ | | K6/11/29/33/48/63 diUb [234], K48 polyUb [234, 235, 327], K63 polyUb [235, 327], ISG15 [235] | Unknown | 4P16, 4PT5, 4R3D, 4REZ, 4RF0, 4RF1, 4RNA, 4WUR |
| | Mouse hepatitis virus | MHV PLP2 | | K11/48/63 diUb [208] | IRF3 [203], TBK1 [477] | 4YPT |
| *Coronaviridae / γ-CoVs* | Avian infectious bronchitis virus | IBV PL$^{pro}$ | Membrane- associated nsp3 that is part of the replication-transcription complex | K48/63 polyUb [232, 484] | Unknown | 4X2Z 5BZ0 |
| *Arteriviridae* | Equine arteritis virus | EAV PLP2 | N-terminal region of membrane-associated nsp2 that is part of the replication-transcription complex | K48/63 polyUb [221] | RIG-I [221] | 4IUM |
| | Porcine reproductive and respiratory syndrome virus | PRRSV PLP2 | | K6/11/27/29/33/48/63 diUb, K48/63 polyUb [494] | IκBα [302], RIG-I [221] | |
| | Lactate dehydrogenase- elevating virus | LDV PLP2 | | N/A | RIG-I [221] | |
| | Simian haemorrhagic fever virus | SHFV PLP2 | | N/A | RIG-I [221] | |

**Table 1. Viral deubiquitinating enzymes and their characterized structures and substrates. (continued)**

| Virus family/ genus | Virus | DUB domain | Location | *In vitro* DUB activity | Cellular targets | PDB ID |
|---|---|---|---|---|---|---|
| *Bunyaviridae / Nairoviruses* | Crimean-Congo haemorrhagic fever virus | CCHFV OTU | N-terminal region of RNA-dependent RNA polymerase-containing L-segment | K48/63 polyUb [219, 222, 502], ISG15 [219, 222-224, 502], K6/11 diUb [502], K63 diUb [222, 224, 502]l K48 diUb [222, 502] | RIG-I [221] | 3PHU, 3PHW, 3PHX, 3PT2, 3PSE, 3PRM, 3PRP |
| | Dugbe virus | DUGV OTU | | K48/63 polyUb [219, 222, 502], ISG15 [219, 222-224, 502], K6/11 diUb [502], K63 diUb [222, 224, 502], K48 diUb [222, 502] | Unknown | 4HXD, 3ZNH |
| | Erve virus | ERVEV OTU | | ISG15 [502] | Unknown | 5JZE |
| | Nairobi sheep disease virus | NSDV OTU | | N/A | Unknown | |
| *Picornaviridae* | Foot-and-mouth disease virus | FMDV $L^{pro}$ | N-terminus of polyprotein | K48/63 polyUb [521] | RIG-I, TBK1, TRAF3, TRAF6 [521] | 1QOL, 4QBB, 1QMY |
| | Enterovirus G | ToV-PLP | 2C/3A junction of the Enterovirus G polyprotein | M1/K48/63 polyUb, ISG15 [507] | Unknown | |
| *Tymoviridae* | Turnip yellow mosaic virus | TYMV PRO | Non-structural protein p206 | K48/63 polyUb [340, 502] | TYMV p66 [340] | 4A5U |

The *in vitro* DUB [196, 197] and deISGylating [197] activities of $PL^{pro}$ were confirmed in parallel by independent groups. This DUB activity has been implicated in the downregulation of cellular innate immune responses [200], consistent with the observation that SARS-CoV infection prevents IFN-β induction in infected cells [270]. Devaraj and co-workers demonstrated that $PL^{pro}$ inhibited RIG-I, MDA5 and TLR3-mediated IFN-β promoter activity, and interfered with signalling components specific to IRF3 activation [200]. Interestingly, while their studies showed no effect on NF-κB-dependent transcripts, others found marked reduction in the activity of an NF-κB-responsive promoter in the presence of $PL^{pro}$ [204]. The role of $PL^{pro}$ in the inhibition of IRF3 activation has been further investigated, and it has been suggested to deubiquitinate and inhibit the ability of constitutively active IRF3 to induce IFN-β promoter activity [458].

A crystal structure of SARS CoV $PL^{pro}$ confirmed it to have domain organisation similar to HAUSP, which consists of a "thumb", "palm" and "fingers" subdomains that organise together to resemble an extended right hand (Fig. 3A) [229, 459]. The α-helical thumb and β-sheet palm domains pack together and host a cysteine-histidine-aspartic acid catalytic triad at their interface, with residues adopting a similar geometry to that found in papain, while the fingers domain harbours a circularly permutated C4 zinc finger as had been predicted (Fig. 3A) [195]. Additionally, a tryptophan residue (Trp107) near the active site was found to be oriented such that the indole ring hydrogen was believed to form part of the oxyanion hole (Fig. 3A). Also situated near the active site was a six amino acid loop flanked by glycine residues. This loop is also present in the cellular HAUSP and USP14, where it is termed blocking-loop 2 (BL2) (Fig. 3A), as it occludes the active site of USP14 in the absence of Ub, and is thus proposed to serve a regulatory function. In $PL^{pro}$, this loop is found to be in an "open" state, although molecular dynamic simulations predict that the loop samples both "open" and "closed" conformations [460]. Intriguingly, the N-terminal domain of $PL^{pro}$ adopts a Ubl β-grasp fold, which packs against the thumb domain (Fig. 3A). While little is known regarding the function of this domain, conflicting data have been reported showing either that this domain is required [204] or dispensable [199] for the immunomodulatory activity of $PL^{pro}$, although the Ubl domain does not appear to be necessary with respect to DUB activity [204, 234].

A crystal structure of a non-covalent SARS-CoV $PL^{pro}$-Ub complex showed that the C-terminal linear RLRGG peptide extending from the Ub substrate was bound at the interface between the α and β domains in cleft leading toward the active site [297], as previous modelling had predicted [229], with the BL2 loop undergoing significant conformational changes toward the C-terminus of Ub [297]. Crystal structures of $PL^{pro}$ bound to the C-terminal domain of human and murine ISG15 (mISG15) have also now been reported, demonstrating that species-specific recognition of ISG15 molecules is mediated by unique interactions between $PL^{pro}$ and the respective ISG15s [461]. Whether or not $PL^{pro}$ also recognizes the N-terminal domain of ISG15(s) remains to be investigated.

Recently, the structural basis for K48-linked polyUb-binding of SARS-CoV $PL^{pro}$ was elucidated by the determination of the crystal structure of $PL^{pro}$ in covalent complex with K48-diUb [236]. The

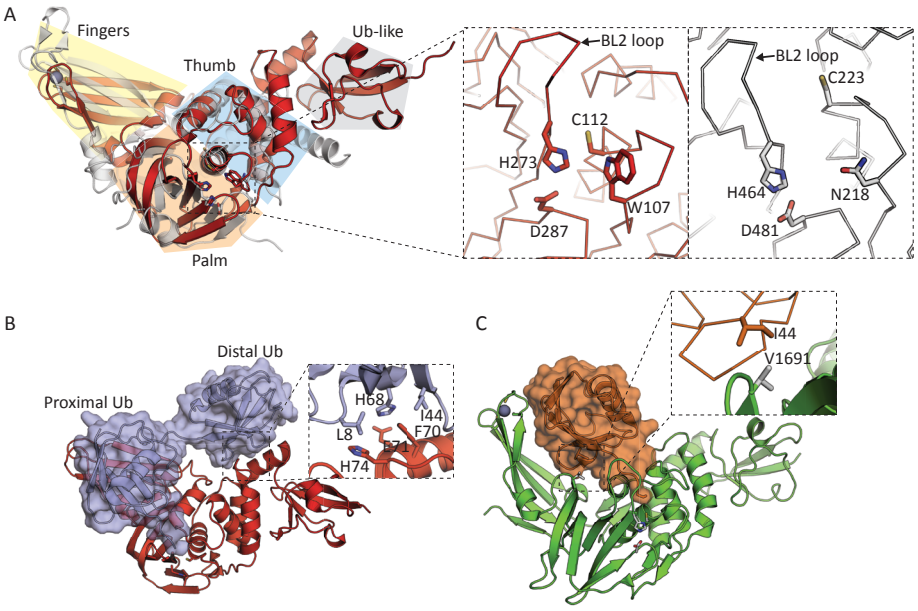


**Figure 3. Crystal structures of zoonotic SARS- and MERS-CoV PL$^{pro}$ domains.** (A) Superposition of SARS-CoV PL$^{pro}$ (PDB ID: 2FE8; red) with HAUSP (PDB ID: 1NB8; transparent grey). Thumb, fingers, palm and Ub-like domain are indicated with blue, yellow, orange and grey shading, respectively. Inset is a close up of the SARS-CoV PL$^{pro}$ (left panel) and HAUSP (right panel) active sites. Backbone atoms are shown as ribbons, and active site residues are shown as sticks. The BL2 loop is indicated with an arrow. (B) Crystal structure of the SARS-CoV K48-linked diUb complex (PDB ID: 5E6J). SARS-CoV PL$^{pro}$ is shown in red, bound to K48-linked diUb, shown as a slate cartoon with transparent surface. Inset is a close up on the hydrophobic interactions occurring between PL$^{pro}$ and the distal domain of K48-linked diUb, with relevant residues shown as sticks. (C) Crystal structure of the MERS-CoV PL$^{pro}$ domain in complex with Ub (PDB ID: 4RF0). MERS-CoV PL$^{pro}$ is depicted in green cartoon and Ub is shown in orange cartoon with transparent surface. Dotted box depicts a close-up of interaction between MERS-CoV PL$^{pro}$ residue V1691, and Ub residue I44, with residues depicted as sticks.



K48 diUb probe was fashioned with a cysteine-reactive alkyne at the C-terminus of the proximal Ub moiety, enabling covalent binding of the molecule to PL$^{pro}$ and interaction of its individual Ub domains associated with S1 and S2 binding sites on the vDUB domain (Fig. 3B) (see [301] for nomenclature). Consistent with earlier predictions [207], the K48 diUb probe bound PL$^{pro}$ in an extended conformation, as opposed to the canonical compact conformation observed with most K48-linked Ub chains. Binding of the distal Ub moiety at the S2 site was governed by a number of solvent-exposed hydrophobic residues at the surface of an α-helix within the thumb domain, which associated with the I44 patch of Ub (Fig. 3B) [207, 236]. These studies supported earlier observations that K48-linked polyUb chains were processed into diUb moieties, and PL$^{pro}$ may recognize K48 diUb preferentially [234].

The involvement of PL$^{pro}$ in the maturation of the viral polyprotein, as well as its role in counteracting cellular antiviral signalling pathways have contributed to its recognition as a promising target for therapeutic intervention, and the availability of X-ray crystallographic data [229, 297], along with work describing the substrate specificity of PL$^{pro}$ at its cognate subsites [462,

463] has contributed to such efforts. High-throughput screening of small-molecule libraries and rational structure-guided design have led to the identification and development of several lead compounds capable of inhibiting the proteolytic activities of SARS-CoV $PL^{pro}$ [342, 397, 464-469].

*Middle East respiratory syndrome coronavirus $PL^{pro}$*

Sequencing of the MERS-CoV genome and phylogenetic analysis indicated that the virus shares most recent common ancestry with bat CoVs HKU4 and HKU5, and led to the identification of a single $PL^{pro}$ domain encoded within nsp3 [26]. The polyprotein cleavage sites were initially predicted based on sequence alignment with other CoV polyproteins [26], and $PL^{pro}$ was later confirmed to process sites at the nsp1↓2, nsp2↓3 and nsp3↓4 junctions [205, 235, 266]. The *in vitro* DUB activity of $PL^{pro}$ was subsequently confirmed, displaying activity toward mono Ub [234, 290, 291, 470], K48- and K63-linked polyUb [234, 235, 327], K6-, K11-, K29-, K33-linked diUb [234] and ISG15 [235]. $PL^{pro}$ was also found to globally deconjugate Ub and ISG15 from cellular targets in cell culture [202, 205, 235, 327].

A crystal structure of the MERS-CoV $PL^{pro}$ domain revealed that the protease adopted a similar fold to SARS-CoV $PL^{pro}$, with thumb, palm and fingers subdomains, including the presence of a circularly permutated C4 zinc finger and an N-terminal Ubl domain [291, 327]. As expected, the active site is comprised of a cysteine-histidine-aspartic acid catalytic triad, although interestingly, the oxyanion hole of MERS-CoV $PL^{pro}$ appears deficient. The tryptophan residue proposed to form part of the oxyanion hole in SARS-CoV $PL^{pro}$ is replaced with a leucine, which is unable to participate in stabilizing the oxyanion since its side chain is entirely non-polar. Consistent with this observation, a tryptophan substitution aimed at restoring the MERS-CoV oxyanion hole increased the catalytic activity of $PL^{pro}$ [290, 291]. Differences have also been noted in the BL2 loop, which in the case of SARS-CoV $PL^{pro}$ was found to interact with small-molecule inhibitors of the enzyme [397, 469]. These SARS-CoV-specific compounds are ineffective toward MERS-CoV $PL^{pro}$, likely due to structural differences in the BL2 loop, and the inability of MERS-CoV $PL^{pro}$ BL2 residues to complete analogous hydrogen bonding and hydrophobic interactions with these compounds [371].

The fact that CoV $PL^{pro}$ domains possess two distinct functions, which comprise both DUB and polyprotein cleavage activities, complicates the ability to study these respective functions exclusively, as both activities depend on the same active site. Studying the role of $PL^{pro}$ DUB activity independent of viral polyprotein processing thus necessitates its selective disruption. To achieve this, the crystal structure of $PL^{pro}$ covalently bound to Ub was determined, providing a clear picture of the $PL^{pro}$-Ub interface (Fig. 3C) [327]. Specifically, mutation V1691R was found to significantly disrupt interaction between $PL^{pro}$ and the hydrophobic I44 patch of Ub by introducing a repulsive charge and steric bulk at a key position on the S1 Ub-binding site of $PL^{pro}$ (Fig. 3C). This mutation, along with others, abrogated DUB activity, yet permitted polyprotein cleavage at the nsp2↓3 junction, thus providing an ideal system to directly assess whether $PL^{pro}$ DUB activity alone disrupts cellular signalling. $PL^{pro}$ inhibited MAVS-mediated IFN-β promoter activity, while DUB-deficient $PL^{pro}$ was unable to interfere, implicating the DUB activity of $PL^{pro}$ directly in the

evasion of cellular signalling pathways involved in innate immunity [327]. While this immune evasive activity had been previously noted [202, 205, 235], it had not been directly linked to the DUB function of $PL^{pro}$. Additionally, $PL^{pro}$ has been found to interfere with the production of pro-inflammatory cytokines [202]. Interestingly, Yang and co-workers observed that $PL^{pro}$ active-site knockout mutants also prevented ubiquitination in cell culture suggesting a protease-independent inhibition of Ub conjugation, although this has not been confirmed by others [205]. Importantly, selective interference of $PL^{pro}$ DUB activity could enable future engineering of replication competent, DUB-deficient MERS-CoV that could be used to investigate the role of $PL^{pro}$ DUB activity during MERS-CoV infection.

Not surprisingly, MERS-CoV $PL^{pro}$ has been identified as a target for small-molecule drug design [291, 343, 385], but development of MERS-CoV-specific antiviral compounds remains in its early stages. Phage display methods have been successful in identifying inhibitors of Ub-binding proteins through the generation Ub variants (UbVs) with significantly enhanced affinity toward their cognate Ub-binding partners, providing a novel and promising platform for the development of Ub-based therapeutics [347, 348, 471, 472]. Recently, UbVs have been identified that potently and selectively inhibit the DUB, deISGylating and polyprotein processing activities of MERS-CoV $PL^{pro}$. Further, expression of the UbVs in MERS-CoV-infected cells resulted in a 4-log reduction in infectious viral progeny [389], demonstrating the promising potential for virus-specific therapies developed using Ub phage display methods.

*Human coronavirus NL63 PLP2*

HCoV-NL63 possesses two PLP domains, PLP1 and PLP2. PLP2 cleaves the viral polyprotein to release nsp2 and nsp3, although it does not cleave following a diglycine motif as found for other CoV PLPs, instead it has been reported to recognize FTKLAG↓GK and VAKQGA↓GF sites within the viral polyprotein [230]. Nevertheless, NL63 PLP2 also possesses DUB activity, cleaving K48-linked [230] and K63-linked polyUb chains [199], as well as ISG15 [473]. Initial work demonstrated that HCoV-NL63 infection resulted in impaired IFN-β secretion in cell culture [199], and subsequent studies investigated the role of PLP2 in downregulating the cellular innate immune response. PLP2 down regulated Sendai virus- and RIG-I-mediated IFN-β promoter activity [204], as well as poly(I:C)-induced, TLR3-dependent IFN-β promoter activity [199]. Consistent with these observations, PLP2 deubiquitinated RIG-I, TBK1, IRF3 and STING in overexpression experiments [474]. Its role in downregulating TNFα-induced NF-κB-dependent signalling pathways was also suggested [204]. Interestingly, PLP2 also appears to downregulate RIG-I-mediated IFN-β production irrespective of its catalytic activity [199].

*Mouse hepatitis virus PLP2*

Sequencing ORF1a and ORF1b of MHV strain JHM identified, besides the main protease, two putative cysteine protease domains, PLP1 and PLP2, which shared homology with cellular PLPs around the putative catalytic cysteine and histidine residues [475]. The autoproteolytic activity

of PLP2 toward the MHV polyprotein was later demonstrated [476], and the cleavage site within the viral polyprotein recognized by PLP2 was determined to be FSLKGG↓AV. DUB activity of MHV PLP2 was predicted based on the conservation of its active site residues with the SARS-CoV $PL^{pro}$ domain, and later confirmed *in vitro*, displaying efficient activity toward K11-, K48- and K63-linked diUb and hISG15 [208]. MHV PLP2 was found to inhibit cellular transcription of IFN-β via RIG-I, MAVS-, TBK1- and IRF3-mediated induction pathways [204, 477], as well as inhibition of IRF3 phosphorylation and nuclear translocation [203]. Further investigation into the mechanism of IRF3-specific inhibition of IFN-β production suggested that TBK1 and, curiously, IRF3 were directly deubiquitinated by PLP2 [203, 477]. The crystal structure of MHV PLP2 was eventually determined and revealed a cysteine-histidine-aspartic acid catalytic triad, with a glutamine residue as a putative contributor to the oxyanion hole, in contrast to the tryptophan residue found in SARS-CoV $PL^{pro}$ [229]. Significant structural homology was observed with respect to other CoV $PLP2/PL^{pro}$ domains, with MHV PLP2 adopting the thumb, palm and fingers domain architecture common to USP DUBs. Interestingly, mutations in the Ubl domain adjacent to MHV PLP2 impaired DUB activity, and reduced the thermostability of PLP2 [478].

*Additional CoV PLPs*

TGEV and PEDV both encode two papain-like protease domains, named $PL1^{pro}/PL2^{pro}$ and PLP1/PLP2, respectively. TGEV $PL1^{pro}$ resides in nsp3, cleaving the viral polyprotein at a single site at the nsp2↓3 junction following a diglycine motif [479], and it was shown to possess DUB activity toward K48- and K63-linked polyUb chains *in vitro* [231]. A crystal structure of TGEV $PL1^{pro}$ revealed that it possesses the palm, thumb and fingers subdomain typical of other coronaviral $PL^{pro}$ and eukaryotic USP domains [231]. In terms of the active site construction of the enzyme, a cysteine-histidine-aspartic acid catalytic triad observed at the interface between the thumb and palm, and a glutamine was found to be a likely contributor to the oxyanion hole, occupying a spatially homologous position to that of W107 found in the SARS-CoV $PL^{pro}$ domain. A notable difference from other PLPs was the absence of an N-terminal Ubl domain, which is only conserved in the region preceding the second PLP domain in CoVs.

The PLP2 domain from PEDV has also been confirmed to deubiquitinate cellular proteins in cell culture, as well as interfere with host innate immune signalling pathways, although its role in polyprotein processing remains to be characterized [201]. PEDV PLP2 inhibited RIG-I-mediated IFN-β expression, and NF-κB-responsive promoter activity, although to a lesser extent than HCoV-NL63 PLP2 [201] . Inhibition of STING-mediated IFN-β expression was also observed [201].

The avian infectious bronchitis virus (IBV), a prototypical member of the CoV family, had a single PLP ($PL^{pro}$) identified at the 5' end of its genome, based on the conservation of catalytic cysteine and histidine residues with cellular PLPs, and two MHV PLPs [475]. IBV $PL^{pro}$ was found to cleave the polyprotein between glycine-glycine residues at two sites, releasing nsp2 and nsp3 [480-483]. It adopts a fold common to USP DUBs, and possesses an N-terminal Ubl domain seen in most other CoV $PL^{pro}$ domains [232] and it cleaves K48- and K63-linked polyUb chains [484],

with an apparent preference for K63 linkages [232]. While DUB activity of IBV $PL^{pro}$ has been demonstrated the importance of this function has not been established.

## Arteriviridae

In addition to the *Coronaviridae* family, the Nidovirales order includes the *Roniviridae*, *Mesoniviridae* and *Arteriviridae* families that contain viruses with smaller positive-sense, ssRNA genomes relative to the CoV, with sizes of roughly 26-, 20-, and 15 kilobases, respectively [73]. The arterivirus family currently consists of four virus species that each infect a specific non-human mammal causing persistent infection or acute disease associated with abortions, respiratory disease or lethal haemorrhagic fever [67]. Equine arteritis virus (EAV) and especially porcine reproductive and respiratory syndrome virus (PRRSV) have a tremendous economic impact on the veterinary industry worldwide [485, 486]. The two other arteriviruses are simian haemorrhagic fever virus (SHFV) and lactate dehydrogenase-elevating virus (LDV), the latter infecting mice. Arteriviruses have a number of features that are similar to CoVs such as virion composition, genome structure, some of the replicase polyprotein functions and their replication strategy. The expression of nsps from large polyproteins is also similar to what was described for CoVs (see former paragraph). The arterivirus polyproteins are cleaved into individual nsps by internally encoded PLPs located in nsp1 and nsp2 to release nsp1 and nsp2, respectively, and a $3CL^{pro}$ in nsp4 that cleaves all junctions downstream of nsp3. While EAV nsp1 contains a single active protease named PLP1, PRRSV and LDV nsp1 contain two protease domains each; PLP1α and PLP1β. In the case of SHFV there are three functional PLPs in nsp1 to release nsp1α, β and γ [67, 487]. The PLP2 protease in nsp2 of arteriviruses was shown to cleave the nsp2↓3 junction [217]. Similar to EAV and PRRSV PLP2, as further elaborated below, SHFV and LDV PLP2 were shown to additionally possess DUB activity and limit innate immune activation by removing Ub from overexpressed RIG-I [221].



*Equine arteritis virus PLP2*

The nsp2 protease has been suggested to belong to a novel OTU-like superfamily of cysteine proteases [218] strengthened by the evidence that conserved cysteine and histidine residues are required for its protease activity [217]. After several human OTU-domain proteins were identified and shown to have DUB activity the Ub-deconjugation activity of a number of viral OTU domains, including EAV PLP2, were examined [219]. Ectopic expression of the PLP2 domain alone, or full-length EAV nsp2 indeed resulted in decreased global levels of both Ub and ISG15 conjugates in cultured cells. Genuine DUB activity of EAV PLP2 on both K48- and K63-linked polyUb chains was further confirmed by *in vitro* assays using purified protein [221]. EAV PLP2 therefore was concluded to have dual activity towards the viral replicase polyproteins and Ub(-like) conjugates. Interestingly, cellular OTU domain containing DUBs generally seem much less promiscuous, as they do not cleave ISG15 conjugates [219] and are usually at least partly specific for certain Ub linkages [238]. NF-κB activation by TNFα was suppressed upon the expression of EAV PLP2 [219], hinting at

an innate immune suppressive function of the vDUB. EAV PLP2 also inhibits RIG-I-mediated innate immune signalling upon overexpression, and is able to deubiquitinate RIG-I [221].

A crystal structure of EAV PLP2 bound to Ub revealed a remarkably compact OTU fold, including a C4 zinc finger not previously observed in OTU domains, and an active site consisting of the conserved cysteine and histidine residues (Fig. 4) [220]. Interestingly, PLP2 bound Ub in an orientation comparable to that of a viral OTU domain Crimean-Congo haemorrhagic fever virus (CCHFV) (see below), with the zinc finger domain performing an analogous role in orienting Ub binding as a β-hairpin present in the CCHFV OTU domain, which appears to assist in expanding the substrate specificity of PLP2 to include ISG15, as was observed for the CCHFV enzyme [299]. Guided by the structure (Fig. 4), the Ub-binding surface on PLP2 was mutated to prevent Ub binding, while leaving the active site of the protease unperturbed [220]. Indeed, recombinant EAV virus containing these mutations displayed wt replication kinetics in cell culture infections, confirming that polyprotein processing by PLP2 was unaffected. Primary equine lung fibroblasts were then infected with the DUB negative viruses and compared to wt EAV. Significantly enhanced innate immune responses were measured in the mutant virus infections (by comparing mRNA levels of IFN-β, MX1 and IL-8), which provided direct evidence that vDUB activity suppresses host antiviral responses. This opens the possibility of using DUB negative viruses that display reduced innate immune suppressive activity (with respect to wt virus) as next-generation attenuated live virus vaccines. A vaccination-challenge trial in horses comparing wt and DUB negative EAV resulted in slightly decreased replication of the DUB negative virus but comparable clinical disease, antibody response and innate immune response [335]. It should be noted that under the experimental conditions no difference was measured between the two viruses, which might be explained by the already high level of protection induced by the wt virus [335].

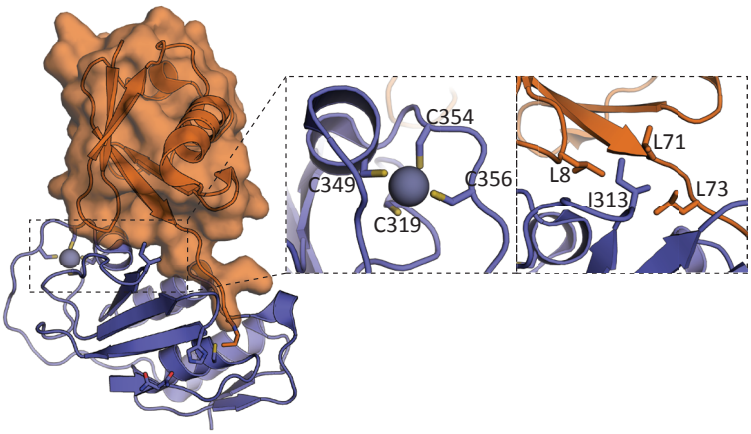


**Figure 4. Crystal structure of the EAV PLP2-Ub complex.** EAV PLP2 (PDB ID: 4IUM) is show in slate, covalently bound to Ub (orange, transparent surface). Depicted inset is the C4 Zn finger (left panel), with Zn-coordinating residues shown as sticks and Zn shown as a grey sphere. EAV PLP2 residue I313 forms hydrophobic interactions with the indicated residues on Ub (inset, right panel), and targeted disruption of I313-mediated interactions selectively abrogated PLP2 DUB activity.

Interestingly, despite the fact that arteriviruses and CoVs are members of the same order of Nidoviridae, suggesting a relatively close evolutionary connection, arteriviruses encode an OTU-like DUB, while CoVs encode a USP DUB. This suggests that the virus families each independently acquired DUBs into their genomes, again emphasizing the apparent importance of such activity for these viruses.

*Porcine reproductive and respiratory syndrome virus PLP2*

PRRSV PLP2 possesses both *in trans* and *in cis* cleavage activities and mutations disrupting only trans-cleavage activity were lethal for the virus [488]. Probing the nsp2↓3 cleavage site revealed that the cleavage site is at the G1198+G1199 dipeptide [488]. Besides full-length nps2, many different isoforms of nsp2 having the same N-terminus were detected during infection in cell culture [489]. These likely at least partly account for cleavage products of nsp2 when other conserved glycine dipeptide sites are processed by PLP2. More recently, two nsp2 products were identified as a result of -2 and -1 ribosomal frameshifting in the nsp2 region of the polyprotein gene, yielding nsp2 transframe (TF) and nsp2N products, respectively [490]. Nsp2TF contains a different C-terminal transmembrane domain compared to nsp2 and localized to different intracellular compartments. Removal of nsp2TF attenuated the virus as it replicated slower than wt virus and reached lower peak titers [490]. For this frameshift event the frameshift site, a frameshift-stimulatory element and, uniquely, a protein factor, nsp1β, are required [491]. Some of the nsp2 isoforms were found to be present in or on virus particles and might participate in entry, early steps of virus replication or suppression of host immune responses [492].

PRRSV PLP2 was shown to possess DUB activity towards Ub and ISG15 conjugates [219, 493]. PLP2 inhibited NF-κB activation in overexpression experiments by interfering with the K48-linked polyubiquitination of IκBα and thereby preventing its degradation [302]. RIG-I was also deubiquitinated upon overexpression of PRRSV PLP2, suggesting that the DUB activity of PLP2 is responsible for evading RIG-I induced innate immune responses [221]. PLP2 of JXwn06, a highly pathogenic PRRSV strain, and that of a modified live virus (MLV) vaccine strain, were shown to cleave all diUb chains linked through the different lysines in Ub, but not linear diUb *in vitro* [494]. The greatest difference between these PLP2s was that JXwn06 was more active towards K63-linked diUb than MLV. *In vitro*, neither PLP2 cleaved hISG15-AMC nor the pro-forms of hISG15 or porcine ISG15, which contradicts the earlier observation of ISG15 conjugate cleavage upon ectopic expression of PLP2 [219, 493, 494]. With respect to the different isoforms of PPRSV nsp2 that include PLP2, no studies have been carried out to assess the specific DUB activities of these variants and their functional contribution during infection.

## Bunyaviridae

Nairoviruses are enveloped, negative-sense ssRNA viruses within the family *Bunyaviridae*, which can be further subdivided into serogroups based on antibody cross-reactivities. The serogroups discussed here include the Crimean-Congo haemorrhagic fever serogroup, which includes the Crimean-Congo haemorrhagic fever virus (CCHFV); the Nairobi sheep disease serogroup, which include the Nairobi sheep disease virus (NSDV) and Dugbe virus (DUGV); and the Thiafora serogroup, which includes the Erve virus (ERVV). Nairovirus genomes share a similar structure, and are comprised of three ssRNA segments, small, medium and large (L), named as such for their respective nucleotide lengths.

CCHFV is a widespread tick-born virus that is transmitted to humans primarily by members of the *Hyalomma* genus [495]. Infection with CCHFV can lead to haemorrhaging and multi organ failure, with a case fatality rate ranging from 10-40%. Currently, there is no protective vaccine and treatment involves only basic management of CCHF symptoms. Contrary to CCHFV, DUGV infection does not lead to serious disease in humans, and is instead associated with mild febrile illness. In contrast, ERVV infections have been postulated to cause 'thunderclap headaches' in humans [496], with mice and shrews suspected as potential reservoirs for the virus [497].

### *Crimean-Congo haemorrhagic fever virus OTU*

In 2000, Makarova and co-workers published the discovery of a novel cysteine protease superfamily, based on sequence homology with the *Drosophila* OTU gene product [218]. While initially an OTU domain was identified at the N-terminus of the Dugbe virus L protein, sequence determination of the CCHFV L-segment later uncovered the presence of a homologous nairovirus OTU domain [498, 499].

Following the discovery that A20, a cellular protein with an OTU domain that negatively regulates NF-κB signalling via deubiquitination [500, 501], Frias-Staheli and co-workers investigated the role of viral OTU domains *in vivo* and demonstrated that the CCHFV OTU domain indeed possessed DUB activity, actively processing K48- and K63-linked polyUb chains, as well as ISG15 *in vitro*, and globally deconjugating Ub and ISG15 from cellular proteins during ectopic expression [219]. Expression of the CCHFV OTU domain diminished activity at an NF-κB-responsive promoter during TNFα stimulation, and established the CCHFV OTU domain as a viral protease involved in the evasion of the cellular innate immune response. The work culminated with the description of a chimeric Sindbis virus expressing the CCHFV OTU domain along with ISG15, which was found to increase lethality in IFN-α/β receptor$^{-/-}$ background mice, effectively preventing ISG15-mediated protection of Sindbis virus lethality. Following work demonstrated that the CCHFV OTU domain mitigates RIG-I-mediated IFN-β expression, suggesting that the enzyme inhibits both antiviral and pro-inflammatory branches of the innate immune response during infection [221].

Crystal structures of the CCHFV OTU domain were subsequently reported bound to Ub [222-224], full-length ISG15 [223] or the C-terminal β-grasp domain of ISG15 [224], as well as in its *apo* form [224], and together provided the first structural insights into a viral OTU protease. The

CCHFV OTU domain was found to contain α-helical and β-sheet lobes [223, 224], and closely resembled the structure of the eukaryotic OTU domain-containing protein from yeast (yOTU1) (Fig. 5A) [280]. The active site of CCHFV OTU was comprised of a cysteine-histidine-aspartic acid catalytic triad, arranged in catalytically competent geometry in all reported structures [223, 224], and while no side chains were suitably oriented to participate in the formation of the oxyanion hole, the backbone amide of the catalytic C40 and a nearby D37 were proposed to serve this function [223].

Interestingly, while Ub and ISG15 bound to CCHFV OTU in similar orientations (Fig. 5A and B), the β-grasp domains of these substrates were rotated ~75 degrees with respect to the orientation that Ub binds to a representative eukaryotic OTU DUB from yeast, yOTU1 (Fig. 5A). Interestingly, the alternate binding orientation of Ub and ISG15 to the CCHFV OTU was due, in-part, to the presence of a unique β-hairpin that forms a substantial part of the substrate binding surface on the viral enzyme (Fig. 5A). The β-hairpin structure was thus proposed to facilitate a rotated binding orientation for Ub that also accommodated basic residues within the C-terminal β-grasp domain of ISG15, which appear to prevent its interaction with the yOTU1 [223]. Using structure-guided mutagenesis, the DUB and deISGylating activities of CCHFV OTU could be decoupled by exploiting unique interactions between the OTU domain and its cognate substrates, targeting a helical arm structure conserved in most OTU domains in order to disrupt deISGylating activity, and a unique hydrogen bonding interaction occurring at the interface of Ub and the novel β-hairpin structure of CCHFV OTU [224].

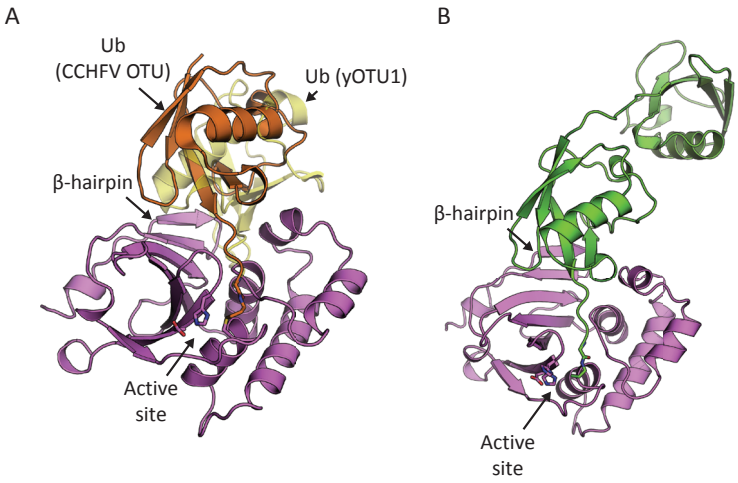


**Figure 5. CCHFV OTU interacts with Ub and ISG15 in a rotated orientation with respect to yOTU1**. (A) Comparison of the Ub-binding orientations of the CCHFV OTU and yeast OTU1 OTU (yOTU1) domains. CCHFV OTU (PDB ID: 3PT2; violet) is shown bound to Ub (PDB ID: 3PT2; orange), and the β-hairpin is indicated with an arrow. yOTU1 in complex with Ub (PDB ID: 3BY4) was superposed onto the CCHFV OTU structure, and yOTU1 was removed for clarity. The yOTU1-bound Ub domain is shown in transparent yellow. (B) Crystal structure of CCHFV OTU (PDB ID: 3PSE; purple) in complex with ISG15 (PDB ID: 3PSE; green). CCHFV OTU binds ISG15 in a comparable orientation to Ub.

*In vitro* work by multiple groups have shown that CCHFV OTU is active toward K6-, K11-, K48- and K63-linked diUb chains [224, 502]. It was also demonstrated that CCHFV OTU cleaves fluorogenic Ub-AMC and ISG15-AMC substrates, with some groups observing a preference for the Ub substrate [222, 224, 502], and others demonstrating similar activities toward both substrates [223]. Further, Akutsu and co-workers saw a marked increase in activity toward a fluorescent K63-linked diUb substrate compared to K48-linked diUb, providing kinetic evidence for CCHFV OTU linkage specificity [224]. While this demonstrates that CCHFV OTU may be somewhat capable of discriminating between Ub linkage types, structural evidence is necessary to confirm the molecular basis for the observed specificities. Recent advancements in CCHFV reverse genetics systems [503] may also soon enable studies that directly reveal the role of the DUB and deISGylating activities of the OTU domain during CCHFV infection.

*Dugbe virus OTU*

Similar to the CCHFV OTU domain, the DUGV OTU domain was found to be an effective DUB and deISGylase removing Ub and mISG15 in cell culture [219, 504], and a potent DUB *in vitro* cleaving K6-, K11-, K48- and K63-linked diUb [502]. It was also demonstrated that the DUGV OTU was ineffective at processing ISG15, and a description of the DUGV OTU crystal structure in complex with Ub, and a comparison with CCHFV OTU suggested the inability of DUGV OTU to process ISG15 was centralized around residue T128, which was unable to form a hydrogen bonding network with ISG15 comparable to the CCHFV OTU residue E128. The introduction of E128 to DUGV OTU indeed increased reactivity toward a fluorogenic ISG15 substrate by 2000% [502]. Additional similarities with the CCHFV OTU domain were found in its ability to down regulate cellular immune response pathways, where both NF-κB- and IFN-responsive promoter activity were disabled upon stimulation in the presence of DUGV OTU [504].

*Erve virus OTU*

In contrast to CCHFV and DUGV OTU domains, the ERVV OTU domain is essentially absent of DUB activity, processing activity against ISG15 only, with a particularly high affinity for hISG15 as determined by isothermal titration calorimetry [502, 505]. Analysis of a crystal structure of ERVV OTU in complex with mISG15 attributed the inability of ERVV OTU to bind Ub to the presence of an electrophilic region (R21, S132, N134) at the interface that binds ISG15, which appears able to accommodate ISG15 residue E87, but not the spatially conserved hydrophobic Ub residue L8 [505].

*Nairobi sheep disease virus OTU*

Transfection of Vero cells with NSDV OTU was found to reduce activity at the IFN-β, and IFN-responsive promoters in a protease-dependent fashion, demonstrating that NSDV OTU interferes with both the production and activity of IFN [506]. Further, NSDV OTU was shown to deubiquitinate and deISGylate cellular proteins during expression, thus establishing it as a deubiquitinating enzyme capable of interfering with the production and activity of IFN [506].

## Picornaviridae

Picornaviruses are small, non-enveloped positive-sense ssRNA viruses. Within the family *Picornaviridae*, several of viruses are known to cause disease in livestock, and indeed the foot-and-mouth disease virus (FMDV) was the first discovered animal virus [451]. As member of the *Aphthovirus* genus, FMDV remains an economically significant pathogen in the livestock industry. FMDV infection is characterized by the formation of vesicles on the feet and mouths of infected animals, and can lead to substantial economic losses due to decreased animal productivity and trade restrictions imposed on infected livestock. Certain members of the *Enterovirus* genus within the family *Picornaviridae* also cause disease in livestock, and recently an isolate of porcine enterovirus species G (EVG) was identified that contained a torovirus (ToV) PLP domain that appears to have been acquired through cross-order recombination [507].

*Foot-and-mouth disease virus $L^{pro}$*

Early research on FMDV identified a cleavage product originating from the N-terminus of the viral polyprotein [508]. The cleavage was initially proposed to result from a host protease, but was later found to be carried out autoproteolytically by a FMDV-encoded leader protease ($L^{pro}$) located within the N-terminus of the nascent polyprotein [509]. Translation of $L^{pro}$ can initiate at one of two in-frame start codons, leading to the production of $Lab^{pro}$ and $Lb^{pro}$ isoforms, the former having an additional 28 amino acids at the N-terminus.

Prior studies identified $L^{pro}$ as a potential virulence factor, with $L^{pro}$ cleaving the host eukaryotic translation initiation factor 4 G (eIF4G) that is involved in translation of cellular capped mRNA transcripts, thereby prioritizing the translation of viral transcripts [510]. Experiments using an FMDV mutant lacking the $L^{pro}$ domain also implicated the protease in the circumvention of cellular innate immune responses by inhibition of cellular IFN-α/β production and associated ISGs, specifically protein kinase R (PKR), a cytoplasmic sensor of viral RNA [511-515]. In an attempt to disrupt this activity, de Los Santos *et al.* generated an FMDV virus with point mutations I83A and L86A within $L^{pro}$, and as predicted, these mutations attenuated viral replication, with infection resulting in an increased in cellular IFN-β expression [516]. Notably the autoprocessing activity of the FMDV $L^{pro}$ mutant was unaffected, as was its ability to cleave eIF4G [516].

Early bioinformatics results predicted $L^{pro}$ to be a PLP [517, 518], sharing sequence similarity with MHV PLPs near the putative catalytic cysteine [519]. This was later confirmed upon determination of the $Lb^{pro}$ crystal structure, which also provided insight into the autocatalytic mechanism of $Lb^{pro}$ [518], and, in fact, represents the first structural characterization of a viral papain-like cysteine protease [518]. The C-terminal polyprotein cleavage site recognized by $Lb^{pro}$ was present in the crystallized construct, and found to occupy the active site of an adjacent $Lb^{pro}$ monomer, mimicking a product-bound complex (Fig. 6). While this *trans* interaction may suggest that $Lb^{pro}$ removal also occurs *in trans* within the context of polyprotein maturation, the authors proposed that removal of $Lb^{pro}$ may also occur *in cis*, due in part to the relatively weak intermolecular contacts between $Lb^{pro}$ monomers, and the propensity for the residues within extended C-terminus

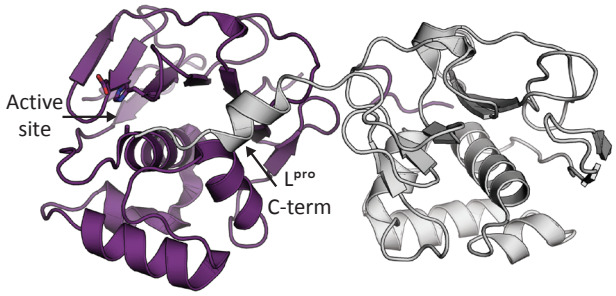


**Figure 6. Crystal structure of FMDV Lb$^{pro}$.** FMDV Lb$^{pro}$ (PDB ID: 1QOL) is shown in cartoon, and an adjacent monomer in the asymmetric unit is depicted in grey, with the C-terminus leading toward the active site of the adjacent Lb$^{pro}$ monomer.

of Lb$^{pro}$ turn over the protease and into the active site cleft. NMR results however, show that Lb$^{pro}$ exists as a homodimer in solution [520].

Wang *et al.* further investigated the structure of Lb$^{pro}$, and using secondary-structure matching discovered that it shared structural homology with SARS-CoV PL$^{pro}$ and the eukaryotic USP14, two previously characterized DUBs, which lead to the hypothesis that L$^{pro}$ may also possess DUB activity [521]. This was confirmed *in vitro*, where L$^{pro}$ cleaved K48- and K63-linked polyUb chains and globally deubiquitinated cellular proteins during ectopic expression [521]. Based on previous findings that the IFN-antagonist and eIF4G processing functions of L$^{pro}$ were apparently independent [516], Wang and co-workers sought to determine if the DUB and eIF4G processing activities were similarly uncoupled. Indeed, the previously characterized I83A/L86A L$^{pro}$ mutant was deficient in DUB and IFN-supressing activities, yet retained the ability to hydrolyse eIF4G, effectively linking the DUB and immunosuppressive properties of L$^{pro}$ [521]. Further, overexpression of L$^{pro}$ resulted in a reduction of Ub-conjugated RIG-I, TBK1, TRAF3, and TRAF6, providing evidence for the role of L$^{pro}$ in supressing host Ub-dependent innate immune signalling pathways via deubiquitination of cellular signalling components [521].

While a considerable amount of work has gone into the structural and functional characterization of L$^{pro}$, a number of questions remain. While the autocatalytic activity and substrate specificity of L$^{pro}$ have been characterized, which have led to the development of peptidomimetic compounds as potential inhibitors of L$^{pro}$ [522-524], the molecular basis for Ub recognition by L$^{pro}$ remains to be elucidated. Mutagenesis has been able to discriminate between the DUB activity and polyprotein/eIF4G processing activities of L$^{pro}$, however it is still unclear how these mutations exert their selective effect. It is interesting to note that I83A/L86A mutations targeted the SAF-A/B, Acinus, and PIAS (SAP) domain within L$^{pro}$ [516], and while these mutations selectively abrogate DUB activity [521] and delay nuclear translocation [516], they do not appear to target the likely Ub-binding interface of L$^{pro}$, which has been demonstrated to be an effective means to inhibit the DUB activity of other vDUBs [220, 327]. Further adding to the complexity of its role in innate immune suppression, L$^{pro}$ has been implicated in the degradation of NF-κB, although

this activity has not been demonstrated directly [515]. The structural characterization of $L^{pro}$ in complex with Ub should shed light on some of these questions.

*Enterovirus G ToV-PLP*

Recently, an EVG isolate was identified containing a previously unseen insertion between non-structural proteins 2C and 3A, flanked by $3C^{pro}$ cleavage sites [507]. Further analysis determined that the inserted sequence shared significant similarity with the Torovirus (a member of the order Nidovirales) nsp3-like PLP at the amino acid level, which was subsequently termed ToV-PLP. Homology modelling predicted structural similarities between ToV-PLP and the FMDV $L^{pro}$, leading to the hypothesis that ToV-PLP may possess DUB/deISGylating activities. These suspicions were confirmed, with ToV-PLP showing global DUB and deISGylating activity in cell culture, and *in vitro* analysis demonstrating that ToV-PLP processed ISG15, K48- and K63-linked polyUb chains, and curiously, showed activity toward M1 linear Ub chains [507]. Infection of swine testicular cells with recombinant EVG lacking ToV-PLP increased cellular type I and type II IFN production, as well as ISG15 transcription, and displayed impaired growth kinetics compared to its ToV-PLP-containing counterpart [507]. Although enteroviruses are known to have high rates of genetic recombination, the cross-order acquisition of a novel DUB by EVG is likely a rare event [507], and the apparent increase in viral fitness with respect to DUB-negative EVG further demonstrates the importance of vDUBs in supressing the innate immune response of their hosts.

## Tymoviridae

The turnip yellow mosaic virus (TYMV) is the type species of the family *Tymoviridae*, a group of positive-sense, ssRNA viruses infecting plants. Their non-structural proteins are expressed from two overlapping open reading frames, ORF-206 and ORF-69 [525], which encode for p206 and p69, respectively. The TYMV papain-like protease (PRO) domain is encoded within ORF-206, and cleaves the translation product, p206, at two sites releasing p98, p42 and p66 [526-529]. During infection by the virus, the host actively supresses accumulation of the TYMV RNA-dependent RNA-polymerase domain (POL), located in p66, by tagging it with K48-linked polyUb, targeting it to the Ub-proteasome system [530]. Appreciating that the TYMV PRO consensus site (K/R) LX(G/A/S)(G/A/S) [529] was compatible with the C-terminus of Ub, Chenon *et al.* suggested that PRO may counter this cellular defence mechanism by stabilizing the POL domain during infection via removal of the K48-Ub chains [340]. Indeed, PRO is able to process K48- and K63-polyUb chains *in vitro*, and pulse-chase analysis determined that expression of PRO stabilized p66 in a protease-dependent manner [340].

Hidden Markov Model comparison predicted that TYMV PRO shared secondary structure elements with a number of eukaryotic and viral OTU domains, and sequence similarities were identified surrounding the catalytic cysteine and histidine residues, in agreement with the characterized OTU domain [218, 340]. The crystal structure of the TYMV PRO domain revealed a compact protease domain, composed of α-helical and β-sheet lobes which hosted the catalytic cysteine

and histidine residues, respectively, as well as a unique N-terminal lobe (Fig. 7) [365]. A structural comparison using the DALI alignment server also detected significant structural similarities with previously reported viral and eukaryotic OTU domains, placing the TYMV PRO domain within the OTU superfamily [299]. In general, the active site of PLPs are canopied by a loop structure. The active site of PRO possesses no such loop, making its active site entirely solvent exposed [365]. Also absent was the third residue thought to align the histidine imidazole ring for proper catalysis. Taken together, the pared-down, solvent exposed active site of PRO was thought to account for its relatively poor DUB activity in comparison to other OTU DUBs, and the relaxed specificity of the enzyme at the P1 site [365]. Structural evidence for the *in trans* cleavage activity of PRO was also revealed, with the C-terminus of one PRO domain bound into the cleft leading toward the active site of a nearby symmetry mate (Fig. 7) [365]. Based on this structure, the strict requirements at P5 and P4 were rationalized by the presence of complementary acidic and hydrophobic pockets, respectively on the surface of PRO [365]. Further *in silico* docking studies predicted that the N-terminal lobe of PRO interacts with the hydrophobic I44 patch of Ub [365].

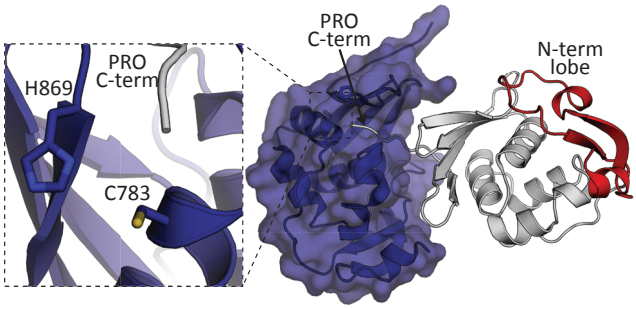


**Figure 7. Crystal structure of TYMV PRO.** The TYMV PRO domain (PDB ID: 4A5U; deep blue, transparent surface) is shown in cartoon. A symmetry mate (grey) is also shown, with the C-terminus bound in the active site of the adjacent PRO monomer. The N-terminal lobe is coloured red in the adjacent symmetry mate. Dotted box shows a close up of the pared-down PRO active site, with catalytic residues shown as sticks.

## CONCLUDING REMARKS

Significant effort has been dedicated to uncovering the cellular substrates and structural biology of vDUBs, and the role of these enzymes during infection is now beginning to emerge. However, more work is needed is clarify the picture, since many experiments used to ascertain the cellular targets of vDUBs have relied on overexpression experiments, and thus may not accurately reflect the circumstances of an actual viral infection. Both the cellular ubiquitination system, and viral protein expression are dynamic processes, with the temporal and spatial regulation of these events likely playing a significant role in determining which substrates are accessible to a given vDUB. To complicate matters further, vDUB domains often exist within larger, multi-domain proteins, some of which are membrane bound, yet they are often studied in isolation as soluble

cytoplasmic proteins in cell culture, likely unable to exhibit subcellular localization patterns which would be found under biologically relevant conditions. Moreover, additional viral factors present during infection may influence the substrate specificity of a vDUB in question. Indeed, emerging technologies are addressing some of the challenges in accurately analysing Ub-dependent signalling pathways, with powerful mass spectrometry and proteomics methods targeted at probing the dynamics of these systems, including the stoichiometry and kinetics of Ub conjugation, and the specific linkage types populating cellular substrates of interest [531]. These technologies could now be directed towards revealing the cellular targets and linkage specificities of vDUBs during the course of live virus infection. Further, it is pertinent to recognize that in cases where a viral protease depends on a single active site for both DUB and proteolytic (*i.e.* non-isopeptide bond cleavage) activity, a complete understanding of their genuine cellular targets necessitates the selective inhibition of DUB activity, as described for a select number of multifunctional vDUBs [220, 327, 521].

Protein X-ray crystallography has provided remarkable insights into the molecular basis for how vDUBs recognize and bind monoUb, yet significant questions remain regarding their ability to recognize a particular Ub linkage type. To date, a single example of a vDUB in complex with a diUb substrate has been described [236]; however, exciting new approaches to generate polyUb probes of varying linkage types [532, 533] will now undoubtedly enable rapid advances in understanding the structural basis for the recognition of specific linkage types by vDUBs. The recent characterization of several bacterial DUBs has also advanced our understanding of the interplay between the cellular ubiquitination pathways and pathogenic bacteria at a structural level, and highlighted key variable regions within bacterial clan CE proteases permitting adaptation to Ub/Ubl domains and specific Ub linkage types [534].

It is now clear that interfering with Ub-dependent cellular processes through deubiquitination is a powerful strategy used by viruses to promote their survival, as evidenced by the large number of DUBs found in diverse virus lineages. While we have made every effort to include all vDUBs expressed by RNA viruses that have been described to date, many more undoubtedly remain to be discovered and characterized. Given the growing body of evidence demonstrating the importance of vDUB activity in viral replication and pathogenesis, vDUBs are now recognized as attractive targets for the design of antiviral therapeutics. Small-molecule inhibitors of vDUBs, and novel, selective protein-based approaches to disrupting the proteolytic activity of vDUBs are under active investigation, alongside the development of novel live attenuated virus vaccine candidates with impaired DUB activity. Selective targeting of vDUBs by therapeutic intervention, or through genetic-based disruption thus holds promising potential for the design of future antivirals and vaccines.

# 7 General discussion

## OUTLINE

The emergence of zoonotic coronaviruses (CoVs) like severe acute respiratory syndrome (SARS) CoV and Middle East respiratory syndrome (MERS) CoV has created awareness that these pathogens are able to create major public health problems on a global scale. These two pathogenic CoVs originate from bats and it is of concern that bat species currently continue to carry SARS-like CoVs, some of which can even infect human cells without prior adaptation, i.e. they can bind efficiently to the human angiotensin-converting enzyme 2 (ACE2) receptor [22]. Similarly, the spike (S) glycoprotein from a MERS-related CoV isolated from bats was able to bind human dipeptidyl peptidase 4 (hDPP4), suggesting it could enter human cells [536]. These and other studies demonstrate that bat CoVs can jump to the human host, as was earlier also proposed for other human CoVs [54-56], and suggest they have the potential to adapt and cause outbreaks.

Coronavirus infection in humans can either be asymptomatic or cause disease ranging from mild symptoms to severe pneumonia that - mostly together with other complications - can cause the death of the infected individual. The more severe symptoms are often observed after infection with emerging zoonotic CoV species. Consequently, characterization of CoVs is pivotal to be able to design approaches to prevent and treat ongoing infections, but also to create strategies to counter future emerging CoVs. Nowadays, the latter is critical because transmission may occur more often due to the intensified ecological relationships between humans and animals, increased population densities, and the ever-increasing frequency of global travel.

For (re-)emerging positive-stranded RNA viruses, viral proteases are interesting and highly "druggable" targets for antiviral therapy. They play an essential role in the virus replication cycle by cleaving replicase polyprotein(s) into functional subunits. Additionally, it has been shown that many of these proteases target host proteins to manipulate cellular processes and counteract innate immunity to promote infection [334]. Likewise, the CoV papain-like protease (PLP) domain in non-structural protein (nsp) 3 is involved in polyprotein processing, but it also functions as a deubiquitinating enzyme (DUB) and has deISGylating activity, which both have been implicated in suppression of the innate immune response. In collaboration with Dr. Brian Mark and his team, we solved the crystal structure of MERS-CoV $PL^{pro}$ in complex with ubiquitin (Ub), which facilitated design of DUB-inactivating mutations in $PL^{pro}$ (Chapter 2). DUB-negative MERS-CoV was found to be attenuated in a mouse model, which was accompanied by an earlier induction of interferons (IFNs), IFN-stimulated genes (ISGs), and pro-inflammatory cytokines relative to infection with wild-type (wt) MERS-CoV (Chapter 3). This study provided the first direct evidence that the DUB activity of MERS-CoV $PL^{pro}$ enhances virulence through innate immune suppression. Since we thus discovered how $PL^{pro}$ binds Ub, this knowledge was used to explore the potential of ubiquitin sequence variants (UbVs) as an antiviral strategy. As an alternative for small-molecule protease inhibitors, a large phage-display library was used to select UbVs that have high affinity for the vDUBs of MERS-CoV or Crimean-Congo haemorrhagic fever virus (CCHFV) and inhibit their proteolytic activity (Chapter 4). Optimization of UbVs that target MERS-CoV $PL^{pro}$ yielded vari-

ants with enhanced stability (Chapter 5), which will be tested in an animal model for MERS-CoV infection in the near future, to assess the level of protection they can provide. The structure and function of known viral DUBs (vDUBs) originating from RNA viruses, including CoVs, was reviewed in Chapter 6. Here, in Chapter 7, the different activities and (potential) targets of CoV PLPs will be discussed in more detail, together with remaining questions and approaches to address these. Reducing vDUB activity as a strategy to attenuate viruses "by-design" during modified live virus (MLV) vaccine development will be discussed. Also, the UbV platform will be compared with previously described small-molecule protease inhibitors and the therapeutic potential of UbVs will be discussed.

## FUNCTIONAL CHARACTERIZATION OF CORONAVIRUS PAPAIN-LIKE PROTEASES

### Polyprotein processing

*PLP-driven processing of the N-terminal region of CoV replicase polyproteins*

In the late 1980s, multiple proteases were predicted to be encoded by the genomes of CoVs (and related nidoviruses) and they were anticipated to have an important role during replication [98]. The nsp3-encoded PLPs were found to cleave the replicase polyproteins at specific sites [212-214], thereby releasing nsp1 to 3, of which the latter is also crucial for the assembly of viral replication organelles [83, 84, 95, 537]. Interestingly, the nsp3 subunits of α- and β-CoVs generally contain two PLPs (designated as PLP1 and PLP2), but the β-CoVs SARS-CoV and MERS-CoV express only one PLP (designated as $PL^{pro}$) in nsp3. Also γ-CoVs have two PLP domains, but only one is functional in polyprotein processing and therefore is also called $PL^{pro}$, and δ-CoV nsp3 contains one putative $PL^{pro}$. $PL^{pro}$s and PLP2s cleave sites with the consensus motif K-X-G-G↓X-X (from P4-P2', with X being any amino acid) and these proteases have the ability to cleave both *in cis* and *in trans* [205, 228, 266, 476] (Chapter 2). In CoV species with two functional PLPs, the processing of the nsp1-3 region can follow alternative pathways, but in all cases PLP2 cleaves the nsp3↓4 site. In the first pathway, as observed for instance for human CoV (HCoV) 229E, PLP1 and PLP2 can both process the nsp1↓2 and nsp2↓3 sites, but PLP1 preferably cleaves the nsp1↓2 site while PLP2 is more likely to cleave the nsp2-3 site [363, 538]. In contrast to PLP2, PLP1 was found to be dispensable for HCoV-229E replication, since replacement of the PLP1 catalytic residues yielded a viable virus, although virus growth was affected and reversion was observed after a few passages in cell culture, indicating that the virus benefits from the proteolytic activity of PLP1 [363]. The second pathway for nsp1-3 processing is exemplified by mouse hepatitis virus (MHV), where PLP1 cleaves both the nsp1↓2 and nsp2↓3 sites while PLP2 only cleaves the nsp3↓4 site. Changing the nsp1↓2 and nsp2↓3 sites to the sequence of the nsp3↓4 site resulted in PLP2-driven processing of the mutated nsp2↓3 but not the mutated nsp1↓2 site [539]. This suggests that there are additional determinants for polyprotein cleavage besides the presence of a cleavable site.

*Interactions between PLP and their polyprotein substrate*

Besides the scissile bond, another likely requirement for polyprotein processing is the (transient) interaction of PLP with specific parts of the nsp(s) in the vicinity of the cleavage site. To better understand these interactions, it would be informative to solve the crystal structure of PLP in complex with larger polyprotein domains containing the nsp1↓2, nsp2↓3 or nsp3↓4 cleavage sites. Such a substrate could be expressed in *E. coli*, purified and subsequently incubated with a PLP active site mutant so that the substrate would not be cleaved. Strikingly, the N-terminal region of nsp3 contains a Ub-like (Ubl) domain, which may play a role in the binding and subsequent cleavage of the upstream nsp2↓3 site by PLPs, as CoV PLPs can also bind Ub, which will be further discussed in the next paragraph. The results of structural studies, as proposed above, might shed light on the interplay between PLPs and the larger polyproteins of which they are part, which, after all, are the most important substrates of the enzyme. Understanding these interactions will also simplify PLP mutagenesis to explore secondary functions, like DUB activity, since it is a prerequisite to preserve the essential polyprotein processing activity of the mutated PLP in order to investigate substitutions in the context of infection. Consequently, we and others always used transient expression systems to verify that the polyprotein processing function was intact, even though the PLP substitutions introduced to prevent Ub-binding were distant from the enzyme's active site (Chapter 2) [207, 336].

Crystallization efforts have yielded insights into the structure of CoV PLPs. Multiple studies noted that the oxyanion hole of MERS-CoV $PL^{pro}$, but not that of SARS-CoV $PL^{pro}$, appeared to be incomplete (Chapter 2, [291, 371]). This might be a reason for the lower proteolytic activity of MERS-CoV $PL^{pro}$ for the substrate peptide R-K-R-G-G-7-amido-4-methylcoumarin (AMC) relative to the activity of SARS-CoV $PL^{pro}$ [235]. To provide hydrogen bonds that can stabilize the oxyanion transition state, MERS-CoV $PL^{pro}$-L1587W was engineered and this mutant protease indeed displayed increased peptide-hydrolysing activity while its DUB activity was only slightly higher [290, 291]. We introduced this substitution into the full-length pBAC-MERS-CoV clone, launched the mutant virus and found it to have a similar plaque phenotype as wt virus, while also growing to wt titers in HuH-7 and MRC5 cells (Fig. 1). These initial results suggest that the putative restoration of the oxyanion hole of the active site has no effect on virus growth in cell culture, although more subtle differences might exist, for example at the level of polyprotein processing, genomic or subgenomic mRNA copy numbers, or the protease's capability to suppress innate immunity. It will therefore be interesting to test this mutant virus also in an animal model for MERS-CoV infection and compare its virulence to that of the wt virus.

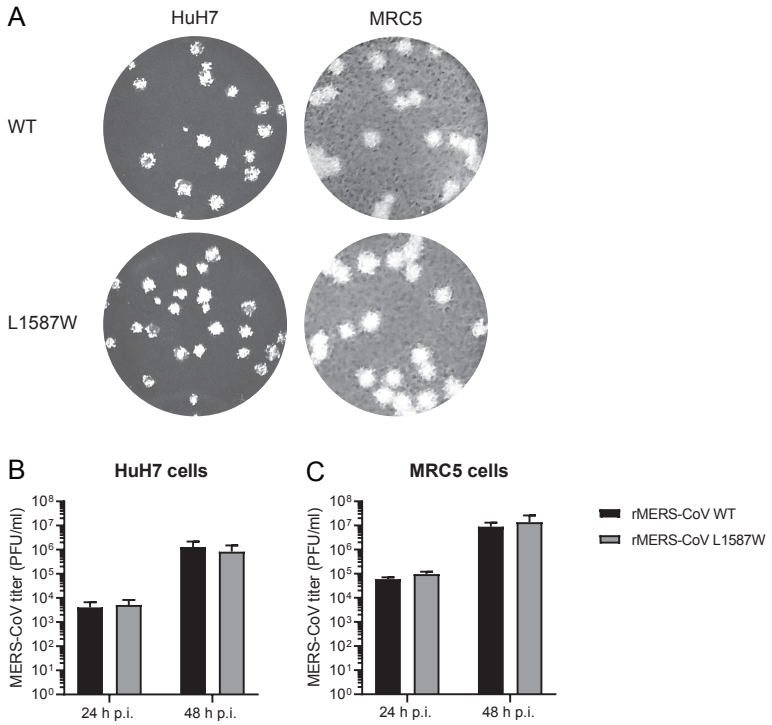


**Figure 1. Analysis of MERS-CoV PL$^{pro}$ mutant L1587W.** Plaque phenotype of wt and L1587W rMERS-CoV on HuH-7 and MRC5 cells is presented in (A). A multiplicity of infection of 0.01 was used to infect HuH-7 cells (B) or MRC5 cells (C) with wt or L1587W rMERS-CoV. At the indicated time points, virus progeny titers in the culture supernatants were determined by plaque assay on HuH-7 cells. Infections were repeated independently three times and the error bars represent the standard deviation.

## Deubiquitinating activity

*Coronavirus PLPs can bind Ub(-like) proteins and remove them from substrates*

Sequence alignments initially did not provide clues to the fact that CoV PLPs could be vDUBs. In general, (human) DUBs within the Ub-specific protease (USP) family share low sequence similarity and, due to fast evolution, viral variants may have markedly diverged from the originally acquired sequence. Sequence conservation is limited to the catalytic domain that contains the catalytic triad composed of cysteine, histidine and aspartic acid residues [211]. The DUB activity of CoV PLPs was first demonstrated for SARS-CoV PL$^{pro}$ and later also for MERS-CoV, avian infectious bronchitis virus (IBV), and transmissible gastroenteritis virus PL$^{pro}$ and for the PLP2s of HCoV-NL63, porcine epidemic diarrhoea virus, and MHV ([196, 197, 199, 201, 202, 208, 231, 232] and reviewed in Chapter 6 and [206]). Recently, PLPs from bat CoVs, both closely and distantly related to SARS-CoV PL$^{pro}$ with 86% and 39% amino acid sequence identity, respectively, were also proven to possess DUB activity [336]. Additionally, CoV PLPs can cleave some Ubl proteins from substrates, such as interferon-stimulated gene 15 (ISG15) and neural precursor cell expressed de-

velopmentally downregulated protein 8 (NEDD8), but not others like small Ubl modifier (SUMO) [198, 199, 202, 208, 382].

Ub can form polyUb chains that can be differently linked depending on the residue that is used for the conjugation of the next Ub moiety. Well-studied are K48- and K63-linked Ub chains that are known for their function in proteasomal degradation and cell signalling, respectively [145]. The function of many other polyUb chains is still unclear, nevertheless, it is interesting to determine whether vDUBs have a preference for a specific Ub linkage type. Purified MHV PLP2 and SARS/MERS-CoV $PL^{pro}$ display no clear specificity for diUb linkages, although it was shown that they cannot cleave linear diUb and possibly K27-linked diUb [208, 234, 235]. It remains a mystery why CoV PLPs cannot process linear Ub chains, because these proteases also cleave linear peptide bonds during replicase polyprotein processing. Like CoV PLPs with DUB activity, human USPs are known for their modest Ub chain preference in contrast to, for example, ovarian tumour (OTU)-domain DUBs, which can be linkage specific [237-239]. Thus far, only a subset of USPs showed linkage type preferences, like USP30 that has preference for K6 linkages, CYLD that prefers linear and K63 linkages and USP18 that has a preference for cleaving ISG15 from its substrates [540, 541].

To enhance our understanding of Ub-binding, we and others solved the structures of SARS-CoV and MERS-CoV $PL^{pro}$ in complex with Ub (Chapter 2, [207, 297, 470] and reviewed in Chapter 6). MonoUb binds in the S1 Ub-binding site of $PL^{pro}$, which includes part of the fingers domain that interacts with the hydrophobic patch of Ub formed by residues L8, I44 and V70 [300], and the substrate channel that binds the C-terminal tail of Ub leading towards the catalytic residues of the active site. Cleavage of diUb requires binding of the proximal Ub in the S1' Ub-binding site and the distal Ub in the S1 site. For clarity, the proximal Ub is the initial Ub of a chain that is attached to a substrate, while distal Ubs are attached to this first Ub through one of the possible linkage types [301]. When a DUB has more Ub-binding sites, these are numbered consecutively; for example S2' S1', S1, S2, and so forth. Specificity towards a linkage type is dictated by interactions between Ub and the DUB, mostly in the S1 and S1' Ub-binding sites and sometimes this is aided by binding of a third Ub in the chain to the S2 Ub-binding site. In contrast with the cleavage of diUb linkages, when longer Ub chains were incubated with purified CoV PLPs, it was demonstrated that SARS-CoV $PL^{pro}$ has a clear preference for K48-linked Ub chains, unlike MERS-CoV $PL^{pro}$ (Chapter 2, [207, 235, 236]). MERS-CoV $PL^{pro}$ and MHV PLP2 process K48-linked and K63-linked polyUb chains into monoUb moieties, suggesting binding in the S1-S1' sites [208, 234-236, 382]. In contrast, SARS-CoV $PL^{pro}$ preferentially hydrolyses K48-linked polyUb chains but in a di-distributive manner [236], meaning that when K48-linked polyUb chains are cleaved, K48-linked diUb accumulates, whereas cleavage of K63-linked polyUb produces monoUb [197, 207, 234, 235]. So far, this phenomenon has only been observed with SARS-CoV $PL^{pro}$ *in vitro*, and therefore it will be important to establish whether K48-linked diUb accumulate in SARS-CoV-infected cells as well. Purified SARS-CoV $PL^{pro}$ was shown to bind K48-linked diUb chains in the S1 and S2 Ub-binding sites instead of the S1-S1' Ub-binding sites, which is the way in which MERS-CoV $PL^{pro}$ binds diUb [236, 382]. SARS-CoV $PL^{pro}$

with K48-linked diUb bound in its S1 and S2 Ub-binding sites was crystallized and subsequent mutagenesis revealed a dominant role for the S2 site in binding this diUb [236]. Besides strong binding of K48-linked diUb in the S1 and S2 sites, SARS-CoV $PL^{pro}$ displays a preference for a K48 linkage across the S1-S1' sites [236]. Overall, this strongly suggests that SARS-CoV $PL^{pro}$ prefers to cleave K48-linked Ub chains over other linkage types, which could suggest that $PL^{pro}$ removes those Ub chains to prevent degradation of (yet unknown) substrates, whereas no clear preference for specific Ub linkage types was observed for MERS-CoV $PL^{pro}$ *in vitro* [235, 236].

*Specific disruption of the DUB activity of CoV PLPs*

To study the DUB activity of MERS-CoV $PL^{pro}$ without affecting polyprotein processing, we abolished this activity by mutating $PL^{pro}$ residues that directly interact with Ub, thus preventing substrate binding (Chapter 2). Of the various tested substitutions, the most effective $PL^{pro}$ substitution concerned V1691, of which the hydrophobic side chain interacts with I44 of Ub (Chapter 2, Fig. 2A). Modification of the Ub-binding surface by targeting V1691 had different outcomes depending on the introduced substitution. On the one hand, inserting a bulky and positively charged R resulted in the loss of $PL^{pro}$'s DUB activity while, on the other hand, a small residue like alanine did not change DUB activity. This illustrates that, when targeting Ub-binding residues of PLP, both their position and the specific substitution made may determine the outcome, which should thus be an important consideration when designing such a mutagenesis approach.

Previously, other laboratories also tried to specifically disrupt CoV PLP DUB activity. For SARS-CoV $PL^{pro}$, substitutions were introduced in the ridge region of the thumb domain of $PL^{pro}$, which is part of the S2 Ub-binding site [207]. Changing F1609 to serine/alanine had the most pronounced effect and reduced DUB activity and NF-κB antagonism in cell-based assays [207]. Later, it was found that this F1609 residue, together with E1610 and H1613, is near I44 of the distal Ub of a K48-linked diUb, which is present in the S2 Ub-binding site (Fig. 2B) [236]. Mutagenesis of these $PL^{pro}$ residues reduced the processing of K48-linked diUb and longer Ub chains, but - as anticipated - did not affect processing of monoUb-AMC [236]. M1748 of SARS-CoV $PL^{pro}$, the equivalent of MERS-CoV V1691, interacts with I44 of the proximal Ub of a K48-linked diUb in the S1 Ub-binding site (Fig. 2C). The M1748S substitution reduced DUB activity of $PL^{pro}$ against all substrates tested [236]. The effects of these substitutions designed by Bekes *et al*. were only tested *in vitro* and it would be informative to also evaluate these mutant $PL^{pro}$s by ectopic expression in cell-based assays [236]. Recently, following up on our published structural study, a SARS-CoV M1748R mutant was generated [336]. The growth kinetics of this DUB-negative virus was slightly delayed compared to the parental virus but an upregulation of IFN-β mRNA was measured [336]. The results of this study by Niemeyer *et al*. [336] are in line with our results (Chapter 3), demonstrating that the DUB activity of CoV PLPs suppresses the innate immune response.

Interactions between MHV PLP2 and Ub were modelled based on the SARS-CoV $PL^{pro}$-Ub structure, and MHV residue F1812, another equivalent of MERS-CoV V1691, was proposed to interact with I44 of Ub (Fig. 2D) [208]. As expected, replacing this residue with alanine reduced

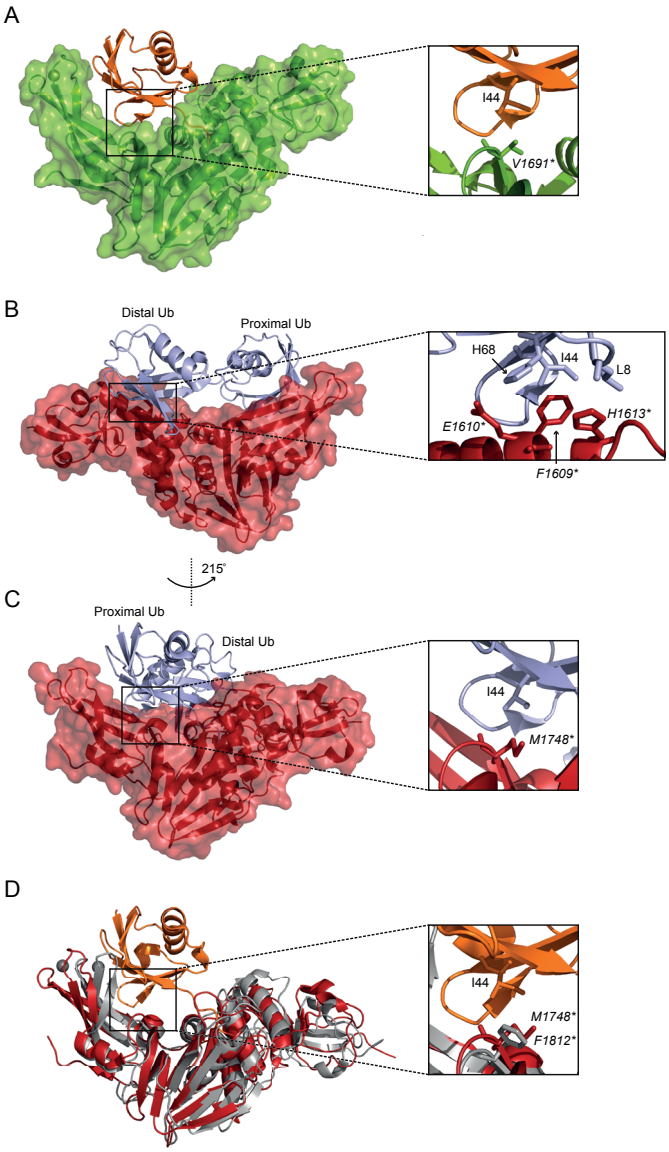


**Figure 2. Interactions between CoV PLPs and Ub.** (A-D) Shown in sticks are important residues of CoVs PLPs and Ub, labelled in italics with asterisks or in regular font, respectively. (A) Crystal structure of MERS-CoV $PL^{pro}$ in complex with Ub (PDB ID: 4RF0; Chapter 2). $PL^{pro}$ is shown in green as cartoon with transparent surface, and Ub in orange cartoon. Dotted box depicts close up of the hydrophobic interaction between V1691 of $PL^{pro}$ in the S1 Ub-binding site with I44 of Ub. (B and C) Crystal structure of SARS-CoV $PL^{pro}$ in complex with K48-linked diUb (PDB ID: 5E6J; [236]). $PL^{pro}$ is depicted in red as cartoon with transparent surface, and K48-linked diUb in slate cartoon. (B) Inset is a close up of the interaction between residues of the S2 Ub-binding site of $PL^{pro}$ with the distal Ub of the K48-linked diUb. (C) Interaction between M1748 in the S1 Ub-binding site and I44 of the proximal Ub of the K48-linked diUb is shown in the inset. (D) Superposition of MHV PLP2 (PDB ID: 4YPT; [208]; flanking N-terminal domain, amino acids 1525-1607 of MHV pp1a/pp1ab, is removed in this structure) with the complex of SARS-CoV $PL^{pro}$-Ub (PDB ID: 4MM3; [207]). MHV PLP2 is shown as grey cartoon, and SARS-CoV $PL^{pro}$ is shown in red as cartoon, and Ub in orange cartoon. Inset is a zoom in on the interaction between M1748 of SARS-CoV $PL^{pro}$ with I44 of Ub and the equivalent of this residue for MHV is displayed (F1812).

PLP2's DUB activity and its ability to suppress innate immune signalling pathways upon ectopic expression of PLP2 [208]. In the case of MHV PLP2, however, introduction of an alanine was sufficient because it replaced the large aromatic phenylalanine and thus prevents the hydrophobic interaction with I44 of Ub. Unfortunately, most of the substitutions in SARS-CoV $PL^{pro}$ and MHV PLP2 described above have not yet been tested in the context of a virus mutant. For SARS-CoV, it would be interesting to analyse mutant viruses with substitutions in the S1 binding surface, which have no DUB activity at all, or with substitutions in the S2 binding surface only, which should specifically reduce activity towards K48-linked Ub chains, and compare the features of such mutants to those of wt virus. To study the DUB function of other CoV PLPs, the approach that will most likely be successful is targeting the S1 residue that interacts with I44 of Ub. To identify that residue, a sequence alignment can be used or a structure model of the PLP of interest could be generated and aligned with solved structures of other CoV PLPs in complex with Ub.

## DeISGylation activity

*Species-dependent function of ISG15?*

Type I IFNs induce the expression of ISGs, which generally are antiviral effector proteins that limit virus replication [136]. ISG15 is one of the most strongly induced ISGs in many cell types and is composed of two connected Ubl domains that share the β-grasp fold of Ub. In a similar fashion as Ub, ISG15 can be conjugated to newly synthesized proteins, which requires the action of an E1 activating enzyme (Ube1L), an E2 conjugating enzyme (UbCH8), and an E3 ligase (Fig. 3) [542, 543]. Expression of all these enzymes required for ISG15 conjugation is also induced by type I IFNs. In contrast to Ub, only monoISGylation takes place, and no polyISG15 chains can be formed. Deconjugation of ISG15 is performed by USP18, which is the only known ISG15-specific cellular protease [540]. Inside the cell, ISG15 thus exists in two forms, either conjugated to a variety of proteins or unconjugated. Furthermore, ISG15 can be released from the cell and act as a cytokine that induces the production of IFN-γ in T-cells and natural killer cells (Fig. 3) [544, 545], thus forming a bridge between the innate- and adaptive immune systems.

Murine ISG15 (mISG15) $^{-/-}$ mice, as well as $Ube1L^{-/-}$ mice (the latter do express mISG15 but fail to conjugate it due to the absence of the E1 conjugating enzyme), are more susceptible to infection with Sindbis virus and influenza A and B virus, supporting the view that conjugation of mISG15 is important for antiviral immunity in mice (Fig. 3A) [339, 383]. The antiviral effects of ISG15 were also observed in tissue culture, via different mechanisms, as cellular or viral proteins were ISGylated thereby inhibiting replication or other steps of the viral cycle [339]. Surprisingly though, recent findings challenge this notion and suggest that human ISG15 (hISG15) does not play a role in antiviral immunity, as was shown for herpes simplex virus 1, Sindbis virus and vesicular stomatitis virus (Fig. 3B) [406, 546]. Instead, hISG15 deficiency is associated with impaired IFN-γ-mediated immunity, due to the lack of secreted ISG15, and increased susceptibility to mycobacterial disease [406]. Additionally, enhanced IFN-α/β responses were observed in hISG15-deficient patients, because USP18 protein levels were also reduced in cells of these patients [407].

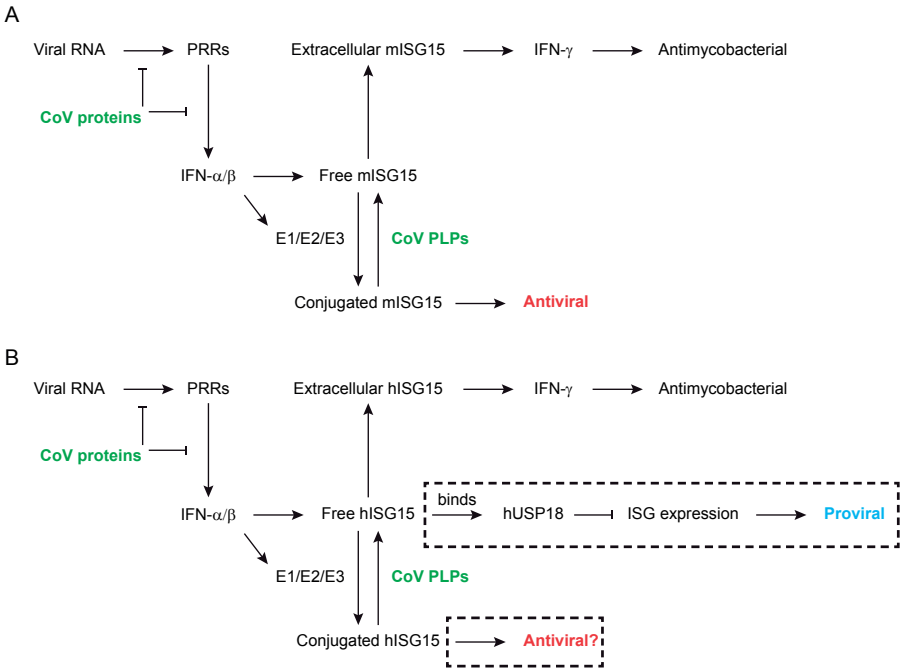


**Figure 3. Interplay between CoV PLPs and ISG15.** Overview of the production and function of ISG15 in mice (A) and humans (B), and the potential role that CoV PLPs with their deISGylation activity can play in these pathways during an infection. Differences in the human pathway, relative to in mice, are indicated by dashed boxes, and with green the interaction of CoV proteins with the pathways is shown. Viral RNA can be sensed by pathogen recognition receptors (PRRs) resulting in activation of a signalling pathway leading to the production of type I IFNs, IFN-α/β, that subsequently can induce the expression of ISGs, like ISG15 and the E1/E2/E3 enzymes. Free intracellular ISG15 can be conjugated to protein targets by means of those three enzymes, and in mice conjugated ISG15 has antiviral activity while this is debated in humans. Free hISG15, but not mISG15, can bind to USP18, thereby delaying degradation of USP18. This drives inhibition of the type I IFN response as USP18 does interact with the IFN-α/β receptor to disrupt type I IFN signalling. Both hISG15 and mISG15 can also function extracellularly as a cytokine and induce expression of IFN-γ that was proven to be antimycobacterial.



USP18 is a negative regulator of the type I IFN response, independent of its deISGylation activity, since it binds to the IFN-α/β receptor and subsequently inhibits the Janus kinase (JAK) and signal transducers and activators of transcription (STAT) pathway [547]. It was found that hISG15 binds to USP18 non-covalently. If this occurs, S-phase kinase-associated protein 2 (SKP2)-mediated proteolysis of USP18 is reduced, leading to higher USP18 levels and thus more suppression of the type I IFN response (Fig. 3B) [407]. Interestingly, this is not the case for mISG15, as it does not bind to mUSP18, and therefore mISG15 deficiency is not associated with downregulation of IFN-α/β signalling [546]. Unlike Ub, which is highly conserved across species, ISG15 is only weakly conserved and this may be a reason for the differences in USP18 binding and ISG15 function between species. The structure of mISG15 was compared to that of hISG15, revealing a considerable difference in the arrangement of the N- and C-terminal domains [461]. Such variation in interdomain arrangement among ISG15s from different species was also observed in the structures

of bat and bovine ISG15 [548-550]. Moreover, due to variation in their amino acid sequences, the electrostatic surfaces of mISG15 and hISG15 are quite different [461].

*Coronavirus PLPs bind and remove ISG15 from substrates*

Viruses can directly target the ISG15 pathway to evade host antiviral responses in mice, while the purpose of this evasive function in human-infecting viruses remains enigmatic [383]. Coronavirus PLPs can cleave ISG15 from substrates and for most purified PLPs the intrinsic activity towards ISG15-AMC is even higher than towards Ub-AMC, suggesting that ISG15 might be PLP's preferred substrate, with the exception that *in vitro* SARS-CoV $PL^{pro}$ prefers K48 polyUb chains over ISG15 [198, 199, 202, 207, 208, 235, 236]. Expression of the CoV PLP domain in cells generally results in an overall reduction of ISG15-conjugates [199, 202]. In an early report, Lenschow and co-workers developed a Sindbis virus vector that can be used to express mISG15 in a IFN-α/β receptor negative background, and showed that ISG15 conjugation protected mice from lethal Sindbis virus infection [551]. Internal ribosome entry site-driven co-expression of catalytically active SARS-CoV or MERS-CoV $PL^{pro}$ abrogated this protection, indicating that $PL^{pro}$-mediated deISGylation can promote Sindbis virus infection in this system [552]. Nevertheless, it would be more relevant to test the effect of PLP's deISGylation activity in the context of a CoV infection. The lack of conservation in the sequence and structure of ISG15 and the apparently different functions of ISG15 across species make it important to study CoVs in their natural host, which for MERS-CoV could be bats, camels or humans. It was demonstrated that SARS-CoV and MERS-CoV $PL^{pro}$s can cleave hISG15, mISG15, camel ISG15, and bat ISG15, whereas MHV PLP2 preferably hydrolyses mISG15 [461]. Interestingly, the C-terminal domains of hISG15 and mISG15 bound to SARS-CoV $PL^{pro}$ with a different orientation. Whereas hydrophobic interactions are primarily driving hISG15-binding, electrostatic interactions mediate binding of mISG15 to SARS-CoV $PL^{pro}$ [461].

*Specific disruption of CoV PLP deISGylation activity*

We studied the DUB activity of MERS-CoV $PL^{pro}$ by modifying the Ub-binding surface of $PL^{pro}$ to prevent Ub binding and thus disrupt its DUB activity (Chapters 2 and 3). A similar approach could be applied to determine the importance of PLP's deISGylation activity. It is predominantly the C-terminal domain of hISG15 (ChISG15) that interacts with MERS-CoV $PL^{pro}$ and the co-crystal structure of these domains revealed specific interactions [384]. The conformation of $PL^{pro}$ in complex with ChISG15 resembles the closed state observed when $PL^{pro}$ binds Ub (Chapter 2), but hISG15 is oriented somewhat differently than Ub relative to $PL^{pro}$ (Fig. 4A and B) [384]. Consequently, specific substitutions in the hISG15-binding surface of $PL^{pro}$ could abolish its deISGylation activity without affecting the DUB activity or polyprotein processing functions of $PL^{pro}$ [384]. The MERS-CoV $PL^{pro}$-ChISG15 co-crystal structure indicates that K1657 of $PL^{pro}$ forms a salt bridge with E132 of hISG15, whereas this same $PL^{pro}$ residue has no interaction with Ub (Fig. 4C). Mutagenesis of K1657 to leucine, alanine or glutamic acid reduced cleavage of ISG15-AMC, whereas no difference was measured when Ub-AMC and peptide-AMC were used as substrates [384]. The most

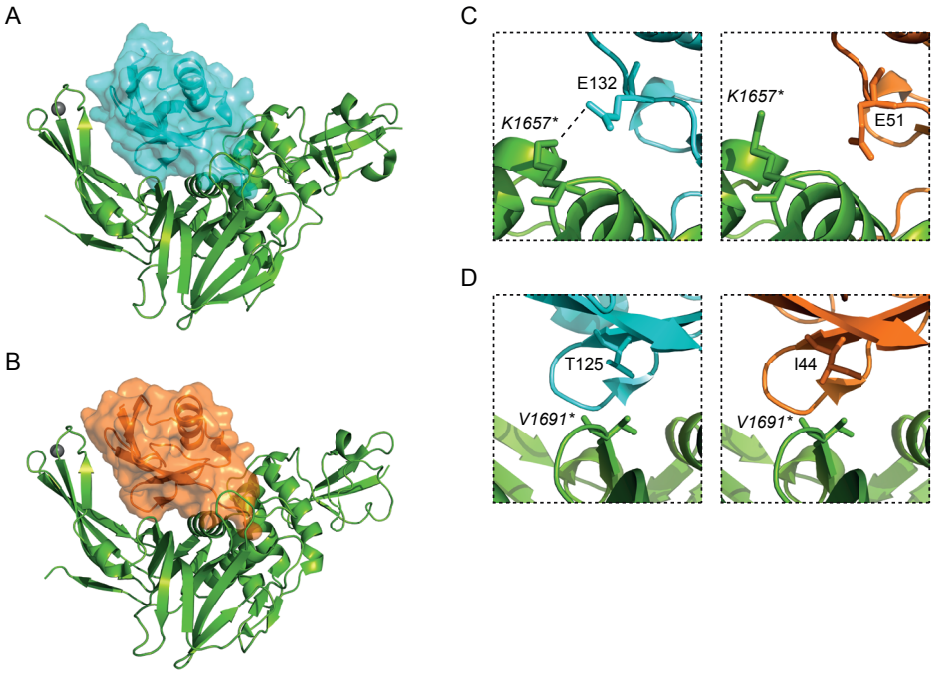


**Figure 4. Interaction between MERS-CoV PL$^{pro}$ with hISG15 or Ub.** (A) MERS-CoV PL$^{pro}$ in complex with ChISG15 (PDB ID: 5W8T; [384]). PL$^{pro}$ is depicted as green cartoon and ChISG15 as cartoon with transparent surface in cyan. (B) MERS-CoV PL$^{pro}$ in complex with Ub (PDB ID: 4RF0; Chapter 2) with PL$^{pro}$ as green cartoon and Ub in orange as cartoon with transparent surface. (C) Zoom in on the K1657 residue of PL$^{pro}$ that interacts with E132 of ChISG15 (left panel), while it has no interaction with Ub (right panel) (D) Close up of MERS-CoV PL$^{pro}$ V1691 and the interacting patches of ChISG15 (left panel), or Ub (right panel).

effective substitution was K1657E, which removed the electrostatic interaction and introduced a negative charge to repel hISG15. Residue V1691 was also targeted, but as described above this residue also interacts with the hydrophobic patch of Ub, making it difficult to mutate this position to only reduce deISGylation activity without affecting DUB activity (Fig. 4D). V1691D had reduced deISGylation activity while the DUB activity was near wt levels, however it is peculiar that this mutant has lower affinity for Ub (lower $K_m$) but a higher $K_{cat}$ [384]. Based on these observations, our previously described V1691R substitution might affect both the DUB and deISGylation activity of PL$^{pro}$, which will be important to verify in future experiments.

The above mentioned K1657E and/or V1691D substitutions can be introduced in a MERS-CoV PL$^{pro}$ expression construct and their effect can be evaluated in cell-based assays. Subsequently, deISGylation-negative MERS-CoV with intact DUB activity could serve as a tool to determine the function of the deISGylation activity during infection. hISG15 conjugation appears not to be involved in antiviral immunity as specifically unconjugated hISG15 was important for downregulation for the type I IFN response by its non-covalent binding to USP18 [407]. Coronavirus PLP-mediated deconjugation of hISG15 can increase the level of unconjugated hISG15, which might enhance USP18 levels and subsequently decrease IFN-α/β signalling (Fig. 3B) [546]. To investigate

the latter hypothesis, the effect of $PL^{pro}$ variants on the levels of conjugated versus unconjugated hISG15 and USP18 should be measured during wt or deISGylation-negative MERS-CoV infection. It is an experimental complication, however, that hISG15 and the required conjugating enzymes are all IFN-induced. Expression of these proteins could be induced by careful pre-treatment of cells with IFN-α/β before the infection with MERS-CoV. This may be challenging, since CoVs are sensitive to type I IFNs and too much IFN signalling will efficiently inhibit infection [89, 156, 246, 553, 554], while the deISGylation-negative MERS-CoV will probably be even more sensitive to the effects of IFN-α/β pre-treatment. Nevertheless, this experimental set-up may yield candidate viral and/or host substrates to which hISG15 is conjugated during a CoV infection, which would then be removed upon wt virus infection, but not during an infection with deISGylation-negative MERS-CoV. Alternatively, substitutions that disrupt deISGylation activity can be introduced into a mutant MERS-CoV that induces a stronger type I IFN response than wt virus, e.g. by removing ORFs 3-5 although it is a potential complication that a virus lacking those proteins is attenuated [181]. Still, using this setup, type I IFNs and ISGs would be produced naturally, and it could be determined whether $PL^{pro}$ suppresses the second 'wave' of the type I IFN response by increasing the amount of free hISG15.

In mice, removal of mISG15 from protein substrates may serve a different purpose and therefore it will be interesting to create MHV mutants with decreased deISGylation activity (Fig. 3A). These viruses can be tested in their natural host, but also in knockout mice that lack Ube1L, mISG15 or USP18. Also, because MERS-CoV $PL^{pro}$ can bind mISG15, deISGylation-negative MERS-CoV might be analysed in a mouse model for MERS-CoV infection. These approaches will hopefully lead to a better understanding of CoV PLP-mediated deISGylation, and its role in CoV-infected cells.

## Cellular and viral substrates of CoV PLPs

*PLP as part of nsp3: its interaction with other nsp3 domains and (viral) proteins*

It is an intriguing question from which protein targets Ub and/or ISG15 are removed by CoV PLPs. To study this, it might be a good strategy to identify other viral proteins that interact with the PLP domain or nsp3 as a whole. Most of the 15 or 16 nsps that are expressed during a CoV infection assemble into membrane-anchored replication and transcription complexes (RTCs). Nsp3 is the largest subunit of the CoV replicase and all CoVs contains the following domains from N- to C-terminus: Ubl domain 1, acidic domain, macrodomain (also known as X domain), Ubl domain 2, $PL^{pro}$/PLP2, ectodomain between two transmembrane (TM) domains, Y1, and CoV-Y [189, 555]. The TM domains anchor nsp3 to the membrane structures that form the CoV replication organelle, which most likely are derived from the endoplasmic reticulum. Consequently, in CoV-infected cells part of nsp3 resides in the lumen whereas PLP is associated with the cytosolic face of the membrane structures [556].

The Ubl2 domain is located directly upstream of PLP. It is highly conserved and its structure has been resolved, however its function is still unclear. Ubl domains are also associated with

human USP DUBs and seem to regulate their activity and interactions with protein partners [292]. In the case of SARS-CoV and MERS-CoV $PL^{pro}$, protease activity towards polyprotein and Ub substrates was not affected in cell-based overexpression studies upon deletion of the Ubl2 domain [204, 235]. For MERS-CoV, Ubl2 was also not required for $PL^{pro}$-mediated suppression of IFN-β promoter activity in over-expression experiments, although this is in contrast with results reported for SARS-CoV [199, 204, 235]. Mutations in MHV-Ubl2 reduced its proteolytic activity by destabilizing PLP2 [478], while no difference in thermal stability was measured for MERS-CoV $PL^{pro}$-ΔUbl2 [385]. Further studies into CoV-Ubl2 are needed to unveil its function in relation to PLP.

A well-characterized function of the macrodomain in CoV nsp3 is the binding of ADP-ribose and its de-ADP-ribosylation activity that has been shown to be is important for virulence in mice for MHV and SARS-CoV [190-192, 479, 557]. In a recent study, an interplay between MHV PLP2 and macrodomain was suggested and a direct or indirect association of the two domains was demonstrated upon their ectopic expression [558]. Intriguingly, separation of the nsp3 domains in yeast-two-hybrid screens revealed that a domain named "papain-like noncanonical" (amino acids 1852-2237 of pp1a/pp1ab of SARS-CoV; just downstream of $PL^{pro}$) interacts with many other domains of nsp3, namely the acidic domain, SARS-unique domain (SUD; a non-conserved region downstream of macrodomain), $PL^{pro}$ and CoV-Y [559]. Potential cellular interaction partners of SARS-CoV nsp3 were found in another yeast-to-hybrid screen that included human proteins [560]. A follow-up study showed that the SUD and $PL^{pro}$ domains can interact with CHY zinc-finger domain-containing 1 (RCHY1), leading to p53 degradation, and that p53 degradation was enhanced upon stronger binding of RCHY1 by a SUD-$PL^{pro}$ expression product [561]. These data indicate that different domains of nsp3 can cooperate to enhance binding to target proteins and might thus influence the substrates that a PLP encounters and possibly its activity as well. Additionally, SARS-CoV nsp3 has many interactions with other nsps, as was revealed by yeast-two-hybrid screens and subsequent validation with pull-down assays [559]. Overall, CoV-nsp3 seems to provide a scaffold for many viral nsps and these may sequester, bind, or recruit cellular proteins as well. All these proteins are potential targets for PLP's DUB/deISGylating activity and it will be interesting to establish the interplay between PLP and these different categories of potential substrates.

*Protein substrates of PLP DUB activity in the innate immune signalling pathway*

Coronavirus PLP's DUB activity was hypothesized to interfere with the innate immune response [195], as the activity of various factors in this response are controlled by ubiquitination, leading to either their activation or their induced degradation (Chapter 6 and [143, 151, 152]). Indeed, expression of CoV PLPs could inhibit IFN-β promoter activation in cell-based assays in which signalling had been activated by overexpression of various inducers (Chapter 6 and [199-205]). Furthermore, it has been suggested that PLPs remove Ub from innate immune signalling factors in cell-based overexpression studies [201, 203, 474, 535, 562]. We and others showed that the DUB activity of PLP is able to prevent activation of IFN-β/NF-κB promoter activity (Chapter 2) [207,

208]. The proteolytic activity of PLP is thought to be required for IFN-β antagonism, however, in some reports inactive PLP was also shown to suppress IFN-β activation, albeit less efficiently [199, 200, 203, 336]. Possibly, proteolytically inactive PLPs can still bind innate immune signalling factors, thus preventing the complex formation required for IRF3 activation [474, 535]. Alternatively, inactive PLP may bind Ub and/or Ubl proteins and thereby manipulate the signalling cascade [336].

In all the studies described above, luciferase-based IFN-β/NF-κB reporter assays were performed using different stimuli, and in most cases the impact of wt PLP and sometimes an active site mutant was tested. To improve the experimental set-up in the future, also a mutant in which the Ub-binding surface is mutated (inducing loss of DUB activity) and the same mutation combined with one in the active site (loss of both Ub binding and proteolytic activity) should be included. In that manner, conclusions could be drawn about the contribution of proteolysis-dependent and proteolysis-independent suppression of the innate immune response pathways by PLP. Such experiments were attempted for SARS-CoV $PL^{pro}$, showing that indeed both proteolysis-dependent and proteolysis-independent $PL^{pro}$ activities are important for IFN-β suppression. The latter activity is Ub-binding dependent, but the exact mechanism for both activities remains unclear thus far [336]. Another disadvantage of many of the cell-based assays is that ectopic expression of the PLP domain results in its cytosolic localization, which is in in sharp contrast to its membrane-bound localization in infected cells [83, 228, 563].The cytosolic PLP localization might also be a reason why the DUB activity appears to be very broad, with Ub-conjugates being removed from the bulk of cellular proteins in overexpression studies [199, 201-204]. Nevertheless, the collective data obtained from cell-based assays clearly demonstrate that activation of the IFN-β/NF-κB promoter can be obstructed by the enzymatic activity of ectopically expressed CoV PLPs.

*Identification of substrates that are deubiquitinated by CoV PLPs*

In order to gain more insight into the mechanisms that PLPs employ to suppress the innate immune response, it would be useful to identify specific PLP targets in CoV-infected cells. To this end, mass spectrometry could be used to compare lysates of wt or DUB-negative virus-infected cells, in which amino acids are labelled with different stable isotopes (SILAC). After trypsin digestion, samples can be enriched for ubiquitinated peptides by pull-down with antibodies that specifically recognize the GG remnant on peptides that were ubiquitinated at the moment of trypsinisation [564]. Comparing wt and DUB-negative virus-infected cells lysates may reveal host proteins that are specifically targeted by the DUB activity of PLP. Based on the data summarized above, ubiquitinated innate immune signalling factors are likely to be among these host substrates, but Ub may also be removed from other cellular proteins by PLP during infection. Analysis of these targets may reveal that the DUB activity of PLP is influencing other pathways in infected cells as well. Considering that PLP is localized to the RTC, the proteins that are deubiquitinated by PLP may be present at this location. Identification of $PL^{pro}$ substrates might thus also provide clues to host factors that are recruited to the RTC, to be involved in virus replication or play a role in for

example the formation or functioning of the replication organelles formed upon CoV infection [376, 565-567].

The proposed proteomics experiment could also identify viral targets of PLP DUB activity. It is quite likely that viral proteins are ubiquitinated by host E3 ligases during infection and are targeted for proteasomal degradation. To prevent this, PLP might cleave K48-linked polyUb chains from viral proteins to prevent their degradation. Interestingly, K48-linked polyUb chains seem to be the main target of SARS-CoV $PL^{pro}$, as these chains were highly preferred *in vitro* [207, 236]. An obvious explanation would therefore be that this activity is used to rescue viral proteins from degradation during infection. The turnip yellow mosaic virus (TYMV) OTU DUB has a similar function, as this vDUB can processes K48- and K63-linked polyUb chains *in vitro*, but in cells it does not exhibit overall DUB activity [340]. Interestingly, the TYMV RNA-dependent RNA polymerase (RdRp) is ubiquitinated and degraded by the proteasome only late during TYMV infection [530]. The TYMV OTU DUB was shown to remove the Ub chains from the RdRp thereby increasing the stability of the RdRp in the early stages of infection contributing to the efficiency of virus replication [340].

Another fascinating possibility of the proposed mass spectrometry approach is that the linkage specificity of PLP during infection can be determined, since the amount of Ub chain-derived peptides can be determined for each of the specific ubiquitin linkages (K6, K11, K27, K29, K33, K48, K63) and compared between wt and DUB-negative virus infected cells. Collectively, an experiment as proposed above can provide substantial insight into the substrates and thus the function of PLP during CoV infection.

## OPTIONS TO PREVENT OR TREAT CORONAVIRUS INFECTIONS BASED ON KNOWLEDGE OF CORONAVIRUS PAPAIN-LIKE PROTEASES



Currently, only supportive care can be given to individuals who are diagnosed with a CoV infection (like MERS), as no specific antiviral treatment has been approved yet. In some MERS-CoV-infected individuals, therapeutic interventions were evaluated in uncontrolled trials with varying outcomes. The nucleoside analogue ribavirin, human immunodeficiency viruses (HIV) protease-inhibitor lopinavir, corticosteroids, or IFN-α/β, or a combination of these drugs, were administered [240]. On the one hand, discovery and development of new antiviral drugs against CoVs are pivotal to control disease. This is important in the current situation of repeated zoonotic transmission of MERS-CoV, often followed by local spread among health care workers and/or household members, but also to be prepared for future emerging CoVs. On the other hand, vaccine development is critical to be able to prevent infections and/or break the transmission chain. In this thesis, I describe my efforts in both directions by targeting MERS-CoV $PL^{pro}$ to create a potential MLV vaccine (Chapters 2 and 3) as well as by identifying unique protein-based $PL^{pro}$ inhibitors (Chapters 4 and 5).

## Coronavirus vaccine development

*Correlates of protection*

Virus-specific humoral and cellular responses both are important in providing protection against CoV infection. Neutralizing antibodies against the viral S protein are key for protective immunity as those antibodies were proven to prevent or limit infection in animal models for CoV infection [568, 569]. Thus, subunit vaccines that display (part of) this S glycoprotein are considered to be a viable strategy to induce the production of neutralizing antibodies [254, 255]. Vaccination with Venezuelan equine encephalitis replicons expressing CoV nucleocapsid protein induced memory $CD4^+$ T cells that mediate a protective immune response in mice, highlighting the importance of cellular immunity upon CoV infection [570]. Neutralizing antibodies as well as CD4+ and/or CD8+ T cell responses were developed in MERS survivors [40, 571-574]. Patients who had mild disease mounted CD8+ T cell responses but not necessarily a detectable antibody response, whereas patients with severe disease and higher viral titers developed both virus-specific antibodies and CD4+ T cell responses. Long-term MERS-CoV-specific antibody and T cells levels should be further evaluated in individuals that had a symptomatic infection [575].

*Coronavirus vaccine strategies*

The goal of vaccination is to induce protective immunity without causing disease. In addition to conferring a health advantage to the individual, the spread of infectious diseases is also reduced if a large part of the population is vaccinated. Besides vaccination of human individuals, vaccination of dromedary camels is also considered a viable strategy to reduce or halt MERS-CoV spread among dromedary camels and - subsequently - the frequency of transmission to humans, explaining the current efforts to create a MERS-CoV vaccine for use in dromedaries [254, 255, 257, 576, 577]. A MERS-CoV vaccine candidate that might be used in humans or dromedaries needs to meet certain criteria. Firstly, a vaccine candidate should be safe to use, and secondly, it needs to stimulate production of S protein-directed antibodies and preferably also cellular immunity to provide long-lasting immunity [338]. Subunit vaccines have a safety advantage as usually the only expressed CoV component in this kind of vaccines is the S protein to which neutralizing antibodies will be produced. MLV vaccines are considered superior over subunit vaccines because of the broader and longer-lasting immunological responses they can induce. To create a modified live MERS-CoV vaccine candidate, pathogenicity of the parental virus should be removed to ensure safety. Like all RNA viruses, CoVs have a high mutation frequency and are also known for their recombination potential. Consequently, any MLVs should be carefully tested for their (reversion to) virulence in cell culture infections and *in vivo*.

*Attenuation-by-design to develop MLV vaccines*

The development of reverse genetics technology enabled the introduction of specific modifications into the CoV genome [578], for example aiming to attenuate viral virulence. In our studies, we selectively impaired the DUB activity of MERS-CoV $PL^{pro}$ with specific substitutions, resulting

in attenuation of the virus in a lethal mouse model (Chapter 3). This led to increased survival rates of DUB-negative virus-infected mice compared to wt-infected mice. The attenuation was accompanied by earlier induction of IFNs and ISGs in the lungs of the DUB-negative virus-infected mice compared to wt virus-infected mice (Chapter 3). Using RNA deep sequencing technology, identification of other transcripts that are up- or down-regulated in DUB-negative-infected mice could reveal whether the (loss of) DUB activity influences additional cellular signalling pathways that may influence the infection and disease outcome.

Further attenuation of DUB-negative CoVs may be recommendable considering that animals did lose substantial weight upon infection with the DUB-negative MERS-CoV, and still one animal died from the infection with this virus (Chapter 3). Moreover, the limited number of mutations used to create the virus may leave a considerable risk of reversion. On the other hand, one should be careful not to over-attenuate the virus because then protective immune responses will not fully develop. Besides the substitutions in $PL^{pro}$, changes that abolish other CoV innate immune evasive functions could be introduced to promote further attenuation. Among the available options would be the removal or mutagenesis of the host shut-off activity of nsp1 [183, 188, 579], de-ADP-ribosylation activity in nsp3 [191], endonuclease activity in nsp15 [173, 174] or 2'-O-methyl-transferase in nsp16 [170]. As an alternative, the accessory proteins, such as those encoded by MERS-CoV ORF3, 4a, 4b, and 5, which are also proven modulators of IFN-β and NF-κB responses, are potential targets for removal or mutagenesis to attenuate the virus [181, 258]. Another approach is to create a replication-competent but propagation-defective virus by removing the MERS-CoV structural envelope (E) protein [258]. Unfortunately, the protection induced by MERS-CoV-ΔE infection has not yet been evaluated in an animal model and therefore the outcome of vaccination with a DUB-negative MERS-CoV-ΔE remains to be investigated.

The strategy of combinatorial attenuation was earlier applied to SARS-CoV to increase vaccine biosafety. SARS-CoV-ΔE was attenuated in different animal models, however, reversion to virulence was observed after multiple passages in mice [580, 581]. Addition of a deletion in nsp1, which by itself induced higher IFN responses, resulted in an attenuated virus that was genetically stable after serial passage in mice [581]. Another illustration of combinatorial attenuation was with a 2'-O-methyl-transferase SARS-CoV mutant that was found to be attenuated in 10-week old mice while pathogenesis was observed in aged mice along with reversion to virulence, although not driven by reversion of the introduced mutation in nsp16 [582]. Interestingly, addition of substitutions to inactivate the exoribonuclease in nsp14 resulted in a potential vaccine candidate as the latter virus was attenuated in both young and aged mice, did not revert, and provided protection upon challenge [582].

*The importance of IFN in CoV immunity*

Removal or modulation of innate immune evasive functions, like PLP's DUB activity, can be an approach to develop efficacious and safe CoV vaccine candidates. This strategy potentially increases the efficacy of the vaccine, since IFNs are crucial for establishing immunity in response to viral in-

fections. Type I IFNs stimulate the expression of ISGs and furthermore activate and enhance adaptive immune responses, thereby enabling a full-blown, protective immune response [141, 311, 312]. Animal models were quickly developed after the emergence of MERS-CoV to study immune responses against the virus and to allow testing of MLV vaccines or antiviral therapies [369, 583]. MERS-CoV can infect dromedary camels, rabbits, rhesus macaques and some genetically modified mice, most of which develop mild clinical disease or none at all, despite virus replication. In a non-lethal mouse model for MERS-CoV infection, type I IFN was required to eliminate the virus as clearance was delayed in IFNAR$^{-/-}$ mice compared to wt mice [368]. It remains an interesting challenge to determine the innate immune responses against MERS-CoV in dromedary camels.

Transgenic mice expressing hDPP4, either together with murine DPP4 (mDPP4) or instead of mDPP4, develop more severe disease, but lethal lung disease was only caused when mouse-adapted (MA) MERS-CoV was used to inoculate these mice [319, 370]. In contrast to the lack of IFN production in cell culture infections [154, 156, 157], levels of innate immune molecules and pro-inflammatory cytokines were upregulated in MERS-CoV-infected hDPP4 KI mice compared to mock-infected mice, but even more upregulated in mice that received MA MERS-CoV, particularly at later stages of the infection [319]. A similarly late IFN response plays a crucial role in the lethal outcome of SARS-CoV infection in mice, because delayed IFN expression drives the influx and exuberant activation of inflammatory monocyte-macrophages that secrete cyto- and chemokines, which causes severe pathology [318]. Recently, a delayed type I IFN response and the subsequent recruitment of inflammatory monocyte-macrophages was also suggested to contribute to lung pathology and lethality in MERS-CoV-infected mice [337]. The innate immune suppressive activities that MERS-CoV possesses are most likely the cause of the late IFN response upon an infection. Therefore, it is important to notice that during a DUB-negative MERS-CoV infection IFNs are expressed earlier compared to a wt virus infection (Chapter 3). In the study by Channappanavar *et al*., it was demonstrated that hDPP4 KI mice infected with a sublethal dose of MA MERS-CoV, which led to substantial weight loss, had a simultaneous peak in their IFN response at the peak of replication [337]. Abolishing IFN signalling by treating those mice with anti-IFN-α/β-receptor antibodies reduced survival rates, indicating that IFN protects the mice during infection. Moreover, early IFN-β treatment protected mice from a lethal MA MERS-CoV infection, whereas late IFN-β treatment reduced survival upon the use of a sublethal dose of the virus [337]. Overall, these results clearly demonstrate that the timing of the type I IFN response is crucial during a MERS-CoV infection, and that an IFN response that peaks earlier or simultaneous with the peak of replication can be protective while a late response promotes inflammation and mortality.

To obtain more detailed proof that DUB-negative MERS-CoV is attenuated because of an accelerated type I IFN response, the virus should further be analysed in a different animal model, in which mice die of lung disease instead of a generalized infection that spreads to the brain as in the cytokeratin18-*hDPP4* mice [319, 370]. DUB-negative MA MERS-CoV is expected to have reduced virulence in hDPP4 KI mice and induce earlier expression of IFNs compared to wt MA virus. To assess the importance of the type I IFN response upon DUB-negative or wt MA MERS-

CoV infection, mice can be treated with anti-IFN-α/β-receptor antibodies to mitigate type I IFN signalling, as described above, or alternatively IFNAR$^{-/-}$ hDPP4 KI mice can be generated. In the absence of a type I IFN response, the DUB-negative virus would be assumed to behave similarly as wt MERS-CoV, which would confirm the role of the DUB activity in disease outcome through its interactions with the type I IFN pathway. Altogether, timing and the level of type I IFNs induction are crucial for the outcome of CoV infection and modifying the virus to induce IFN production earlier in infection can be an approach in the design of MLV vaccine candidates.

## Antiviral compounds targeting CoV PLPs

*Small-molecule PLP inhibitors*

Another long-term research aim is to discover antiviral compounds that inhibit virus replication to prevent serious disease or death in CoV-infected individuals. After the SARS-CoV outbreak, for which no antiviral therapy was available, the search for antiviral compounds was accelerated so that society would be better prepared for future CoV outbreaks. Viral enzymes are key in the replication cycle of viruses and can usually be inhibited without negative side effects for the host cell. For those reasons, they are potential targets for antiviral therapies [240]. Among CoV enzymes, PLP is a target for the development of *pan*-CoV inhibitors that could inhibit the PL$^{pro}$ activity of MERS-CoV as well as other emerging CoVs [346]. As in the case of cellular DUBs, it will be a challenge to identify compounds that block the activity of virus-encoded PLPs with sufficient specificity, thus avoiding undesirable side effects of drug treatment. It is noteworthy that six Ub pathway-associated drugs have been FDA-approved, three of which are proteasome inhibitors while the other three target an E3 ligase complex [584, 585]. The main issue with DUB inhibitors is that these generally target the conserved active site of the enzyme [586]. Consequently, small-molecules that block the activity of a particular DUB usually exhibit low specificity. This was also the case for the initially discovered small-molecules targeting the active site of USP7. This cellular DUB is one of the best studied USPs, because it is crucial for regulating the level and activity of p53 and its manipulation could therefore yield promising anti-cancer activity. Recently, highly specific USP7 inhibitors were described, two of which bind in the active site [587, 588]. The most potent inhibitor, however, binds in an allosteric pocket that is 5.5 Å from the catalytic cysteine [589]. In the studies by Lamberto *et al.* and Gavory *et al.*, co-crystal structures of USP7 with an inhibitor enabled structure-based design to optimize the initial hits. This was done based on earlier success with the generation of SARS-CoV PL$^{pro}$ inhibitors that were produced in a similar manner; the initial hits were identified by high-throughput screening (HTS) [397] and subsequently structure-based modifications were applied to increase the potency of these compounds [342, 466, 467, 469]. Inhibitor 3e ($EC_{50}$ = 8.3 μM), does not target the protease's active site but binds to the blocking loop 2 (BL2) [342, 469]. This flexible region is located near the active site and regulates substrate binding. Thus, inhibitors targeting BL2 prevent substrates from entering the active site. The sequence of the BL2 region is not conserved between CoV PLPs, which is the reason why these inhibitors do not cross-react with MERS-CoV PL$^{pro}$ [371, 469]. HTS was exploited

to discover novel small-molecules targeting SARS- or MERS-CoV $PL^{pro}$, but the specificity of an identified compound that inhibited both $PL^{pro}$s is debated because they were later reported to also inhibit other viral and cellular DUBs [371, 385]. Recent identification and characterization of two other competitive inhibitors may be a new starting point for structure-based modifications, aiming to increase the potency of these compounds against MERS-CoV $PL^{pro}$ [590].

*Screening for novel PLP inhibitors*

Generally, compounds identified by HTS that block a vDUB need optimization to increase their potency and specificity. This is a time-consuming process, which implies that preparedness needs to be created before the emergence of any pathogenic CoV as time will be a crucial and limiting factor during an outbreak. SARS- and MERS-like CoVs were discovered in bats, consequently, it will be informative to determine whether the $PL^{pro}$ inhibitors block the activity of $PL^{pro}$ from bat-derived SARS- and MERS-like CoVs. On a small scale, this was explored with a SARS-CoV $PL^{pro}$ inhibitor, compound 3e, which was also shown to inhibit $PL^{pro}$ from a bat CoV related to SARS-CoV $PL^{pro}$ [336]. It could be an option to characterize PLPs from bat CoVs that can bind to human cellular receptors like ACE2 or DPP4, and perform HTS and subsequent optimization of hits for these PLPs. In this manner, our preparedness to deal with emerging CoVs might be improved. Alternatively, quicker selection methods for potent and selective antiviral compounds should be designed. We attempted this by selection of UbVs from a phage library, yielding highly potent and selective inhibitors for vDUBs of MERS-CoV and CCHFV within a couple of weeks' time (Chapter 4), and this strategy can also be applied to select UbVs against bat CoV PLPs.

*Ubiquitin variants as inhibitors of vDUBs*

Deubiquitinating enzymes interact with low affinity with Ub but through a large interaction surface [347, 591]. For the vDUBs MERS-CoV $PL^{pro}$ and CCHFV OTU the binding to monoUb was determined in a phage enzyme-linked immunosorbent assay and the half maximal effective binding concentration ($EC_{50}$) was found to be in the µM range (Chapter 4). The Ub-binding surfaces of DUBs belonging to the USP family share a common fold, but have low sequence similarity. Consequently, the interaction of Ub with residues of the Ub-binding surface is usually based on residues that are non-conserved in the DUB. The above has two important implications. Firstly, UbVs can be selected that have a higher affinity for DUBs than Ub, because of optimized interactions. Secondly, interactions of UbVs with non-conserved residues of the DUB will determine the specificity of the UbV for its target. UbVs were initially selected for cellular DUBs, but immediately extended to Ub-conjugating enzymes, Ub ligases, and vDUBs (Chapter 4)[347, 348, 387, 388]. Advantages of the UbV method are that within a few weeks highly potent UbVs, with $EC_{50}$ values in the nM range, can be selected. Unfortunately, two MERS-CoV-specific UbVs turned out to be biologically instable, an issue that was overcome by modification of a region that was not important for the binding of the UbV to $PL^{pro}$, but which stabilized these molecules (Chapter 5). The MERS-CoV-specific UbVs that were selected thus far all showed high specify for their cognate

DUB and did not cross-react with other, structurally related DUBs. This narrow specificity was exemplified by the MERS-CoV-specific UbVs that did not inhibit SARS-CoV $PL^{pro}$ or bind to any of the other tested cellular DUBs (Chapter 4). In parallel, no toxicity was measured in cells upon expression of these UbVs.

MERS-CoV replication was severely inhibited upon lentivirus-driven expression of MERS-CoV-specific UbVs, with the strongest inhibitor (ME.4) reducing virus progeny titers by 3 to 4 logs, depending on the MERS-CoV dose (Chapters 4 and 5). The safety and potency of ME.4 now needs to be verified in an animal model for MERS-CoV infection, for which the stabilized version of ME.4 is the best candidate. To develop an UbV into a therapeutic option, the main hurdle is to develop a method to efficiently deliver the UbV into the cells of an organism, preferably in the infected tissue. Strategies for intracellular delivery of proteins, such as using cell-penetrating peptides, lipid-based molecules or nanoparticles, are under development, however it remains to be determined whether the levels of delivered UbVs will be sufficient to inhibit virus replication [592-594]. If UbV protein levels in target cells would need to be increased, the antiviral agent could be delivered in the form of UbV-encoding mRNA that can be translated into protein, or adenoviruses or adeno-associated viruses can be used to deliver UbV genes [595-597]. These viral vector options could even be designed in such a way that cells in the respiratory tract are specifically targeted, by using adenoviruses with capsids that mediate binding to specific cell-surface receptors [598]. In summary, various delivery technologies could be explored to determine the best strategy to attain sufficient UbV inside the cells to effectively suppress CoV replication.

Recent results demonstrate that the UbV (CC.4) with the highest affinity for the CCHFV OTU blocked the DUB-, deISGylating- and immune-suppressive activity of the protease in cell-based assays [599], similarly as the MERS-CoV-specific UbVs inhibited the activity of MERS-CoV $PL^{pro}$ (Chapter 4). Moreover, CC.4 selectively inhibited CCHFV OTUs but no other OTUs of nairovirus species, highlighting its specificity. Stable expression of CC.4 in cells severely inhibited CCHFV replication, and this was independent of innate immune responses in those cells [599]. This is important to note because CCHFV is a segmented negative-stranded RNA virus and the OTU protease is thus not required for polyprotein processing, as CoV PLPs, but it plays a role in suppressing antiviral responses [225]. Therefore it was expected that CC.4 expression would influence OTU-mediated suppression of innate immunity, but maybe also would affect viral polymerase activity as the OTU is a domain on the viral polymerase (Chapter 4). The study by Scholte *et al*., indicates that CC.4 also inhibits CCHFV transcription and/or replication, which was suggested to be the result of a defect in ribonucleoprotein complex formation upon binding of CC.4 to the OTU [599]. Overall, this illustrates that UbVs can be potential antiviral agents as well as research tools to study vDUBs.

## CONCLUDING REMARKS

The primary substrates of CoV proteases are their replicase polyproteins, which need to be processed to initiate replication and establish an infection. In addition, many viral proteases have secondary functions and cleave cellular substrates, for example to modulate host immunity and other cellular processes. Studies have unravelled the 3-D structures and activity of CoV PLPs, and their functions were explored in cell-based assays. The results described in this thesis include the first evidence that the DUB activity of a CoV PLP is important for viral virulence by suppressing the activation of the innate immune response. However, many questions still need to be answered to better understand the function of CoV PLPs. How do PLPs interact with other domains of nsp3 and other CoV nsps? What - if any - are the specific host or viral substrates that are deubiquitinated and/or deISGylated by PLPs? And what is the function of PLP's deISGylation activity in different species?

Such knowledge can also be used to develop countermeasures against emerging CoVs, which is important as, 17 years after the SARS-CoV outbreak, therapeutic options for emerging CoVs are still not available, despite the fact that they continue to be considered a threat to human society [600]. Coronavirus PLPs are a potential target for mutagenesis to attenuate a virus to develop an MLV vaccine or for protease inhibitors. Innovative approaches, like the UbVs described in this thesis, may help to efficiently target PLPs. Additionally, creating a deeper understanding of bat CoV PLPs could increase chances to have a therapeutic option ready before the next emerging CoV, since future human-infecting viruses are likely to originate from the virus pools hidden in bat populations.

References
List of abbreviations
Dutch summary
Curriculum vitae
List of publications

## REFERENCES


1. te Velthuis, A.J., *Common and unique features of viral RNA-dependent polymerases.* Cell Mol Life Sci, 2014. **71**(22): p. 4403-20.
2. Lauring, A.S. and R. Andino, *Quasispecies theory and the behavior of RNA viruses.* PLoS Pathog, 2010. **6**(7): p. e1001005.
3. Domingo, E., J. Sheldon, and C. Perales, *Viral quasispecies evolution.* Microbiol Mol Biol Rev, 2012. **76**(2): p. 159-216.
4. Vignuzzi, M., et al., *Quasispecies diversity determines pathogenesis through cooperative interactions in a viral population.* Nature, 2006. **439**(7074): p. 344-8.
5. Drosten, C., et al., *Identification of a novel coronavirus in patients with severe acute respiratory syndrome.* N Engl J Med, 2003. **348**(20): p. 1967-76.
6. Ksiazek, T.G., et al., *A novel coronavirus associated with severe acute respiratory syndrome.* N Engl J Med, 2003. **348**(20): p. 1953-66.
7. Kuiken, T., et al., *Newly discovered coronavirus as the primary cause of severe acute respiratory syndrome.* Lancet, 2003. **362**(9380): p. 263-70.
8. Peiris, J.S., et al., *Coronavirus as a possible cause of severe acute respiratory syndrome.* Lancet, 2003. **361**(9366): p. 1319-25.
9. Peiris, J.S., Y. Guan, and K.Y. Yuen, *Severe acute respiratory syndrome.* Nat Med, 2004. **10**(12 Suppl): p. S88-97.
10. Yu, I.T., et al., *Evidence of airborne transmission of the severe acute respiratory syndrome virus.* N Engl J Med, 2004. **350**(17): p. 1731-9.
11. Shen, Z., et al., *Superspreading SARS events, Beijing, 2003.* Emerg Infect Dis, 2004. **10**(2): p. 256-60.
12. Wang Sh, X., et al., *The SARS outbreak in a general hospital in Tianjin, China -- the case of super-spreader.* Epidemiol Infect, 2006. **134**(4): p. 786-91.
13. Leung, G.M., et al., *SARS-CoV antibody prevalence in all Hong Kong patient contacts.* Emerg Infect Dis, 2004. **10**(9): p. 1653-6.
14. Marra, M.A., et al., *The Genome sequence of the SARS-associated coronavirus.* Science, 2003. **300**(5624): p. 1399-404.
15. Rota, P.A., et al., *Characterization of a novel coronavirus associated with severe acute respiratory syndrome.* Science, 2003. **300**(5624): p. 1394-9.
16. Guan, Y., et al., *Isolation and characterization of viruses related to the SARS coronavirus from animals in southern China.* Science, 2003. **302**(5643): p. 276-8.
17. Lau, S.K., et al., *Severe acute respiratory syndrome coronavirus-like virus in Chinese horseshoe bats.* Proc Natl Acad Sci U S A, 2005. **102**(39): p. 14040-5.
18. Li, W., et al., *Bats are natural reservoirs of SARS-like coronaviruses.* Science, 2005. **310**(5748): p. 676-9.
19. Li, W., et al., *Angiotensin-converting enzyme 2 is a functional receptor for the SARS coronavirus.* Nature, 2003. **426**(6965): p. 450-4.
20. Li, W., et al., *Receptor and viral determinants of SARS-coronavirus adaptation to human ACE2.* EMBO J, 2005. **24**(8): p. 1634-43.
21. Song, H.D., et al., *Cross-host evolution of severe acute respiratory syndrome coronavirus in palm civet and human.* Proc Natl Acad Sci U S A, 2005. **102**(7): p. 2430-5.
22. Ge, X.Y., et al., *Isolation and characterization of a bat SARS-like coronavirus that uses the ACE2 receptor.* Nature, 2013. **503**(7477): p. 535-8.
23. Menachery, V.D., et al., *SARS-like WIV1-CoV poised for human emergence.* Proc Natl Acad Sci U S A, 2016. **113**(11): p. 3048-53.

24. Menachery, V.D., et al., *A SARS-like cluster of circulating bat coronaviruses shows potential for human emergence.* Nat Med, 2015. **21**(12): p. 1508-13.
25. Zaki, A.M., et al., *Isolation of a novel coronavirus from a man with pneumonia in Saudi Arabia.* N Engl J Med, 2012. **367**(19): p. 1814-20.
26. van Boheemen, S., et al., *Genomic characterization of a newly discovered coronavirus associated with acute respiratory distress syndrome in humans.* MBio, 2012. **3**(6).
27. de Groot, R.J., et al., *Middle East respiratory syndrome coronavirus (MERS-CoV): announcement of the Coronavirus Study Group.* J Virol, 2013. **87**(14): p. 7790-2.
28. Kim, K.H., et al., *Middle East respiratory syndrome coronavirus (MERS-CoV) outbreak in South Korea, 2015: epidemiology, characteristics and public health implications.* J Hosp Infect, 2017. **95**(2): p. 207-213.
29. Oh, M.D., et al., *Middle East respiratory syndrome: what we learned from the 2015 outbreak in the Republic of Korea.* Korean J Intern Med, 2018. **33**(2): p. 233-246.
30. Chan, J.F., et al., *Middle East respiratory syndrome coronavirus: another zoonotic betacoronavirus causing SARS-like disease.* Clin Microbiol Rev, 2015. **28**(2): p. 465-522.
31. Choi, W.S., et al., *Clinical Presentation and Outcomes of Middle East Respiratory Syndrome in the Republic of Korea.* Infect Chemother, 2016. **48**(2): p. 118-26.
32. Hui, D.S., et al., *Middle East respiratory syndrome coronavirus: risk factors and determinants of primary, household, and nosocomial transmission.* Lancet Infect Dis, 2018. **18**(8): p. e217-e227.
33. Perlman, S. and P.B. McCray, Jr., *Person-to-person spread of the MERS coronavirus--an evolving picture.* N Engl J Med, 2013. **369**(5): p. 466-7.
34. Cotten, M., et al., *Transmission and evolution of the Middle East respiratory syndrome coronavirus in Saudi Arabia: a descriptive genomic study.* Lancet, 2013. **382**(9909): p. 1993-2002.
35. Reusken, C.B., et al., *Middle East Respiratory Syndrome coronavirus (MERS-CoV) serology in major livestock species in an affected region in Jordan, June to September 2013.* Euro Surveill, 2013. **18**(50): p. 20662.
36. Hemida, M.G., et al., *Middle East Respiratory Syndrome (MERS) coronavirus seroprevalence in domestic livestock in Saudi Arabia, 2010 to 2013.* Euro Surveill, 2013. **18**(50): p. 20659.
37. Reusken, C.B., et al., *Geographic distribution of MERS coronavirus among dromedary camels, Africa.* Emerg Infect Dis, 2014. **20**(8): p. 1370-4.
38. Muller, M.A., et al., *MERS coronavirus neutralizing antibodies in camels, Eastern Africa, 1983-1997.* Emerg Infect Dis, 2014. **20**(12): p. 2093-5.
39. Corman, V.M., et al., *Antibodies against MERS coronavirus in dromedary camels, Kenya, 1992-2013.* Emerg Infect Dis, 2014. **20**(8): p. 1319-22.
40. Muller, M.A., et al., *Presence of Middle East respiratory syndrome coronavirus antibodies in Saudi Arabia: a nationwide, cross-sectional, serological study.* Lancet Infect Dis, 2015. **15**(5): p. 559-64.
41. Adney, D.R., et al., *Replication and shedding of MERS-CoV in upper respiratory tract of inoculated dromedary camels.* Emerg Infect Dis, 2014. **20**(12): p. 1999-2005.
42. Raj, V.S., et al., *Isolation of MERS coronavirus from a dromedary camel, Qatar, 2014.* Emerg Infect Dis, 2014. **20**(8): p. 1339-42.
43. Haagmans, B.L., et al., *Middle East respiratory syndrome coronavirus in dromedary camels: an outbreak investigation.* Lancet Infect Dis, 2014. **14**(2): p. 140-5.
44. Memish, Z.A., et al., *Human infection with MERS coronavirus after exposure to infected camels, Saudi Arabia, 2013.* Emerg Infect Dis, 2014. **20**(6): p. 1012-5.
45. Corman, V.M., et al., *Rooting the phylogenetic tree of middle East respiratory syndrome coronavirus by characterization of a conspecific virus from an African bat.* J Virol, 2014. **88**(19): p. 11297-303.

46. Anthony, S.J., et al., *Further Evidence for Bats as the Evolutionary Source of Middle East Respiratory Syndrome Coronavirus.* MBio, 2017. **8**(2).
47. van der Hoek, L., *Human coronaviruses: what do they cause?* Antivir Ther, 2007. **12**(4 Pt B): p. 651-8.
48. Kahn, J.S. and K. McIntosh, *History and recent advances in coronavirus discovery.* Pediatr Infect Dis J, 2005. **24**(11 Suppl): p. S223-7, discussion S226.
49. van der Hoek, L., et al., *Identification of a new human coronavirus.* Nat Med, 2004. **10**(4): p. 368-73.
50. Fouchier, R.A., et al., *A previously undescribed coronavirus associated with respiratory disease in humans.* Proc Natl Acad Sci U S A, 2004. **101**(16): p. 6212-6.
51. Hamre, D. and J.J. Procknow, *A new virus isolated from the human respiratory tract.* Proc Soc Exp Biol Med, 1966. **121**(1): p. 190-3.
52. McIntosh, K., et al., *Recovery in tracheal organ cultures of novel viruses from patients with respiratory disease.* Proc Natl Acad Sci U S A, 1967. **57**(4): p. 933-40.
53. Woo, P.C., et al., *Characterization and complete genome sequence of a novel coronavirus, coronavirus HKU1, from patients with pneumonia.* J Virol, 2005. **79**(2): p. 884-95.
54. Vijaykrishna, D., et al., *Evolutionary insights into the ecology of coronaviruses.* J Virol, 2007. **81**(8): p. 4012-20.
55. Woo, P.C., et al., *Coronavirus diversity, phylogeny and interspecies jumping.* Exp Biol Med (Maywood), 2009. **234**(10): p. 1117-27.
56. Drexler, J.F., V.M. Corman, and C. Drosten, *Ecology, evolution and classification of bat coronaviruses in the aftermath of SARS.* Antiviral Res, 2014. **101**: p. 45-56.
57. Anthony, S.J., et al., *Global patterns in coronavirus diversity.* Virus Evol, 2017. **3**(1): p. vex012.
58. Corman, V.M., et al., *Hosts and Sources of Endemic Human Coronaviruses.* Adv Virus Res, 2018. **100**: p. 163-188.
59. Tao, Y., et al., *Surveillance of Bat Coronaviruses in Kenya Identifies Relatives of Human Coronaviruses NL63 and 229E and Their Recombination History.* J Virol, 2017. **91**(5).
60. Pfefferle, S., et al., *Distant relatives of severe acute respiratory syndrome coronavirus and close relatives of human coronavirus 229E in bats, Ghana.* Emerg Infect Dis, 2009. **15**(9): p. 1377-84.
61. Corman, V.M., et al., *Evidence for an Ancestral Association of Human Coronavirus 229E with Bats.* J Virol, 2015. **89**(23): p. 11858-70.
62. Corman, V.M., et al., *Link of a ubiquitous human coronavirus to dromedary camels.* Proc Natl Acad Sci U S A, 2016. **113**(35): p. 9864-9.
63. Vijgen, L., et al., *Evolutionary history of the closely related group 2 coronaviruses: porcine hemagglutinating encephalomyelitis virus, bovine coronavirus, and human coronavirus OC43.* J Virol, 2006. **80**(14): p. 7270-4.
64. Lau, S.K., et al., *Discovery of a novel coronavirus, China Rattus coronavirus HKU24, from Norway rats supports the murine origin of Betacoronavirus 1 and has implications for the ancestor of Betacoronavirus lineage A.* J Virol, 2015. **89**(6): p. 3076-92.
65. Kuhn, J.H., et al., *Reorganization and expansion of the nidoviral family Arteriviridae.* Arch Virol, 2016. **161**(3): p. 755-68.
66. den Boon, J.A., et al., *Equine arteritis virus is not a togavirus but belongs to the coronaviruslike superfamily.* J Virol, 1991. **65**(6): p. 2910-20.
67. Snijder, E.J., M. Kikkert, and Y. Fang, *Arterivirus molecular biology and pathogenesis.* J Gen Virol, 2013. **94**(Pt 10): p. 2141-63.
68. Balasuriya, U.B., Y.Y. Go, and N.J. MacLachlan, *Equine arteritis virus.* Vet Microbiol, 2013. **167**(1-2): p. 93-122.

69. Lunney, J.K., et al., *Porcine Reproductive and Respiratory Syndrome Virus (PRRSV): Pathogenesis and Interaction with the Immune System.* Annu Rev Anim Biosci, 2016. **4**: p. 129-54.
70. Holtkamp, D.J., et al., *Assessment of the economic impact of porcine reproductive and respiratory syndrome virus on United States pork producers.* Journal of Swine Health and Production, 2013. **21**(2): p. 72.
71. Nan, Y., et al., *Improved Vaccine against PRRSV: Current Progress and Future Perspective.* Front Microbiol, 2017. **8**: p. 1635.
72. Fehr, A.R. and S. Perlman, *Coronaviruses: an overview of their replication and pathogenesis.* Methods Mol Biol, 2015. **1282**: p. 1-23.
73. Lauber, C., et al., *The footprint of genome architecture in the largest genome expansion in RNA viruses.* PLoS Pathog, 2013. **9**(7): p. e1003500.
74. Bukhari, K., et al., *Description and initial characterization of metatranscriptomic nidovirus-like genomes from the proposed new family Abyssoviridae, and from a sister group to the Coronavirinae, the proposed genus Alphaletovirus.* Virology, 2018. **524**: p. 160-171.
75. Saberi, A., et al., *A planarian nidovirus expands the limits of RNA genome size.* PLoS Pathog, 2018. **14**(11): p. e1007314.
76. Gorbalenya, A.E., et al., *Nidovirales: evolving the largest RNA virus genome.* Virus Res, 2006. **117**(1): p. 17-37.
77. Sims, A.C., et al., *Severe acute respiratory syndrome coronavirus infection of human ciliated airway epithelia: role of ciliated cells in viral spread in the conducting airways of the lungs.* J Virol, 2005. **79**(24): p. 15511-24.
78. Hofmann, H., et al., *Human coronavirus NL63 employs the severe acute respiratory syndrome coronavirus receptor for cellular entry.* Proc Natl Acad Sci U S A, 2005. **102**(22): p. 7988-93.
79. Raj, V.S., et al., *Dipeptidyl peptidase 4 is a functional receptor for the emerging human coronavirus-EMC.* Nature, 2013. **495**(7440): p. 251-4.
80. Li, F., *Structure, Function, and Evolution of Coronavirus Spike Proteins.* Annu Rev Virol, 2016. **3**(1): p. 237-261.
81. Hulswit, R.J., C.A. de Haan, and B.J. Bosch, *Coronavirus Spike Protein and Tropism Changes.* Adv Virus Res, 2016. **96**: p. 29-57.
82. Anand, K., et al., *Structure of coronavirus main proteinase reveals combination of a chymotrypsin fold with an extra alpha-helical domain.* EMBO J, 2002. **21**(13): p. 3213-24.
83. Snijder, E.J., et al., *Ultrastructure and origin of membrane vesicles associated with the severe acute respiratory syndrome coronavirus replication complex.* J Virol, 2006. **80**(12): p. 5927-40.
84. Gosert, R., et al., *RNA replication of mouse hepatitis virus takes place at double-membrane vesicles.* J Virol, 2002. **76**(8): p. 3697-708.
85. Goldsmith, C.S., et al., *Ultrastructural characterization of SARS coronavirus.* Emerg Infect Dis, 2004. **10**(2): p. 320-6.
86. Orenstein, J.M., B. Banach, and S.C. Baker, *Morphogenesis of Coronavirus HCoV-NL63 in Cell Culture: A Transmission Electron Microscopic Study.* Open Infect Dis J, 2008. **2**: p. 52-58.
87. Maier, H.J., et al., *Infectious bronchitis virus generates spherules from zippered endoplasmic reticulum membranes.* MBio, 2013. **4**(5): p. e00801-13.
88. Knoops, K., et al., *SARS-coronavirus replication is supported by a reticulovesicular network of modified endoplasmic reticulum.* PLoS Biol, 2008. **6**(9): p. e226.
89. de Wilde, A.H., et al., *MERS-coronavirus replication induces severe in vitro cytopathology and is strongly inhibited by cyclosporin A or interferon-alpha treatment.* J Gen Virol, 2013. **94**(Pt 8): p. 1749-60.

90. Miller, S. and J. Krijnse-Locker, *Modification of intracellular membrane structures for virus replication.* Nat Rev Microbiol, 2008. **6**(5): p. 363-74.
91. den Boon, J.A., A. Diaz, and P. Ahlquist, *Cytoplasmic viral replication complexes.* Cell Host Microbe, 2010. **8**(1): p. 77-85.
92. Romero-Brey, I. and R. Bartenschlager, *Membranous replication factories induced by plus-strand RNA viruses.* Viruses, 2014. **6**(7): p. 2826-57.
93. Oudshoorn, D., et al., *Antiviral Innate Immune Response Interferes with the Formation of Replication-Associated Membrane Structures Induced by a Positive-Strand RNA Virus.* MBio, 2016. **7**(6).
94. van der Hoeven, B., et al., *Biogenesis and architecture of arterivirus replication organelles.* Virus Res, 2016. **220**: p. 70-90.
95. Oudshoorn, D., et al., *Expression and Cleavage of Middle East Respiratory Syndrome Coronavirus nsp3-4 Polyprotein Induce the Formation of Double-Membrane Vesicles That Mimic Those Associated with Coronaviral RNA Replication.* MBio, 2017. **8**(6).
96. Lundin, A., et al., *Targeting membrane-bound viral RNA synthesis reveals potent inhibition of diverse coronaviruses including the middle East respiratory syndrome virus.* PLoS Pathog, 2014. **10**(5): p. e1004166.
97. Angelini, M.M., et al., *Severe acute respiratory syndrome coronavirus nonstructural proteins 3, 4, and 6 induce double-membrane vesicles.* MBio, 2013. **4**(4).
98. Gorbalenya, A.E., et al., *Coronavirus genome: prediction of putative functional domains in the non-structural polyprotein by comparative amino acid sequence analysis.* Nucleic Acids Res, 1989. **17**(12): p. 4847-61.
99. te Velthuis, A.J., et al., *The RNA polymerase activity of SARS-coronavirus nsp12 is primer dependent.* Nucleic Acids Res, 2010. **38**(1): p. 203-14.
100. Posthuma, C.C., A.J.W. Te Velthuis, and E.J. Snijder, *Nidovirus RNA polymerases: Complex enzymes handling exceptional RNA genomes.* Virus Res, 2017. **234**: p. 58-73.
101. Seybert, A., et al., *The human coronavirus 229E superfamily 1 helicase has RNA and DNA duplex-unwinding activities with 5'-to-3' polarity.* RNA, 2000. **6**(7): p. 1056-68.
102. Gorbalenya, A.E., et al., *Two related superfamilies of putative helicases involved in replication, recombination, repair and expression of DNA and RNA genomes.* Nucleic Acids Res, 1989. **17**(12): p. 4713-30.
103. Ivanov, K.A., et al., *Multiple enzymatic activities associated with severe acute respiratory syndrome coronavirus helicase.* J Virol, 2004. **78**(11): p. 5619-32.
104. Kirchdoerfer, R.N. and A.B. Ward, *Structure of the SARS-CoV nsp12 polymerase bound to nsp7 and nsp8 co-factors.* Nat Commun, 2019. **10**(1): p. 2342.
105. Subissi, L., et al., *One severe acute respiratory syndrome coronavirus protein complex integrates processive RNA polymerase and exonuclease activities.* Proc Natl Acad Sci U S A, 2014. **111**(37): p. E3900-9.
106. Imbert, I., et al., *A second, non-canonical RNA-dependent RNA polymerase in SARS coronavirus.* EMBO J, 2006. **25**(20): p. 4933-42.
107. te Velthuis, A.J., S.H. van den Worm, and E.J. Snijder, *The SARS-coronavirus nsp7+nsp8 complex is a unique multimeric RNA polymerase capable of both de novo initiation and primer extension.* Nucleic Acids Res, 2012. **40**(4): p. 1737-47.
108. Tvarogova, J., et al., *Identification and characterization of a human coronavirus 229E nonstructural protein 8-associated RNA 3'-terminal adenylyltransferase activity.* J Virol, 2019.
109. Ferron, F., et al., *Structural and molecular basis of mismatch correction and ribavirin excision from coronavirus RNA.* Proc Natl Acad Sci U S A, 2018. **115**(2): p. E162-E171.

110. Snijder, E.J., et al., *Unique and conserved features of genome and proteome of SARS-coronavirus, an early split-off from the coronavirus group 2 lineage.* J Mol Biol, 2003. **331**(5): p. 991-1004.
111. Eckerle, L.D., et al., *Infidelity of SARS-CoV Nsp14-exonuclease mutant virus replication is revealed by complete genome sequencing.* PLoS Pathog, 2010. **6**(5): p. e1000896.
112. Denison, M.R., et al., *Coronaviruses: an RNA proofreading machine regulates replication fidelity and diversity.* RNA Biol, 2011. **8**(2): p. 270-9.
113. Smith, E.C. and M.R. Denison, *Coronaviruses as DNA wannabes: a new model for the regulation of RNA virus replication fidelity.* PLoS Pathog, 2013. **9**(12): p. e1003760.
114. Eckerle, L.D., et al., *High fidelity of murine hepatitis virus replication is decreased in nsp14 exoribonuclease mutants.* J Virol, 2007. **81**(22): p. 12135-44.
115. Smith, E.C., et al., *Coronaviruses lacking exoribonuclease activity are susceptible to lethal mutagenesis: evidence for proofreading and potential therapeutics.* PLoS Pathog, 2013. **9**(8): p. e1003565.
116. Minskaia, E., et al., *Discovery of an RNA virus 3'->5' exoribonuclease that is critically involved in coronavirus RNA synthesis.* Proc Natl Acad Sci U S A, 2006. **103**(13): p. 5108-13.
117. Becares, M., et al., *Mutagenesis of Coronavirus nsp14 Reveals Its Potential Role in Modulation of the Innate Immune Response.* J Virol, 2016. **90**(11): p. 5399-5414.
118. Ogando, N.S., et al., *The Curious Case of the Nidovirus Exoribonuclease: Its Role in RNA Synthesis and Replication Fidelity.* Front Microbiol, 2019. **10**: p. 1813.
119. Bouvet, M., et al., *RNA 3'-end mismatch excision by the severe acute respiratory syndrome coronavirus nonstructural protein nsp10/nsp14 exoribonuclease complex.* Proc Natl Acad Sci U S A, 2012. **109**(24): p. 9372-7.
120. Chen, Y., et al., *Functional screen reveals SARS coronavirus nonstructural protein nsp14 as a novel cap N7 methyltransferase.* Proc Natl Acad Sci U S A, 2009. **106**(9): p. 3484-9.
121. Bouvet, M., et al., *In vitro reconstitution of SARS-coronavirus mRNA cap methylation.* PLoS Pathog, 2010. **6**(4): p. e1000863.
122. Decroly, E., et al., *Crystal structure and functional analysis of the SARS-coronavirus RNA cap 2'-O-methyltransferase nsp10/nsp16 complex.* PLoS Pathog, 2011. **7**(5): p. e1002059.
123. Decroly, E., et al., *Coronavirus nonstructural protein 16 is a cap-0 binding enzyme possessing (nucleoside-2'O)-methyltransferase activity.* J Virol, 2008. **82**(16): p. 8071-84.
124. Menachery, V.D., K. Debbink, and R.S. Baric, *Coronavirus non-structural protein 16: evasion, attenuation, and possible treatments.* Virus Res, 2014. **194**: p. 191-9.
125. Bouvet, M., et al., *Coronavirus Nsp10, a critical co-factor for activation of multiple replicative enzymes.* J Biol Chem, 2014. **289**(37): p. 25783-96.
126. Pasternak, A.O., W.J. Spaan, and E.J. Snijder, *Nidovirus transcription: how to make sense...?* J Gen Virol, 2006. **87**(Pt 6): p. 1403-21.
127. Sawicki, S.G., D.L. Sawicki, and S.G. Siddell, *A contemporary view of coronavirus transcription.* J Virol, 2007. **81**(1): p. 20-9.
128. tenOever, B.R., *The Evolution of Antiviral Defense Systems.* Cell Host Microbe, 2016. **19**(2): p. 142-9.
129. Garcia-Sastre, A., *Ten Strategies of Interferon Evasion by Viruses.* Cell Host Microbe, 2017. **22**(2): p. 176-184.
130. Beachboard, D.C. and S.M. Horner, *Innate immune evasion strategies of DNA and RNA viruses.* Curr Opin Microbiol, 2016. **32**: p. 113-9.
131. Hoffmann, H.H., W.M. Schneider, and C.M. Rice, *Interferons and viruses: an evolutionary arms race of molecular interactions.* Trends Immunol, 2015. **36**(3): p. 124-38.
132. Roth-Cross, J.K., S.J. Bender, and S.R. Weiss, *Murine coronavirus mouse hepatitis virus is recognized by MDA5 and induces type I interferon in brain macrophages/microglia.* J Virol, 2008. **82**(20): p. 9829-38.

133. Chow, K.T., M. Gale, Jr., and Y.M. Loo, *RIG-I and Other RNA Sensors in Antiviral Immunity.* Annu Rev Immunol, 2018. **36**: p. 667-694.
134. Goubau, D., et al., *Antiviral immunity via RIG-I-mediated recognition of RNA bearing 5'-diphosphates.* Nature, 2014. **514**(7522): p. 372-5.
135. Kato, H., et al., *Length-dependent recognition of double-stranded ribonucleic acids by retinoic acid-inducible gene-I and melanoma differentiation-associated gene 5.* J Exp Med, 2008. **205**(7): p. 1601-10.
136. Schneider, W.M., M.D. Chevillotte, and C.M. Rice, *Interferon-stimulated genes: a complex web of host defenses.* Annu Rev Immunol, 2014. **32**: p. 513-45.
137. Andreakos, E., et al., *Interferon-lambdas: Front-Line Guardians of Immunity and Homeostasis in the Respiratory Tract.* Front Immunol, 2017. **8**: p. 1232.
138. Lazear, H.M., J.W. Schoggins, and M.S. Diamond, *Shared and Distinct Functions of Type I and Type III Interferons.* Immunity, 2019. **50**(4): p. 907-923.
139. Le Bon, A. and D.F. Tough, *Links between innate and adaptive immunity via type I interferon.* Curr Opin Immunol, 2002. **14**(4): p. 432-6.
140. Le Bon, A., et al., *Cutting edge: enhancement of antibody responses through direct stimulation of B and T cells by type I IFN.* J Immunol, 2006. **176**(4): p. 2074-8.
141. Hervas-Stubbs, S., et al., *Direct effects of type I interferons on cells of the immune system.* Clin Cancer Res, 2011. **17**(9): p. 2619-27.
142. Liu, J., C. Qian, and X. Cao, *Post-Translational Modification Control of Innate Immunity.* Immunity, 2016. **45**(1): p. 15-30.
143. Chiang, C. and M.U. Gack, *Post-translational Control of Intracellular Pathogen Sensing Pathways.* Trends Immunol, 2017. **38**(1): p. 39-52.
144. Zhou, Y., et al., *Post-translational regulation of antiviral innate signaling.* Eur J Immunol, 2017. **47**(9): p. 1414-1426.
145. Komander, D. and M. Rape, *The ubiquitin code.* Annu Rev Biochem, 2012. **81**: p. 203-29.
146. Kulathu, Y. and D. Komander, *Atypical ubiquitylation - the unexplored world of polyubiquitin beyond Lys48 and Lys63 linkages.* Nat Rev Mol Cell Biol, 2012. **13**(8): p. 508-23.
147. Yau, R. and M. Rape, *The increasing complexity of the ubiquitin code.* Nat Cell Biol, 2016. **18**(6): p. 579-86.
148. Swatek, K.N. and D. Komander, *Ubiquitin modifications.* Cell Res, 2016. **26**(4): p. 399-422.
149. Herhaus, L. and I. Dikic, *Expanding the ubiquitin code through post-translational modification.* EMBO Rep, 2015. **16**(9): p. 1071-83.
150. Clague, M.J., S. Urbe, and D. Komander, *Breaking the chains: deubiquitylating enzyme specificity begets function.* Nat Rev Mol Cell Biol, 2019.
151. Davis, M.E. and M.U. Gack, *Ubiquitination in the antiviral immune response.* Virology, 2015. **479-480**: p. 52-65.
152. Heaton, S.M., N.A. Borg, and V.M. Dixit, *Ubiquitin in the activation and attenuation of innate antiviral immunity.* J Exp Med, 2016. **213**(1): p. 1-13.
153. Chan, R.W., et al., *Tropism of and innate immune responses to the novel human betacoronavirus lineage C virus in human ex vivo respiratory organ cultures.* J Virol, 2013. **87**(12): p. 6604-14.
154. Kindler, E., et al., *Efficient replication of the novel human betacoronavirus EMC on primary human epithelium highlights its zoonotic potential.* MBio, 2013. **4**(1): p. e00611-12.
155. Lau, S.K., et al., *Delayed induction of proinflammatory cytokines and suppression of innate antiviral response by the novel Middle East respiratory syndrome coronavirus: implications for pathogenesis and treatment.* J Gen Virol, 2013. **94**(Pt 12): p. 2679-90.

156. Zielecki, F., et al., *Human cell tropism and innate immune system interactions of human respiratory coronavirus EMC compared to those of severe acute respiratory syndrome coronavirus.* J Virol, 2013. **87**(9): p. 5300-4.
157. Menachery, V.D., et al., *Pathogenic influenza viruses and coronaviruses utilize similar and contrasting approaches to control interferon-stimulated gene responses.* MBio, 2014. **5**(3): p. e01174-14.
158. Zhou, J., et al., *Active replication of Middle East respiratory syndrome coronavirus and aberrant induction of inflammatory cytokines and chemokines in human macrophages: implications for pathogenesis.* J Infect Dis, 2014. **209**(9): p. 1331-42.
159. Rose, K.M. and S.R. Weiss, *Murine Coronavirus Cell Type Dependent Interaction with the Type I Interferon Response.* Viruses, 2009. **1**(3): p. 689-712.
160. Frieman, M., M. Heise, and R. Baric, *SARS coronavirus and innate immunity.* Virus Res, 2008. **133**(1): p. 101-12.
161. Weber, F., et al., *Double-stranded RNA is produced by positive-strand RNA viruses and DNA viruses but not in detectable amounts by negative-strand RNA viruses.* J Virol, 2006. **80**(10): p. 5059-64.
162. Cervantes-Barragan, L., et al., *Control of coronavirus infection through plasmacytoid dendritic-cell-derived type I interferon.* Blood, 2007. **109**(3): p. 1131-7.
163. Scheuplein, V.A., et al., *High secretion of interferons by human plasmacytoid dendritic cells upon recognition of Middle East respiratory syndrome coronavirus.* J Virol, 2015. **89**(7): p. 3859-69.
164. Channappanavar, R. and S. Perlman, *Pathogenic human coronavirus infections: causes and consequences of cytokine storm and immunopathology.* Semin Immunopathol, 2017. **39**(5): p. 529-539.
165. Kindler, E. and V. Thiel, *To sense or not to sense viral RNA--essentials of coronavirus innate immune evasion.* Curr Opin Microbiol, 2014. **20**: p. 69-75.
166. Case, J.B., et al., *Mutagenesis of S-Adenosyl-l-Methionine-Binding Residues in Coronavirus nsp14 N7-Methyltransferase Demonstrates Differing Requirements for Genome Translation and Resistance to Innate Immunity.* J Virol, 2016. **90**(16): p. 7248-7256.
167. Habjan, M., et al., *Sequestration by IFIT1 impairs translation of 2'O-unmethylated capped RNA.* PLoS Pathog, 2013. **9**(10): p. e1003663.
168. Menachery, V.D., et al., *Attenuation and restoration of severe acute respiratory syndrome coronavirus mutant lacking 2'-o-methyltransferase activity.* J Virol, 2014. **88**(8): p. 4251-64.
169. Zust, R., et al., *Ribose 2'-O-methylation provides a molecular signature for the distinction of self and non-self mRNA dependent on the RNA sensor Mda5.* Nat Immunol, 2011. **12**(2): p. 137-43.
170. Menachery, V.D., et al., *Middle East Respiratory Syndrome Coronavirus Nonstructural Protein 16 Is Necessary for Interferon Resistance and Viral Pathogenesis.* mSphere, 2017. **2**(6).
171. Ricagno, S., et al., *Crystal structure and mechanistic determinants of SARS coronavirus nonstructural protein 15 define an endoribonuclease family.* Proc Natl Acad Sci U S A, 2006. **103**(32): p. 11892-7.
172. Kang, H., et al., *Biochemical and genetic analyses of murine hepatitis virus Nsp15 endoribonuclease.* J Virol, 2007. **81**(24): p. 13587-97.
173. Kindler, E., et al., *Early endonuclease-mediated evasion of RNA sensing ensures efficient coronavirus replication.* PLoS Pathog, 2017. **13**(2): p. e1006195.
174. Deng, X., et al., *Coronavirus nonstructural protein 15 mediates evasion of dsRNA sensors and limits apoptosis in macrophages.* Proc Natl Acad Sci U S A, 2017. **114**(21): p. E4251-E4260.
175. Zhao, L., et al., *Antagonism of the interferon-induced OAS-RNase L pathway by murine coronavirus ns2 protein is required for virus replication and liver pathology.* Cell Host Microbe, 2012. **11**(6): p. 607-16.
176. Thornbrough, J.M., et al., *Middle East Respiratory Syndrome Coronavirus NS4b Protein Inhibits Host RNase L Activation.* MBio, 2016. **7**(2): p. e00258.

177. Reineke, L.C. and R.E. Lloyd, *Diversion of stress granules and P-bodies during viral infection.* Virology, 2013. **436**(2): p. 255-267.
178. Nakagawa, K., et al., *Inhibition of Stress Granule Formation by Middle East Respiratory Syndrome Coronavirus 4a Accessory Protein Facilitates Viral Translation, Leading to Efficient Virus Replication.* J Virol, 2018. **92**(20).
179. Rabouw, H.H., et al., *Middle East Respiratory Coronavirus Accessory Protein 4a Inhibits PKR-Mediated Antiviral Stress Responses.* PLoS Pathog, 2016. **12**(10): p. e1005982.
180. Narayanan, K., C. Huang, and S. Makino, *SARS coronavirus accessory proteins.* Virus Res, 2008. **133**(1): p. 113-21.
181. Menachery, V.D., et al., *MERS-CoV Accessory ORFs Play Key Role for Infection and Pathogenesis.* MBio, 2017. **8**(4).
182. Liu, D.X., et al., *Accessory proteins of SARS-CoV and other coronaviruses.* Antiviral Res, 2014. **109**: p. 97-109.
183. Kamitani, W., et al., *A two-pronged strategy to suppress host protein synthesis by SARS coronavirus Nsp1 protein.* Nat Struct Mol Biol, 2009. **16**(11): p. 1134-40.
184. Narayanan, K., et al., *Coronavirus nonstructural protein 1: Common and distinct functions in the regulation of host and viral gene expression.* Virus Res, 2015. **202**: p. 89-100.
185. Lokugamage, K.G., et al., *Severe acute respiratory syndrome coronavirus protein nsp1 is a novel eukaryotic translation inhibitor that represses multiple steps of translation initiation.* J Virol, 2012. **86**(24): p. 13598-608.
186. Huang, C., et al., *SARS coronavirus nsp1 protein induces template-dependent endonucleolytic cleavage of mRNAs: viral mRNAs are resistant to nsp1-induced RNA cleavage.* PLoS Pathog, 2011. **7**(12): p. e1002433.
187. Narayanan, K., et al., *Severe acute respiratory syndrome coronavirus nsp1 suppresses host gene expression, including that of type I interferon, in infected cells.* J Virol, 2008. **82**(9): p. 4471-9.
188. Lokugamage, K.G., et al., *Middle East Respiratory Syndrome Coronavirus nsp1 Inhibits Host Gene Expression by Selectively Targeting mRNAs Transcribed in the Nucleus while Sparing mRNAs of Cytoplasmic Origin.* J Virol, 2015. **89**(21): p. 10970-81.
189. Lei, J., Y. Kusov, and R. Hilgenfeld, *Nsp3 of coronaviruses: Structures and functions of a large multi-domain protein.* Antiviral Res, 2018. **149**: p. 58-74.
190. Fehr, A.R., et al., *The nsp3 macrodomain promotes virulence in mice with coronavirus-induced encephalitis.* J Virol, 2015. **89**(3): p. 1523-36.
191. Fehr, A.R., et al., *The Conserved Coronavirus Macrodomain Promotes Virulence and Suppresses the Innate Immune Response during Severe Acute Respiratory Syndrome Coronavirus Infection.* MBio, 2016. **7**(6).
192. Egloff, M.P., et al., *Structural and functional basis for ADP-ribose and poly(ADP-ribose) binding by viral macro domains.* J Virol, 2006. **80**(17): p. 8493-502.
193. Li, C., et al., *Viral Macro Domains Reverse Protein ADP-Ribosylation.* J Virol, 2016. **90**(19): p. 8478-86.
194. Grunewald, M.E., et al., *The coronavirus macrodomain is required to prevent PARP-mediated inhibition of virus replication and enhancement of IFN expression.* PLoS Pathog, 2019. **15**(5): p. e1007756.
195. Sulea, T., et al., *Deubiquitination, a new function of the severe acute respiratory syndrome coronavirus papain-like protease?* J Virol, 2005. **79**(7): p. 4550-1.
196. Barretto, N., et al., *The papain-like protease of severe acute respiratory syndrome coronavirus has deubiquitinating activity.* J Virol, 2005. **79**(24): p. 15189-98.
197. Lindner, H.A., et al., *The papain-like protease from the severe acute respiratory syndrome coronavirus is a deubiquitinating enzyme.* J Virol, 2005. **79**(24): p. 15199-208.

198. Lindner, H.A., et al., *Selectivity in ISG15 and ubiquitin recognition by the SARS coronavirus papain-like protease.* Arch Biochem Biophys, 2007. **466**(1): p. 8-14.
199. Clementz, M.A., et al., *Deubiquitinating and interferon antagonism activities of coronavirus papain-like proteases.* J Virol, 2010. **84**(9): p. 4619-29.
200. Devaraj, S.G., et al., *Regulation of IRF-3-dependent innate immunity by the papain-like protease domain of the severe acute respiratory syndrome coronavirus.* J Biol Chem, 2007. **282**(44): p. 32208-21.
201. Xing, Y., et al., *The papain-like protease of porcine epidemic diarrhea virus negatively regulates type I interferon pathway by acting as a viral deubiquitinase.* J Gen Virol, 2013. **94**(Pt 7): p. 1554-67.
202. Mielech, A.M., et al., *MERS-CoV papain-like protease has deISGylating and deubiquitinating activities.* Virology, 2014. **450-451**: p. 64-70.
203. Zheng, D., et al., *PLP2, a potent deubiquitinase from murine hepatitis virus, strongly inhibits cellular type I interferon production.* Cell Res, 2008. **18**(11): p. 1105-13.
204. Frieman, M., et al., *Severe acute respiratory syndrome coronavirus papain-like protease ubiquitin-like domain and catalytic domain regulate antagonism of IRF3 and NF-kappaB signaling.* J Virol, 2009. **83**(13): p. 6689-705.
205. Yang, X., et al., *Proteolytic processing, deubiquitinase and interferon antagonist activities of Middle East respiratory syndrome coronavirus papain-like protease.* J Gen Virol, 2014. **95**(Pt 3): p. 614-26.
206. Mielech, A.M., et al., *Nidovirus papain-like proteases: multifunctional enzymes with protease, deubiquitinating and deISGylating activities.* Virus Res, 2014. **194**: p. 184-90.
207. Ratia, K., et al., *Structural Basis for the Ubiquitin-Linkage Specificity and deISGylating activity of SARS-CoV papain-like protease.* PLoS Pathog, 2014. **10**(5): p. e1004113.
208. Chen, Y., et al., *X-ray Structural and Functional Studies of the Three Tandemly Linked Domains of Nonstructural Protein 3 (nsp3) from Murine Hepatitis Virus Reveal Conserved Functions.* J Biol Chem, 2015. **290**(42): p. 25293-306.
209. Abdul Rehman, S.A., et al., *MINDY-1 Is a Member of an Evolutionarily Conserved and Structurally Distinct New Family of Deubiquitinating Enzymes.* Mol Cell, 2016. **63**(1): p. 146-55.
210. Kwasna, D., et al., *Discovery and Characterization of ZUFSP/ZUP1, a Distinct Deubiquitinase Class Important for Genome Stability.* Mol Cell, 2018. **70**(1): p. 150-164 e6.
211. Nijman, S.M., et al., *A genomic and functional inventory of deubiquitinating enzymes.* Cell, 2005. **123**(5): p. 773-86.
212. Baker, S.C., et al., *Identification of a domain required for autoproteolytic cleavage of murine coronavirus gene A polyprotein.* J Virol, 1989. **63**(9): p. 3693-9.
213. Denison, M. and S. Perlman, *Identification of putative polymerase gene product in cells infected with murine coronavirus A59.* Virology, 1987. **157**(2): p. 565-8.
214. Baker, S.C., et al., *Identification of the catalytic sites of a papain-like cysteine proteinase of murine coronavirus.* J Virol, 1993. **67**(10): p. 6056-63.
215. Snijder, E.J., A.L. Wassenaar, and W.J. Spaan, *The 5' end of the equine arteritis virus replicase gene encodes a papainlike cysteine protease.* J Virol, 1992. **66**(12): p. 7040-8.
216. Denison, M.R., et al., *Intracellular processing of the N-terminal ORF 1a proteins of the coronavirus MHV-A59 requires multiple proteolytic events.* Virology, 1992. **189**(1): p. 274-84.
217. Snijder, E.J., et al., *The arterivirus Nsp2 protease. An unusual cysteine protease with primary structure similarities to both papain-like and chymotrypsin-like proteases.* J Biol Chem, 1995. **270**(28): p. 16671-6.
218. Makarova, K.S., L. Aravind, and E.V. Koonin, *A novel superfamily of predicted cysteine proteases from eukaryotes, viruses and Chlamydia pneumoniae.* Trends Biochem Sci, 2000. **25**(2): p. 50-2.

219. Frias-Staheli, N., et al., *Ovarian tumor domain-containing viral proteases evade ubiquitin- and ISG15-dependent innate immune responses.* Cell Host Microbe, 2007. **2**(6): p. 404-16.
220. van Kasteren, P.B., et al., *Deubiquitinase function of arterivirus papain-like protease 2 suppresses the innate immune response in infected host cells.* Proc Natl Acad Sci U S A, 2013. **110**(9): p. E838-47.
221. van Kasteren, P.B., et al., *Arterivirus and nairovirus ovarian tumor domain-containing Deubiquitinases target activated RIG-I to control innate immune signaling.* J Virol, 2012. **86**(2): p. 773-85.
222. Capodagli, G.C., et al., *Structural analysis of a viral ovarian tumor domain protease from the Crimean-Congo hemorrhagic fever virus in complex with covalently bonded ubiquitin.* J Virol, 2011. **85**(7): p. 3621-30.
223. James, T.W., et al., *Structural basis for the removal of ubiquitin and interferon-stimulated gene 15 by a viral ovarian tumor domain-containing protease.* Proc Natl Acad Sci U S A, 2011. **108**(6): p. 2222-7.
224. Akutsu, M., et al., *Molecular basis for ubiquitin and ISG15 cross-reactivity in viral ovarian tumor domains.* Proc Natl Acad Sci U S A, 2011. **108**(6): p. 2228-33.
225. Scholte, F.E.M., et al., *Crimean-Congo Hemorrhagic Fever Virus Suppresses Innate Immune Responses via a Ubiquitin and ISG15 Specific Protease.* Cell Rep, 2017. **20**(10): p. 2396-2407.
226. Herold, J., S.G. Siddell, and A.E. Gorbalenya, *A human RNA viral cysteine proteinase that depends upon a unique Zn2+-binding finger connecting the two domains of a papain-like fold.* J Biol Chem, 1999. **274**(21): p. 14918-25.
227. Thiel, V., et al., *Mechanisms and enzymes involved in SARS coronavirus genome expression.* J Gen Virol, 2003. **84**(Pt 9): p. 2305-15.
228. Harcourt, B.H., et al., *Identification of severe acute respiratory syndrome coronavirus replicase products and characterization of papain-like protease activity.* J Virol, 2004. **78**(24): p. 13600-12.
229. Ratia, K., et al., *Severe acute respiratory syndrome coronavirus papain-like protease: structure of a viral deubiquitinating enzyme.* Proc Natl Acad Sci U S A, 2006. **103**(15): p. 5717-22.
230. Chen, Z., et al., *Proteolytic processing and deubiquitinating activity of papain-like proteases of human coronavirus NL63.* J Virol, 2007. **81**(11): p. 6007-18.
231. Wojdyla, J.A., et al., *Papain-like protease 1 from transmissible gastroenteritis virus: crystal structure and enzymatic activity toward viral and cellular substrates.* J Virol, 2010. **84**(19): p. 10063-73.
232. Kong, L., et al., *Structural View and Substrate Specificity of Papain-like Protease from Avian Infectious Bronchitis Virus.* J Biol Chem, 2015. **290**(11): p. 7160-8.
233. Hu, X., et al., *Transmissible Gastroenteritis Virus Papain-Like Protease 1 Antagonizes Production of Interferon-beta through Its Deubiquitinase Activity.* Biomed Res Int, 2017. **2017**: p. 7089091.
234. Bekes, M., et al., *SARS hCoV papain-like protease is a unique Lys48 linkage-specific di-distributive deubiquitinating enzyme.* Biochem J, 2015. **468**(2): p. 215-26.
235. Baez-Santos, Y.M., et al., *Catalytic function and substrate specificity of the papain-like protease domain of nsp3 from the Middle East respiratory syndrome coronavirus.* J Virol, 2014. **88**(21): p. 12511-27.
236. Bekes, M., et al., *Recognition of Lys48-Linked Di-ubiquitin and Deubiquitinating Activities of the SARS Coronavirus Papain-like Protease.* Mol Cell, 2016. **62**(4): p. 572-85.
237. Faesen, A.C., et al., *The differential modulation of USP activity by internal regulatory domains, interactors and eight ubiquitin chain types.* Chem Biol, 2011. **18**(12): p. 1550-61.
238. Mevissen, T.E., et al., *OTU deubiquitinases reveal mechanisms of linkage specificity and enable ubiquitin chain restriction analysis.* Cell, 2013. **154**(1): p. 169-84.
239. Mevissen, T.E.T. and D. Komander, *Mechanisms of Deubiquitinase Specificity and Regulation.* Annual Review of Biochemistry, Vol 86, 2017. **86**: p. 159-192.
240. Zumla, A., et al., *Coronaviruses - drug discovery and therapeutic options.* Nat Rev Drug Discov, 2016. **15**(5): p. 327-47.

241. Omrani, A.S., et al., *Ribavirin and interferon alfa-2a for severe Middle East respiratory syndrome coronavirus infection: a retrospective cohort study.* Lancet Infect Dis, 2014. **14**(11): p. 1090-1095.
242. Al-Tawfiq, J.A., et al., *Ribavirin and interferon therapy in patients infected with the Middle East respiratory syndrome coronavirus: an observational study.* Int J Infect Dis, 2014. **20**: p. 42-6.
243. Shalhoub, S., et al., *IFN-alpha2a or IFN-beta1a in combination with ribavirin to treat Middle East respiratory syndrome coronavirus pneumonia: a retrospective study.* J Antimicrob Chemother, 2015. **70**(7): p. 2129-32.
244. Khalid, M., et al., *Ribavirin and interferon-alpha2b as primary and preventive treatment for Middle East respiratory syndrome coronavirus: a preliminary report of two cases.* Antivir Ther, 2015. **20**(1): p. 87-91.
245. Falzarano, D., et al., *Inhibition of novel beta coronavirus replication by a combination of interferon-alpha2b and ribavirin.* Sci Rep, 2013. **3**: p. 1686.
246. Falzarano, D., et al., *Treatment with interferon-alpha2b and ribavirin improves outcome in MERS-CoV-infected rhesus macaques.* Nat Med, 2013. **19**(10): p. 1313-7.
247. de Wilde, A.H., et al., *Screening of an FDA-approved compound library identifies four small-molecule inhibitors of Middle East respiratory syndrome coronavirus replication in cell culture.* Antimicrob Agents Chemother, 2014. **58**(8): p. 4875-84.
248. Dyall, J., et al., *Repurposing of clinically developed drugs for treatment of Middle East respiratory syndrome coronavirus infection.* Antimicrob Agents Chemother, 2014. **58**(8): p. 4885-93.
249. Sheahan, T.P., et al., *Broad-spectrum antiviral GS-5734 inhibits both epidemic and zoonotic coronaviruses.* Sci Transl Med, 2017. **9**(396).
250. Agostini, M.L., et al., *Coronavirus Susceptibility to the Antiviral Remdesivir (GS-5734) Is Mediated by the Viral Polymerase and the Proofreading Exoribonuclease.* MBio, 2018. **9**(2).
251. Pascal, K.E., et al., *Pre- and postexposure efficacy of fully human antibodies against Spike protein in a novel humanized mouse model of MERS-CoV infection.* Proc Natl Acad Sci U S A, 2015. **112**(28): p. 8738-43.
252. Du, L., et al., *Identification of a receptor-binding domain in the S protein of the novel human coronavirus Middle East respiratory syndrome coronavirus as an essential target for vaccine development.* J Virol, 2013. **87**(17): p. 9939-42.
253. Mou, H., et al., *The receptor binding domain of the new Middle East respiratory syndrome coronavirus maps to a 231-residue region in the spike protein that efficiently elicits neutralizing antibodies.* J Virol, 2013. **87**(16): p. 9379-83.
254. Perlman, S. and R. Vijay, *Middle East respiratory syndrome vaccines.* Int J Infect Dis, 2016. **47**: p. 23-8.
255. Okba, N.M., V.S. Raj, and B.L. Haagmans, *Middle East respiratory syndrome coronavirus vaccines: current status and novel approaches.* Curr Opin Virol, 2017. **23**: p. 49-58.
256. Wang, L., et al., *Evaluation of candidate vaccine approaches for MERS-CoV.* Nat Commun, 2015. **6**: p. 7712.
257. Haagmans, B.L., et al., *An orthopoxvirus-based vaccine reduces virus excretion after MERS-CoV infection in dromedary camels.* Science, 2016. **351**(6268): p. 77-81.
258. Almazan, F., et al., *Engineering a replication-competent, propagation-defective Middle East respiratory syndrome coronavirus as a vaccine candidate.* MBio, 2013. **4**(5): p. e00650-13.
259. de Wit, E., et al., *SARS and MERS: recent insights into emerging coronaviruses.* Nature Reviews Microbiology, 2016. **14**: p. 523-534.
260. *Middle East respiratory syndrome coronavirus (MERS-CoV) – update (United Arab Emirates).* 2014, World Health Organization.

261. *WHO | Summary of probable SARS cases with onset of illness from 1 November 2002 to 31 July 2003*. Available from: http://www.who.int/csr/sars/country/table2004_04_21/en/.
262. Azhar, E.I., et al., *Evidence for camel-to-human transmission of MERS coronavirus.* New England Journal of Medicine, 2014. **370**(26): p. 2499-505.
263. Reusken, C., et al., *Middle East respiratory syndrome coronavirus (MERS-CoV) RNA and neutralising antibodies in milk collected according to local customs from dromedary camels, Qatar, April 2014.* Euro Surveillance, 2014. **19**(23): p. 20829.
264. Firth, A.E. and I. Brierley, *Non-canonical translation in RNA viruses.* Journal of General Virology, 2012. **93**: p. 1385-409.
265. Perlman, S. and J. Netland, *Coronaviruses post-SARS: update on replication and pathogenesis.* Nat Rev Microbiol, 2009. **7**(6): p. 439-50.
266. Kilianski, A., et al., *Assessing activity and inhibition of Middle East respiratory syndrome coronavirus papain-like and 3C-like proteases using luciferase-based biosensors.* J Virol, 2013. **87**(21): p. 11955-62.
267. Komander, D., M.J. Clague, and S. Urbe, *Breaking the chains: structure and function of the deubiquitinases.* Nat Rev Mol Cell Biol, 2009. **10**(8): p. 550-63.
268. Jensen, S. and A.R. Thomsen, *Sensing of RNA viruses: a review of innate immune receptors involved in recognizing RNA virus invasion.* Journal of Virology, 2012. **86**: p. 2900-10.
269. Jiang, X. and Z.J. Chen, *The role of ubiquitylation in immune defence and pathogen evasion.* Nat Rev Immunol, 2012. **12**(1): p. 35-48.
270. Spiegel, M., et al., *Inhibition of Beta interferon induction by severe acute respiratory syndrome coronavirus suggests a two-step model for activation of interferon regulatory factor 3.* J Virol, 2005. **79**(4): p. 2079-86.
271. Spiegel, M. and F. Weber, *Inhibition of cytokine gene expression and induction of chemokine genes in non-lymphatic cells infected with SARS coronavirus.* Virology Journal, 2006. **3**: p. 17-17.
272. Cheung, C.Y., et al., *Cytokine responses in severe acute respiratory syndrome coronavirus-infected macrophages in vitro: possible relevance to pathogenesis.* J Virol, 2005. **79**(12): p. 7819-26.
273. Chu, H., et al., *Productive replication of Middle East respiratory syndrome coronavirus in monocyte-derived dendritic cells modulates innate immune response.* Virology, 2014. **454-455**: p. 197-205.
274. Gack, M.U., et al., *Influenza A virus NS1 targets the ubiquitin ligase TRIM25 to evade recognition by the host viral RNA sensor RIG-I.* Cell Host Microbe, 2009. **5**(5): p. 439-49.
275. Fitzgerald, K.A., et al., *IKKepsilon and TBK1 are essential components of the IRF3 signaling pathway.* Nature Immunology, 2003. **4**: p. 491-6.
276. Gack, M.U., et al., *TRIM25 RING-finger E3 ubiquitin ligase is essential for RIG-I-mediated antiviral activity.* Nature, 2007. **446**: p. 916-920.
277. Seth, R.B., et al., *Identification and characterization of MAVS, a mitochondrial antiviral signaling protein that activates NF-kappaB and IRF 3.* Cell, 2005. **122**(5): p. 669-82.
278. Lin, R., et al., *Virus-dependent phosphorylation of the IRF-3 transcription factor regulates nuclear translocation, transactivation potential, and proteasome-mediated degradation.* Mol Cell Biol, 1998. **18**(5): p. 2986-96.
279. Gohara, D.W., et al., *Production of "authentic" poliovirus RNA-dependent RNA polymerase (3D(pol)) by ubiquitin-protease-mediated cleavage in Escherichia coli.* Protein Expr Purif, 1999. **17**(1): p. 128-38.
280. Messick, T.E., et al., *Structural basis for ubiquitin recognition by the Otu1 ovarian tumor domain protein.* J Biol Chem, 2008. **283**(16): p. 11038-49.
281. Borodovsky, A., et al., *Chemistry-based functional proteomics reveals novel members of the deubiquitinating enzyme family.* Chem Biol, 2002. **9**(10): p. 1149-59.
282. Kabsch, W., *XDS.* Acta Crystallographica. Section D: Biological Crystallography, 2010. **66**: p. 125-32.

283. Evans, P., *Scaling and assessment of data quality.* Acta Crystallographica. Section D: Biological Crystallography, 2006. **62**: p. 72-82.
284. Grosse-Kunstleve, R.W. and P.D. Adams, *Substructure search procedures for macromolecular structures.* Acta Crystallographica. Section D: Biological Crystallography, 2003. **59**: p. 1966-73.
285. Terwilliger, T.C., *Maximum-likelihood density modification.* Acta Crystallographica. Section D: Biological Crystallography, 2000. **56**: p. 965-72.
286. Terwilliger, T.C., et al., *Decision-making in structure solution using Bayesian estimates of map quality: the PHENIX AutoSol wizard.* Acta Crystallographica. Section D: Biological Crystallography, 2009. **65**: p. 582-601.
287. Emsley, P., et al., *Features and development of Coot.* Acta Crystallographica. Section D: Biological Crystallography, 2010. **66**: p. 486-501.
288. Afonine, P.V., et al., *Towards automated crystallographic structure refinement with phenix.refine.* Acta Crystallogr D Biol Crystallogr, 2012. **68**(Pt 4): p. 352-67.
289. Graham, F.L. and A.J. van der Eb, *A new technique for the assay of infectivity of human adenovirus 5 DNA.* Virology, 1973. **52**(2): p. 456-67.
290. Lin, M.H., et al., *Structural and functional characterization of MERS coronavirus papain-like protease.* J Biomed Sci, 2014. **21**: p. 54.
291. Lei, J., et al., *Crystal structure of the papain-like protease of MERS coronavirus reveals unusual, potentially druggable active-site features.* Antiviral Res, 2014. **109**: p. 72-82.
292. Faesen, A.C., M.P. Luna-Vargas, and T.K. Sixma, *The role of UBL domains in ubiquitin-specific proteases.* Biochemical Society Transactions, 2012. **40**: p. 539-45.
293. Rawlings, N.D., et al., *MEROPS: the database of proteolytic enzymes, their substrates and inhibitors.* Nucleic Acids Research, 2014. **42**: p. D503-9.
294. Krishna, S.S., I. Majumdar, and N.V. Grishin, *Structural classification of zinc fingers: survey and summary.* Nucleic Acids Research, 2003. **31**: p. 532-50.
295. Renatus, M., et al., *Structural basis of ubiquitin recognition by the deubiquitinating protease USP2.* Structure, 2006. **14**: p. 1293-302.
296. Ye, Y., et al., *Polyubiquitin binding and cross-reactivity in the USP domain deubiquitinase USP21.* EMBO Rep., 2011. **12**: p. 350-7.
297. Chou, C.Y., et al., *Structural basis for catalysis and ubiquitin recognition by the severe acute respiratory syndrome coronavirus papain-like protease.* Acta Crystallogr D Biol Crystallogr, 2014. **70**(Pt 2): p. 572-81.
298. Hu, M., et al., *Structure and mechanisms of the proteasome-associated deubiquitinating enzyme USP14.* EMBO Journal, 2005. **24**: p. 3747-56.
299. Bailey-Elkin, B.A., et al., *Viral OTU deubiquitinases: a structural and functional comparison.* PLoS Pathog, 2014. **10**(3): p. e1003894.
300. Dikic, I., S. Wakatsuki, and K.J. Walters, *Ubiquitin-binding domains - from structures to functions.* Nat Rev Mol Cell Biol, 2009. **10**(10): p. 659-71.
301. Eletr, Z.M. and K.D. Wilkinson, *Regulation of proteolysis by human deubiquitinating enzymes.* Biochim Biophys Acta, 2014. **1843**(1): p. 114-28.
302. Sun, Z., et al., *The cysteine protease domain of porcine reproductive and respiratory syndrome virus nonstructural protein 2 possesses deubiquitinating and interferon antagonism functions.* J Virol, 2010. **84**(15): p. 7832-46.
303. Randow, F. and P.J. Lehner, *Viral avoidance and exploitation of the ubiquitin system.* Nat Cell Biol, 2009. **11**(5): p. 527-34.

304. Hadari, T., et al., *A ubiquitin C-terminal isopeptidase that acts on polyubiquitin chains. Role in protein degradation.* Journal of Biological Chemistry, 1992. **267**(2): p. 719-27.
305. Schrodinger, LLC, *The PyMOL Molecular Graphics System, Version 1.3r1*. 2010.
306. World Health Organization, *Middle East respiratory syndrome coronavirus (MERS-CoV).* 2019.
307. Reusken, C.B., et al., *Middle East respiratory syndrome coronavirus neutralising serum antibodies in dromedary camels: a comparative serological study.* Lancet Infect Dis, 2013. **13**(10): p. 859-66.
308. Sabir, J.S., et al., *Co-circulation of three camel coronavirus species and recombination of MERS-CoVs in Saudi Arabia.* Science, 2016. **351**(6268): p. 81-4.
309. Cui, J., F. Li, and Z.L. Shi, *Origin and evolution of pathogenic coronaviruses.* Nat Rev Microbiol, 2018.
310. Liu, T., et al., *NF-kappaB signaling in inflammation.* Signal Transduct Target Ther, 2017. **2**.
311. Kiefer, K., et al., *Role of type I interferons in the activation of autoreactive B cells.* Immunol Cell Biol, 2012. **90**(5): p. 498-504.
312. Tough, D.F., *Modulation of T-cell function by type I interferon.* Immunol Cell Biol, 2012. **90**(5): p. 492-7.
313. Akutsu, M., I. Dikic, and A. Bremm, *Ubiquitin chain diversity at a glance.* J Cell Sci, 2016. **129**(5): p. 875-80.
314. Zhang, Y., et al., *RING-Domain E3 Ligase-Mediated Host-Virus Interactions: Orchestrating Immune Responses by the Host and Antagonizing Immune Defense by Viruses.* Front Immunol, 2018. **9**: p. 1083.
315. Bailey-Elkin, B.A., et al., *Structure and Function of Viral Deubiquitinating Enzymes.* J Mol Biol, 2017. **429**(22): p. 3441-3470.
316. Kint, J., et al., *Activation of the chicken type I interferon response by infectious bronchitis coronavirus.* J Virol, 2015. **89**(2): p. 1156-67.
317. Zhou, H. and S. Perlman, *Mouse hepatitis virus does not induce Beta interferon synthesis and does not inhibit its induction by double-stranded RNA.* J Virol, 2007. **81**(2): p. 568-74.
318. Channappanavar, R., et al., *Dysregulated Type I Interferon and Inflammatory Monocyte-Macrophage Responses Cause Lethal Pneumonia in SARS-CoV-Infected Mice.* Cell Host Microbe, 2016. **19**(2): p. 181-93.
319. Li, K., et al., *Mouse-adapted MERS coronavirus causes lethal lung disease in human DPP4 knockin mice.* Proc Natl Acad Sci U S A, 2017. **114**(15): p. E3119-E3128.
320. Kindler, E., V. Thiel, and F. Weber, *Interaction of SARS and MERS Coronaviruses with the Antiviral Interferon Response.* Adv Virus Res, 2016. **96**: p. 219-243.
321. Yang, Y., et al., *The structural and accessory proteins M, ORF 4a, ORF 4b, and ORF 5 of Middle East respiratory syndrome coronavirus (MERS-CoV) are potent interferon antagonists.* Protein Cell, 2013. **4**(12): p. 951-61.
322. Niemeyer, D., et al., *Middle East respiratory syndrome coronavirus accessory protein 4a is a type I interferon antagonist.* J Virol, 2013. **87**(22): p. 12489-95.
323. Canton, J., et al., *MERS-CoV 4b protein interferes with the NF-kappaB-dependent innate immune response during infection.* PLoS Pathog, 2018. **14**(1): p. e1006838.
324. Garcia-Sastre, A., et al., *Influenza A virus lacking the NS1 gene replicates in interferon-deficient systems.* Virology, 1998. **252**(2): p. 324-30.
325. Talon, J., et al., *Influenza A and B viruses expressing altered NS1 proteins: A vaccine approach.* Proc Natl Acad Sci U S A, 2000. **97**(8): p. 4309-14.
326. Wacheck, V., et al., *A novel type of influenza vaccine: safety and immunogenicity of replication-deficient influenza virus created by deletion of the interferon antagonist NS1.* J Infect Dis, 2010. **201**(3): p. 354-62.

327. Bailey-Elkin, B.A., et al., *Crystal structure of the Middle East respiratory syndrome coronavirus (MERS-CoV) papain-like protease bound to ubiquitin facilitates targeted disruption of deubiquitinating activity to demonstrate its role in innate immune suppression.* J Biol Chem, 2014. **289**(50): p. 34667-82.
328. Tischer, B.K., et al., *Two-step red-mediated recombination for versatile high-efficiency markerless DNA manipulation in Escherichia coli.* Biotechniques, 2006. **40**(2): p. 191-7.
329. van den Worm, S.H., et al., *Reverse genetics of SARS-related coronavirus using vaccinia virus-based recombination.* PLoS One, 2012. **7**(3): p. e32857.
330. Hierholzer, J.C. and R.A. Killington, *2 - Virus isolation and quantitation*, in *Virology Methods Manual*, B.W.J. Mahy and H.O. Kangro, Editors. 1996, Academic Press: London. p. 25-46.
331. Andersen, C.L., J.L. Jensen, and T.F. Orntoft, *Normalization of real-time quantitative reverse transcription-PCR data: a model-based variance estimation approach to identify genes suited for normalization, applied to bladder and colon cancer data sets.* Cancer Res, 2004. **64**(15): p. 5245-50.
332. Li, K., et al., *Middle East Respiratory Syndrome Coronavirus Causes Multiple Organ Damage and Lethal Disease in Mice Transgenic for Human Dipeptidyl Peptidase 4.* J Infect Dis, 2016. **213**(5): p. 712-22.
333. Scobey, T., et al., *Reverse genetics with a full-length infectious cDNA of the Middle East respiratory syndrome coronavirus.* Proc Natl Acad Sci U S A, 2013. **110**(40): p. 16157-62.
334. Lei, J. and R. Hilgenfeld, *RNA-virus proteases counteracting host innate immunity.* FEBS Lett, 2017. **591**(20): p. 3190-3210.
335. van Kasteren, P.B., et al., *In vivo assessment of equine arteritis virus vaccine improvement by disabling the deubiquitinase activity of papain-like protease 2.* Vet Microbiol, 2015. **178**(1-2): p. 132-7.
336. Niemeyer, D., et al., *The papain-like protease determines a virulence trait that varies among members of the SARS-coronavirus species.* PLoS Pathog, 2018. **14**(9): p. e1007296.
337. Channappanavar, R., et al., *IFN-I response timing relative to virus replication determines MERS coronavirus infection outcomes.* J Clin Invest, 2019. **130**.
338. Enjuanes, L., et al., *Molecular Basis of Coronavirus Virulence and Vaccine Development.* Adv Virus Res, 2016. **96**: p. 245-286.
339. Morales, D.J. and D.J. Lenschow, *The antiviral activities of ISG15.* J Mol Biol, 2013. **425**(24): p. 4995-5008.
340. Chenon, M., et al., *A viral deubiquitylating enzyme targets viral RNA-dependent RNA polymerase and affects viral infectivity.* EMBO J, 2012. **31**(3): p. 741-53.
341. Isaacson, M.K. and H.L. Ploegh, *Ubiquitination, ubiquitin-like modifiers, and deubiquitination in viral infection.* Cell Host Microbe, 2009. **5**(6): p. 559-70.
342. Baez-Santos, Y.M., S.E. St John, and A.D. Mesecar, *The SARS-coronavirus papain-like protease: structure, function and inhibition by designed antiviral compounds.* Antiviral Res, 2015. **115**: p. 21-38.
343. Hilgenfeld, R., *From SARS to MERS: crystallographic studies on coronaviral proteases enable antiviral drug design.* FEBS J, 2014. **281**(18): p. 4085-96.
344. Calistri, A., et al., *The ubiquitin-conjugating system: multiple roles in viral replication and infection.* Cells, 2014. **3**(2): p. 386-417.
345. Heideker, J. and I.E. Wertz, *DUBs, the regulation of cell identity and disease.* Biochem J, 2015. **465**(1): p. 1-26.
346. Kemp, M., *Recent Advances in the Discovery of Deubiquitinating Enzyme Inhibitors.* Prog Med Chem, 2016. **55**: p. 149-92.
347. Ernst, A., et al., *A strategy for modulation of enzymes in the ubiquitin system.* Science, 2013. **339**(6119): p. 590-5.
348. Zhang, W., et al., *System-Wide Modulation of HECT E3 Ligases with Selective Ubiquitin Variant Probes.* Mol Cell, 2016. **62**(1): p. 121-36.

349. Tonikian, R., et al., *Identifying specificity profiles for peptide recognition modules from phage-displayed peptide libraries.* Nat Protoc, 2007. **2**(6): p. 1368-86.
350. D'Arcy, A., F. Villard, and M. Marsh, *An automated microseed matrix-screening method for protein crystallization.* Acta Crystallogr D Biol Crystallogr, 2007. **63**(Pt 4): p. 550-4.
351. Ireton, G.C. and B.L. Stoddard, *Microseed matrix screening to improve crystals of yeast cytosine deaminase.* Acta Crystallogr D Biol Crystallogr, 2004. **60**(Pt 3): p. 601-5.
352. Georgieva, D.G., et al., *Heterogeneous nucleation of three-dimensional protein nanocrystals.* Acta Crystallogr D Biol Crystallogr, 2007. **63**(Pt 5): p. 564-70.
353. Carlotti, F., et al., *Lentiviral vectors efficiently transduce quiescent mature 3T3-L1 adipocytes.* Mol Ther, 2004. **9**(2): p. 209-17.
354. Krissinel, E. and K. Henrick, *Inference of macromolecular assemblies from crystalline state.* J Mol Biol, 2007. **372**(3): p. 774-97.
355. Auger, A., et al., *Efficient Delivery of Structurally Diverse Protein Cargo into Mammalian Cells by a Bacterial Toxin.* Mol Pharm, 2015. **12**(8): p. 2962-71.
356. D'Astolfo, D.S., et al., *Efficient intracellular delivery of native proteins.* Cell, 2015. **161**(3): p. 674-90.
357. Gaj, T., et al., *Protein delivery using Cys2-His2 zinc-finger domains.* ACS Chem Biol, 2014. **9**(8): p. 1662-7.
358. Uppalapati, M., et al., *A Potent d-Protein Antagonist of VEGF-A is Nonimmunogenic, Metabolically Stable, and Longer-Circulating in Vivo.* ACS Chem Biol, 2016. **11**(4): p. 1058-65.
359. Leung, I., et al., *Saturation scanning of ubiquitin variants reveals a common hot spot for binding to USP2 and USP21.* Proc Natl Acad Sci U S A, 2016.
360. Arkin, M.R., Y. Tang, and J.A. Wells, *Small-molecule inhibitors of protein-protein interactions: progressing toward the reality.* Chem Biol, 2014. **21**(9): p. 1102-14.
361. Inn, K.S., et al., *Inhibition of RIG-I-mediated signaling by Kaposi's sarcoma-associated herpesvirus-encoded deubiquitinase ORF64.* J Virol, 2011. **85**(20): p. 10899-904.
362. Wang, S., et al., *Herpes simplex virus 1 ubiquitin-specific protease UL36 inhibits beta interferon production by deubiquitinating TRAF3.* J Virol, 2013. **87**(21): p. 11851-60.
363. Ziebuhr, J., et al., *Human coronavirus 229E papain-like proteases have overlapping specificities but distinct functions in viral replication.* J Virol, 2007. **81**(8): p. 3922-32.
364. Bergeron, E., et al., *Crimean-Congo hemorrhagic fever virus-encoded ovarian tumor protease activity is dispensable for virus RNA polymerase function.* J Virol, 2010. **84**(1): p. 216-26.
365. Lombardi, C., et al., *A compact viral processing proteinase/ubiquitin hydrolase from the OTU family.* PLoS Pathog, 2013. **9**(8): p. e1003560.
366. Miao, X., *Recent advances in the development of new transgenic animal technology.* Cell Mol Life Sci, 2013. **70**(5): p. 815-28.
367. Agrawal, A.S., et al., *Generation of a transgenic mouse model of Middle East respiratory syndrome coronavirus infection and disease.* J Virol, 2015. **89**(7): p. 3659-70.
368. Zhao, J., et al., *Rapid generation of a mouse model for Middle East respiratory syndrome.* Proc Natl Acad Sci U S A, 2014. **111**(13): p. 4970-5.
369. van Doremalen, N. and V.J. Munster, *Animal models of Middle East respiratory syndrome coronavirus infection.* Antiviral Res, 2015. **122**: p. 28-38.
370. Cockrell, A.S., et al., *A mouse model for MERS coronavirus-induced acute respiratory distress syndrome.* Nat Microbiol, 2016. **2**: p. 16226.
371. Lee, H., et al., *Inhibitor recognition specificity of MERS-CoV papain-like protease may differ from that of SARS-CoV.* ACS Chem Biol, 2015. **10**(6): p. 1456-65.

372. Deng, X., et al., *Coronaviruses resistant to a 3C-like protease inhibitor are attenuated for replication and pathogenesis, revealing a low genetic barrier but high fitness cost of resistance.* J Virol, 2014. **88**(20): p. 11886-98.
373. Schrodinger, LLC, *The PyMOL Molecular Graphics System, Version 1.8*. 2015.
374. McCoy, A.J., et al., *Phaser crystallographic software.* J Appl Crystallogr, 2007. **40**(Pt 4): p. 658-674.
375. Evans, P.R., *An introduction to data reduction: space-group determination, scaling and intensity statistics.* Acta Crystallogr D Biol Crystallogr, 2011. **67**(Pt 4): p. 282-92.
376. van Hemert, M.J., et al., *SARS-coronavirus replication/transcription complexes are membrane-protected and need a host factor for activity in vitro.* PLoS Pathog, 2008. **4**(5): p. e1000054.
377. Matthews, K.L., et al., *The ORF4b-encoded accessory proteins of Middle East respiratory syndrome coronavirus and two related bat coronaviruses localize to the nucleus and inhibit innate immune signalling.* J Gen Virol, 2014. **95**(Pt 4): p. 874-82.
378. Reusken, C.B., et al., *Occupational Exposure to Dromedaries and Risk for MERS-CoV Infection, Qatar, 2013-2014.* Emerg Infect Dis, 2015. **21**(8): p. 1422-5.
379. Poletto, C., et al., *Assessment of the Middle East respiratory syndrome coronavirus (MERS-CoV) epidemic in the Middle East and risk of international spread using a novel maximum likelihood analysis approach.* Euro Surveill, 2014. **19**(23).
380. Dudas, G., et al., *MERS-CoV spillover at the camel-human interface.* Elife, 2018. **7**.
381. Snijder, E.J., E. Decroly, and J. Ziebuhr, *The Nonstructural Proteins Directing Coronavirus RNA Synthesis and Processing.* Adv Virus Res, 2016. **96**: p. 59-126.
382. Geurink, P.P., et al., *Profiling DUBs and Ubl-specific proteases with activity-based probes.* Methods Enzymol, 2019. **618**: p. 357-387.
383. Perng, Y.C. and D.J. Lenschow, *ISG15 in antiviral immunity and beyond.* Nat Rev Microbiol, 2018. **16**(7): p. 423-439.
384. Daczkowski, C.M., et al., *Structurally Guided Removal of DeISGylase Biochemical Activity from Papain-Like Protease Originating from Middle East Respiratory Syndrome Coronavirus.* J Virol, 2017. **91**(23).
385. Clasman, J.R., et al., *X-ray Structure and Enzymatic Activity Profile of a Core Papain-like Protease of MERS Coronavirus with utility for structure-based drug design.* Sci Rep, 2017. **7**: p. 40292.
386. Zhang, W. and S.S. Sidhu, *Generating Intracellular Modulators of E3 Ligases and Deubiquitinases from Phage-Displayed Ubiquitin Variant Libraries.* Methods Mol Biol, 2018. **1844**: p. 101-119.
387. Gabrielsen, M., et al., *A General Strategy for Discovery of Inhibitors and Activators of RING and U-box E3 Ligases with Ubiquitin Variants.* Mol Cell, 2017. **68**(2): p. 456-470 e10.
388. Gorelik, M. and S.S. Sidhu, *Specific targeting of the deubiquitinase and E3 ligase families with engineered ubiquitin variants.* Bioeng Transl Med, 2017. **2**(1): p. 31-42.
389. Zhang, W., et al., *Potent and selective inhibition of pathogenic viruses by engineered ubiquitin variants.* PLoS Pathog, 2017. **13**(5): p. e1006372.
390. Hemsley, A., et al., *A simple method for site-directed mutagenesis using the polymerase chain reaction.* Nucleic Acids Res, 1989. **17**(16): p. 6545-51.
391. Schneider, C.A., W.S. Rasband, and K.W. Eliceiri, *NIH Image to ImageJ: 25 years of image analysis.* Nat Methods, 2012. **9**(7): p. 671-5.
392. Chen, P.Y., et al., *The role of a beta-bulge in the folding of the beta-hairpin structure in ubiquitin.* Protein Sci, 2001. **10**(10): p. 2063-74.
393. Piana, S., K. Lindorff-Larsen, and D.E. Shaw, *Atomic-level description of ubiquitin folding.* Proc Natl Acad Sci U S A, 2013. **110**(15): p. 5915-20.
394. Pantoliano, M.W., et al., *High-density miniaturized thermal shift assays as a general strategy for drug discovery.* J Biomol Screen, 2001. **6**(6): p. 429-40.

395. Edfors, F., et al., *Gene-specific correlation of RNA and protein levels in human cells and tissues.* Mol Syst Biol, 2016. **12**(10): p. 883.
396. Liu, Y., A. Beyer, and R. Aebersold, *On the Dependency of Cellular Protein Levels on mRNA Abundance.* Cell, 2016. **165**(3): p. 535-50.
397. Ratia, K., et al., *A noncovalent class of papain-like protease/deubiquitinase inhibitors blocks SARS virus replication.* Proc Natl Acad Sci U S A, 2008. **105**(42): p. 16119-24.
398. Mao, G., et al., *DNA context and promoter activity affect gene expression in lentiviral vectors.* Acta Biomed, 2008. **79**(3): p. 192-6.
399. Qin, J.Y., et al., *Systematic comparison of constitutive promoters and the doxycycline-inducible promoter.* PLoS One, 2010. **5**(5): p. e10611.
400. Earnest, J.T., et al., *The tetraspanin CD9 facilitates MERS-coronavirus entry by scaffolding host cell receptors and proteases.* PLoS Pathog, 2017. **13**(7): p. e1006546.
401. Husnjak, K. and I. Dikic, *Ubiquitin-binding proteins: decoders of ubiquitin-mediated cellular functions.* Annu Rev Biochem, 2012. **81**: p. 291-322.
402. Hochstrasser, M., *Origin and function of ubiquitin-like proteins.* Nature, 2009. **458**(7237): p. 422-9.
403. Cappadocia, L. and C.D. Lima, *Ubiquitin-like Protein Conjugation: Structures, Chemistry, and Mechanism.* Chem Rev, 2017.
404. van der Veen, A.G. and H.L. Ploegh, *Ubiquitin-like proteins.* Annu Rev Biochem, 2012. **81**: p. 323-57.
405. Hermann, M. and D. Bogunovic, *ISG15: In Sickness and in Health.* Trends Immunol, 2017. **38**(2): p. 79-93.
406. Bogunovic, D., et al., *Mycobacterial disease and impaired IFN-gamma immunity in humans with inherited ISG15 deficiency.* Science, 2012. **337**(6102): p. 1684-8.
407. Zhang, X., et al., *Human intracellular ISG15 prevents interferon-alpha/beta over-amplification and auto-inflammation.* Nature, 2015. **517**(7532): p. 89-93.
408. Fraile, J.M., et al., *Deubiquitinases in cancer: new functions and therapeutic options.* Oncogene, 2012. **31**(19): p. 2373-88.
409. Gan, J., et al., *Manipulation of ubiquitin/SUMO pathways in human herpesviruses infection.* Rev Med Virol, 2016. **26**(6): p. 435-445.
410. Luo, H., *Interplay between the virus and the ubiquitin-proteasome system: molecular mechanism of viral pathogenesis.* Curr Opin Virol, 2016. **17**: p. 1-10.
411. Wimmer, P. and S. Schreiner, *Viral Mimicry to Usurp Ubiquitin and SUMO Host Pathways.* Viruses, 2015. **7**(9): p. 4854-72.
412. Minor, M.M. and B.L. Slagle, *Hepatitis B virus HBx protein interactions with the ubiquitin proteasome system.* Viruses, 2014. **6**(11): p. 4683-702.
413. Wilson, V.G., *The role of ubiquitin and ubiquitin-like modification systems in papillomavirus biology.* Viruses, 2014. **6**(9): p. 3584-611.
414. Mattoscio, D., C.V. Segre, and S. Chiocca, *Viral manipulation of cellular protein conjugation pathways: The SUMO lesson.* World J Virol, 2013. **2**(2): p. 79-90.
415. Everett, R.D., C. Boutell, and B.G. Hale, *Interplay between viruses and host sumoylation pathways.* Nat Rev Microbiol, 2013. **11**(6): p. 400-11.
416. Rajsbaum, R. and A. Garcia-Sastre, *Viral evasion mechanisms of early antiviral responses involving regulation of ubiquitin pathways.* Trends Microbiol, 2013. **21**(8): p. 421-9.
417. Schulz, K.S. and K.L. Mossman, *Viral Evasion Strategies in Type I IFN Signaling – A Summary of Recent Developments.* Frontiers in Immunology, 2016. **7**(498).
418. Ivashkiv, L.B. and L.T. Donlin, *Regulation of type I interferon responses.* Nat Rev Immunol, 2014. **14**(1): p. 36-49.

419. Smith, S. and C. Jefferies, *Role of DNA/RNA sensors and contribution to autoimmunity.* Cytokine Growth Factor Rev, 2014. **25**(6): p. 745-57.
420. Hu, H. and S.C. Sun, *Ubiquitin signaling in immune responses.* Cell Res, 2016. **26**(4): p. 457-83.
421. Jiang, X. and Z.J. Chen, *The role of ubiquitylation in immune defence and pathogen evasion.* Nat Rev Immunol, 2011. **12**(1): p. 35-48.
422. Sparrer, K.M. and M.U. Gack, *Intracellular detection of viral nucleic acids.* Curr Opin Microbiol, 2015. **26**: p. 1-9.
423. McFadden, M.J., N.S. Gokhale, and S.M. Horner, *Protect this house: cytosolic sensing of viruses.* Curr Opin Virol, 2017. **22**: p. 36-43.
424. Chen, Q., L. Sun, and Z.J. Chen, *Regulation and function of the cGAS-STING pathway of cytosolic DNA sensing.* Nat Immunol, 2016. **17**(10): p. 1142-9.
425. Rajsbaum, R., A. Garcia-Sastre, and G.A. Versteeg, *TRIMmunity: the roles of the TRIM E3-ubiquitin ligase family in innate antiviral immunity.* J Mol Biol, 2014. **426**(6): p. 1265-84.
426. May, M.J. and S. Ghosh, *Signal transduction through NF-κB.* Immunology Today, 1998. **19**(2): p. 80-88.
427. Wang, Q., et al., *The E3 Ubiquitin Ligase AMFR and INSIG1 Bridge the Activation of TBK1 Kinase by Modifying the Adaptor STING.* Immunity, 2014. **41**(6): p. 919-933.
428. Malynn, B.A. and A. Ma, *Ubiquitin makes its mark on immune regulation.* Immunity, 2010. **33**(6): p. 843-52.
429. Jiang, X., et al., *Ubiquitin-induced oligomerization of the RNA sensors RIG-I and MDA5 activates antiviral innate immune response.* Immunity, 2012. **36**(6): p. 959-73.
430. Reikine, S., J.B. Nguyen, and Y. Modis, *Pattern Recognition and Signaling Mechanisms of RIG-I and MDA5.* Front Immunol, 2014. **5**: p. 342.
431. Chen, J. and Z.J. Chen, *Regulation of NF-kappaB by ubiquitination.* Curr Opin Immunol, 2013. **25**(1): p. 4-12.
432. Chattopadhyay, S., et al., *Ubiquitination of the Transcription Factor IRF-3 Activates RIPA, the Apoptotic Pathway that Protects Mice from Viral Pathogenesis.* Immunity, 2016. **44**(5): p. 1151-61.
433. Zhao, X., et al., *c-Cbl-mediated ubiquitination of IRF3 negatively regulates IFN-beta production and cellular antiviral response.* Cell Signal, 2016. **28**(11): p. 1683-93.
434. Zinngrebe, J., et al., *Ubiquitin in the immune system.* EMBO Rep, 2014. **15**(1): p. 28-45.
435. Friedman, C.S., et al., *The tumour suppressor CYLD is a negative regulator of RIG-I-mediated antiviral response.* EMBO Rep, 2008. **9**(9): p. 930-6.
436. Kayagaki, N., et al., *DUBA: a deubiquitinase that regulates type I interferon production.* Science, 2007. **318**(5856): p. 1628-32.
437. Wertz, I.E., et al., *De-ubiquitination and ubiquitin ligase domains of A20 downregulate NF-kappaB signalling.* Nature, 2004. **430**(7000): p. 694-9.
438. Ma, A. and B.A. Malynn, *A20: linking a complex regulator of ubiquitylation to immunity and human disease.* Nat Rev Immunol, 2012. **12**(11): p. 774-85.
439. Parvatiyar, K., G.N. Barber, and E.W. Harhaj, *TAX1BP1 and A20 inhibit antiviral signaling by targeting TBK1-IKKi kinases.* J Biol Chem, 2010. **285**(20): p. 14999-5009.
440. Shembade, N., A. Ma, and E.W. Harhaj, *Inhibition of NF-kappaB signaling by A20 through disruption of ubiquitin enzyme complexes.* Science, 2010. **327**(5969): p. 1135-9.
441. Lopez-Castejon, G. and M.J. Edelmann, *Deubiquitinases: Novel Therapeutic Targets in Immune Surveillance?* Mediators Inflamm, 2016. **2016**: p. 3481371.
442. Elliott, P.R. and D. Komander, *Regulation of Met1-linked polyubiquitin signalling by the deubiquitinase OTULIN.* FEBS J, 2016. **283**(1): p. 39-53.

443. Sun, S.C., *Deubiquitylation and regulation of the immune response.* Nat Rev Immunol, 2008. **8**(7): p. 501-11.
444. Sun, H., et al., *USP13 negatively regulates antiviral responses by deubiquitinating STING.* Nat Commun, 2017. **8**: p. 15534.
445. Mathis, B.J., et al., *CYLD-mediated signaling and diseases.* Curr Drug Targets, 2015. **16**(4): p. 284-94.
446. Catrysse, L., et al., *A20 in inflammation and autoimmunity.* Trends Immunol, 2014. **35**(1): p. 22-31.
447. Lauring, A.S., J. Frydman, and R. Andino, *The role of mutational robustness in RNA virus evolution.* Nat Rev Microbiol, 2013. **11**(5): p. 327-36.
448. Koonin, E.V., V.V. Dolja, and M. Krupovic, *Origins and evolution of viruses of eukaryotes: The ultimate modularity.* Virology, 2015. **479-480**: p. 2-25.
449. Chan, Y.K. and M.U. Gack, *Viral evasion of intracellular DNA and RNA sensing.* Nat Rev Microbiol, 2016. **14**(6): p. 360-73.
450. Gu, Z. and W. Shi, *Manipulation of viral infection by deubiquitinating enzymes: new players in host-virus interactions.* Future Microbiol, 2016. **11**: p. 1435-1446.
451. Knipe, D.M. and P.M. Howley, *Fields virology*. 6th ed. 2013, Philadelphia, PA: Wolters Kluwer/Lippincott Williams & Wilkins Health.
452. Zhong, N.S., et al., *Epidemiology and cause of severe acute respiratory syndrome (SARS) in Guangdong, People's Republic of China, in February, 2003.* Lancet, 2003. **362**(9393): p. 1353-8.
453. WHO. *Middle East respiratory syndrome coronavirus (MERS-CoV) – Saudi Arabia*. Available from: http://www.who.int/csr/don/10-march-2017-mers-saudi-arabia/en/.
454. van der Hoek, L., et al., *Croup is associated with the novel coronavirus NL63.* PLoS Med, 2005. **2**(8): p. e240.
455. Lane, T.E. and M.P. Hosking, *The pathogenesis of murine coronavirus infection of the central nervous system.* Crit Rev Immunol, 2010. **30**(2): p. 119-30.
456. Lee, C., *Porcine epidemic diarrhea virus: An emerging and re-emerging epizootic swine virus.* Virol J, 2015. **12**: p. 193.
457. Ruan, Y.J., et al., *Comparative full-length genome sequence analysis of 14 SARS coronavirus isolates and common mutations associated with putative origins of infection.* Lancet, 2003. **361**(9371): p. 1779-85.
458. Matthews, K., et al., *The SARS coronavirus papain like protease can inhibit IRF3 at a post activation step that requires deubiquitination activity.* Virol J, 2014. **11**: p. 209.
459. Hu, M., et al., *Crystal structure of a UBP-family deubiquitinating enzyme in isolation and in complex with ubiquitin aldehyde.* Cell, 2002. **111**(7): p. 1041-54.
460. Chaudhuri, R., et al., *Comparison of SARS and NL63 papain-like protease binding sites and binding site dynamics: inhibitor design implications.* J Mol Biol, 2011. **414**(2): p. 272-88.
461. Daczkowski, C.M., et al., *Structural insights into the interaction of coronavirus papain-like proteases and interferon-stimulated gene product 15 from different species.* J Mol Biol, 2017.
462. Drag, M., et al., *Positional-scanning fluorigenic substrate libraries reveal unexpected specificity determinants of DUBs (deubiquitinating enzymes).* Biochem J, 2008. **415**(3): p. 367-75.
463. Han, Y.S., et al., *Papain-like protease 2 (PLP2) from severe acute respiratory syndrome coronavirus (SARS-CoV): expression, purification, characterization, and inhibition.* Biochemistry, 2005. **44**(30): p. 10349-59.
464. Chou, C.Y., et al., *Thiopurine analogues inhibit papain-like protease of severe acute respiratory syndrome coronavirus.* Biochem Pharmacol, 2008. **75**(8): p. 1601-9.

465. Chen, X., C.Y. Chou, and G.G. Chang, *Thiopurine analogue inhibitors of severe acute respiratory syndrome-coronavirus papain-like protease, a deubiquitinating and deISGylating enzyme.* Antivir Chem Chemother, 2009. **19**(4): p. 151-6.
466. Ghosh, A.K., et al., *Structure-based design, synthesis, and biological evaluation of a series of novel and reversible inhibitors for the severe acute respiratory syndrome-coronavirus papain-like protease.* J Med Chem, 2009. **52**(16): p. 5228-40.
467. Ghosh, A.K., et al., *Severe acute respiratory syndrome coronavirus papain-like novel protease inhibitors: design, synthesis, protein-ligand X-ray structure and biological evaluation.* J Med Chem, 2010. **53**(13): p. 4968-79.
468. Lee, H., et al., *Synergistic inhibitor binding to the papain-like protease of human SARS coronavirus: mechanistic and inhibitor design implications.* ChemMedChem, 2013. **8**(8): p. 1361-72.
469. Baez-Santos, Y.M., et al., *X-ray structural and biological evaluation of a series of potent and highly selective inhibitors of human coronavirus papain-like proteases.* J Med Chem, 2014. **57**(6): p. 2393-412.
470. Lei, J. and R. Hilgenfeld, *Structural and mutational analysis of the interaction between the Middle-East respiratory syndrome coronavirus (MERS-CoV) papain-like protease and human ubiquitin.* Virol Sin, 2016. **31**(4): p. 288-99.
471. Gorelik, M., et al., *Inhibition of SCF ubiquitin ligases by engineered ubiquitin variants that target the Cul1 binding site on the Skp1-F-box interface.* Proc Natl Acad Sci U S A, 2016. **113**(13): p. 3527-32.
472. Manczyk, N., et al., *Structural and functional characterization of a ubiquitin variant engineered for tight and specific binding to an alpha-helical ubiquitin interacting motif.* Protein Sci, 2017. **26**(5): p. 1060-1069.
473. Nicholson, B., et al., *Characterization of ubiquitin and ubiquitin-like-protein isopeptidase activities.* Protein Sci, 2008. **17**(6): p. 1035-43.
474. Sun, L., et al., *Coronavirus papain-like proteases negatively regulate antiviral innate immune response through disruption of STING-mediated signaling.* PLoS One, 2012. **7**(2): p. e30802.
475. Lee, H.J., et al., *The complete sequence (22 kilobases) of murine coronavirus gene 1 encoding the putative proteases and RNA polymerase.* Virology, 1991. **180**(2): p. 567-82.
476. Kanjanahaluethai, A. and S.C. Baker, *Identification of mouse hepatitis virus papain-like proteinase 2 activity.* J Virol, 2000. **74**(17): p. 7911-21.
477. Wang, G., et al., *PLP2 of mouse hepatitis virus A59 (MHV-A59) targets TBK1 to negatively regulate cellular type I interferon signaling pathway.* PLoS One, 2011. **6**(2): p. e17192.
478. Mielech, A.M., et al., *Murine coronavirus ubiquitin-like domain is important for papain-like protease stability and viral pathogenesis.* J Virol, 2015. **89**(9): p. 4907-17.
479. Putics, A., A.E. Gorbalenya, and J. Ziebuhr, *Identification of protease and ADP-ribose 1''-monophosphatase activities associated with transmissible gastroenteritis virus non-structural protein 3.* J Gen Virol, 2006. **87**(Pt 3): p. 651-6.
480. Liu, D.X., et al., *Identification, expression, and processing of an 87-kDa polypeptide encoded by ORF 1a of the coronavirus infectious bronchitis virus.* Virology, 1995. **208**(1): p. 48-57.
481. Lim, K.P. and D.X. Liu, *Characterization of the two overlapping papain-like proteinase domains encoded in gene 1 of the coronavirus infectious bronchitis virus and determination of the C-terminal cleavage site of an 87-kDa protein.* Virology, 1998. **245**(2): p. 303-12.
482. Lim, K.P. and D.X. Liu, *Characterisation of a papain-like proteinase domain encoded by ORF1a of the coronavirus IBV and determination of the C-terminal cleavage site of an 87 kDa protein.* Adv Exp Med Biol, 1998. **440**: p. 173-84.

483. Lim, K.P., L.F. Ng, and D.X. Liu, *Identification of a novel cleavage activity of the first papain-like proteinase domain encoded by open reading frame 1a of the coronavirus Avian infectious bronchitis virus and characterization of the cleavage products.* J Virol, 2000. **74**(4): p. 1674-85.
484. Yu, L., et al., *The papain-like protease of avian infectious bronchitis virus has deubiquitinating activity.* Arch Virol, 2017.
485. Neumann, E.J., et al., *Assessment of the economic impact of porcine reproductive and respiratory syndrome on swine production in the United States.* J Am Vet Med Assoc, 2005. **227**(3): p. 385-92.
486. Holtkamp, D.J., et al., *Porcine reproductive and respiratory syndrome (PRRS) is the most economically important disease of swine in North America, Europe and Asia, costing producers in North America more than $600 million annually.* J Swine Health Prod, 2013. **21**(2): p. 72-84.
487. Vatter, H.A., et al., *Functional analyses of the three simian hemorrhagic fever virus nonstructural protein 1 papain-like proteases.* J Virol, 2014. **88**(16): p. 9129-40.
488. Han, J., M.S. Rutherford, and K.S. Faaberg, *The porcine reproductive and respiratory syndrome virus nsp2 cysteine protease domain possesses both trans- and cis-cleavage activities.* J Virol, 2009. **83**(18): p. 9449-63.
489. Han, J., M.S. Rutherford, and K.S. Faaberg, *Proteolytic products of the porcine reproductive and respiratory syndrome virus nsp2 replicase protein.* J Virol, 2010. **84**(19): p. 10102-12.
490. Fang, Y., et al., *Efficient -2 frameshifting by mammalian ribosomes to synthesize an additional arterivirus protein.* Proc Natl Acad Sci U S A, 2012. **109**(43): p. E2920-8.
491. Li, Y., et al., *Transactivation of programmed ribosomal frameshifting by a viral protein.* Proc Natl Acad Sci U S A, 2014. **111**(21): p. E2172-81.
492. Kappes, M.A., C.L. Miller, and K.S. Faaberg, *Highly divergent strains of porcine reproductive and respiratory syndrome virus incorporate multiple isoforms of nonstructural protein 2 into virions.* J Virol, 2013. **87**(24): p. 13456-65.
493. Sun, Z., et al., *Nonstructural protein 2 of porcine reproductive and respiratory syndrome virus inhibits the antiviral function of interferon-stimulated gene 15.* J Virol, 2012. **86**(7): p. 3839-50.
494. Deaton, M.K., et al., *The vOTU domain of highly-pathogenic porcine reproductive and respiratory syndrome virus displays a differential substrate preference.* Virology, 2014. **454-455**: p. 247-53.
495. Bente, D.A., et al., *Crimean-Congo hemorrhagic fever: history, epidemiology, pathogenesis, clinical syndrome and genetic diversity.* Antiviral Res, 2013. **100**(1): p. 159-89.
496. Treib, J., et al., *Thunderclap headache caused by Erve virus?* Neurology, 1998. **50**(2): p. 509-11.
497. Woessner, R., et al., *The Erve virus: possible mode of transmission and reservoir.* Infection, 2000. **28**(3): p. 164-6.
498. Kinsella, E., et al., *Sequence determination of the Crimean-Congo hemorrhagic fever virus L segment.* Virology, 2004. **321**(1): p. 23-8.
499. Honig, J.E., J.C. Osborne, and S.T. Nichol, *Crimean-Congo hemorrhagic fever virus genome L RNA segment and encoded protein.* Virology, 2004. **321**(1): p. 29-35.
500. Evans, P.C., et al., *Zinc-finger protein A20, a regulator of inflammation and cell survival, has deubiquitinating activity.* Biochem J, 2004. **378**(Pt 3): p. 727-34.
501. Boone, D.L., et al., *The ubiquitin-modifying enzyme A20 is required for termination of Toll-like receptor responses.* Nat Immunol, 2004. **5**(10): p. 1052-60.
502. Capodagli, G.C., et al., *Diversity of ubiquitin and ISG15 specificity among nairoviruses' viral ovarian tumor domain proteases.* J Virol, 2013. **87**(7): p. 3815-27.
503. Bergeron, E., et al., *Recovery of Recombinant Crimean Congo Hemorrhagic Fever Virus Reveals a Function for Non-structural Glycoproteins Cleavage by Furin.* PLoS Pathog, 2015. **11**(5): p. e1004879.

504. Bakshi, S., et al., *Dugbe virus ovarian tumour domain interferes with ubiquitin/ISG15-regulated innate immune cell signalling.* J Gen Virol, 2013. **94**(Pt 2): p. 298-307.
505. Deaton, M.K., et al., *Biochemical and Structural Insights into the Preference of Nairoviral DeISGylases for Interferon-Stimulated Gene Product 15 Originating from Certain Species.* J Virol, 2016. **90**(18): p. 8314-27.
506. Holzer, B., et al., *Inhibition of interferon induction and action by the nairovirus Nairobi sheep disease virus/Ganjam virus.* PLoS One, 2011. **6**(12): p. e28594.
507. Shang, P., et al., *A naturally occurring recombinant enterovirus expresses a torovirus deubiquitinase.* J Virol, 2017.
508. Burroughs, J.N., et al., *Multiple proteases in foot-and-mouth disease virus replication.* J Virol, 1984. **50**(3): p. 878-83.
509. Strebel, K. and E. Beck, *A second protease of foot-and-mouth disease virus.* J Virol, 1986. **58**(3): p. 893-9.
510. Kirchweger, R., et al., *Foot-and-mouth disease virus leader proteinase: purification of the Lb form and determination of its cleavage site on eIF-4 gamma.* J Virol, 1994. **68**(9): p. 5677-84.
511. Piccone, M.E., et al., *The foot-and-mouth disease virus leader proteinase gene is not required for viral replication.* J Virol, 1995. **69**(9): p. 5376-82.
512. de Los Santos, T., et al., *The leader proteinase of foot-and-mouth disease virus inhibits the induction of beta interferon mRNA and blocks the host innate immune response.* J Virol, 2006. **80**(4): p. 1906-14.
513. Chinsangaram, J., M. Koster, and M.J. Grubman, *Inhibition of L-deleted foot-and-mouth disease virus replication by alpha/beta interferon involves double-stranded RNA-dependent protein kinase.* J Virol, 2001. **75**(12): p. 5498-503.
514. Chinsangaram, J., M.E. Piccone, and M.J. Grubman, *Ability of foot-and-mouth disease virus to form plaques in cell culture is associated with suppression of alpha/beta interferon.* J Virol, 1999. **73**(12): p. 9891-8.
515. de Los Santos, T., F. Diaz-San Segundo, and M.J. Grubman, *Degradation of nuclear factor kappa B during foot-and-mouth disease virus infection.* J Virol, 2007. **81**(23): p. 12803-15.
516. de los Santos, T., et al., *A conserved domain in the leader proteinase of foot-and-mouth disease virus is required for proper subcellular localization and function.* J Virol, 2009. **83**(4): p. 1800-10.
517. Gorbalenya, A.E., E.V. Koonin, and M.M. Lai, *Putative papain-related thiol proteases of positive-strand RNA viruses. Identification of rubi- and aphthovirus proteases and delineation of a novel conserved domain associated with proteases of rubi-, alpha- and coronaviruses.* FEBS Lett, 1991. **288**(1-2): p. 201-5.
518. Guarne, A., et al., *Structure of the foot-and-mouth disease virus leader protease: a papain-like fold adapted for self-processing and eIF4G recognition.* EMBO J, 1998. **17**(24): p. 7469-79.
519. Gorbalenya, A.E. and E.V. Koonin, *Endonuclease (R) subunits of type-I and type-III restriction-modification enzymes contain a helicase-like domain.* FEBS Lett, 1991. **291**(2): p. 277-81.
520. Cencic, R., et al., *Investigating the substrate specificity and oligomerisation of the leader protease of foot and mouth disease virus using NMR.* J Mol Biol, 2007. **373**(4): p. 1071-87.
521. Wang, D., et al., *The leader proteinase of foot-and-mouth disease virus negatively regulates the type I interferon pathway by acting as a viral deubiquitinase.* J Virol, 2011. **85**(8): p. 3758-66.
522. Santos, J.A., et al., *Hydrolytic properties and substrate specificity of the foot-and-mouth disease leader protease.* Biochemistry, 2009. **48**(33): p. 7948-58.
523. Nogueira Santos, J.A., et al., *Foot and mouth disease leader protease (Lbpro): Investigation of prime side specificity allows the synthesis of a potent inhibitor.* Biochimie, 2012. **94**(3): p. 711-8.

524. Steinberger, J., et al., *Foot-and-mouth disease virus leader proteinase: structural insights into the mechanism of intermolecular cleavage.* Virology, 2014. **468-470**: p. 397-408.
525. Morch, M.D., J.C. Boyer, and A.L. Haenni, *Overlapping open reading frames revealed by complete nucleotide sequencing of turnip yellow mosaic virus genomic RNA.* Nucleic Acids Res, 1988. **16**(13): p. 6157-73.
526. Bransom, K.L., J.J. Weiland, and T.W. Dreher, *Proteolytic maturation of the 206-kDa nonstructural protein encoded by turnip yellow mosaic virus RNA.* Virology, 1991. **184**(1): p. 351-8.
527. Bransom, K.L. and T.W. Dreher, *Identification of the essential cysteine and histidine residues of the turnip yellow mosaic virus protease.* Virology, 1994. **198**(1): p. 148-54.
528. Rozanov, M.N., G. Drugeon, and A.L. Haenni, *Papain-like proteinase of turnip yellow mosaic virus: a prototype of a new viral proteinase group.* Arch Virol, 1995. **140**(2): p. 273-88.
529. Jakubiec, A., et al., *Proteolytic processing of turnip yellow mosaic virus replication proteins and functional impact on infectivity.* J Virol, 2007. **81**(20): p. 11402-12.
530. Camborde, L., et al., *The ubiquitin-proteasome system regulates the accumulation of Turnip yellow mosaic virus RNA-dependent RNA polymerase during viral infection.* Plant Cell, 2010. **22**(9): p. 3142-52.
531. Ordureau, A., C. Munch, and J.W. Harper, *Quantifying ubiquitin signaling.* Mol Cell, 2015. **58**(4): p. 660-76.
532. Flierman, D., et al., *Non-hydrolyzable Diubiquitin Probes Reveal Linkage-Specific Reactivity of Deubiquitylating Enzymes Mediated by S2 Pockets.* Cell Chem Biol, 2016. **23**(4): p. 472-82.
533. Mulder, M.P., et al., *A native chemical ligation handle that enables the synthesis of advanced activity-based probes: diubiquitin as a case study.* Chembiochem, 2014. **15**(7): p. 946-9.
534. Pruneda, J.N., et al., *The Molecular Basis for Ubiquitin and Ubiquitin-like Specificities in Bacterial Effector Proteases.* Mol Cell, 2016. **63**(2): p. 261-76.
535. Chen, X., et al., *SARS coronavirus papain-like protease inhibits the type I interferon signaling pathway through interaction with the STING-TRAF3-TBK1 complex.* Protein Cell, 2014. **5**(5): p. 369-81.
536. Luo, C.M., et al., *Discovery of Novel Bat Coronaviruses in South China That Use the Same Receptor as Middle East Respiratory Syndrome Coronavirus.* J Virol, 2018. **92**(13).
537. Ziebuhr, J., E.J. Snijder, and A.E. Gorbalenya, *Virus-encoded proteinases and proteolytic processing in the Nidovirales.* J Gen Virol, 2000. **81**(Pt 4): p. 853-79.
538. Ziebuhr, J., V. Thiel, and A.E. Gorbalenya, *The autocatalytic release of a putative RNA virus transcription factor from its polyprotein precursor involves two paralogous papain-like proteases that cleave the same peptide bond.* J Biol Chem, 2001. **276**(35): p. 33220-32.
539. Gadlage, M.J. and M.R. Denison, *Exchange of the coronavirus replicase polyprotein cleavage sites alters protease specificity and processing.* J Virol, 2010. **84**(13): p. 6894-8.
540. Malakhov, M.P., et al., *UBP43 (USP18) specifically removes ISG15 from conjugated proteins.* J Biol Chem, 2002. **277**(12): p. 9976-81.
541. Basters, A., et al., *Structural basis of the specificity of USP18 toward ISG15.* Nat Struct Mol Biol, 2017.
542. Zhang, D. and D.E. Zhang, *Interferon-stimulated gene 15 and the protein ISGylation system.* J Interferon Cytokine Res, 2011. **31**(1): p. 119-30.
543. Durfee, L.A., et al., *The ISG15 conjugation system broadly targets newly synthesized proteins: implications for the antiviral function of ISG15.* Mol Cell, 2010. **38**(5): p. 722-32.
544. D'Cunha, J., et al., *Immunoregulatory properties of ISG15, an interferon-induced cytokine.* Proc Natl Acad Sci U S A, 1996. **93**(1): p. 211-5.
545. Swaim, C.D., et al., *Extracellular ISG15 Signals Cytokine Secretion through the LFA-1 Integrin Receptor.* Mol Cell, 2017. **68**(3): p. 581-590 e5.

546. Speer, S.D., et al., *ISG15 deficiency and increased viral resistance in humans but not mice.* Nat Commun, 2016. **7**: p. 11496.
547. Malakhova, O.A., et al., *UBP43 is a novel regulator of interferon signaling independent of its ISG15 isopeptidase activity.* EMBO J, 2006. **25**(11): p. 2358-67.
548. Langley, C., et al., *Structure of interferon-stimulated gene product 15 (ISG15) from the bat species Myotis davidii and the impact of interdomain ISG15 interactions on viral protein engagement.* Acta Crystallogr D Struct Biol, 2019. **75**(Pt 1): p. 21-31.
549. Jiang, Y. and X. Wang, *Structural insights into the species preference of the influenza B virus NS1 protein in ISG15 binding.* Protein Cell, 2018.
550. Dzimianski, J.V., et al., *ISG15: It's Complicated.* J Mol Biol, 2019.
551. Lenschow, D.J., et al., *Identification of interferon-stimulated gene 15 as an antiviral molecule during Sindbis virus infection in vivo.* J Virol, 2005. **79**(22): p. 13974-83.
552. Deng, X., et al., *A chimeric virus-mouse model system for evaluating the function and inhibition of papain-like proteases of emerging coronaviruses.* J Virol, 2014. **88**(20): p. 11825-33.
553. Zheng, B., et al., *Potent inhibition of SARS-associated coronavirus (SCOV) infection and replication by type I interferons (IFN-alpha/beta) but not by type II interferon (IFN-gamma).* J Interferon Cytokine Res, 2004. **24**(7): p. 388-90.
554. Haagmans, B.L., et al., *Pegylated interferon-alpha protects type 1 pneumocytes against SARS coronavirus infection in macaques.* Nat Med, 2004. **10**(3): p. 290-3.
555. Neuman, B.W., et al., *Atlas of coronavirus replicase structure.* Virus Res, 2014. **194**: p. 49-66.
556. Neuman, B.W., *Bioinformatics and functional analyses of coronavirus nonstructural proteins involved in the formation of replicative organelles.* Antiviral Res, 2016. **135**: p. 97-107.
557. Putics, A., et al., *ADP-ribose-1"-monophosphatase: a conserved coronavirus enzyme that is dispensable for viral replication in tissue culture.* J Virol, 2005. **79**(20): p. 12721-31.
558. Deng, X., et al., *Analysis of coronavirus temperature-sensitive mutants reveals an interplay between the macrodomain and papain-like protease impacting replication and pathogenesis.* J Virol, 2019.
559. Imbert, I., et al., *The SARS-Coronavirus PLnc domain of nsp3 as a replication/transcription scaffolding protein.* Virus Res, 2008. **133**(2): p. 136-48.
560. Pfefferle, S., et al., *The SARS-coronavirus-host interactome: identification of cyclophilins as target for pan-coronavirus inhibitors.* PLoS Pathog, 2011. **7**(10): p. e1002331.
561. Ma-Lauer, Y., et al., *p53 down-regulates SARS coronavirus replication and is targeted by the SARS-unique domain and PLpro via E3 ubiquitin ligase RCHY1.* Proc Natl Acad Sci U S A, 2016. **113**(35): p. E5192-201.
562. Li, S.W., et al., *SARS Coronavirus Papain-Like Protease Inhibits the TLR7 Signaling Pathway through Removing Lys63-Linked Polyubiquitination of TRAF3 and TRAF6.* Int J Mol Sci, 2016. **17**(5).
563. Kanjanahaluethai, A., et al., *Membrane topology of murine coronavirus replicase nonstructural protein 3.* Virology, 2007. **361**(2): p. 391-401.
564. Udeshi, N.D., et al., *Large-scale identification of ubiquitination sites by mass spectrometry.* Nat Protoc, 2013. **8**(10): p. 1950-60.
565. V'Kovski, P., et al., *Determination of host proteins composing the microenvironment of coronavirus replicase complexes by proximity-labeling.* Elife, 2019. **8**.
566. de Wilde, A.H., et al., *Host Factors in Coronavirus Replication.* Curr Top Microbiol Immunol, 2017.
567. Vogels, M.W., et al., *Identification of host factors involved in coronavirus replication by quantitative proteomics analysis.* Proteomics, 2011. **11**(1): p. 64-80.
568. Du, L., et al., *The spike protein of SARS-CoV--a target for vaccine and therapeutic development.* Nat Rev Microbiol, 2009. **7**(3): p. 226-36.

569. Du, L., et al., *MERS-CoV spike protein: a key target for antivirals.* Expert Opin Ther Targets, 2017. **21**(2): p. 131-143.
570. Zhao, J., et al., *Airway Memory CD4(+) T Cells Mediate Protective Immunity against Emerging Respiratory Coronaviruses.* Immunity, 2016. **44**(6): p. 1379-91.
571. Shin, H.S., et al., *Immune responses to MERS coronavirus during the acute and convalescent phases of human infection.* Clin Infect Dis, 2018.
572. Zhao, J., et al., *Recovery from the Middle East respiratory syndrome is associated with antibody and T-cell responses.* Sci Immunol, 2017. **2**(14).
573. Alshukairi, A.N., et al., *Antibody Response and Disease Severity in Healthcare Worker MERS Survivors.* Emerg Infect Dis, 2016. **22**(6).
574. Alshukairi, A.N., et al., *High Prevalence of MERS-CoV Infection in Camel Workers in Saudi Arabia.* MBio, 2018. **9**(5).
575. Payne, D.C., et al., *Persistence of Antibodies against Middle East Respiratory Syndrome Coronavirus.* Emerg Infect Dis, 2016. **22**(10): p. 1824-6.
576. Alharbi, N.K., *Vaccines against Middle East respiratory syndrome coronavirus for humans and camels.* Rev Med Virol, 2017. **27**(2).
577. Alharbi, N.K., et al., *ChAdOx1 and MVA based vaccine candidates against MERS-CoV elicit neutralising antibodies and cellular immune responses in mice.* Vaccine, 2017. **35**(30): p. 3780-3788.
578. Almazan, F., et al., *Coronavirus reverse genetic systems: infectious clones and replicons.* Virus Res, 2014. **189**: p. 262-70.
579. Zust, R., et al., *Coronavirus non-structural protein 1 is a major pathogenicity factor: implications for the rational design of coronavirus vaccines.* PLoS Pathog, 2007. **3**(8): p. e109.
580. DeDiego, M.L., et al., *A severe acute respiratory syndrome coronavirus that lacks the E gene is attenuated in vitro and in vivo.* J Virol, 2007. **81**(4): p. 1701-13.
581. Jimenez-Guardeno, J.M., et al., *Identification of the Mechanisms Causing Reversion to Virulence in an Attenuated SARS-CoV for the Design of a Genetically Stable Vaccine.* PLoS Pathog, 2015. **11**(10): p. e1005215.
582. Menachery, V.D., et al., *Combination Attenuation Offers Strategy for Live Attenuated Coronavirus Vaccines.* J Virol, 2018. **92**(17).
583. Baseler, L., E. de Wit, and H. Feldmann, *A Comparative Review of Animal Models of Middle East Respiratory Syndrome Coronavirus Infection.* Vet Pathol, 2016. **53**(3): p. 521-31.
584. Morrow, J.K., et al., *Targeting ubiquitination for cancer therapies.* Future Med Chem, 2015. **7**(17): p. 2333-50.
585. Gandolfi, S., et al., *The proteasome and proteasome inhibitors in multiple myeloma.* Cancer Metastasis Rev, 2017. **36**(4): p. 561-584.
586. Harrigan, J.A., et al., *Deubiquitylating enzymes and drug discovery: emerging opportunities.* Nat Rev Drug Discov, 2018. **17**(1): p. 57-78.
587. Turnbull, A.P., et al., *Molecular basis of USP7 inhibition by selective small-molecule inhibitors.* Nature, 2017. **550**(7677): p. 481-486.
588. Lamberto, I., et al., *Structure-Guided Development of a Potent and Selective Non-covalent Active-Site Inhibitor of USP7.* Cell Chem Biol, 2017. **24**(12): p. 1490-1500 e11.
589. Gavory, G., et al., *Discovery and characterization of highly potent and selective allosteric USP7 inhibitors.* Nat Chem Biol, 2018. **14**(2): p. 118-125.
590. Lee, H., et al., *Identification and design of novel small molecule inhibitors against MERS-CoV papain-like protease via high-throughput screening and molecular modeling.* Bioorg Med Chem, 2019.
591. Hurley, J.H., S. Lee, and G. Prag, *Ubiquitin-binding domains.* Biochem J, 2006. **399**(3): p. 361-72.

592. Fu, A., et al., *Promises and pitfalls of intracellular delivery of proteins.* Bioconjug Chem, 2014. **25**(9): p. 1602-8.
593. Cerrato, C.P., K. Kunnapuu, and U. Langel, *Cell-penetrating peptides with intracellular organelle targeting.* Expert Opin Drug Deliv, 2017. **14**(2): p. 245-255.
594. Ray, M., et al., *Intracellular delivery of proteins by nanocarriers.* Nanomedicine (Lond), 2017. **12**(8): p. 941-952.
595. Schott, J.W., et al., *Viral and Synthetic RNA Vector Technologies and Applications.* Mol Ther, 2016.
596. Kaczmarek, J.C., P.S. Kowalski, and D.G. Anderson, *Advances in the delivery of RNA therapeutics: from concept to clinical reality.* Genome Med, 2017. **9**(1): p. 60.
597. Naso, M.F., et al., *Adeno-Associated Virus (AAV) as a Vector for Gene Therapy.* BioDrugs, 2017. **31**(4): p. 317-334.
598. Lee, C.S., et al., *Adenovirus-Mediated Gene Delivery: Potential Applications for Gene and Cell-Based Therapies in the New Era of Personalized Medicine.* Genes Dis, 2017. **4**(2): p. 43-63.
599. Scholte, F.E.M., et al., *Stable Occupancy of the Crimean-Congo Hemorrhagic Fever Virus-Encoded Deubiquitinase Blocks Viral Infection.* MBio, 2019. **10**(4).
600. World Health Organization, *https://www.who.int/blueprint/priority-diseases/en/.* 2018.

## LIST OF ABBREVIATIONS

| | |
|---|---|
| ARDS | acute respiratory distress syndrome |
| $3CL^{pro}$ | 3C-like protease |
| ACE2 | angiotensin-converting enzyme 2 |
| $AmSO_4$ | ammonium sulphate |
| BAC | bacterial artificial chromosome |
| BHK | baby hamster kidney |
| BL2 | blocking loop 2 |
| BLI | bio-layer interferometry |
| BSL3 | biosafety level 3 |
| CARD | caspase activation and recruitment domain |
| CCHFV | Crimean-Congo haemorrhagic fever virus |
| CCL5 | chemokine ligand 5 |
| cDNA | complementary DNA |
| cGAMP | cyclic-GMP-AMP |
| cGAS | cyclic-GMP-AMP synthase |
| ChISG15 | C-terminal domain of human interferon-stimulated gene 15 |
| CoV | coronavirus |
| CPE | cytopathogenic effect |
| diUb | diubiquitin |
| DMEM | Dulbecco's modified Eagle's medium |
| DMV | double membrane vesicle |
| DPP4 | dipeptidyl peptidase 4 |
| DSC | differential scanning calorimetry |
| DTT | dithiothreitol |
| dsRNA | double-stranded RNA |
| DUB | deubiquitinating enzyme |
| DUGV | Dugbe virus |
| E | envelope protein |
| *E. coli* | *Escherichia coli* |
| EAV | equine arteritis virus |
| $EC_{50}$ | half maximal effective binding concentration |
| EDTA | ethylenediaminetetraacetic acid |
| eIF4G | eukaryotic translation initiation factor 4 G |
| EMEM | Eagle's minimum essential medium |
| EndoU | endoribonuclease |
| ER | endoplasmic reticulum |
| ERVV | Erve virus |

| | |
|---|---|
| EVG | enterovirus species G |
| ExoN | 3’-5’ exoribonuclease |
| FCoV | feline coronavirus |
| FCS | foetal calf serum |
| FMDV | foot-and-mouth disease virus |
| Fwd | Forward |
| GFP | green fluorescent protein |
| HAUSP | herpesvirus-associated ubiquitin-specific protease |
| HCoV | human coronavirus |
| HEPES | 4-(2-hydroxyethyl)-1-piperazineethanesulfonic acid |
| hISG15 | human interferon-stimulated gene 15 |
| HRP | horseradish peroxidase |
| HTS | high-throughput screening |
| IBV | infectious bronchitis virus |
| $IC_{50}$ | half maximum inhibitory concentration |
| ICTV | International Committee on Taxonomy of Viruses |
| IFIT | interferon-induced protein with tetratricopeptide repeats |
| IFN | interferon |
| IKK | inhibitor of NF-κB kinase |
| IL-6 | interleukin 6 |
| IL-8 | interleukin 8 |
| IPTG | isopropyl β-D-1-thiogalactopyranoside |
| IRAK1 | interleukin-1 receptor-associated kinase 1 |
| IRF | interferon regulatory factor |
| ISG | interferon-stimulated gene |
| ISG15 | interferon-stimulated gene 15 |
| ISG15-AMC | interferon-stimulated gene 15-7-amino-4-methylcoumarin |
| IκBα | inhibitor of NF-κB-α |
| JAK | Janus kinase |
| JAMM | JAB1/MPN/MOV34 |
| K | cytokeratin |
| $K_d$ | dissociation constant |
| kb | kilobase |
| kDa | kilodalton |
| LB | lysogeny broth |
| LDV | lactate dehydrogenase-elevating virus |
| LSB | Laemmli sample buffer |
| MA | mouse-adapted |
| MAVS | mitochondrial antiviral-signalling protein |

| | |
|---|---|
| MDA5 | melanoma differentiation-associated gene 5 |
| MERS | Middle East respiratory syndrome |
| MHV | mouse hepatitis virus |
| MINDY | motif interacting with Ub-containing novel DUB family |
| mISG15 | murine interferon-stimulated gene 15 |
| MJD | Machado-Joseph disease proteases |
| MLV | modified live virus |
| MOI | multiplicity of infection |
| mRNA | messenger RNA |
| MTase | methyltransferase |
| NEDD8 | neural precursor cell expressed developmentally downregulated protein 8 |
| NEM | N-ethylmaleimide |
| NEMO | NF-κB essential modulator |
| NF-κB | nuclear factor kappa-light-chain-enhancer of activated B cells |
| Ni-NTA | nickel nitrilotriacetic acid |
| NSDV | Nairobi sheep disease virus |
| nsp | non-structural protein |
| OAS | 2',5'-oligoadenylate synthetase |
| $OD_{600}$ | optical density at a wavelength of 600 nm |
| ORF | open reading frame |
| OTU | ovarian tumour protease |
| p.i. | post inoculation |
| PAGE | polyacrylamide gel electrophoresis |
| PBS | phosphate-buffered saline |
| PCR | polymerase chain reaction |
| PDB | Protein Data Bank |
| PEDV | porcine epidemic diarrhoea virus |
| PEG | polyethylene glycol |
| PFU | plaque-forming units |
| PKR | protein kinase R |
| $PLP/PL^{pro}$ | papain-like protease |
| PMSF | phenylmethanesulfonyl fluoride |
| polyUb | polyubiquitin |
| pp | polyprotein |
| PRRs | pattern-recognition receptors |
| PRRSV | porcine reproductive and respiratory syndrome virus |
| pt | post transduction |
| PTMs | post-translational modifications |
| qPCR | quantitative polymerase chain reaction |

| | |
|---|---|
| RBD | receptor-binding domain |
| RCHY1 | RING finger and CHY zinc-finger domain-containing 1 |
| RdRp | RNA-dependent RNA polymerase |
| Rev | Reverse |
| RIG-I | retinoic acid-inducible gene-I |
| RIP1 | receptor-interacting protein 1 |
| RLRs | retinoic acid-inducible gene-I-like receptors |
| RMSD | root-mean-square deviation |
| RPL13a | ribosomal protein L13a |
| RT | reverse transcription |
| RTC | replication and transcription complex |
| S | spike protein |
| SARS | severe acute respiratory syndrome |
| SDS | sodium dodecyl sulphate |
| SHFV | simian haemorrhagic fever virus |
| ssRNA | single-strandedRNA |
| STAT | signal transducers and activators of transcription |
| STING | stimulator of interferon genes |
| SUD | severe acute respiratory syndrome-unique domain |
| SUMO | small ubiquitin-like modifier |
| TBK1 | TANK-binding kinase 1 |
| $TCID_{50}$ | 50% tissue culture infectious dose |
| TGEV | transmissible gastroenteritis virus |
| TLR | toll-like receptor |
| $T_m$ | melting temperature |
| TM | transmembrane |
| TNFα | tumour necrosis factor alpha |
| TRAF | TNF receptor-associated factor |
| TRIF | TIR-domain-containing adaptor-inducing IFN-β |
| TYMV | turnip yellow mosaic virus |
| Ub | ubiquitin |
| Ub.wt | ubiquitin wild-type |
| Ub-3Br | ubiquitin-3-bromopropylamine |
| Ub-AFC | ubiquitin-7-amino-4-trifluoro-methylcoumarin |
| Ub-AMC | ubiquitin-7-amino-4-methylcoumarin |
| Ubl | ubiquitin-like |
| UbV | ubiquitin (sequence) variant |
| UCH | ubiquitin C-terminal hydrolase |
| USP | ubiquitin-specific protease |

| | |
|---|---|
| vDUB | viral deubiquitinating enzyme |
| VNT | virus neutralization test |
| wt | wild-type |
| ZUFSP | zinc finger with UFM1-specific peptidase domain protein |

## DUTCH SUMMARY

In de 17e eeuw nam Antoni van Leeuwenhoek voor het eerst micro-organismen waar met zijn zelfgebouwde microscoop. Nu weten wij dat er naast bacteriën, die waren gezien door van Leeuwenhoek, vele andere micro-organismen bestaan die infectieziekten kunnen veroorzaken, zoals schimmels, parasieten en virussen. Dit soort infecties kan onopgemerkt blijven maar kan ook leiden tot ernstige gezondheidsproblemen in het geïnfecteerde individu.

Virussen behoren tot de kleinste micro-organismen die we kennen, en zij infecteren niet alleen mensen maar in principe ook elke andere levensvorm. Een van de pioniers in het virusonderzoek was Martinus Beijerinck, een Nederlandse microbioloog die aan het eind van de 19e eeuw ontdekte dat de mozaïekziekte van tabaksplanten werd veroorzaakt door micro-organismen die zich vermenigvuldigden in de groeiende delen van de plant. Deze waarneming had een belangrijke implicatie, namelijk dat dit micro-organisme, dat later een virus bleek te zijn bestaande uit een complex van eiwit en nucleïnezuur, altijd een gastheer nodig heeft om zich daarin te kunnen repliceren. De interacties die zich voltrekken tussen het replicatieproces van het virus en de componenten en processen in de gastheercel hebben daardoor veel invloed op de uitkomst van de infectie. Dit proefschrift richt zich op een voorbeeld van dergelijke virus-gastheer interacties.

Door klimaat- en ecosysteemveranderingen, toenemende internationale reizen en handel is de verspreiding van virussen onvoorspelbaarder en slechter beheersbaar geworden. Recent zijn er grote virusuitbraken geweest van bijvoorbeeld het Ebolavirus en het Zikavirus met elk aanzienlijke sociale en economische impact. Zo werd in 2012 ook een nieuw coronavirus geïsoleerd, uit een patiënt die overleden was aan een combinatie van een acute longontsteking en nierfalen. Het virus werd Middle East respiratory syndrome coronavirus (MERS-CoV) genoemd en per september 2019 waren er 851 MERS-gerelateerde sterfgevallen geregistreerd. Op dit moment worden nog steeds met regelmaat nieuwe gevallen ontdekt, die waarschijnlijk ontstaan doordat het virus op de mens wordt overgedragen door dromedarissen, die de intermediaire gastheer zijn voor het oorspronkelijk uit vleermuizen afkomstige MERS-CoV.

Coronavirussen worden zo genoemd doordat het spike eiwit een trimeer vormt op de virale envelop waardoor een karakteristieke kroonvormige (kroon in het Latijn: corona) verschijning op het virusdeeltje te zien is als gebruik wordt gemaakt van een elektronenmicroscoop. Naast de virale structurele eiwitten bevat het virusdeeltje een RNA-genoom van positieve polariteit met een 5’ cap structuur en 3’ poly(A)-staart. Om een gastheercel te infecteren bindt het spike eiwit aan de cellulaire receptor waarna, via fusie van cellulaire en virale membranen, het RNA-genoom in de cel vrijkomt. Ribosomen vertalen dan als eerste een deel van het genoom in twee, gedeeltelijk overlappende eiwitten. Deze virale polyproteïnen worden tot functionele niet-structurele eiwitten geknipt door proteasen die onderdeel uitmaken van deze zelfde polyproteïnen. De niet-structurele eiwitten zorgen voor de transcriptie en replicatie van virale RNAs, wat uiteindelijk leidt tot de vorming van nieuwe virusdeeltjes in de geïnfecteerde cel. Deze worden uitgescheiden,

waarna infectie van nieuwe cellen kan plaatsvinden. Op dit moment zijn er geen antivirale vaccins of geneesmiddelen beschikbaar om MERS-CoV infecties te voorkomen of te behandelen.

Gastheercellen zijn uitgerust met primaire aangeboren mechanismen om (delen van) virussen te herkennen, zodat er maatregelen kunnen worden genomen om de gevolgen van een infectie te beperken. Als onderdeel van het aangeboren immuunsysteem kan viraal RNA worden herkend in de geïnfecteerde cel, hetgeen leidt tot activatie van signaaltransductieroutes en de productie van type I interferon en cytokinen. Het vrijkomen van interferon kan naburige cellen waarschuwen en ervoor zorgen dat infectie van deze cellen wordt tegengewerkt door het activeren van interferon-gestimuleerde antivirale genen. Ook zorgt activatie van het aangeboren immuunsysteem voor het rekruteren en activeren van cellen die betrokken zijn bij de zogenaamde adaptieve immuunrespons, die bestaat uit cellulaire en humorale afweer.

Een van de regulatiemechanismen die het aangeboren immuunsysteem aanstuurt is ubiquitinering, waarbij een klein eiwit genaamd ubiquitine, of ketens van meerdere ubiquitine moleculen, worden geconjugeerd aan andere eiwitten, bijvoorbeeld factoren betrokken bij de aangeboren immuunreacties. Deze koppeling van ubiquitine kan onder meer zorgen voor de specifieke activatie of afbraak van het betreffende eiwit. Ubiquitinering is een reversibele modificatie en er zijn deubiquitinerende enzymen (DUBs), proteasen, die ubiquitine kunnen verwijderen van eiwitten en daarmee het signaal opheffen.

Als evolutionaire reactie op het aangeboren immuunsysteem brengen coronavirussen, net als vele andere virussen, eiwitten tot expressie met activiteiten die het aangeboren immuunsysteem onderdrukken, om zo onder de radar van dit systeem te kunnen blijven en zich desondanks goed te kunnen vermenigvuldigen. Het werk beschreven in dit proefschrift betreft de interactie tussen het MERS-CoV papaine-achtige protease (papain-like protease; $PL^{pro}$) en de door ubiquitine-gereguleerde aangeboren immuniteit. Het $PL^{pro}$ is onderdeel van MERS-CoV niet-structureel eiwit 3 (nsp3) en primair betrokken bij het knippen van de virale polyproteïnen waardoor de drie N-terminaal gelegen niet-structurele eiwitten vrijkomen. Daarnaast is $PL^{pro}$ in staat om ubiquitine en interferon-gestimuleerd gen 15, een klein eiwit dat een ubiquitine-achtige vouwing heeft, te binden en los te knippen van substraten. Onze hypothese was dat deze DUB-activiteit door het virus gebruikt wordt om de activatie van het aangeboren immuunsysteem te onderdrukken. Om dit te kunnen bewijzen is het belangrijk om eerst een aangepast virus te genereren dat nog wel in staat is om de polyproteïnen te knippen, zodat het virus kan blijven repliceren, maar niet meer in staat is om ubiquitine te deconjugeren. Met behulp van een dergelijke virusmutant kan de functie van de DUB-activiteit worden bestudeerd. Om dit te kunnen realiseren zijn de kristalstructuren van MERS-CoV $PL^{pro}$ opgehelderd, zowel zonder als met gebonden ubiquitine, zodat precies duidelijk werd welke aminozuren van $PL^{pro}$ interacteren met ubiquitine (Hoofdstuk 2). Enkele van deze posities die op afstand liggen van het katalytische centrum van het protease werden vervolgens gemuteerd om zo de interactie met ubiquitine te verstoren. Vervolgens zijn

in cellijnen de activiteiten van het gemuteerde protease bestudeerd. Allereerst werd gekeken of het aangepaste protease nog in staat is om de herkenningssequentie tussen niet-structureel eiwit 3 en 4 te knippen. Daarnaast werd de DUB-activiteit vergeleken met die van het oorspronkelijke protease. Met name de V1691R aminozuurverandering zorgde ervoor dat het protease geen ubiquitine meer kon deconjugeren, terwijl het onverminderd het virale polyproteïne kon knippen. Ook was dit gemuteerde protease niet meer in staat om activatie van de interferon-bèta promoter te onderdrukken wanneer het aangeboren immuunsysteem werd gestimuleerd, iets wat het oorspronkelijke protease wel deed. Dit toonde aan dat specifiek de DUB-activiteit van MERS-CoV $PL^{pro}$ inderdaad immuunsysteem onderdrukkende werking heeft.

Om deze observaties in de context van een volledige virusinfectie te kunnen bevestigen werden enkele veranderingen in $PL^{pro}$, waaronder de V1691R mutatie, in het MERS-CoV genoom geïntroduceerd (Hoofdstuk 3). Deze gemuteerde virussen werden gekarakteriseerd in twee verschillende humane cellijnen, waarbij geen verschil in de productie van nieuwe virusdeeltjes meetbaar was in vergelijking met het wild-type virus. Wel was er in MRC5 cellen die geïnfecteerd waren met het mutante virus sprake van een verhoging van de mRNA niveaus van interferon-bèta en enkele interferon-gestimuleerde genen ten opzichte van met wild-type virus-geïnfecteerde cellen. Vervolgens is het virus met de V1691R mutatie gebruikt voor de infectie van muizen die de cellulaire MERS-CoV receptor tot expressie brengen, zodat ze vatbaar zijn voor het virus. De meerderheid van de muizen die het gemuteerde, DUB-negatieve virus kregen overleefde de infectie, terwijl het wild-type virus lethaal was voor deze muizen. Opvallend was dat de mRNA niveaus van interferonen, cytokinen en interferon-gestimuleerde genen sneller stegen in muizen die geïnfecteerd waren met het DUB-negatieve virus dan in muizen met een wild-type virusinfectie. Ook was deze respons beter gecontroleerd dan in de wild-type virus-geïnfecteerde muizen, waarin een vertraagde en daarna excessieve respons optrad. Daarnaast daalde de virus titers in de DUB-negatieve virus-geïnfecteerde muizen sneller dan in muizen die geïnfecteerd waren met het wild-type virus. Deze resultaten lieten voor het eerst zien dat de DUB-activiteit van MERS-CoV $PL^{pro}$ een rol heeft in het ontwijken van het aangeboren immuunsysteem, en dat deze functie belangrijk bijdraagt aan de virale pathogenese. Het uitschakelen van de DUB-activiteit van een coronavirus $PL^{pro}$ kan dus een manier zijn om het virus op een gecontroleerde manier te verzwakken, waarbij tegelijkertijd een sterkere aangeboren immuunreactie kan worden opgewekt. Deze aanpak kan daarom een basis vormen voor toekomstige vaccinontwikkeling.

Virale proteasen zijn essentiële enzymen in de replicatiecyclus van virussen en daardoor zijn ze vaak een aantrekkelijk doelwit voor de ontwikkeling van antivirale geneesmiddelen. Dit wordt in het geval van MERS-CoV $PL^{pro}$ echter bemoeilijkt doordat deze virale DUB structurele overeenkomstigheden heeft met humane DUBs, voornamelijk in het katalytische centrum, waartegen de meeste middelen gericht zijn. In Hoofdstuk 4 wordt de selectie en analyse van een nieuw soort antivirale eiwitten beschreven, als alternatief voor het meer klassieke gebruik van kleine chemische moleculen als antiviraal middel. Uit onderzoek was bekend dat de binding van ubi-

quitine en ubiquitine-achtige eiwitten met DUBs vaak kortdurend is en dat ze interacteren met niet-geconserveerde aminozuren van de DUB. Dit maakte het mogelijk om te onderzoeken of een ubiquitine sequentie variant (Ub variant) krachtiger zou kunnen binden aan $PL^{pro}$. Daarnaast zou, indien deze Ub variant bindt aan niet-geconserveerde aminozuren van de DUB, dit ook kruisreactie met cellulaire componenten kunnen voorkomen. Uit een bibliotheek met meer dan 10 miljard Ub varianten werden de beste vier varianten, de sterkste binders van het MERS-CoV $PL^{pro}$, geselecteerd. Op eenzelfde manier werden ook Ub varianten geïdentificeerd die aan de DUB van Krim-Congo hemorragische koorts virus bonden. *In vitro* bonden deze Ub varianten specifiek en met hoge affiniteit aan de virale DUBs en remden ze hun activiteit. Co-kristallisatie van de virale DUBs met de Ub varianten bracht de veranderingen ten opzichte van gewoon ubiquitine in kaart. Dit maakte duidelijk dat de sterke binding van de Ub varianten voortkwam uit verbeterde hydrofobe interacties en waterstofbrugnetwerken. Expressie van Ub varianten in cellen remde de activiteit van MERS-CoV $PL^{pro}$ en tijdens een infectie ook de replicatie en productie van nieuwe virusdeeltjes, waardoor de antivirale kracht van de Ub varianten duidelijk werd.

De Ub varianten die binden aan MERS-CoV $PL^{pro}$ werden verder gekarakteriseerd door de mutaties ten opzichte van wild-type ubiquitine te onderzoeken, zoals beschreven in Hoofdstuk 5. Met modificaties van specifieke posities in de Ub varianten is geprobeerd om de affiniteit verder te verhogen, helaas zonder aanzienlijk succes. Dit onderzoek toonde wel aan dat de sterkste binder aan $PL^{pro}$, ME.4, instabiel was. Dit probleem werd opgelost door de sequentie van het N-terminale gebied van ME.4 (aminozuren 1-14) te optimaliseren, zonder dat dit invloed had op de binding aan $PL^{pro}$ dan wel het remmen van de activiteit van $PL^{pro}$. Het resultaat was dat inderdaad hogere expressieniveaus van de gestabiliseerde Ub variant werden gevonden. Dit biedt een goede uitgangspositie om in vervolgstudies het beschermingsniveau vast te stellen dat Ub varianten kunnen bieden in een diermodel voor MERS-CoV infectie.

Naast MERS-CoV $PL^{pro}$ en de DUB van Krim-Congo hemorragische koorts virus zijn er meer virale DUBs ontdekt die virussen met een RNA-genoom tot expressie brengen. In Hoofdstuk 6 is een overzicht gemaakt van deze DUBs en is gefocust op de structuurbiologie van deze enzymen en hun functie tijdens infectie, voornamelijk toegelegd op de interactie met het aangeboren immuunsysteem.

## CURRICULUM VITAE

Robert Cornelis Martinus Knaap was born on December 8th, 1989 in Goes, the Netherlands. After completing his secondary education at 'het Goese lyceum' in 2007, he started to study Life Science & Technology at the Universities of Delft and Leiden. During his training, he completed a Science & Research-based business minor and a short internship at Leiden University Medical Center (LUMC). He completed a project at the departments of Toxicogenetics and Dermatology, under supervision of prof. dr. Leon Mullenders and dr. Frank de Gruijl, after which he received his Bachelor of Science degree in 2011. He continued with a Life Science & Technology research master programme, including a one-year internship at the LUMC department of Medical Microbiology. Supervised by dr. Peter Bredenbeek, he investigated RNA structure requirements for the generation of small flavivirus RNAs and their role in viral pathogenicity. After obtaining his Master's degree in 2012, he started with his PhD research at the LUMC department of Medical Microbiology under supervision of dr. ir. Marjolein Kikkert and prof. dr. Eric Snijder in 2013. Besides the research described in this PhD thesis, he was involved in a project aiming to create improved porcine reproductive and respiratory syndrome virus vaccines, which was a collaborative effort with MSD Animal Health NL / Intervet Nederland B.V and dr. Brian Mark and his team at the University of Manitoba, Winnipeg, Canada. In 2018, Robert was awarded a PhD transition fellowship from the Health programme of the European Institute of Innovation and Technology to further explore the potential of ubiquitin variants as antiviral agents. As part of this award, he followed the Institute of Biomedical Entrepreneurship London certificate program. Since 2019, he works as a researcher at the LUMC department of Medical Microbiology. In March 2020, Robert will continue his career as Scientist at the Analytical Development department at Janssen Vaccines and Prevention.

## LIST OF PUBLICATIONS

In chronological order

1. Paul P. Geurink, Gerbrand J. van der Heden van Noort, Monique P.C. Mulder, **Robert C.M. Knaap**, Marjolein Kikkert and Huib Ovaa (2019). Profiling DUBs and Ubl-specific proteases with activity-based probes. Methods Enzymol 618: 357-387.
2. Ben A. Bailey-Elkin, **Robert C.M. Knaap**, Marjolein Kikkert and Brian L. Mark (2017). Structure and function of viral deubiquitinating enzymes. J Mol Biol 429(22): 3441-3470.
3. Wei Zhang[#], Ben A. Bailey-Elkin[#], **Robert C.M. Knaap**[#], Baldeep Khare, Tim J. Dalebout, Garrett G. Johnson, Puck B. van Kasteren, Nigel J. McLeish, Jun Gu, Wenguang He, Marjolein Kikkert[*], Brian L. Mark[*] and Sachdev S. Sidhu[*] (2017). Potent and selective inhibition of pathogenic viruses by engineered ubiquitin variants. PLoS Pathog 13(5): e1006372.
4. Huib H. Rabouw, Martijn A. Langereis[#], **Robert C.M. Knaap**[#], Tim J. Dalebout, Javier Canton, Isabel Sola, Luis Enjuanes, Peter J. Bredenbeek, Marjolein Kikkert, Raoul J. de Groot and Frank J.M. van Kuppeveld (2016). Middle East respiratory coronavirus accessory protein 4a inhibits PKR-mediated antiviral stress responses. PLoS Pathog 12(10): e1005982.
5. Ben A. Bailey-Elkin[#], **Robert C.M. Knaap**[#], Garrett G. Johnson, Tim J. Dalebout, Dennis K. Ninaber, Puck B. van Kasteren, Peter J. Bredenbeek, Eric J. Snijder, Marjolein Kikkert[*] and Brian L. Mark[*] (2014). Crystal structure of the Middle East respiratory syndrome coronavirus (MERS-CoV) papain-like protease bound to ubiquitin facilitates targeted disruption of deubiquitinating activity to demonstrate its role in innate immune suppression. J Biol Chem 289(50): 34667-34682.
6. Puck B. van Kasteren, **Robert C.M. Knaap**, Paul van den Elzen, Eric J. Snijder, Udeni B.R. Balasuriya, Erwin van den Born and Marjolein Kikkert (2015). *In vivo* assessment of equine arteritis virus vaccine improvement by disabling the deubiquitinase activity of papain-like protease 2. Vet Microbiol 178(1-2): 132-137.

[#] These authors contributed equally to this work.

[*] These authors contributed equally to this work.